Adjustment of the decay kinetics of photogenerated endoperoxides embedded in various carrier materials aiming at medical applications

DISSERTATION ZUR ERLANGUNG DES DOKTORGRADES DER NATURWISSENSCHAFTEN (DR. RER. NAT.) DER NATURWISSENSCHAFTLICHEN FAKULTÄT IV -CHEMIE UND PHARMAZIE-

DER UNIVERSITÄT REGENSBURG

vorgelegt von

Damir Posavec

aus Sisak, Kroatien

im Oktober 2010

Die vorliegende Arbeit entstand in der Zeit von November 2006 bis September 2010 unter der Anleitung von Herrn Prof. Dr. Günther Bernhardt am Institut für Pharmazie der Naturwissenschaftlichen Fakultät IV – Chemie und Pharmazie- der Universität Regensburg und Herrn Prof. Dr. Günther Knör am Institut für Anorganische Chemie der Technisch-Naturwissenschaftliche Fakultät der Johannes Keppler Universität Linz.

Das Promotionsgesuch wurde eingereicht am: 05. Oktober 2010

Tag der mündlichen Prüfung: 10. November 2010

Prüfungsausschuss: Prof. Dr. J. Wegener (Vorsitzender)

Prof. Dr. G. Bernhardt (Erstgutachter)

Prof. Dr. G. Knör (Zweitgutachter)

Prof. Dr. B. Dick (Prüfer)

Acknowledgements

I kindly thank:

Prof. Dr. G. Bernhardt, Prof. Dr. G. Knör and Dr. U. Bogner for supervision of this mutidisciplinary work, for constructive critics when reading this thesis, for their support and help in search of solutions of any issues that occured during this work, for numerous discussions and for assistance in organizing and preparing all the equipment and materials used in this work;

Dr. S. Nagl of the Institute of Analytical Chemistry, University of Leipzig for all the advice and help regarding polymer nanoparticles preparation, in particular PVB nanobeads;

All coworkers of Institute of Physical and Theoretical Chemistry (chair Prof. Dr. B. Dick), University of Regensburg for hospitability and use of laboratory equipment, and especially Dr. K. Sadeghian for discussions and help making three dimensional figures of endoperoxide molecules;

The Department of Pharmaceutical/Medicinal Chemistry II (chair Prof. Dr. A. Buschauer), Institute of Pharmacy, University of Regensburg and its coworkers for enabling the use of pharmaceutical equipment and a very friendly atmosphere; especially Dr. D. Gross, M. Lopuch and Dr. N. Pop for help regarding confocal microscopy, Dr. M. Memminger, Dr. P. Höcherl, Dr. M. Kühnle, S. Dirrigl, M. Beer-Krön, U. Nördemann for tutoring and help regarding the cell handling and the chemosensitivity assay;

All coworkers of Institute of Inorganic Chemistry (chair Prof. Dr. G. Knör), Johannes Keppler University Linz for a very relaxed atmosphere while staying in Linz, especially Dr. W. Schöfberger and L. M. Reith for numerous ^{13}C and ^{1}H NMR measurements and discussions, Dr. U. Monkowius for help regarding many „small“ problems; and B. Fröhlich for help and patience with bureaucratic issues;

Dr. Y. Yenilmez Akkurt and Dr. B. Akkurt of the Istanbul Technical University (Istanbul, Turkey) for help with the synthesis of novel porphyrin derivatives;

The Department of Pharmaceutical Technology (chair Prof. Dr. A. Göpferich), Institute of Pharmacy, University of Regensburg, especially Dr. M. Breunig for introductionary course

and allowance to use the confocal miscroscope and K. Pollinger for advice regarding particle dispersion measurements on Malvern Zetasizer 3000 HR;

Institute of Analytical Chemistry, Chemo- and Biosensors (chair Prof. Dr. O. Wolfbeiss), University of Regensburg, especially Dr. A. Dürkop and the group of PD Dr. M. Schäferling for extensive use of spectrometers during measurements and information regarding ethyl cellulose nanoparticles;

Dr. R. Müller (Institute of Physical Chemistry II (chair Prof. Dr. W. Kunz), University of Regensburg) for FTIR measurements and advice regarding polymer esterification reaction;

H. I. Siegmund and Dr. J. Schröder (Institute of Pathology, University Hospital Regensburg) for prompt transmission electron microscopy measurements;

Dr. M. Frank of Kuraray Specialities Europe GmbH (Frankfurt, Germany) for donation of polyvinyl butyral Mowital LPB 16H;

Osram GmbH (Regensburg, Germany) for lending the blue (λ=420 ± 10 nm) high-power LED

J. Putzger and E. Hans (Faculty of Physics, University of Regensburg) for the construction of the diode laser's collimator optics and of the cooling systems of the high-power LEDs;

F. Czentner for collaboration in the preparation and measurements of PVB film samples;

N. Bachhuber for collaboration in the preparation and measurements of liposome samples;

Department of Pharmacology and Toxicology (chair Prof. Dr. J. Schlossmann), Institute of Pharmacy, University of Regensburg for use of a laboratory centrifuge;

Dr. R. Czerwieniec (Institute of Physical and Theoretical Chemistry, University of Regensburg) for most of all patience and for advice regarding chemical synthesis;

Deutsche Forschungsgemeinschaft (DFG) for the scholarship in the graduate college GRK 640 Sensory Photoreceptors in Natural and Artificial Systems;

My friends and family for the emotional support.

TABLE OF CONTENTS

ABBREVIATIONS

$^1O_2$	singlet oxygen
$^3O_2$	triplet oxygen
A	(Arrhenius) pre-exponential factor
Ab	antibody
A_C	yield of thermal endoperoxide cycloreversion
A_D	yield of thermal endoperoxide decomposition
ALA	5-aminolevulinic acid
ATCC	American Type Culture Collection
BP	band pass filter
CCD	charge-coupled device
CLSM	confocal laser scanning microscopy
CTAB	cetyltrimethylammonium bromide
D	diffusion coefficient
D	donor molecule
DCC	dicyclohexylcarbodiimide
ddH_2O	doubly distilled water
Deep Red	Cell Mask Deep Red plasma membrane stain
DHPN	N,N'-di(2,3-dihydroxypropyl)-1,4-naphthalenedipropanamide
DLS	dynamic light scattering
DMAP	N,N-dimethylaminopyridine
DMF	N,N-dimethylformamide
DMN	1,4-dimethylnaphthalene
DMPC	1,2-dimyristoyl-L-α-phosphatidylcholine
DMSO	dimethylsulfoxide
DNA	deoxyribonucleic acid
DPA	9,10-diphenylanthracene
DPBF	1,3-diphenylisobenzofurane

E	energy
E_a	(Arrhenius) activation energy
EC	ethyl cellulose
EI-MS	electron impact mass spectroscopy
EPO	endoperoxide
EPR	enhanced permeability and retention
FCS	fetal calf serum
FDA	United States Food and Drug Administration
FDE	fast-decaying endoperoxides
H	hydrogen
HPD	“hematoporphyrin derivative”
HPMA	*N*-(2-hydroxy- propyl)methacrylamide
hν	light photon
I_{abs}	overlap of the light source intensity and the absorption of a sensitizer
IARC	International Agency for Research on Cancer
IR	infra-red
ISC	intersystem crossing
k	endoperoxide decay rate constant
LDL	low-density lipoproteins
LED	lihgt-emitting diode
LP	long pass filter
MB	methylene blue
MNEA	4-methyl-*N,N,N*-trimethyl-1-naphthaleneethanaminium chloride
MNP	4-methyl-1-naphthalenepropanoate
MS	mass spectroscopy
MSDS	material safety datasheet
*m*THPC	*m*-tetrahydroxyphenylchlorin
N	derivative of 1,4-dimethylnaphthalene

N_A	Avogadro's number
NDMOL	1,4-naphthalenedimethanol
NDP	1,4-naphthalenedipropanoate
NE	derivative of 1,4-dimethylnaphthalene-1,4-endoperoxide
NIR	near infra-red
NMR	nuclear magnetic resonance
NP	nanoparticle
N1	1,4-dimethylnaphthalene
N1E	1,4-dimethylnaphthalene-1,4-endoperoxide
N2	1,4,5-trimethylnaphthalene
N2E	1,4,5-trimethylnaphthalene-1,4-endoperoxide
N3 ethanone	1-(1,4-dimethyl-naphthalen-2-yl)-ethanone 1-(1,4-dimethyl-naphthalen-2-yl)-
N4	1-(1,4-dimethyl-naphthalen-2-yl)-ethanol
N4	1-(1,4-dimethyl-naphthalen-2-yl)-ethanol-1,4-endoperoxide
N5	di-1-(1,4-dimethylnaphthene-2-yl)-ethylether
N5E	di-1-(1,4-dimethylnaphthene-2-yl)-ethylether-1,4-endoperoxide
N6	1,4-dimethyl-2-vinylnaphthalene
N7	poly**(**1,4-dimethyl-2-vinylnaphthalene)
N7E	poly**(**1,4-dimethyl-2-vinylnaphthalene-1,4-endoperoxide)
OPO	optical parametric oscillator
P	power
PBCA	poly(butylcyanoacrylate)
PBS	phosphate buffered saline
PCS	photon correlation spectroscopy
PDT	photodynamic therapy
PEG	poly(ethylene glycol)
PDLA	poly(D-lactide)

PLA	poly(D,L-lactide)
PLLA	poly(L-lactide)
PLGA	poly(D,L-lactide-coglycolide)
PpIX	protoporphyrin IX
PpIX-DME	protoporphyrin-IX-dimethylester
PS	photosensitizer
PVAL	poly(vinyl alcohol)
PVB	polyvinyl butyral
PTC	*N,N'*-bis(2,6 -dimethylphenyl)- perylene-3,4,9,10- tetracarboxylic diimide
P1	5,10,15,20-tetrakis-(4-methyl-naphthyl)porphyrin
P2	5,10,15,20-tetrakis-(4-methyl-naphthyl)porphyrinato-zinc(II)
Q_C	quantum yield of endoperoxide cycloreversion
Q_D	quantum yield of endoperoxide decomposition
r	diffusion radius
ROS	reactive oxygen species
RT	room temperature
S	the irradiated area of the cell
S_1	lowest excited singlet state
SDE	slow-decaying endoperoxides
SDS	sodium dodecyl sulfate
SF	(endoperoxide) stability factor
t	time
t_u	cellular uptake time period
$t_{1/2}$	endoperoxide decay (half-life) time
T	temperature
T_c	temperature of liposome phase transition from gel to liquid-crystalline phase
TEM	transmission electron microscopy
TEMED	N,N,N',N'-tetramethylethane-1,2-diamine

THF	tetrahydrofuran
TPFPP-Pd(II)	5,10,15,20-tetrakis-(2,3,4,5,6-pentafluorophenyl)-porphyrin-Pd(II)
UV	ultraviolet
V	reaction volume
ZnTPP	zinc(II)-meso-tetraphenylporphyrin
$\Delta H\neq$	activation enthalpy
$\Delta S^{\neq}$	activation enthropy
Φ	light flux
ϕ_{Δ}	singlet oxygen yield
ϕ_{ISC}	inter-system crossing yield
λ	wavelength
τ	lifetime

1. GENERAL INTRODUCTION

1.1. SINGLET OXYGEN

1.1.1. Photophysical Properties

The lowest lying excited electronic state of dioxygen (see below) is $O_2(a^1\Delta_g)$ [1, 2]. Historically $O_2(a^1\Delta_g)$ has simply been called "singlet oxygen", thus distinguishing it from the triplet ground state that is 94.2 kJ/mol lower in energy (Fig. 1.1.) Reactions of singlet oxygen are associated with significant applications in several fields, including organic synthesis, bleaching processes, and, most importantly, the photodynamic therapy.

Molecular oxygen has a remarkable electronic structure, as its highest occupied electronic level is constituted of two degenerate π^* orbitals. In the ground state each of two unpaired electrons lies in one π^* orbital and their spins are parallel, thus molecular oxygen is a triplet biradical, $O_2(X^3\Sigma_g^-)$ [1] or short $^3O_2$, in the ground state. The lowest electronically excited state is a singlet state, $O_2(a^1\Delta_g)$, with 2 electrons in the same π^* orbital with anti-parallel spin and energy of 94.2 kJ/mol or 0.977 eV, which shows a NIR phophorescence at 1269 nm (see Fig. 1.1.) However, the second electronically excited state is also a singlet state, $O_2(b^1\Sigma_g^+)$, in which both anti-parallel spins aren't paired. The energy difference to the ground state is 156.9 kJ/mol or 1.627 eV and the emission occurs at 762 nm. Although it has been speculated that the singlet sigma state, $O_2(b^1\Sigma_g^+)$, could play a role in solution-phase systems, it has only recently become possible to address this issue using direct spectroscopic measurements, see review article [1]. Because the relaxation to the triplet ground state from both of these excited states is spin forbidden, the 1269 nm and 762 nm emission are very weak. [3] For more details see review article [4]. In further text, the descriptor singlet oxygen ($^1O_2$) will be used for the lowest excited singlet state.

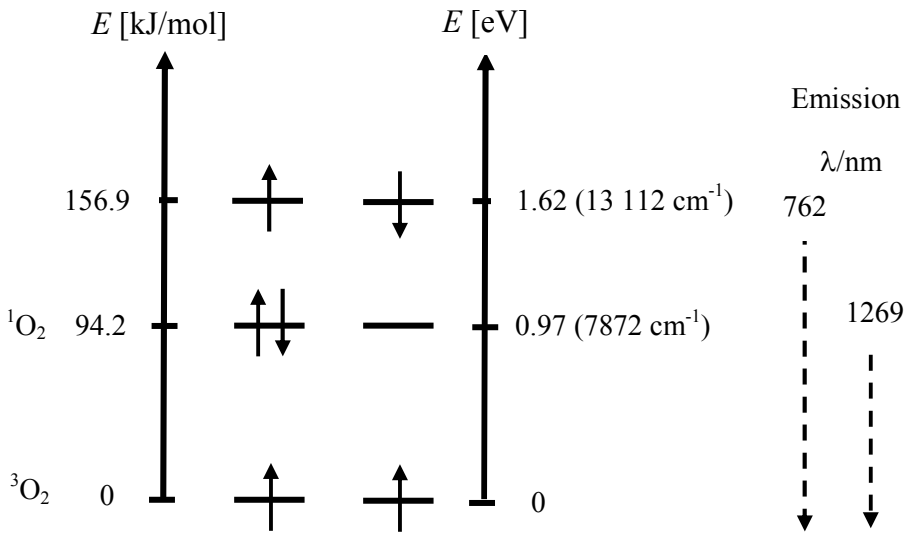

Figure 1.1. Simplified energy diagram of dioxygen ($1\pi_g$)-orbital electron states: ground state and first two excited states.

1.1.2. Biophysical Properties

In Table 1.1. lifetimes of $^1O_2$ in various solvents are given. The $^1O_2$ lifetime in water is about 5 μs and the diffusion radius over a period *t* of twice its lifetime can then be estimated using a diffusion coefficient, *D*, for oxygen in water of $2 \cdot 10^{-5}$ cm^2 s^{-1} [5], according to equation 1 [6]:

$$r = (6tD)^{1/2} \qquad (1)$$

to be about 350 nm. However, this is rather controversial, because the same research group in a recent report [7] measured the singlet oxygen lifetime in cytoplasm and nucleus of HeLa cells using the time-resolved singlet oxygen phosphorescence signals and found it to be in 30-40 μs range. But, despite a relatively long intracellular lifetime, singlet oxygen did not diffuse a great distance from its site of production by irradiation of a sensitizer. This is a consequence of an apparent intracellular viscosity that is comparatively large [7].

Table 1.1. $^1O_2$ lifetimes in various solvents. [3]

solvent	*t*/μs	solvent	*t*/μs	biological environment	*t*/μs
acetone	34-65	diethylether	26-35	water	3.3-7.4
acetonitrile	54-69	ethanol	10-15	blood plasma	1.0
chloroform	160-265	THF	20-30	leukemia cells	0.17-0.32

Thus, due to its high reactivity, singlet oxygen has a short lifespan in a cellular environment and limited diffusivity in tissue, which will be further discussed in Chapter 6.1.

1.1.3. $^1O_2$ Generation and Photochemical Properties

Through interaction with photosensitizers (PS) $^3O_2$ can be converted into other reactive oxygen species (ROS). Various possible interactions of excited PS in the triplet state ^{3}PS*, with molecular oxygen are usually divided into three kinds of reactions [3].

Type I processes lead to the production of free radicals or radical ions, via hydrogen or electron transfer:

$$^{1,3}PS^* + H - M \longrightarrow PS - H^\bullet + M^\bullet \quad (2)$$

which can then react with $^3O_2$ to form peroxides, peroxyl radicals etc. Type II reactions generate $^1O_2$ via energy transfer from ^{3}PS* (see equation 3). Type II reactions, in contrast, require an energy transfer mechanism from the triplet-state sensitizer to the ground state molecular oxygen, [8]:

$$^3PS^* + {}^3O_2 \longrightarrow PS + {}^1O_2 \quad (3)$$

Type III reactions involve reductive quenching of an excited photosensitizer and electron transfer from a donor, D, with subsequent reduction of $^3O_2$, in case of suitable redox potentials:

$$\begin{aligned} {}^{1,3}PS^* + D &\longrightarrow PS^{\bullet-} + D^{\bullet+} \\ PS^{\bullet-} + {}^3O_2 &\longrightarrow PS + O_2^{\bullet-} \end{aligned} \qquad (4)$$

Another possibility which belongs to Type III reactions is photoinduced electron transfer from excited photosensitizer to ground-state oxygen and superoxide-anion generation with subsequent regeneration of PS with electron transfer from a donor molecule, D:

$$\begin{aligned} {}^{1,3}PS^* + {}^3O_2 &\longrightarrow PS^{\bullet+} + O_2^{\bullet-} \\ PS^{\bullet+} + D &\longrightarrow PS + D^{\bullet+} \end{aligned} \qquad (5)$$

It is difficult to differentiate which of the three reaction types is occurring upon irradiation of a photosensitizer. When a PS absorbs light in the visible region, usually fast energy transfer (Type II) dominates and Type III reactions occur in the background. If a PS has a relatively high triplet-state energy (UV absorption), Type III reactions are more pronounced because a larger range of potential donors may be oxidized. Type I reactions dominate in the case of PS with n-π* configurations, such as ketones and anthrachinones. [3]

To determine the singlet oxygen quantum yields of various photosensitizers several methods are used:

- $^1O_2$ phosphorescence measurements at 1269 nm [9]
- stationary and time-dependent photothermal and photoacoustic methods [10]
- chemical quenching of $^1O_2$ using selective probes, such as 1,3-diphenylisobenzofuran (DPBF) [11]

Apart from interactions with photosensitizers, the mentioned reactive oxygen species (ROS) including $^1O_2$ can also be generated from various other reactions. For example, $^1O_2$ is known to be formed in almost quantitative yields by oxidation of hypochlorite with hydrogen peroxide, by disproportionation of H_2O_2 catalyzed with MoO_4^{2-} or WO_4^{2-}, by reduction of ozone with triphenylphosphite, by reactions in biological systems catalyzed with peroxidases or oxygenases, or by the thermolysis of polycyclic aromatic endoperoxides [12]. Unfortunately, these chemical sources of $^1O_2$ are not compatible with conditions required by

biological systems (aqueous environment, neutral pH). Therefore, efforts have been devoted to develop suitable $^1O_2$ generators based on endoperoxide thermolysis.

1.2. AROMATIC ENDOPEROXIDES AS A SINGLET OXYGEN SOURCE

1.2.1. Endoperoxide Formation

Many polycyclic aromatic hydrocarbons are able to trap singlet oxygen. Some of the endoperoxides (EPOs), thus obtained, exhibit the exceptional feature of releasing oxygen, frequently in the excited singlet state, under heating or UV irradiation. [13] More than 400 EPOs derived from polycyclic aromatic hydrocarbons have been described in the literature. [14] Most of them were prepared by photosensitized oxygenation involving a [4+2]cycloaddition of $^1O_2$ on the electron-rich carbons of the aromatic substrate (Fig. 1.2.)

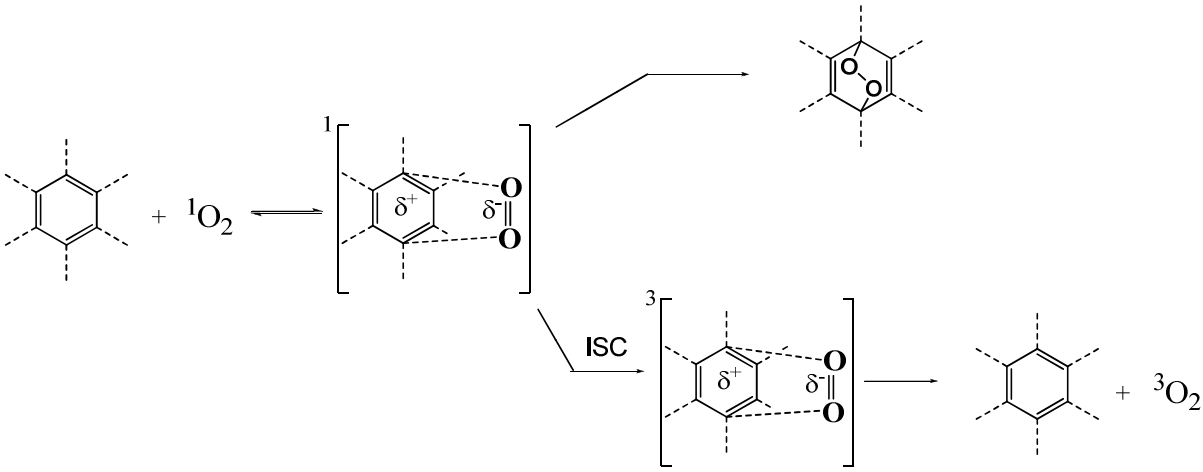

Figure 1.2. Mechanism of [4+2] cycloaddition of $^1O_2$ on aromatic hydrocarbons.

The reactivity of aromatic hydrocarbons toward $^1O_2$ increases with the electron density of the aromatic substrate, reflecting the electrophilic nature of $^1O_2$. [15] A first structural effect is the number of fused rings of the substrate. The comparison of anthracene, tetracene, and pentacene shows that the reactivity increases by about 2 orders of magnitude for each supplementary fused ring. [13] The grafting of electron-releasing groups on the site of $^1O_2$ addition increases the rate constants in the order $H < C_6H_5 < CH_3 \leq OCH_3$. For example, 1-methylnaphthalene reacts slowly with $^1O_2$, whereas naphthalene itself is completely unreactive. In the same way, neither benzene, toluene, xylene, nor tri- and

tetramethyl benzene react with $^1O_2$, whereas penta- and hexamethyl-benzene provide the corresponding EPOs as primary oxidation products. [13] Steric strain is also an important parameter which can modify both the reactivity of the substrate and the regioselectivity of the cycloaddition of $^1O_2$. Peri-interactions between two neighboring methyl groups bound to a polycyclic aromatic hydrocarbon enhance its reactivity toward $^1O_2$ because the steric strain is somewhat relieved in the transition state. This phenomenon explains why, for example, 1,8-dimethylnaphthalene is 4 times more reactive than the 1,5-isomer. [13]

The cycloaddition of $^1O_2$ to 1,4-dimethylnaphthalene (DMN) and derivatives has been studied in many solvents. It was found that the rate constant of $^1O_2$ addition increases by more than 2 orders of magnitude from cyclohexane to formamide and it was even much higher in water when using water-soluble derivatives of DMN. This strong solvent effect on kinetics is thought to be caused by several solvent parameters, including dipolarity, polarizability, and solubility. [16]

The mechanism of [4+2] cycloaddition of $^1O_2$ to conjugated systems [16 - 18] is assumed to be very similar to the concerted mechanism of the Diels-Alder reaction. A theoretical study suggests that $^1O_2$ addition occurs through a single-step concerted mechanism with a symmetric transition structure exhibiting significant charge transfer from the organic donor to oxygen. [17]. The first step of the reaction involves the reversible formation of an exciplex in the singlet state. This exciplex exhibits a charge-transfer character due to the strong electron attraction by $^1O_2$. Subsequently, the solvated exciplex either collapses through a concerted mechanism into EPO (chemical quenching of $^1O_2$) or goes through a spin-forbidden intersystem crossing (ISC), giving a triplet state complex which dissociates into $^3O_2$ and the starting substrate (physical quenching of $^1O_2$). [18]

Under suitable conditions, appropriate aromatic substrates can trap most of the $^1O_2$ available, even when the rate of $^1O_2$ generation is very low because the concentration of EPO formed is proportional to the cumulative amount of $^1O_2$ generated. Water-soluble derivatives of rubrene, anthracene and methylnaphthalene are typical examples of this type of traps. [19] Chemical trapping by water-soluble aromatic hydrocarbons is also specific for $^1O_2$ and can be much more sensitive than monitoring the $^1O_2$ luminescence at 1275 nm for quantification of $^1O_2$ in aqueous media.

The reversibility of oxygen binding to polycyclic aromatic compounds was discovered by Dufraisse. [20, 12] The state of released oxygen by thermolysis of aromatic EPOs was determined by Wasserman and Larsen using EPO of 9,10-diphenylanthracene (DPA). [21,

12] When warmed to 80 °C, this EPO decays to the parent molecule and oxygen, with 32 % being $^1O_2$. [12] In general, two primary pathways of transformation compete during thermolysis or photolysis of aromatic EPOs (Fig. 1.3.): cycloreversion, leading to the parent aromatic molecule and to oxygen, in a singlet or a triplet state; and homolytic cleavage of the peroxide bond, followed by rearrangement to more or less stable diepoxides or decomposition, leading to hydroxy-ketones or quinones. Endoperoxide thermolysis proceeds with A_C, the yield of thermal cycloreversion, and A_D, the yield of thermal decomposition: $A_D = 1 - A_C$. During photolysis Q_C, quantum yield of cycloreversion, and Q_D, quantum yield of decomposition apply. The relative amount of both processes depends on endoperoxide structures and experimental conditions.

1.2.2. Endoperoxide Thermolysis

The ratio between cycloreversion and cleavage may depend on the relative activation energies, as stated by Turro et al. [22] The activation enthalpy $\Delta H\neq$ for cycloreversion increases from benzenic [23] to naphthalenic [24] and 1,4-anthracenic EPOs, and then to the meso-substituted ones. Consequently, the cleavage starts to compete with cycloreversion in meso-substituted anthracenic EPOs, as well as in even more condensed analogues. However, the cycloreversion is greatly favored over cleavage by the presence of aromatic substituents at the peroxide bridgehead meso positions (for example, EPOs of DMN or DPA).

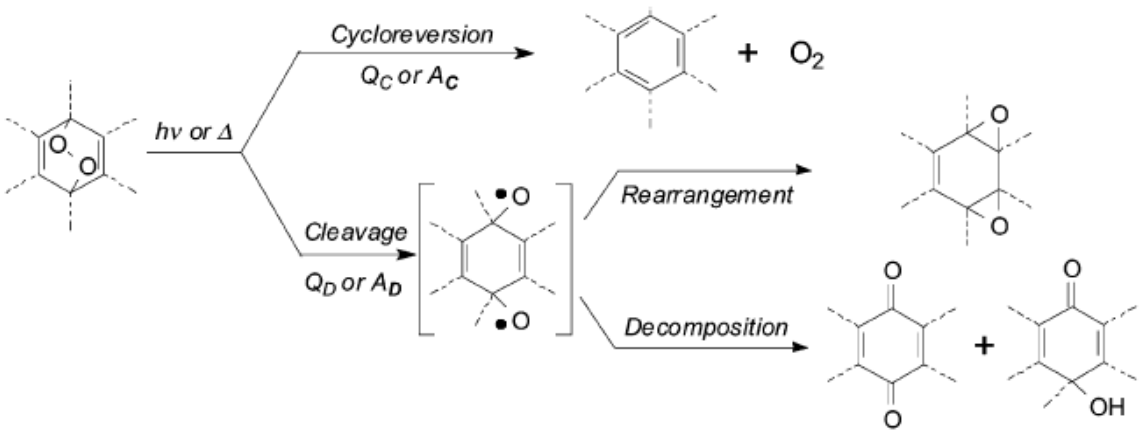

Figure 1.3. Mechanism of endoperoxide transformation during thermolysis or photolysis.

A mechanistic hypothesis for thermal cycloreversion has also been suggested by Turro et al., [22] where they found that the yields of generated $^1O_2$ were much higher for EPOs of parent molecules with endoperoxide bridge on 1,4 positions of the aromatic cyclic core (e.g. 1,4-dimethyl-9,10-diphenylanthracene-1,4-endoperoxide), than for the 9,10-position of endoperoxide bridge, (e.g. 1,4-dimethyl-9,10-diphenylanthracene-9,10-endoperoxide). This hypothesis was based on the observation that activation enthropies, $\Delta S^{\neq}$ for EPOs of 1,4-type were 0 or slightly negative, while substantially positive values (+30 to +40 $JK^{-1}mol^{-1}$) were found for EPOs of 9,10-type.

This Turro hypothesis invokes the two basic and potentially competing pathways for EPO thermolysis, as shown in Fig. 1.4.: a) a concerted mechanism, producing $^1O_2$ quantitatively, which would take place with 1,4-endoperoxide type, and b) a sequence leading successively to diradicals, at first singlet diradical, ^1D, and then triplet, ^3D, which are able to fragment to $^1O_2$ and $^3O_2$, respectively. The latter would take place with 9,10-endoperoxide type. Thus, a quantitative prediction of the yield of evolved $^1O_2$ would not be possible. When homolysis of the peroxidic bond competes with cycloreversion, rearrangement and decomposition occur (Fig. 1.3.). For more detail, see references [13, 22].

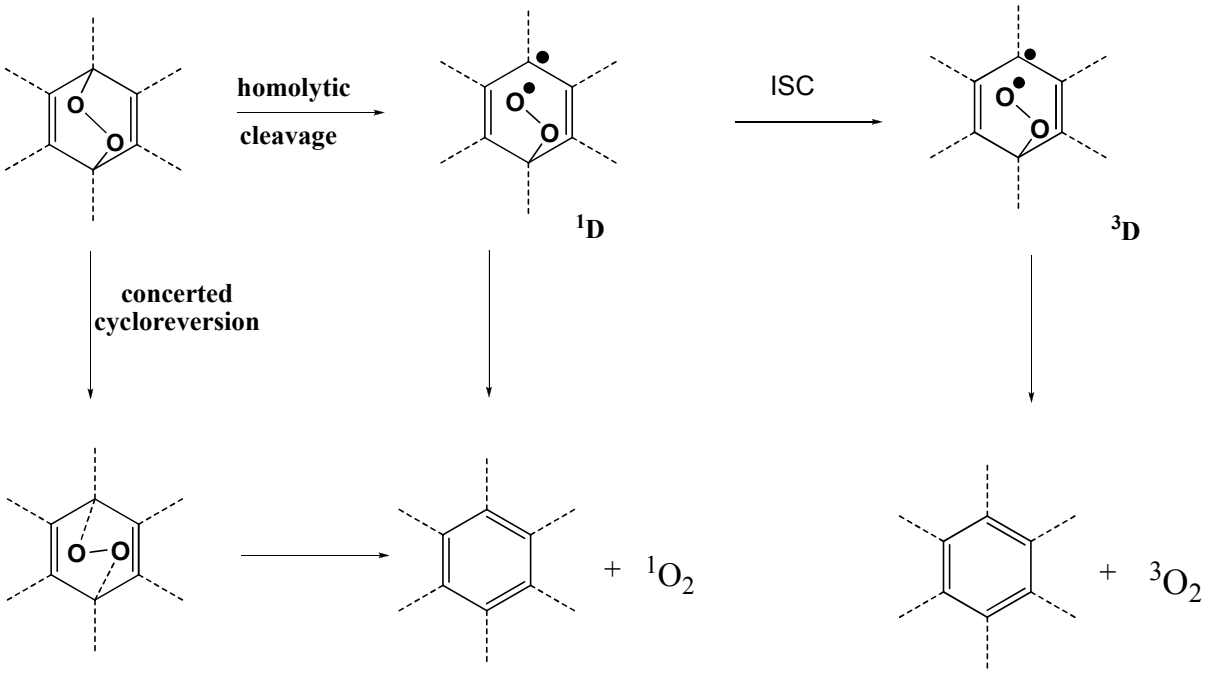

Figure 1.4. Scheme of competing pathways during endoperoxide thermolysis.

1.2.3. Endoperoxide Photolysis

The same primary reactions as during thermolysis (Fig. 1.4.) compete during photolysis of EPOs. Irradiation of the 9,10-endoperoxide of 9,10-diphenylanthracene with wavelengths $\lambda > 250$ nm initiates cycloreversion, yielding the parent molecule and O_2, whereas $\lambda > 400$ nm excitation initiates O-O bond cleavage and rearrangement producing a diepoxide, which undergoes irreversible subsequent reactions. [25] The detailed study of many EPOs showed that decomposition occurs from the lowest excited singlet state $S_1(\pi^*_{OO}\sigma^*_{OO})$, corresponding to the locally excited peroxide chromophore, with quantum yield Q_D^{S1}. [26, 27] Nonsubstituted aromatic EPOs have maximum values of A_D and Q_D^{S1}. These values are smaller if the atoms next to the O-O bridge are bound to methyl or phenyl groups and even smaller if the phenyl substituents are additionally bound to the anthracene frame. [13]

It was shown that cycloreversion of EPOs originates from an upper excited $\pi\pi^*$ singlet state, and that O_2 is produced in its excited singlet state. [28] Further investigations revealed that cycloreversion of EPOs generally leads to formation of $^1O_2$ and ground-state parent aromatic molecule in 1:1 ratio and occurs from upper excited $S_n(\pi\pi^*)$ ($n \geq 2$), but not from S_1 ($\pi^*_{OO}\sigma^*_{OO}$) state. Moreover, cycloreversion quantum yield Q_C increases for many nonsymmetrical EPOs stepwise with decreasing λ, indicating that cycloreversion occurs from several excited $S_n(\pi\pi^*)$ ($n = 2, 3...$) states. [29, 30]

1.2.4. Aromatic Endoperoxides as Singlet Oxygen Carriers

In general, EPOs are metastable and endoperoxide formation is a reversible reaction, see equation 6. When induced by thermolysis or photolysis EPOs are able to revert to the parent aromatic molecule releasing a mixture of $^1O_2$ and $^3O_2$. The rate of EPO decay via cycloreversion pathway and $^1O_2$ yield both depend on the same structural, steric and solvent effects stated above for the endoperoxide formation. Whereas electron density is the main determinant of EPO formation, steric factors are most important in influencing the stability of EPOs [31]. It could be argued that even aromatic hydrocarbons with low electron density, such as benzene, toluene, naphthalene do form EPOs with a too short of lifetimes to be

detectable. On the other hand, there are EPOs too stable for $^1O_2$-release by thermolysis, in which case photolysis is the only option. For example, up to four oxygen molecules are bound in the self-sensitized photoreaction of octaphenyltetraanthraporphyrazinato palladium complex, Fig. 1.5. [32] This fascinating complex with four endoperoxide bridges releases step-by-step all O_2 when excited by consecutive two-photon absorption at 662 nm.

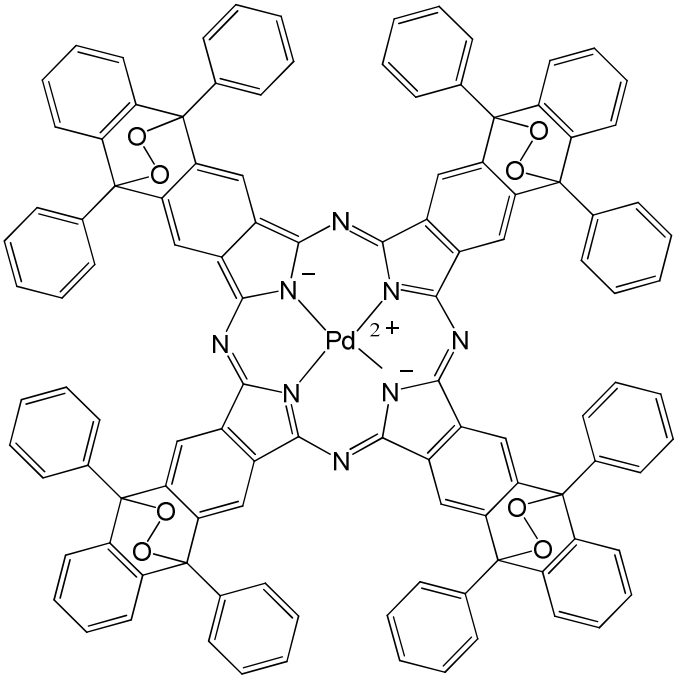

Figure 1.5. Example of a thermally stable self-sensitized complex with four endoperoxide bridges on anthracene substituents. [32]

However, the focus of this work is on the endoperoxide thermolysis, not on photolysis. In order to achieve a chemical source of $^1O_2$ in biological media, many efforts to develop suitable $^1O_2$ generators based on the thermolysis of water-soluble naphthalene endoperoxides (equation 6) have been made. [12]

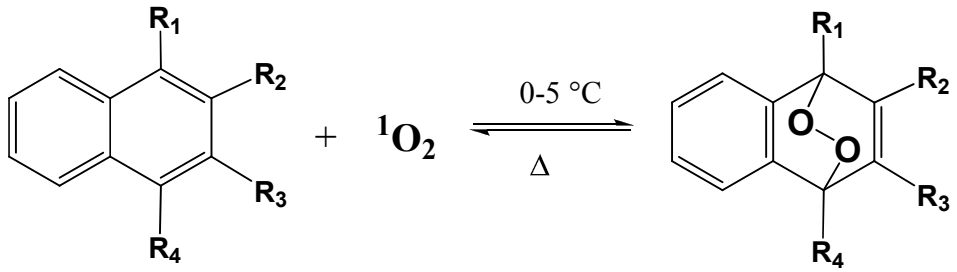

(6)

R_1 = CH_2-CO_2Na	$R_2 = R_3 = R_4 = H$	**MNP**
$R_1 = R_4$ = CH_2-CO_2Na	$R_2 = R_3 = H$	**NDP**
R_1 = CH_2-$N(CH_3)_3Cl$	$R_2 = R_3 = R_4 = H$	**MNEA**
$R_1 = R_4$ = CH_2-CONH-CH_2-CHOH-CH_2OH	$R_2 = R_3 = H$	**DHPN**
$R_1 = R_4$ = CH-(CONH-CH_2-CHOH-$CH_2OH)_2$	$R_2 = R_3 = H$	
R_1 = CH_2-CO_2Na, $R_2 = R_4 = H$	R_3 = CH_2-CH_2-CO_2Na	
$R_1 = R_4$ = CH_2-CO_2Na	$R_2 = R_3$ = CH_3	

The first prepared water-soluble $^1O_2$ carriers were 4-methyl-1-naphthalenepropanoate (MNP), [33, 12] and anionic disodium 1,4-naphthalenedipropanoate (NDP), [34] bearing one or two sodium propanoate substituents grafted onto the 1,4 positions of the naphthalene core. However, these anionic compounds release $^1O_2$ in the aqueous phase, far from potential biological targets in medical applications. Subsequently, a second generation of $^1O_2$ carriers with specific groups, such as quaternary ammonium group in 4-methyl-*N,N,N*-trimethyl-1-naphthaleneethanaminium chloride (MNEA), or nonionic hydrophilic groups in 1,4-naphthalenedimethanol (NDMOL) or N,N'-di(2,3-dihydroxypropyl)-1,4-naphthalenedipropanamide (DHPN), has been synthesized.

All the mentioned water-soluble naphthalenic carriers of $^1O_2$ can be prepared from the cheap 1-methylnaphthalene compound as a starting material [12], as presented in Fig. 1.6.

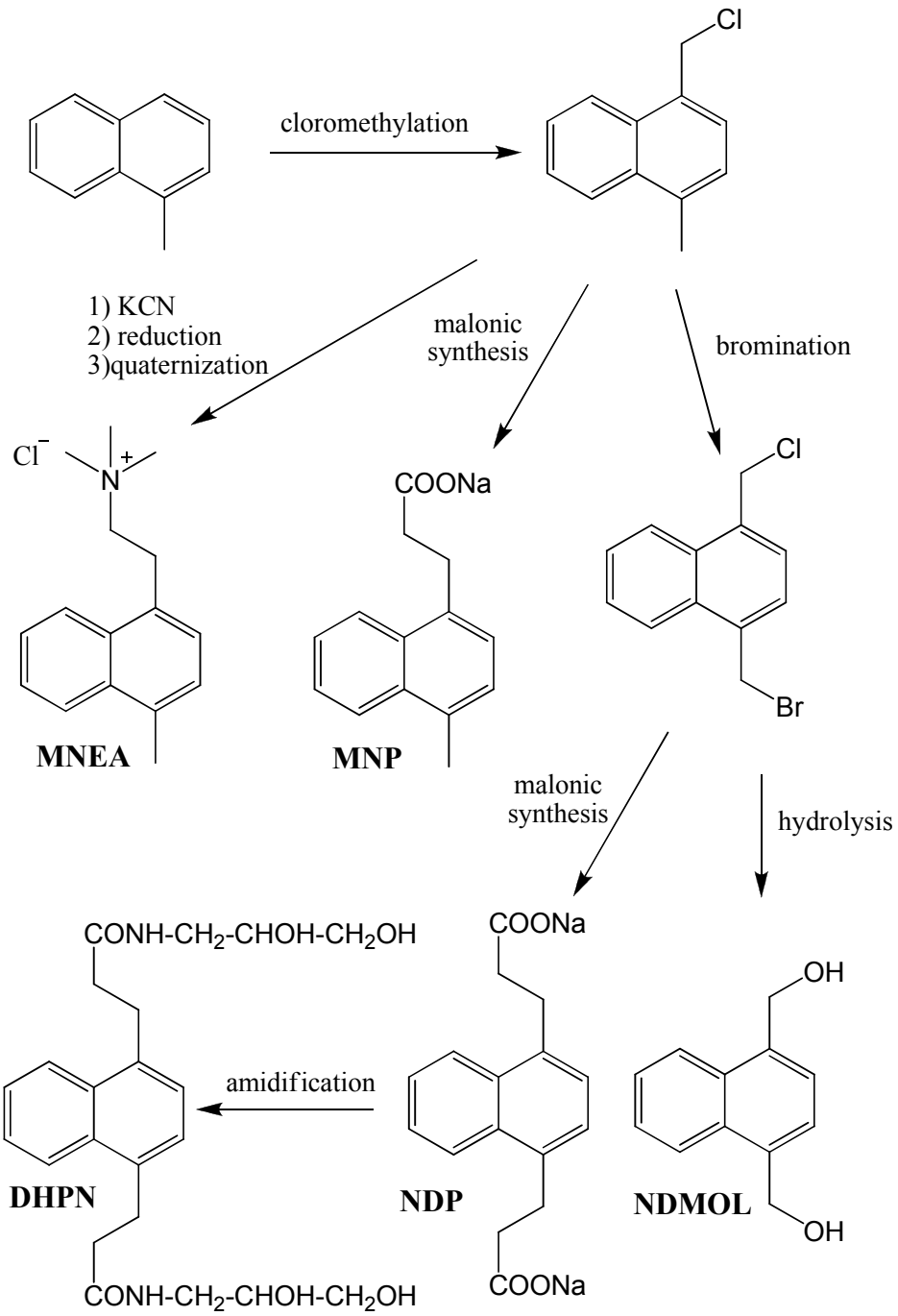

Figure 1.6. Reaction pathways for synthesis of water-soluble naphthalenic carriers of $^1O_2$.

The interaction of $^1O_2$ with a naphthalene derivative **N** can be described by reactions 7 and 8. Singlet oxygen produced by a chemical or photochemical source (see Chapter 1.1.3.) is either quenched by **N** with rate constant k_q (reaction 7) or it reacts with forming an endoperoxide, **NE**, with rate constant k_r (reaction 8). The overall reactivity of **N** toward $^1O_2$ can be expressed by the sum ($k_r + k_q$), which is readily determined by flash photolysis.

$$^1O_2 + \mathbf{N} \xrightarrow{k_q} {}^3O_2 + \mathbf{N} \quad (7)$$

$$^1O_2 + \mathbf{N} \xrightarrow{k_r} \mathbf{NE} \quad (8)$$

To explain the difference in reactivity of 1,4-substituted carriers toward $^1O_2$, two phenomena have to be considered: the electron density of the naphthalene core and the steric hindrance induced by the substituents. Electronic effects are of primary importance when a short spacer separates the hydrophilic group from the naphthalene core. Thus, the electron-attractive effect by the quaternary ammonium group of MNEA or by the –OH groups of NDMOL cause 5 and 17 times, respectively, lower $^1O_2$ reactivity than for the MNP compound. [12] Longer alkyl spacers increase the electron density of the aromatic ring, but the resulting steric hindrance lowers the rate of reaction with $^1O_2$ significantly. For instance, the overall rate constant (k_r + k_q), of NDP ($2.8 \cdot 10^6$ M^{-1} s^{-1}) and of the more crowded DHPN ($1.0 \cdot 10^6$ M^{-1} s^{-1}) are much lower than the value for MNP ($7.0 \cdot 10^6$ M^{-1} s^{-1}). [12] For very crowded and poorly reactive compounds**,** 5,8-cycloaddition of $^1O_2$ competes with the usual $^1O_2$ addition on the 1,4-positions. [35] The reactivity of naphthalene compounds can be considerably increased by grafting supplementary methyl groups on the same ring. [19, 36] However, the half-life time of such EPOs becomes > 50h at 37 °C in water, converting these compounds into $^1O_2$ traps.

1.2.5. Aromatic Endoperoxides' Decay Kinetics

Thermolysis of naphthalenic EPOs (equation 9) gives back oxygen quantitatively according to first-order kinetics with a rate constant *k*.

$$\mathbf{NE} \xrightarrow[\text{water}]{37\ ^\circ C} \mathbf{N} + \alpha\ {}^1O_2 + (1-\alpha)\ {}^3O_2 \quad (9)$$

From rate constant *k* value, typically the half-life time of a specific endoperoxide is calculated: $t_{1/2} = \ln 2 / k$. In Table 1.2. half-life times of EPOs of water-soluble naphthalene derivatives at 37 °C in water and cumulative yields of produced $^1O_2$ by EPO thermolysis are given. [12]

Table 1.2. Half-life times of endoperoxides in water at 37 °C and $^1O_2$ yields by endoperoxide thermolysis. [12]

EndoPerOxide of	MNP	NDP	MNEA	NDMOL	DHPN
$t_{1/2}$ (min)	23	23	22	70	23
$^1O_2$ yield (%)	45	50	65	51	59

The only systematic study concerning the stability of EPOs of various naphthalene derivatives has concentrated on the influence of steric factors connected with the pattern of alkyl substitution on naphthalene core using experimental as well as theoretical calculation data [31]. Half-life times of EPOs of various methylnaphthalene derivatives at 25 °C in $CDCl_3$ from this reference are given in Table 1.3.

Table 1.3. Stability of methylnaphthalene endoperoxides in $CDCl_3$ at 25 °C, determined by ^1H NMR. [31]

EndoPerOxide	$t_{1/2}$ (h)
1,4-dimethylnaphthalene-1,4-endoperoxide	5
1,8-dimethylnaphthalene-1,4-endoperoxide	30
1,2,4-trimethylnaphthalene-1,4-endoperoxide	70
1,4,5-trimethylnaphthalene-1,4-endoperoxide	290
1,2,3,4-tetramethylnaphthalene-1,4-endoperoxide	indefinite

1.2.6. Polymeric Carriers of Singlet Oxygen

Polymer-immobilized naphthalenes have been obtained by grafting the sodium salt of MNP on a chloromethylated styrenedivinyl benzene beads or by polymerization of methylsubstituted vinylnaphthalene [37, 38, 39]. After photosensitized oxygenation, both systems give EPOs storable at low temperature. Half-life times of EPOs of polymer-immobilized methylnaphthalene derivatives at 30 °C in dichloromethane [38] are given in Table 1.4. The $t_{1/2}$ values at 37 °C were calculated using the $t_{1/2}$ values at 30 °C and values of Arrhenius activation parameters E_a and ln A [38].

Table 1.4. Half-life time values for thermolysis of polymer-immobilized naphthalene EPOs in dichloromethane.

EndoPerOxide	$t_{1/2}$ (min) at 30 °C	$t_{1/2}$ (min) at 37 °C
Poly(1,4-dimethyl-6-vinylnaphthalene-1,4-endoperoxide)	80	31
Poly(1,2,4-trimethyl-6-vinylnaphthalene-1,4-endoperoxide)	419	153

Unfortunately, these hydrophobic polymers are unsuitable for aqueous media because the corresponding EPOs, prepared by photooxygenation, do not release a significant amount of $^1O_2$ in water. Despite considerable efforts devoted to this problem, the design of polymeric carriers of $^1O_2$ suitable for aqueous media remains an open challenge.

1.2.7. Endoperoxide Characterization

The naphthalene endoperoxides are characterized by their spectroscopic properties. In the IR, the aromatic band at 1580-1600 cm^{-1} disappears on photooxidation and a strong band appears at 1200-1250 cm^{-1}. The UV absorption spectrum, endoperoxide formation is indicated by the disappearance of the naphthalene band at about 290 nm [31]. Hence, the EPOs thermolysis reaction rate can be conveniently determined by using UV absorption spectrometry to follow the rise of naphthalene concentration (corresponding to the absorption peak) with time [12, 31, 38].

1.3. SINGLET OXYGEN APPLICATION IN THE PHOTODYNAMIC THERAPY

Photodynamic therapy (PDT) is a strategy for treatment of cancer and other diseases with a combination of a photosensitizer and oxygen molecules which are present at the site of the treatment. Over the past decades, there was a period of intense PDT investigation, both in the laboratory and in the clinic. Although still widely considered to be an academic technique, its status and value within modern clinical practice gradually continues to grow. The PDT has to date been dominated by a small number of pharmaceutical companies and is used mostly by the scientists and clinicians involved in fundamental research. Pharmaceutical formulation development has been limited.

PDT is based on the singlet oxygen generation after the irradiation of an intracellular photosensitising drug (which possesses no dark toxicity) with subsequent biochemical events to cause selective cell destruction [40]. When the photosensitizer is introduced into the body, it accumulates in tumour cells and a light source of appropriate wavelength (visible or near-infrared) and intensity is then used to irradiate the target tissue [41, 42]. Light irradiation activates the drug through electronic excitation and triggers a series of cytotoxic reactions, which can be dependent on, or independent of, the generation of reactive oxygen species [43]. Typical photosensitizers (PS) used, such as tetrapyrrole derivatives, have a closed-shell electronic configuration, which leads to a singlet state in their lowest energy or ground state level, with no unpaired electron spins (Fig. 1.7.) [44, 45]. Following the absorption of a photon of a specific wavelength, the photosensitizer molecule is promoted to an excited state, ^{1}PS*, which is also a singlet state and is usually short-lived with a half life between 10^{-6} and 10^{-9} seconds [45, 46]. The photosensitizer can return to the ground state by emitting light energy as photons (fluorescence) or by internal conversion with energy loss as heat. Alternatively, the molecule may convert to the triplet state, ^{3}PS*. This conversion occurs via intersystem crossing which involves a change in the spin multiplicity [47].

$$PS \xrightarrow{h\nu} {}^1PS^* \xrightarrow{ISC} {}^3PS^* \qquad (10)$$

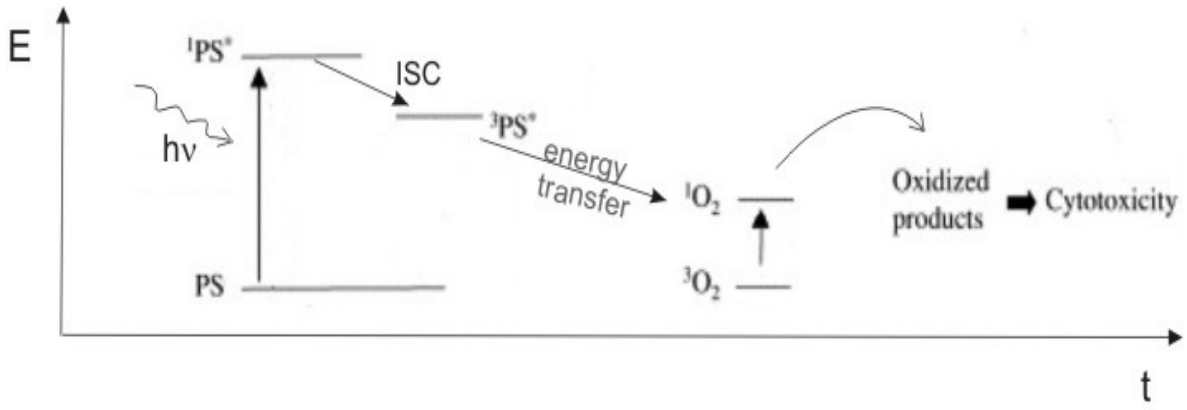

Figure 1.7. Mechanism of PDT cytototoxicity: a simplified scheme of relevant photophysical processes and reactions represented in a modified Jablonski diagram.

The triplet state photosensitizer has lower energy than the singlet state but has a longer lifetime, typically in the μs to ms range. PS in both singlet and triplet state can interact with surrounding oxygen molecules to form reactive oxygen species (see Chapter 1.1.3., reactions Type I-III). These reactive species, such as singlet oxygen and superoxide and peroxide anions, then attack cellular targets [48]. However, Type I reactions (equation 2) do not necessarily require oxygen and can cause cellular damage directly, through electron transfer processes and the action of free radicals, which may include sensitizer radicals.

Moreover, via Type II reactions (equation 3) a sufficient concentration of highly cytotoxic singlet oxygen, $^1O_2$, is produced to induce irreversible cell damage [45, 46]. In addition, the photosensitizer is not necessarily destroyed, but can return to its ground state by phosphorescence without chemical alteration and may be able to repeat the process of energy transfer many times [47]. Alternatively, the sensitizer may return to the ground state by transferring its energy to molecular oxygen, and may even be destroyed by photobleaching due to oxidation [49]. Evidently, many effects of PDT are oxygen-dependent and rely on the oxygen tension within the target tissue. Type I and Type II reactions can occur simultaneously and the ratio between the two depends on many factors, such as the photosensitizer, substrate, oxygen concentration and sensitizer to substrate binding [48].

Singlet oxygen, formed in Type II mechanism, is widely believed to be the major damaging species in PDT [40, 41, 45]. However, the Type I reactions are most efficient at low oxygen and high substrate concentrations. [50]

The PDT efficiency crucially depends on the chemistry of the PS, the pharmaceutical formulations, the localization and the amount of PS in treated tissue, time of activation with light, the light doses and the amount of oxygen in irradiated region.

1.3.1. Photosensitizers Used for Photodynamic Therapy

The choice of a photosensitizer and its subsequent phototherapeutic effect depends on its physicochemical properties in the ground and excited states, pharmacokinetic and pharmacodynamic behavior, and photoactivity in vivo. Ideally, the photosensitizer should have the following properties: high selectivity, a high tumour to normal tissue accumulation ratio, rapid accumulation in tumour tissue, efficient body clearance, stability against molecular oxygen or other reactive oxygen species (ROS) generated in situ, no toxicity in dark state, have a high inter-system crossing yield, ϕ_{ISC} from $^1PS^*$ to $^3PS^*$ with a long lifetime of $^3PS^*$ state, to allow efficient energy or electron transfer to the oxygen molecule (energy $E[^3PS^*] > E[^1O_2]$ is a prerequisite for one photon excitation), thus having a high singlet oxygen yield, ϕ_Δ. Moreover, a photosensitizer should show intensive absorption bands within the phototherapeutic window (ca. 620-850 nm), but its absorption in the range from 400-600 nm should be as low as possible. This requirement is necessary to allow sufficient absorption inside the tissue and to avoid prolonged skin sensitivity toward solar irradiation following drug administration. Furthermore, PS should be sufficiently stable under physiological conditions. An amphiphilic character of the compound is advantageous, enabling its uptake and accumulation in membranes and cytoplasm. [51, 52]

The first-generation photosensitizers in PDT are based on chemically modified natural hematoporphyrin. The most widely used first generation PS in clinical PDT is photofrin® [51], a purified “hematoporphyrin derivative” (HPD), porphyrin mixture containing several porphyrins, monomers as well as dimers and oligomers [46]. However, first-generation PS posses certain limitations such as weak absorption in the phototherapeutic window, ill-defined chemical composition, as well as a relatively poor specificity of uptake and retention

with respect to malignant and healthy tissues. In addition, they cause prolonged skin photosensitivity (usually 2-3 months). [52]

Subsequent extensive research helped to develop modern photosensitizers of the second and third generations. The second generation PDT sensitizers are mainly based on engineered, synthetic, and semisynthetic porphyrins with various substituents at the pyrrole rings and the methylene bridges [52] (see Fig. 1.8.) They are structurally homogeneous compounds with long-wavelength absorption bands of high intensity. So far many compounds have been tested as potential photosensitizers for application in PDT. [52, 53] They can be divided into the following groups: organic dyes (eosin, rose bengal, methylene blue), aromatic hydrocarbons (naphthalenes, anthracenes, biphenyls, quinines), tetrapyrrole and metallo-tetrapyrrole compounds (e.g. porphyrins, chlorins, bacteriochlorins, phthalocyanines, naphthalocyanines, texaphyrins, Fig. 1.8.) [52, 54]

In Table 1.5. some examples of singlet oxygen yields of selected second-generation PS are given. [55]

Table 1.5. Singlet oxygen yields, ϕ_Δ, of selected second-generation photosensitizers in various solvents. [55]

PS	Solvent	ϕ_Δ	PS	Solvent	ϕ_Δ
Bacteriochlorophyll a	C_6H_6	0.38	Chlorophyll b	$C_6H_5CH_3$	0.75
Methylene blue	EtOH H_2O	0.52 0.60	Porphyrin-Zn(II)	C_6H_6	0.68
Phthalocyanine-Zn(II)	EtOH DMF	0.53 0.51	Porphyrin, metal free	C_6H_6	0.63

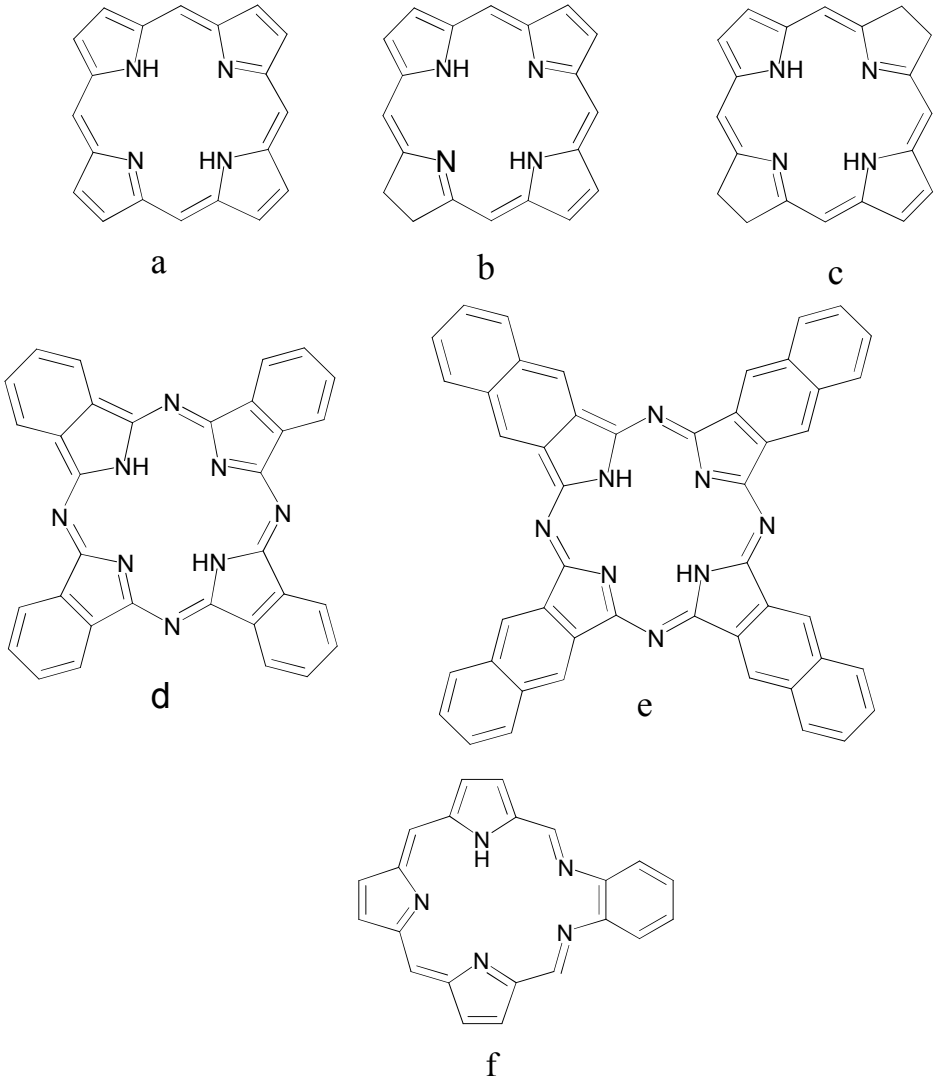

Figure 1.8. Structures of tetrapyrrolic photosensitizers: (a) porphyrin, (b) chlorin, (c) bacteriochlorin, (d) phthalocyanine, (e) naphthalocyanine, and (f) texaphyrin.

The third-generation PS consist of the photosensitizer moiety linked to biomolecules such as monoclonal antibodies used for targeting, in order to allow selective delivery. [56]

Other photosensitizers which have been already accepted for clinical applications are a precursor of protoporphyrin IX (PpIX), 5-aminolevulinic acid (ALA) and its methyl, hexyl and benzyl ester derivatives; and the synthetic *m*-tetrahydroxyphenylchlorin (*m*THPC) as well as the luthetium texaphyrin complex. [46, 51, 57, 58] Aminolevulinic acid is a small, water-soluble, prodrug that is the naturally occurring precursor in the biosynthetic pathway of heme in mitochondria. Administration of excess of exogenous ALA avoids the negative feedback control that heme exerts over its biosynthetic pathway. Due to the limited capacity of ferrochelatase to convert PpIX into heme, the presence of an excess of exogenous ALA in

cells induces accumulation of PpIX [59, 60]. This effect is pronounced in sebaceous glands and also in neoplastic cells. [61]

1.3.2. Light Sources Used in the PDT

Typically, light fluxes of 50–500 J/cm^2 of red light are needed in clinical PDT with photofrin®. [46] New sensitizers, e.g., mTHPC, are usually more efficient, mainly due to larger extinction coefficients in the red region. Consequently, a smaller light flux is required, typically 10 J/cm^2. [62] If the surface irradiance exceeds 200 mW/cm^2, local heating (hyperthermia) may also contribute to the PDT effect. [63, 64, 65, 66] For interstitial treatment with diffusing fibers inserted into the tumor, the hyperthermia limit is below 400 mW/cm^2 diffusing fiber [66]. Diode lasers giving a few watts of red light down to 630 nm are now commercially available and are probably the light sources of choice if only one sensitizer is to be used. [67] For surface irradiation LED arrays may be applied. However, for scientific purposes wavelength variation is necessary. Dye lasers, which can give up to a few watts of light in the red and near infrared region, have been the most widely used as light sources in PDT. For pumping the dye lasers either argon ion, copper vapors, or frequency-doubled Nd-YAG lasers are being used. The sophisticated state-of-the-art light sources used are pulsed lasers based on nonlinear crystal oscillators, so-called optical parametric oscillators (OPOs), which can be tuned in a very wide wavelength region (220–2200 nm). [68]

1.3.3. Medical Indications of the PDT

To date, clinical applications of PDT have been limited to areas of the body easily amenable to irradiation from laser or incoherent light sources. Consequently, PDT has been primarily investigated as a treatment for tumours of the skin, bladder, mouth and female reproductive tract [40 - 43]. The first health agency approval for PDT (with photofrin®) was obtained in 1993 in Canada for the prophylactic treatment of bladder cancer [69]. Subsequently, approvals for photofrin® were obtained in the Netherlands and France for treatment of advanced esophageal and lung cancers; Germany for treatment of early stage lung cancer; Japan for early stage lung, esophageal, gastric, and cervical cancers as well as

cervical dysplasia; and in the United States for advanced esophageal cancer. In 1998 U.S. Food and Drug Administration (FDA) approved photofrin for use in PDT off early stage lung cancer. [46]

In recent years, PDT has also been employed to treat other non-neoplastic diseases occurring at body sites accessible to irradiation, such as psoriasis, age-related macular degeneration of the eye and microbiological infections of skin wounds, burns and ulcers [70, 71, 72].

ALA, a photosensitiser prodrug with a relatively low molecular weight of 167.8 daltons, is the most frequently employed agent in modern anti-cancer PDT [65]. ALA is typically applied to lesions in a topical cream, solution or patch-based formulation. PDT, based on topical application of ALA, has been successfully used in the treatment of basal cell carcinoma, actinic keratosis, Bowen's disease, vulval intraepithelial neoplasia, vulval Paget's disease and cervical intraepithelial neoplasia. [73]

Results and patents based on formulations and clinical studies of ALA and derivatives thereof are described extensively in a review by Donelly et al. [61] Clinical status of PDT of advanced stage esophageal tumors, lung cancer, head and neck cancers**, s**uperficial bladder cancer and brain tumors using photofrin® and new sensitizers such as *m*THPC is reviewed in detail by Dougherty et al. [46]

1.3.4. Mechanism of Tumour Destruction by the PDT

PDT *in vivo* acts through at least three principal modes: (i) direct cell killing by lethal oxidative damage of tumor cells (necrosis, apoptosis); (ii) indirect cell killing due to photodynamic damage or shutdown of the (neo)vasculature with loss of oxygen and nutrients supply to the tumor; and (iii) additional antitumor contributions from the inflammatory and immune responses. [74]

The reactive oxygen species (and especially singlet oxygen) produced during the PDT are responsible for irreversible damage to various cell membranes including plasma, mitochondria, lysosomal and nuclear membranes and of protein modifications, depending on the PS localization site. Sensitizers that localize in mitochondria, like photofrin, or are produced in mitochondria, like 5-aminolevulinic acid (ALA)-induced protoporphyrin IX, are likely to induce apoptosis, while sensitizers localized in the plasma membrane are likely to

cause necrosis during light exposure [46]. There are reports that PDT can rapidly induce apoptosis, both *in vitro* [75, 76] and *in vivo* [77, 78]. Apoptosis is a mechanism whereby organisms initiate cellular death *via* a process that is normally part of the genetic apparatus [79]. The end result is fragmentation of nuclear DNA and dissociation of the cell into membrane-bound particles that are surrounded by adjoining cells, minimizing release of inflammatory products. A novel feature of PDT is the rapid apoptosis as the DNA ladders appear as early as 30 minutes after photodamage.

Biological targets of $^1O_2$ include unsaturated fatty acids, proteins, and DNA. [12] This, combined with the facts that normal tissue may not contain photosensitizer or may not be perfused by blood vessels damaged by PDT, means that healthy tissue is usually unaffected by exposure to light [41].

However, a parameter that can limit direct tumor cell death is the reduced availability of oxygen within the tissue undergoing PDT treatment. Two mechanisms can produce such limitations: The photochemical consumption of oxygen during the photodynamic process and the effects of PDT on the tissue microvasculature. The rate of oxygen consumption during photofrin–PDT can be enough to move a fraction of the tumor into very low levels of oxygenation, outpacing the rate of oxygen diffusion from the capillaries, and shrinking the radius of oxygenated tissue volume around them [80]. Preliminary clinical studies at the Roswell Park Cancer Institute showed oxygen depletion also occurring during PDT in patients. The kinetics for this depletion varied from very rapid (within seconds of light exposure) to slow (>10 minutes of light exposure) and to no effect at all in basal cell carcinoma lesions in patients undergoing photofrin (1 mg/kg)–PDT at a light dose rate of 150 mW/cm^2. [46]

The oxygen supply in the tissue can also be diminished by the damaging effects of PDT on the microvasculature. With high doses of certain photosensitizers, e.g., photofrin, these effects can be sufficient to limit the oxygen supply to the tumor during PDT [81].

1.3.5. Limitations and Drawbacks of the PDT

The main limitation of PDT is the depth of light penetration through human tissue, typically no more than 1 cm, depending on the light source energy. Thus, the application of PDT is restricted to the treatment of tumours on or under the skin, or on the lining of some

internal organs. PDT is less effective in treatment of large tumours and metastases and is mostly used as a complementary treatment with chemotherapy. Therefore, it is a local treatment, comparable to a surgery. Typically, the tumour surgery is preferred in comparison to PDT, except for cosmetically relevant cases (e.g. facial treatment). Moreover, after the treatment the patient has to avoid excessive exposure to sunlight if a photosensitizer has accumulated in healthy tissues.

1.4. DRUG DELIVERY SYSTEMS USED IN THE PDT

As most photosensitizers are characterized by high lipophilicity, various encapsulation strategies have been studied to protect the hydrophobic photosensitizer from the aqueous environment. Ideally, the drug delivery system should be biodegradable, have minimum immunogenicity, incorporate the photosensitizer without loss or alteration of its activity and provide an environment where the photosensitizer can be administered in monomeric form (reducing aggregation which can decrease singlet oxygen quantum yields). Importantly, the delivery system should enable selective accumulation of the PS within the diseased tissue in therapeutic concentrations with little or no uptake by non-target cells.

Delivery systems based on micellar oil-dispersions, liposomes, hydrophilic polymer-photosensitizer conjugates or polymeric particles (nanoparticles and microparticles) have been developed, with varying degrees of success. Oil-based micellar drug formulations using polyoxyethylated castor oils (e.g., polysorbate-80, cremophor-EL etc.) enhance drug loading and improve tumour uptake over free drugs, presumably due to the interaction with plasma lipoproteins in blood. However, such emulsifying agents elicit acute hypersensibility (anaphylactic) reactions. Liposomal formulations can substantially improve efficacy and safety of photosensitizers, but are generally unable to establish elevated tumour-to-normal tissue ratios, because of short plasma lifetimes. [82]

Nanoparticles (NPs) have a great potential as drug carriers because (a) they can transport hydrophobic drugs in blood, (b) their large surface area can be modified with functional groups for additional chemical/biochemical properties, (c) they have large volumes of distribution and are generally taken up efficiently by cells; (d) controlled release of drug is possible; and (e) numerous synthetic strategies exist. [82] Nanoparticle coating with poly(ethylene glycol) (PEG) increases the blood circulation time and subsequent accumulation in tumors. This is due to the “enhanced permeability and retention effect” observed in solid tumors whereby circulating nanoparticles are trapped in tumors by a combination of leaky vasculature, poor lymphatic drainage and increased vessel permeability. [83]

An extensive review about carrier materials, especially nanoparticles, used in PDT with a functional classification of nanoparticles in PDT dividing them into passive carriers and active participants in photosensitizer excitation was written by Chatterjee et al. [82]

Passive carriers are then sub-classified by material composition into (a) biodegradable polymer-based nanoparticles and (b) non- biodegradable nanoparticles, e.g. ceramic (silica) and metallic (gold, iron oxide) nanoparticles. Biodegradable NPs are based mainly on polyesters poly(D,L-lactide-coglycolide (PLGA)) and poly(D,L-lactide (PLA)). For example, Alleman et al. [84] have studied the potential incorporation of phthalocyanine derivatives into PLA, which is approved by U. S. Food and Drug Administration. Active nanoparticles can be sub-classified by mechanism of activation into photosensitizer nanoparticles, [85, 86] self-illuminating nanoparticles [87] and upconverting nanoparticles [88].

It should be pointed out that the effectiveness of photosensitizer drug delivery to the tumour cells using biodegradable PLGA nanoparticles depends on the particle size [89]. This could be due to the increased rate at which small-sized nanoparticles are internalised and released into the interior of the tumour cells (by endocytosis), thus allowing an increase of the drug concentration at its site of action. Moreover, smaller-sized PLGA particles also show higher drug release rates, possibly due to a corresponding increase in the total particle surface area, resulting in a larger fraction exposed to the leaching medium. The study [89] indicated that particle size was an important characteristic related to obtaining optimal in vitro efficacy. Specifically, a particle diameter of less than 200 nm is likely to be an optimal size, not only for the effective blood-tumour transfer of nanoparticles, but also for their long retention in tumour tissue. [82]

Another example are surfactant-coated polymer NPs formulated using dioctyl sodium sulfosuccinate (aerosol OT) and sodium alginate used as a carrier to enhance the therapeutic efficacy of methylene blue as a photosensitizer resulting in higher cytotoxicity and necrosis of MCF-7 and 4T1 cancer cells. [90]

Different strategies for PS drug delivery, including polymer–PS conjugation or encapsulation of the drug in colloidal carriers, such as oil-dispersions, liposomes and polymeric particles, have been reviewed in detail in [45]. Although these colloidal carriers tend to accumulate selectively in tumour tissues, they are rapidly taken up by the mononuclear phagocytic system. [91] In order to reduce this undesirable uptake by phagocytic cells, long-circulating carriers that consist of surface modified carriers, such as PEG-coated PLA NPs (see above) have been developed.

However, systemic health effects and body distribution of mentioned carriers, especially nanoparticles, as comprehensively reviewed in [92, 93], have to be taken into account when they are used as a drug carrier. Irrespective of the uptake route, the body

distribution of NPs is mostly dependent on the surface characteristics and the size of the particles. For example, coating poly(methyl methacrylate) NPs with different types and concentrations of surfactants significantly changes their body distribution. Coating these NPs with ≥ 0.5 % polysorbate 80 surfactant reduces their liver concentration significantly after intravenous injection [94].

Interesting possibilities were opened by increasing the hydrophilicity of the PS through the conjugation with an appropriate polymer including *N*-(2-hydroxy-propyl)methacrylamide (HPMA) [95] to cationic, anionic or neutral poly-L-lysine [96], polyethylene glycol (pegylation) [97, 98, 99] or poly(vinyl alcohol) (PVAL) [100]. Another approach is to use quantum dots as photosensitizers or radiosensitizers for cancer therapy [101].

Moreover, considerable effort has been directed towards using other types of carriers to improve tumour targeting and to minimize the side effects. Lipoprotein-mediated delivery and monoclonal antibodies have been used to reach these goals. One approach is to entrap PS into the lipophilic core of low-density lipoproteins (LDL) without altering the physical or biological properties of LDL (no alteration of the LDL recognition by LDL receptor). The LDL receptor pathway is an important factor in the selective accumulation of PS in tumour tissue owing to the increased number of LDL receptors on the proliferating cell surface. [45, 102, 103]

Antibody (Ab)-based drug delivery is another approach to improve the specificity of PDT and to overcome side effects associated with this therapy. This strategy consists of linking PS with monoclonal antibodies against specific antigens of malignant cells. For detailed overview, see reference [45].

Finally, the most recent review of drug delivery systems for PDT [61] concentrates on patented advanced formulations (gels, creams, injections, etc.) for delivery of PS such as ALA already used in clinical studies. Love *et al.* [104] describe an innovative system for delivery of preformed porphyrin-type photosensitisers. The photosensitisers can be chemically-bound to the surface of biocompatible insoluble supports, or can be coated on the surface. The insoluble supports are polymeric materials, such as poly(acrylamide), poly(propylene) or silicon-based polymers. Such systems could be implanted directly into target tissue and release their drug payload to allow local photosensitisation without causing widespread photosensitivity of the rest of the body. Love *et al.* [105] also described formulations of various photosensitiser-loaded solution-, gel-, and powder-based systems for

use in PDT of bacterial infections. The formulations described could be injected, applied topically, sucked or inhaled. Taylor *et al.* [106] apply aqueous-based topical gel formulations containing zinc phthalocyanine for PDT of plaque psoriasis.

In general, only a few patents exist on innovative formulations for photosensitiser delivery. There are several reasons for this. Firstly, despite the vast number of studies published in the area of topical PDT, a rational approach to formulation design has not taken place. This may be because this field is dominated by clinicians and basic scientists, rather than those involved in pharmaceutical formulation development. Secondly, the majority of clinical studies carried out to date have been sponsored by the pharmaceutical companies who own the patents on the small number of proprietary products approved [61].

Thus, the drug delivery is one of the main challenges in PDT to be overcomed.

2. SCOPE AND OBJECTIVES

The lifetime, τ, of singlet oxygen ($^1O_2$) in a biological environment, e.g. intracellularly lifetime, is in μs range [6, 7]. Concerning medical applications, the distance between the location of $^1O_2$ generation (by irradiation of a photosensitizer) and the effect of $^1O_2$, is short, i. e. within the $^1O_2$ diffusion radius, which is substantially less than 1 μm. [6] $^1O_2$ can also be generated by the thermolysis of polycyclic aromatic endoperoxides [3]. Considerable efforts have been devoted to develop suitable $^1O_2$ generators based on endoperoxide thermolysis in biological environment (see Chapter 1.2.4.).

One of the polycyclic aromatic compounds capable of reacting with $^1O_2$ in an organic solvent and subsequently releasing (thermally induced) of $^1O_2$ is 1, 4-dimethylnaphthalene (**N1**). **N1** is a commercially available material, typically used as a potato sprout inhibitor [107, 108] and is therefore approved for biological use. 1,4-dimethylnaphthalene-1,4-endoperoxide (**N1E**) is chemically stable and able to release $^1O_2$ with 76 % yield [22], with half-life time values of $t_{1/2}$ = 1.5 h at 35 °C [22] and $t_{1/2}$ = 5 h at 25 °C in organic solvents [109]. **N1E** is synthesized by reaction of **N1** with $^1O_2$ upon a photosensitzer irradiation at low temperature (0-5 °C) and is storable for months at -80 °C [22]. When gently warmed, it releases a definite amount of $^1O_2$ free of other reactive oxygen species. However, until now **N1E** has not been generated in aqueous media. In order to use $^1O_2$ generated by thermolysis of endoperoxides such as **N1E** in possible medical applications, it is necessary to load a biocompatible carrier with the endoperoxide and deliver it to the place of interest for the particular application (e.g. cancer cells). During the delivery time, the endoperoxide molecule should not thermally decay and release the $^1O_2$. Therefore, the endoperoxide decay kinetics has to be adjusted to the demands of the particular application: in case of carrier delivery to the cancer cells, the endoperoxide half-life time, $t_{1/2}$, should be significantly larger than the carrier cell-uptake time, t_u, $t_{1/2} > t_u$.

The objectives of this work were the following:

- synthesis of several derivatives of **N1**, capable of endoperoxide generation and $^1O_2$-release, in order to extend the range of $^1O_2$-release time at 37 °C and to enable their incorporation in various carrier material types;

- preparation of various biocompatible carrier types (liposomes, polymer films, especially polymer nanoparticles), and examination of carrier uptake time in human breast cancer cells, line MDA-MB-231 [110] (used as a model for pharmaceutical applications) using confocal laser scanning microscopy; choice of appropriate carrier for delivery of $^1O_2$-releasing endoperoxides

- examination of endoperoxide decay kinetics in various biocompatible matrices with a systematical adjustment of the decay kinetics by means of various chemical and physical parameters in order to meet the condition that $t_{1/2}$ is substantially longer than t_u (e. g. for possible cancer treatment application), and the establishment of a microscopic model describing the chemical and physical modifications of the decay kinetics;

- kinetic chemosensitivity assay [111] of various $^1O_2$-releasing endoperoxides (with adjusted decay kinetics) in biocompatible carriers on MDA-MB-231 breast cancer cells *in vitro*;

- synthesis and characterization of multichromophore molecules consisting of covalently linked, but electronically weakly coupled subunits: a red light absorbing photosensitizer core and up to four endoperoxide-forming aromatic units (derivatives of **N1**) on the periphery. These novel compounds with two chromophores combined in one molecule were studied with respect to their photophysical and photochemical properties.

The motivation for the last issue was that such a system with an internal reactivity to generate and store $^1O_2$ would combine the useful properties of tetrapyrrole derivatives as a sensitizer for photodynamic therapy with the ability of aromatic endoperoxides to release $^1O_2$ independently of the conditions in the tissue. Hence, after long-term irradiation such a system would react with $^1O_2$ to form endoperoxides, which could later potentially serve as an internal source of $^1O_2$. Contrary to the classical PDT where $^1O_2$ is generated only upon irradiation, after the activation by light our system would conceivably also have a delayed $^1O_2$ production by endoperoxide decay.

The general concept of this thesis was to develop systems based on the controlled release of $^1O_2$, consisting of an appropriate carrier containing endoperoxide-forming

molecules in order to adjust the decay kinetics. A photosensitizer is either also embedded in the carrier, or preferably dissolved in aqueous medium, where it can be extracted after the irradiation. If this concept would be realized, then a new type of $^1O_2$ generation procedure would be developed [112]: in which the photosensitizer irradiation and subsequent endoperoxide formation could be performed outside of the patient body. Singlet oxygen would be temporarily "stored" in the endoperoxide-containing carrier, which should provide the adjustment of the $^1O_2$ release in the human body. Finally, a long-term outlook would be the possiblity to use this procedure for the treatment of various diseases, including microbial infections and cancer. In contrast to conventional PDT, restrictions due to light penetration depth and post-treatment photosensibilization problems would not exist.

3. MATERIALS AND METHODS

3.1. METHODS USED FOR SUBSTANCE CHARACTERIZATION

Elemental analyses, as well as the NMR and MS spectroscopy and X-ray crystal structure determinations, were carried out by the Centre for Chemical Analysis of the Faculty of Chemistry and Pharmacy of the University of Regensburg.

NMR spectroscopy

NMR spectra were recorded with a Bruker Avance 300 Spectrometer (1H: 300.1 MHz; T = 300 K). The chemical shifts are reported in ppm releative to external standards (solvent residual peak) and coupling constants are given in Hertz.

EI-MS spectroscopy

Mass spectra were recorded with a Varian CH-5 spectrometer.

X-ray crystal structure determinations

Diffraction data for synthesized compounds‘ crystals were collected with an Oxford Diffraction Gemini Ultra CCD diffractometer [113] with multilayer optics and Cu-K_α radiation (λ = 1.5418 Å).

UV-Vis Absorption

Absorption spectra were recorded with a Varian Cary 300 Bio UV/Vis Spectrometer with a 1-cm quartz cell (Hellma GmbH & Co. KG, Müllheim, Germany) and Uvasol® quality solvents from Sigma-Aldrich (Munich, Germany).

Emission spectroscopy

Fluorescence spectra were recorded with an Aminco-Bowman Series 2 Spectrometer and a Perkin Elmer LS 50 B Spectrometer with a 1-cm quartz cell (Hellma GmbH & Co. KG, Müllheim, Germany) and Uvasol® quality solvents.

Dynamic light scattering

Dynamic light scattering (DLS) experiments were performed on a Malvern Zetasizer 3000 HR (Malvern, United Kingdom) using 633 nm laser scatter. Samples obtained from dialysis were diluted by a factor of ten, results shown are averages of ten independent measurement runs. Correlation curves and particle size distributions were calculated by Malvern software using the photon correlation spectroscopy (PCS) method.

Transmission electron microscopy (TEM)

TEM experiments were made at the Department of Pathology of the University Hospital Regensburg.

The sample (drops of nanoparticles suspension in ddH_2O) was placed on Formvar- and carbon-coated positively glow-discharge treated cupper grid (400 mesh) and subsequently blotted dry with filter paper.

The sample was examined with a Zeiss LEO912AB electron microscope operating at 100 kV, equipped with a side-mounted CCD-camera capable of recording images with 1k•1k pixels. The documentation was done with the iTEM –software, Ver. 5.0 (Olympus Soft Imaging Solutions GmbH, Muenster, Germany).

3.2. CHEMICALS AND MATERIALS

All chemicals used were of analytical grade or better. Methanol, 2-propanol, dichloromethane, chloroform, sodium chloride, potassium chloride, disodiumhydrogenphosphate dihydrate, potassium dihydrogenphosphate, sodium dodecyl sulfate (SDS), cetyltrimethylammonium bromide (CTAB) , sulphuric acid, sodium sulfite, sodium bisulfite, ammonium molybdate, glutardialdehyde, crystal violet and sulphuric acid were purchased from Merck KGaA (Darmstadt, Germany). 1-amino-2-naphthol-4-sulfonic acid was obtained from Serva Fine Chemicals (Heidelberg, Germany). 1-propanol, acetone, N,N-dimethylformamide (DMF), dimethylsulfoxide (DMSO), and N,N,N',N'-

tetramethylethane-1,2-diamine (TEMED), tween 20, polysorbate 80 and triton X-100 and were obtained from Sigma-Aldrich (Munich, Germany).

1,4-dimethylnaphthalene (**N1**) in a form of 95% pure liquid was obtained from Merck KGaA (Darmstadt, Germany), and 1,4.5-trimethylnaphthalene (**N2**) in form of white crystals was obtained from ABCR GmbH & Co. KG (Karlsruhe, Germany).

1,2-dimyristoyl-L-α-phosphatidylcholine (DMPC) was obtained from Sigma-Aldrich (Munich, Germany). Polyvinyl butyral (PVB, Mowital LPB 16H, molar mass 16 kDa) was obtained from Kuraray Europe GmbH (Frankfurt, Germany). *N*,*N'*-bis(2,6 -dimethylphenyl)-perylene-3,4,9,10- tetracarboxylic diimide (PTC) was from BASF (Ludwigshafen, Germany). Cell Mask Deep Red plasma membrane stain (Deep Red) was purchased from Invitrogen GmbH (Darmstadt, Germany). DRAQ5 nuclear stain (DRAQ5) was obtained from Biostatus Limited (Shepshed, United Kingdom). Doubly distilled water (ddH_2O) was produced in-house. LabTek II chambered cover glasses with 8 chambers were supplied by Nunc GmbH (Langenselbold, Germany).

Phosphate buffered saline (PBS) pH 7.4, was made by adding 8.0 g of NaCl, 200 mg of KCl, 1.0 g of $Na_2HPO_4 \cdot 2H_2O$, 200 mg of KH_2PO_4 and 150 mg of NaH_2PO_4 to 900 mL Millipore quality H_2O, titrating to pH 7.4 at room temperature (RT) and adding Millipore quality H_2O to a final volume of 1 L. Cellulose filter paper type 595 (4 – 7 μm pores) was from Whatman GmbH (Dassel, Germany). Cellulose dialysis tubes type Visking (molecular weight cut off 14,000) were obtained from Carl Roth (Karlsruhe, Germany). Amicon Ultra-4 cellulose centrifugal filter membranes (molecular weight cut off 10,000) were from Millipore GmbH (Schwalbach, Germany).

3.3. SYNTHESIS OF ENDOPEROXIDE-FORMING MOLECULES: NAPHTHALENE DERIVATIVES

3.3.1. 1-(1,4-Dimethyl-Naphthalen-2-yl)-Ethanone 1-(1,4-Dimethyl-Naphthalen-2-yl)-Ethanone (**N3**)

N3 was synthesized from **N1** using the Friedel-Crafts benzolyation by the Perrier addition procedure [114]: to a stirred solution of anhydrous $AlCl_3$, (13.17 g, 0.1 mol) in dichloroethane (150 mL) was added dropwise acetyl chloride (7.1 mL, 0.1 mol) and than also dropwise **N1** (14 g, 0.09 mol). The mixture was stirred overnight at 0-5 ºC and afterwards poured into ice-water bath. Concentrated hydrochloric acid was added dropwise until the brown precipitate dissolved. The organic layer was separated and the water layer was extracted with chloroform. The combined organic layers were dried over $MgS0_4$, and concentrated. The brown precipitate appeared from cold methanol and was then purified by column chromatography on Al_2O_3 with hexane and successively ethyl acetate as eluents to yield 8.14 g of white **N3** (46 %). During this reaction a mixture of ketone products, 1-(1,4-dimethyl-naphthalen-2-yl)-ethanone and 1-(1,4-dimethyl-naphthalen-6-yl)-ethanone, is formed, but only 1-(1,4-dimethyl-naphthalen-2-yl)-ethanone crystallizes from methanol. It is possible to isolate 1-(1,4-dimethyl-naphthalen-6-yl)-ethanone by treating the ketone mixture with an excess of hydroxylamine to give the a mixure of oxymes, treating the mixture with concentrated HCl and then crystallizing 1-(1,4-dimethyl-naphthalen-6-yl)-ethanone [38, 114]. Product characterization was done with elemental analysis, mass spectrum and ^{1}H NMR:

Elemental analysis:

N3 molecule requires: 84.80% C, 7.07% H, and it was found: 84.55 % C, 7.22 % H.

EI-MS:

Detected were ions of the following mass/ion- charge (m/z) ratios: 198.1 ($\mathbf{N3}^+$); 183.1 ($\mathbf{N3}^+$ - CH_3); 155.1 ($\mathbf{N3}^+$ - CH_3 - CO).

^{1}H NMR:

^{1}H (300 MHz, $CDCl_3$): δ 2.60 (s, 3H), 2.65 (s, 3H), 2.71 (s, 3H), 7.35 (s, 1H) 7.55 (m, 2H), 7.97 (m, 1H), 8.14 (m, 1H).

3.3.2. 1-(1,4-Dimethyl-Naphthalen-2-yl)-Ethanol (**N4**)

To a stirred solution of **N3** (7.2 g, 36 mmol) in anhydrous ether (100 mL) was added slowly a suspension of $LiAlH_4$, (1.05 g, 28 mmol) in anhydrous ether (100 mL) at room temperature. The mixture was stirred for 3h and poured into an ice-water bath. Hydrochloric acid was added to the contents until the white solid was dissolved. The organic layer was separated and the aqueous layer was extracted with ether. The combined organic layers were dried over $MgSO_4$, and concentrated. The crude product was purified from **N3** remains and from **N5** product (see later) by column chromatography on Al_2O_3 with hexane and successively ethyl acetate as eluents. Subsequently from n-hexane 1.15 g of white crystals of **N4** (16 %) were obtained.
Product characterization was done with elemental analysis, mass spectrum, ^{1}H NMR and x-ray crystal structure analysis:

Elemental analysis:

N4 molecule requires: 84.00% C, 8.00% H, and it was found: 83.88 % C, 8,20 % H.

EI-MS:

Detected were ions of the following m/z ratios: 200.1 ($\mathbf{N4}^+$); 185.1 ($\mathbf{N4}^+$ - CH_3); 182.1 ($\mathbf{N4}^+$ - H_2O).

^{1}H NMR (300 MHz, $CDCl_3$): δ 1.42 (d, 3H, $^3J_{HH}$ 6.8 Hz) 1.56 (s, 1H) 2.29 (s, 3H), 2.74 (s, 3H) 4.74 (q, 1H, $^3J_{HH}$ 6.8 Hz) 7.54 (m, 3H), (m, 2H).

X-ray crystal structure determination:

Suitable X-ray single crystal (colourless) of compound **N4** was obtained as described above and was mounted on top of glass fiber in a random orientation. Crystal data, data collection, and refinement parameters are given in Table 3.1.

Table 3.1. Crystal data, data collection, and structure refinement parameters for **N4** compound.

parameter	N4
empirical formula	$C_{14}H_{16}O$
formula mass, g mol^{-1}	200.27
collection *T*, K	123
crystal system	monoclinic
space group	P $2_{1/n}$
***a* (Å)**	8.1442(3)
***b* (Å)**	4.8533(2)
***c* (Å)**	27.8100(11)
***β* (deg)**	94.010(4)
***V* (Å^3)**	1096.53(7)
Z	4
***D*$_{calcd}$ (g cm^{-3})**	1.213
crystal size (mm)	0.210 x 0.042 x 0.008
***F*(000)**	432
abs coeff (mm^{-1})	0.574
***θ* range (deg)**	3.19 to 66.33
range *h, k, l*	-9/7, -5/5, -29/32
no. total refl.	4568
no. unique refl.	1897
data/restraints/parameters	1897 / 0 / 143
final *R*	R_1 = 0.0392
[*I* > 2*σ*(*I*)]	wR_2 = 0.1094
***R* indices (all data)**	R_1 = 0.0464, wR_2 = 0.1136
goodness of fit/*F*^{2}	1.051
largest diff. Peak and hole (e Å^{-3})	0.171 and -0.223

3.3.3. Di-1-(1,4-Dimethylnaphthene-2-yl)-Ethylether (**N5**)

Synthesis procedure was the same as for **N4**. **N5** was a novel, unexpected product of an *in situ* reaction: condensation of **N4**, H_2O elimination and ether bound forming with an excess of $LiAlH_4$ in anhydrous ether (see Scheme 1). The mixture of **N5** and **N4** and **N3** was purified by column chromatography on Al_2O_3 with hexane and successively ethyl acetate as eluents. Subsequently from dichloromethane 2.1 g of white crystals of **N5** (31 %) were obtained.

Product characterization was done with elemental analysis, mass spectrum, ^{1}H NMR and x-ray crystal structure analysis:

Elemental analysis:

N5 molecule requires: 87.96% C, 7.85% H, and it was found: 87.85 % C, 7.58 % H.

EI-MS:

Detected were ions of the following m/z ratios: 382.3 (**N5**$^+$); 184.2 (**N5**$^+$ - $C_{14}H_{14}O$).

^{1}H NMR:

^{1}H NMR (300 MHz, acetone): δ 1.38 (d, 6H, $^3J_{HH}$ 6.6 Hz), 2.29 (s, 6H), 2.73 (s, 6H), 4.76 (q, 2H, $^3J_{HH}$ 6.6 Hz) 7.56 (m, 6H), 8.06 (m, 4H).

X-ray crystal structure determination:

Suitable X-ray single crystal (translucent, colourless) of compound **N5** was obtained as described above and was mounted on top of glass fiber in a random orientation. Crystal data, data collection, and refinement parameters are given in Table 3.2.

Table 3.2. Crystal data, data collection, and structure refinement parameters for **N5** compound.

parameter	N5
empirical formula	$C_{28}H_{30}O$
formula mass, g mol^{-1}	382.52
collection *T*, K	123
crystal system	orthorhombic
space group	P b c n
***a* (Å)**	7.6851(3)
***b* (Å)**	16.8705(5)
***c* (Å)**	16.3611(5)
***β* (deg)**	90
***V* (Å^3)**	2121.24(12)
Z	4
***D*$_{calcd}$ (g cm^{-3})**	1.198
crystal size (mm)	0.210 x 0.042 x 0.008
***F*(000)**	824
abs coeff (mm^{-1})	0.536
***θ* range (deg)**	5.24 to 65.05
range *h, k, l*	-8/6, -17/19, -9/18
no. total refl.	6017
no. unique refl.	1772
data/restraints/parameters	1772 / 0 / 133
final *R*	R_1 = 0.0444
[*I* > 2*σ*(*I*)]	wR_2 = 0.1234
R indices (all data)	R_1 = 0.0510, wR_2 = 0.1282
goodness of fit/*F*^{2}	1.059
largest diff. Peak and hole (e Å^{-3})	0.263 and -0.225

3.3.4. 1,4-Dimethyl-2-Vinylnaphthalene (**N6**)

To a stirred solution of **N4** (300 mg, 1.5 mmol) in 5 ml CH_2Cl_2 was dropwise added $SOCl_2$, (0.22mL, 3.0 mmol) at 0 °C. The reaction mixture was stirred for 4 h and excess of $SOCl_2$ and the solvent were removed in vacuo. The residue (brown oil) was dissolved in DMF (6 mL). To the solution was added t-BuOK (0.26 g, 2.4 mmol) in small portions at ice-water bath temperature with stirring. The mixture was stirred for 3 h, afterwards poured into ice-water bath, and extracted three times with ether. The combined ether layers were dried over $MgSO_4$; the solvent was later evaporated. The yellow residue was purified by column chromatography on silica gel with hexane as eluent to give 150 mg of **N6** (55%) white crystals.
Product characterization was done with mass spectroscopy, and ^{1}H NMR.

EI-MS:

Detected were ions of the following m/z ratios: 182.1 (**N6**$^+$) and 167.1 (**N6**$^+$ - CH_3).

^{1}H NMR (300 MHz, DMSO): δ 2.60 (s, 3H), and 2.62 (s, 3H), 5.41 (dd, 1H, $^5J_{HH}$ 1.6 Hz, $^3J_{HH}$ 17.5 Hz), 5.82 (dd, 1H, $^5J_{HH}$ 1.6 Hz, $^3J_{HH}$ 11.1 Hz) 7.26 (m, 1H) 7.55 (m, 3H), 7.97 (m, 1H), 8.11 (m, 1H).

3.3.5. Poly(1,4-Dimethyl-2-Vinylnaphthalene), (**N7**)

N7 was synthesized in a form of nanoparticles as suggested by Dr. S. Nagl, similar to his polystyrene-based nanobeads synthesis procedure [115] directly from the monomer **N6**. 410 mg **N6** was mixed with 2 g sodium dodecyl sulfate (SDS) in 10 ml ddH_2O in a 100 mL round flask equipped with reflux condenser and temperature control. 25 mg $(NH_4)_2S_2O_8$ was dissolved in 1 ml ddH_2O and immediately added to the **N6**/water mixture. It was then heated to 90 °C under reflux for 2 h. After cooling down to the room temperature, the synthesized particles were dialyzed for several days against ddH_2O using cellulose membranes to remove traces of monomers, side products and impurities.

After irradiation and prior to the kinetic chemosensitivity assay on cancer cells, (see Chapter 3.6.2.), polysorbate 80™ surfactant was added to the larger (95 ±24 nm diameter, Figure 4.4. and 58 ± 9 nm diameter) **N7** nanoparticle aqueous suspension (1% v/v polysorbate 80™ in dd H_2O) in order to enable faster nanoparticle uptake by the breast cancer cells. Smaller **N7** nanoparticles (diameter 12 ±3 nm) were not coated with polysorbate 80™ surfactant.

3.4. PHOTOSENSITIZERS AND LIGHT SOURCES

Several light-harvesting photosensitizers were used for the generation of $^1O_2$, which then reacted with naphthalene derivatives to form endoperoxides.

In addition to the standard photosensitizer properties (see Chapter 1.3.1.) for the sample preparation several other conditions had to be fulfilled, such as a good solubility of the photosensitizer in the used solvent (H_2O, ethanol, $CHCl_3$) and/or high enough embedding of the photosensitizer in the carrier matrix, which was critical with polymer nanoparticles preparation procedure. Depending on the carrier material and sample preparation procedure, one of the following photosensitizers was chosen:

3.4.1. Protoporphyrin-IX-Dimethylester (PpIX-DME)

PpIX-DME was obtained from Sigma-Aldrich (Munich, Germany). On Figure 3.1. its structure and absorption spectrum are shown.

This photosensitizer was preferably used in systems with liposome carrier because of good solubility in $CHCl_3$ (solvent used for liposomes preparation), and subsequently good embedding in liposomes.

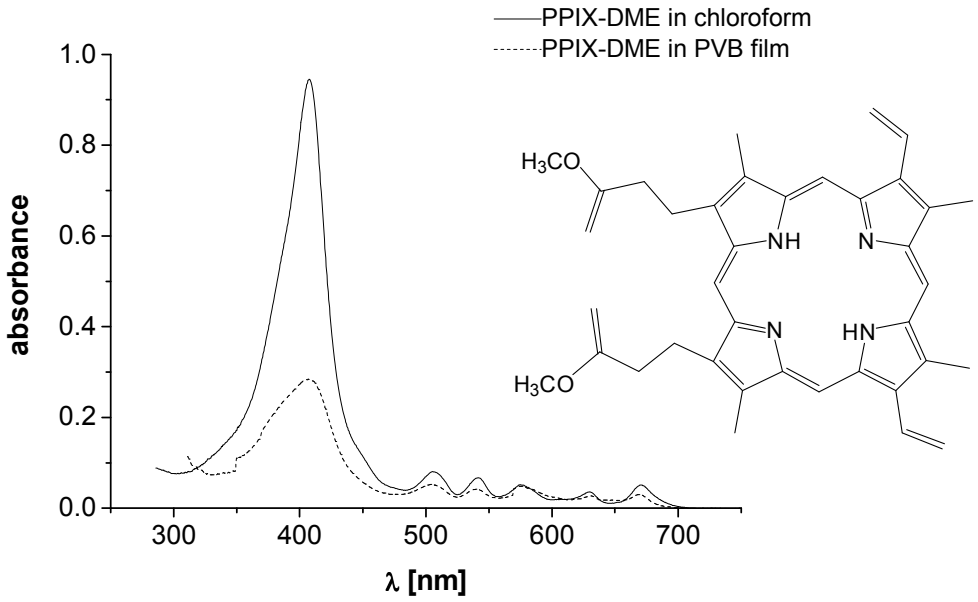

Figure 3.1. Structure and absorption spectrum of PpIX-DME photosensitizer in $CHCl_3$ and a PVB polymer film.

3.4.2. 5,10,15,20-Tetrakis-(2,3,4,5,6-Pentafluorophenyl)-Porphyrin-Pd(Ii), TPFPP-Pd(II)

TPFPP- Pd(II) was obtained from Porphyrin Systems GbR (Lübeck, Germany). On Figure 3.2. its structure and absorption spectrum are shown. This photosensitizer was preferred in PVB films and in PVB nanoparticles because of good solubility in ethanol (solvent used for PVB films and PVB nanoparticles preparation).

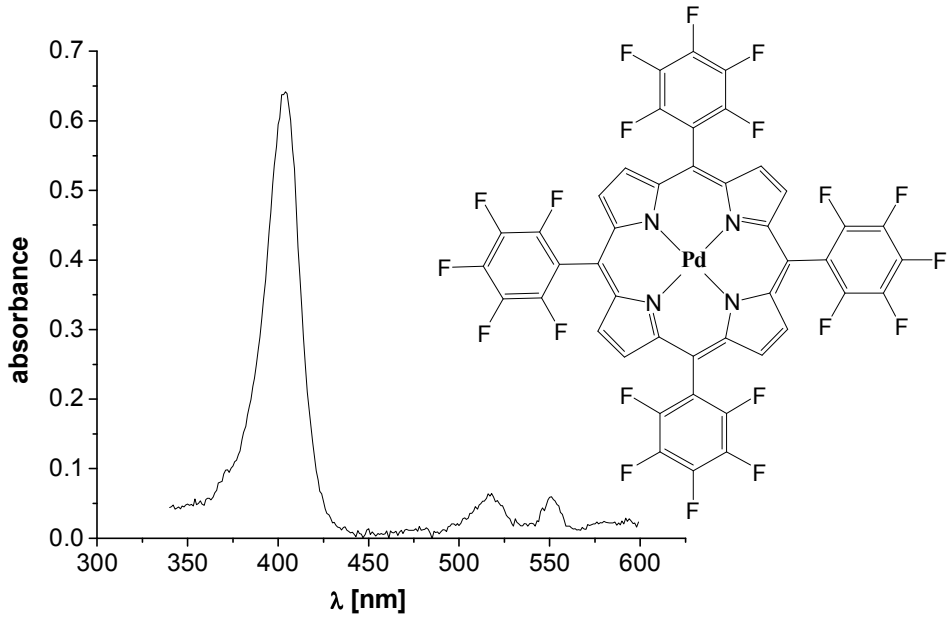

Figure 3.2. Structure and absorption spectrum of 10^{-6} M TPFPP-Pd(II) photosensitizer in EtOH.

3.4.3. Methylene Blue (MB)

MB photosensitizer was obtained from Sigma-Aldrich (Munich, Germany). On Fig. 3.3. its structure and absorption spectrum are shown. Because of its excellent water solubility, 3,7-bis(Dimethylamino)phenazathionium chloride or commonly known as methylene blue was used in systems with nanoparticles suspension in H_2O as a photosensitizer, dissolved in H_2O, separately from endoperoxide-forming molecules embedded in polymer nanoparticles.

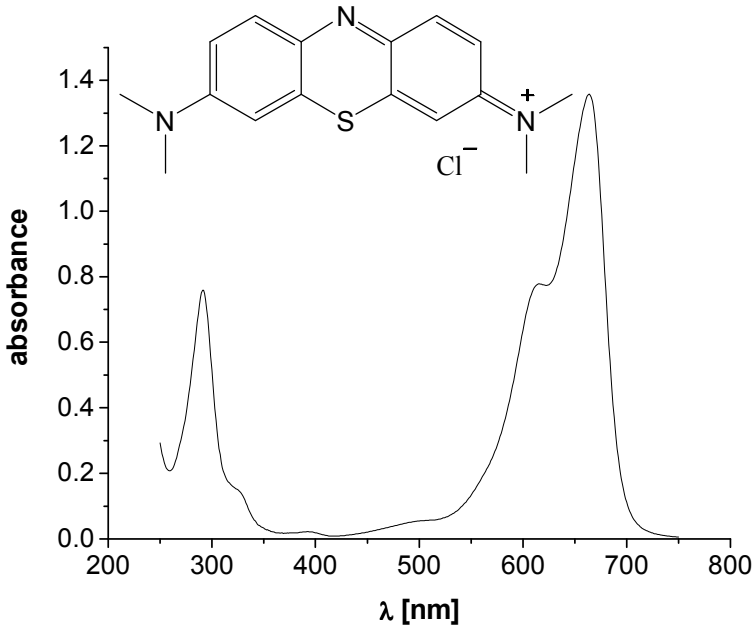

Figure 3.3. Structure and absorption spectrum of 2 •10^{-5} M methylene blue photosensitizer in H_2O.

In Table 3.3. molar extinction coefficient values of used photosensitizers at available light sources' wavelengths are given.

Table 3.3. Molar extinction coefficient values (ε / cm^{-1} M^{-1}) of used photosensitizers at wavelengths of (in this work used) light sources.

λ/nm	**PpIX-DME in $CHCl_3$**	**TPFPP-Pd(II) in EtOH**	**MB in H_2O [116]**
420	150 000	120 000	598
514	17 200	37 000	2 900
658	5 300	/	70 280

3.4.4. Light Sources

Depending on the photosensitizer molecule present in the system, different light sources were used throughout this work.

For porphyrin-based photosensitizers (PpIX-DME, TPFPP-Pd(II) and **P2**) a blue (λ=420 ± 10 nm) high-power LED from R&D laboratory of Osram GmbH, (Regensburg, Germany) or an argon-ion laser (λ=514 nm, Model 2025 by Newport Spectra-Physics GmbH, (Darmstadt, Germany) was used.

When MB photosensitizer was present in the system, a red (λ=658 nm) hand-made laser (by Mr. Putzcka, Faculty of Physics, University of Regensburg) or a red (λ=660 ± 15 nm) high-power LED array of 16 power LED chips (type LED660-66-16100 from Roithner Lasertechnik, Vienna, Austria) was used.

3.5. CARRIER MATERIALS

3.5.1. Liposomes, Preparation and Characterization

In this work conventional, uncoated liposomes in an aqueous suspension were prepared from 1,2-dimyristoyl-sn-glycero-3-phosphatidylcholine (DMPC) with an extrusion technique (extrusion includes pressing liposomes through a membrane with well-defined pores in order to get liposomes of a homogenous size-distribution). DMPC was commercially available from Sigma-Aldrich (Munich, Germany). DMPC structure with its polar, hydrophilic "head" and an apolar, hydrophobic "tail" is shown in Fig. 3.4., as well as a scheme of a formed liposome bilayer sphere. Hydrophylic layers enable homogenous dispersion of liposome particles in water suspension, whereas hydrophobic compounds such as endoperoxide-forming naphthalene derivatives and photosensitizers (porphyrine derivatives), are stored and transported in alkyl centre of the lipid bilayer.

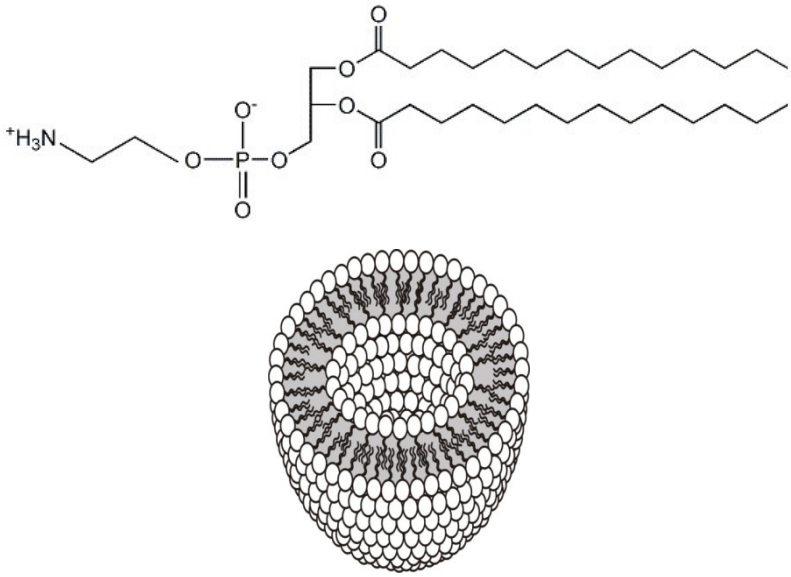

Figure 3.4. DMPC lipid structure and a scheme of a unilammelar liposome.

3.5.1.1. Liposome Preparation Procedure

10 mg/ml DMPC were dissolved in chloroform. To the solution were added endoperoxide-forming naphthalene derivative (e.g. **N1**/DMPC = 1/50) and PpIX-DME (PpIX-DME/DMPC = 1/5000) in chloroform. Then, solvent was totally evaporated using rotary evaporator at 35 °C, leaving a lipid film on flask wall. To the dry lipid film dd H_2O was added, and the film was let to swell from the flask wall for 30 minutes forming a suspension of multilamillar liposomes of varying sizes. This suspension was shaken 3 times during these 30 minutes in order to detach the entire lipid from flask wall. Subsequently the liposome suspension was pressed 30 times through a 100 nm polycarbonate membrane using a Liposofast™ (from Avestin Europe GmbH, Mannheim, Germany) device to form a unilamellar liposome suspension.

Average hydrodynamic diameter of so formed liposomes was determined with DLS technique to be 116 ±32 nm.

3.5.1.2. Determination of Lipid Concentration

The lipid concentration in aqueous suspensions of liposomes was determined indirectly, measuring the phosphate content of the sample using a modification of the Bartlett assay [117]. In brief, organic phospholipids of an aqueous liposome suspension (0.4 ml aliquot) were transformed to inorganic phosphate by adding 0.1 ml of concentrated H_2SO_4 to. The liquid was evaporated on flame leaving a film on the flask wall. The cooled film was dissolved in 1 ml of H_2O and heated up to the boiling point for 15 min. Afterwards, an excess of 2.5 % (w/w) ammonium molybdate and a drop of p-nitrophenol indicator were added to the cooled sample to transform phosphates to phosphato-molybdenum acid. This was finally reduced with 1-amino-2-naphthol-4-sulfonic acid in combination with sodium sulfite and sodium metabisulfite to molybdenum blue [118], an unstoichiometrical mixture of molybdates (Mo^{4+} to Mo^{6+}), to give a blue solution. From the absorbance values of this solution at 720 nm exactly 10 minutes after reduction to molybdenum blue, the phosphate concentration, and subsequently the DMPC lipid concentration, in the sample were calculated. Calibration curve was made with solutions of KH_2PO_4 at known concentration using the same procedure.

3.5.1.3. Endoperoxide Formation in Liposomes

Formulation of a naphthalene derivative and PpIX-DME embedded in liposome suspension was irradiated with a blue ($\lambda = 420 \pm 10$ nm) high-power LED or an argon-ion laser ($\lambda = 514$ nm) for 30 minutes at 15 °C to from endoperoxides embedded in liposome suspension. In this manner prepared sample of endoperoxides embedded in liposomes (an aqueous suspension) was tested for endoperoxide thermolysis or kinetic chemosensitivity assay (see Chapter 3.6.2.) on the human breast cancer cells. Prior to the chemosensitivity assay the liposome aqueous suspension was diluted in McCoy's 5A or RPMI 1640 cell medium containing 5% fetal calf serum (see Chapter 3.6.) For chemosensitivity assay on human breast cancer cells a formulation of undoped liposome suspension with the same extrusion method was prepared, as well.

For the absorption and emission measurements during endoperoxide thermolysis, liposome suspension was dissolved in methanol prior to the measurement in order to prevent light scattering skewing the UV spectra of naphthalene derivatives.

Concentration of embedded naphthalene-derivative (**N1**, **N2**, **N4**, **N5**) in aqueous suspension of the liposome carrier was determined spectroscopically with a standard addition method according to Lambert-Beer's law. For each naphthalene-derivative (**N1**, **N2**, **N4**, **N5**) a set of absorbance measurements in UV region at **N1**, **N2**, **N4**, **N5** compound's peak wavelength, respectively, was done. Prior to the measurement liposomes were dissolved in methanol in order to prevent light scattering on liposome spheres. From each sample three various aliquots were diluted in methanol and measured to check the fulfilling of Lambert-Beer's law linear dependence of absorbance on sample concentration. A calibration curve was made with a standard solution of known concentration of a particular naphthalene-derivative (**N1**, **N2**, **N4**, **N5**) in methanol.

3.5.2. Polyvinyl Butyral Film, Characteristics and Preparation

Polyvinyl butyral (PVB) was received as ®Mowital LP B 16H powder product from Kuraray Specialities Europe GmbH (Frankfurt, Germany) with an average molar weight of 16 kDa [119]. PVB is made by acetalisation of polyvinyl alcohol (PVAl) with butyraldehyde. PVAl itself is produced from the precursor polyvinyl acetate (PVAc) via transesterification. Because of this sequential production PVB is never obtained in a pure acetal form, but rather a copolymer consisting of (sequences) of polyvinyl alcohol, polyvinyl acetate and polyvinyl butyral with up to 30 % hydroxyl and around 1 - 5 % acetyl groups present (see Fig. 3.5. where the indexes m, n, o, represent the weight percentage of a particular group in the PVB polymer product) depending on the synthetic procedure.

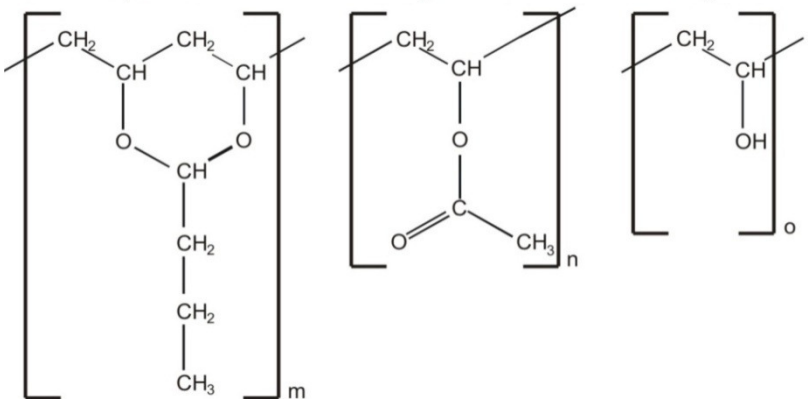

Figure 3.5. PVB polymer structure. Indexes m, n, o, represent the w/w percentage of a particular group in the final PVB product.

In Table 3.4. the weight percentages of a each group in the polyvinyl butyral ®Mowital LP B 16H are given [120].

Table 3.4. Polyvinyl butyral ®Mowital LP B 16H group weight percentages.

PVB grade	m (w/w %)	n (w/w %)	o (w/w %)	non-volatile content (DIN 53216) (w/w %)
Mowital LP B 16 H	75-81	1-4	18-21	> 97.5

3.5.2.1. PVB Film Sample Preparation

PVB was dissolved (0.20 % w/w) in ethanol, spectroscopic quality, and stirred overnight. To the PVB solution any of the endoperoxide-forming naphthalene derivative and the TPFPP-Pd(II) photosensitizer were added and stirred for 2 more hours. Such a mixture was then left to stand until air bubbles disappeared. A drop of the solution was put on a glass substrate and left in ethanol atmosphere for 1-2 days in order to let the ethanol slowly evaporate from the sample and to form a fairly evenly spread, highly concentrated thick polymer film. PVB film on a glass substrate was then mounted onto a special in-house hand-made holder and was ready for optical investigations.

Such a PVB film sample was then irradiated with Ar+ laser light (514 nm, P = 250 mW, Φ = 600 mWcm^{-2}) for 1 h at various temperatures to form endoperoxides embedded in the PVB matrix. Thereby prepared samples of endoperoxides in PVB matrix were examined for thermolytic decay of the endoperoxides.

3.5.3. Polyvinyl Butyral Nanoparticles, Preparation and Characterization

The nanoparticle synthesis devised here is a modification of previously described syntheses of polyacrylonitrile beads and derivatives thereof [115, 121]. It can be classified in the group of precipitation methods. A polymer in solution is brought to precipitation via addition of a non-solvent (here: double distilled H_2O). Controlling the experimental conditions during addition of water leads to precipitation of polymer chains forming particles in the nanometer scale. The solvent was then fully removed via evaporation or dialysis.

PVB nanoparticle syntheses were varied with respect to polymer concentration, solvent, temperature, additives, addition speed, pH and ionic composition of the non-solvent water. In general, PVB was taken in appropriate amounts from stock solutions of PVB in the respective solvent. Stock solutions were magnetically stirred for at least two days at room temperature prior to use to ensure complete dissolution. The polymer solution was diluted to a volume of 50 mL with solvent (e.g. 2-propanol), and a total of 100 mL of non-solvent was

added via a peristaltic pump (Watson Marlow 505 Du) through a 400 µm (diameter) syringe. When the synthesis was carried out at different temperatures (see later in Chapter 4.4.1), the suspension of PVB nanoparticles in a solvent mixture (e.g. 2-propanol/ddH_2O) was allowed to warm or cool down to room temperature (RT), and was filtrated using cellulose filter paper. Finally, the suspension was dialyzed in cellulose membranes against ddH_2O for two days and used for characterization or further steps.

The PVB nanoparticle concentration in aqueous suspension (w/w %) was determined gravimetrically: by measuring the mass of the PVB aqueous suspension and the mass of the PVB left after careful water evaporation using a rotary evaporator at 55 °C.

3.5.3.1. Doping of PVB Nanoparticles

The preparation method of the beads was based on aggregation allowing incorporation of dopant molecules in comparatively high concentration (up to several percent w/w) if the dopant and the polymer PVB possess comparable solubilites in the solvent and the non-solvent, respectively.

For confocal microscopy the PVB nanoparticles were doped with *N,N'*-bis(2,6 -dimethylphenyl)-perylene-3,4,9,10-tetracarboxylic diimide (PTC): PTC and PVB were dissolved in 20 mL 2-propanol, and 40 mL of dd H_2O was added via a peristaltic pump (Watson Marlow 505 Du) through a 400 µm (diameter) syringe. The rest of particles production procedure (filtration, dialysis) was the same as described above.

The synthetic protocol that yielded the smallest (141 nm average diameter) PTC-doped PVB nanobeads used in confocal microscopy (see Chapter 4.4.3.) was as follows: 8.0 mg of PVB in 2-propanol and 160 µg of PTC in 2-propanol were combined and diluted with 2-propanol to a total volume of 20 mL. 1.0 mL of CH_2Cl_2 were added, and the solution was stirred for 1 hour at 4 °C. 40 mL dd H_2O (T = 4 °C) were added at a rate of 9 mL/min at 4 °C. Concentration of nanospheres was performed several times successively using Amicon Ultra-4 centrifugal filter membranes in a laboratory centrifuge at 3000 g for several minutes.

The same preparation procedure was used to synthesize PVB nanobeads doped with endoperoxide-forming naphthalene derivatives. Typically, 80 µg of the respective naphthalene derivative were added to 8.0 mg of PVB in 2-propanol with all the other

preparation parameters being constant. Concentration of embedded naphthalene-derivative (**N1, N2, N4, N5**) in aqueous suspension of PVB nanoparticles was determined spectroscopically with a standard addition method according to Lambert-Beer's law. For each naphthalene-derivative (**N1**, **N2**, **N4**, **N5**) a set of absorbance measurements in UV region at **N1**, **N2**, **N4**, **N5** compound's peak wavelength, respectively, was done. Prior to the measurement PVB nanoparticles were dissolved in methanol in order to prevent light scattering on nanoparticles. From each sample three various aliquots were diluted in methanol and measured to check the fulfilling of Lambert-Beer's law linear dependence of absorbance on sample concentration. A calibration curve was made with a standard solution of known concentration of a particular naphthalene-derivative (**N1**, **N2**, **N4**, **N5**) in methanol.

3.5.3.2. Endoperoxide Formation in PVB Nanoparticles

Methylene blue in H_2O was added to the prepared and purified (after dialysis) aqueous suspension of naphthalene-derivative embedded in PVB nanoparticles. Afterwards this suspension was irradiated with red laser light (658 nm, P = 70 mW, Φ = 140 mWcm^{-2}) for 1 h at 15 °C to form endoperoxides in PVB nanoparticles. In this manner prepared samples of endoperoxides in PVB nanoparticles (aqueous suspension) were tested for the endoperoxide thermolysis and $^1O_2$-release or kinetic chemosensitivity assay (see Chapter 3.6.2.) on the human breast cancer cells. Prior to the chemosensitivity assay the samples were diluted in McCoy's 5A or RPMI 1640 cell medium containing 5% fetal calf serum (see Chapter 3.6.)

3.5.4. Ethylcellulose Nanoparticles, Preparation and Characterization

Ethylcellulose (EC) was commercially available from Sigma-Aldrich, (Munich, Germany). EC nanoparticles were also prepared via a precipitation procedure from a mixture of solvents. The ethylcellulose nanoparticles preparation procedure was described elsewhere [122]. In short, to 20 mL of 0.2 % (w/w) of ethylcellulose in acetone/tetrahydrofuran = 1/1, 40 mL of ddH_2O (non-solvent) were poured fast to form ethylcellulose nanoparticles. Acetone and THF were subsequently evaporated from such a suspension of ethylcellulose particles in ddH_2O /acetone/THF on a rotary evaporator, resulting in EC nanoparticles suspended in ddH_2O (cca. 0.1 % w/w) with a diameter of 62 ± 18 nm (measured with DLS).

The EC nanoparticle concentration in aqueous suspension (w/w) was determined gravimetrically: by measuring the mass of the EC aqueous suspension and the mass of the EC left after careful water evaporation using a rotary evaporator at 55 °C.

3.5.4.1. Doping of EC Nanoparticles

In order to load EC particles with **N4** derivative, 10.0 mg of **N4** in acetone were added to 20 mL of 0.2 % (w/w) solution of EC in acetone/tetrahydrofuran = 1/1 and stirred for 10 minutes at room temperature. Then 40 mL of dd H_2O were poured fast into this „cocktail“ to get ethylcellulose nanoparticles. Acetone and THF were subsequently evaporated with a rotary evaporator, resulting in EC nanoparticles doped with **N4 (**diameter of 98 ± 25 nm, measured with DLS) and **N4** concentration of $8.2 \cdot \bullet 10^{-4}$ M in aqueous suspension of EC nanoparticle carrier. A very similar procedure was done to prepare an aqueous suspension of **N5** embedded in EC nanoparticles. A slightly different outcome was in the average diameter of the particles (136 ± 38 nm) and in the end concentration of **N5** in dd H_2O suspension ($4.2 \bullet 10^{-4}$ M).

The concentration of doped naphthalene derivatives (**N4, N5**) aqueous suspension of EC nanoparticles was determined spectroscopically with a standard addition method according to Lambert-Beer’s law. For each naphthalene-derivative (**N4**, **N5**) a set of

absorbance measurements in UV region at **N4**, **N5** compound's peak wavelength, respectively, was done. Prior to the measurement EC nanoparticles were dissolved in methanol in order to prevent light scattering on nanoparticles. From each sample three various aliquots were diluted in methanol and measured to check the fulfilling of Lambert-Beer's law linear dependence of absorbance on sample concentration. A calibration curve was made with a standard solution of known concentration of a particular naphthalene-derivative (**N4**, **N5**) in methanol.

For confocal laser microscopy experiments (see Chapter 3.6.1.) EC nanoparticles were doped with PTC: EC and PTC (1% w/w to EC weight) were dissolved in 20 mL acetone/THF=1/1 and 40 mL of dd H_2O were poured fast into this „cocktail" to get EC nanoparticles. Acetone and THF were subsequently evaporated with a rotary evaporator, resulting in EC nanoparticles doped with PTC.

3.5.4.2. Endoperoxide Formation in EC Nanoparticles

Methylene blue photosensitizer dissolved in H_2O was added to the prepared aqueous suspension of naphthalene-derivative embedded in EC nanoparticles, to make the end concentration $1.0 \bullet 10^{-5}$ M of MB in dd H_2O. Afterwards this suspension was irradiated with a red laser light (658 nm, P = 70 mW, Φ = 140 $mWcm^{-2}$) for various periods of time at different temperatures (e.g. 15 h at 4 °C) to form **N4E** and **N5E** in EC nanoparticles.

In this manner prepared sample of endoperoxides embedded in EC nanoparticles (aqueous suspension) was tested for endoperoxide thermolysis and $^1O_2$-release or kinetic chemosensitivity assay (see Chapter 3.6.2.) on the human breast cancer cells. Furthermore, after the irradiation and just prior to the chemosensitivity assay, polysorbate 80™ surfactant (by Sigma-Aldrich, Munich, Germany) was added to the EC nanoparticles suspension (1% w/w end concentration of polysorbate 80™ in dd H_2O) in order to enable faster uptake of the EC nanoparticles by the breast cancer cells. The samples were left for 5 minutes in an ultrasonic bath to promote the adsorption of polysorbate 80™ on the EC nanoparticle surface.

3.6. CELL LINE AND CULTURE CONDITIONS

The human estrogen receptor negative MDA-MB-231 (HTB 26) breast cancer cells were obtained from the American Type Culture Collection (ATCC), Rockville, USA. Cell banking and quality control were performed according to the "seed stock concept". Cells were cultured in RPMI 1640 or McCoy´s 5A medium (Sigma Aldrich, Munich, Germany) containing L-glutamine, 2.2 g/l $NaHCO_3$ and 5 % fetal calf serum, FCS (Biochrom, Berlin, Germany). Cells were maintained in a water saturated atmosphere (95 % air / 5 % carbon dioxide) at 37°C in 75-cm² culture flasks (Greiner, Frickenhausen, Germany), and were serially passaged following trypsinization using 0.05% trypsin/0.02% EDTA (Roche Diagnostics, Mannheim, Germany). *Mycoplasma* contamination was routinely monitored, and only Mycoplasma free cultures were used.

3.6.1. Confocal Laser Scanning Microscopy Procedure

Two days prior to the experiment the MDA-MB-231 cells (100 % confluency) were trypsinized and seeded in Nunc LabTek™ II chambered cover glasses with 8 chambers in RPMI 1640 or McCoy´s 5A medium (250 µl) that contained 5 % FCS. On the day of the experiment the confluency of the cells was 40-50 %. After the culture medium was removed, the cells were washed once with Leibowitz's L-15 culture medium (Invitrogen GmbH, Darmstadt, Germany). Subsequently, the cells were stained in L-15 medium containing 2.5 µg/ml CellMask™ Deep Red plasma membrane stain for 5 minutes at 37 °C. This staining solution was removed and the cells were washed 3 times with L-15 medium. Finally, the cells were covered with 250 µl of L-15 medium containing a 5 µM DRAQ5™ nuclear stain and suspension of polymer (PVB or EC) nanoparticles doped with *N*,*N'*-bis(2,6 -dimethylphenyl)-perylene-3,4,9,10- tetracarboxylic diimide (PTC, see Figure 3.6.) The polymer nanoparticle suspension was diluted 1:50 with L-15 medium.

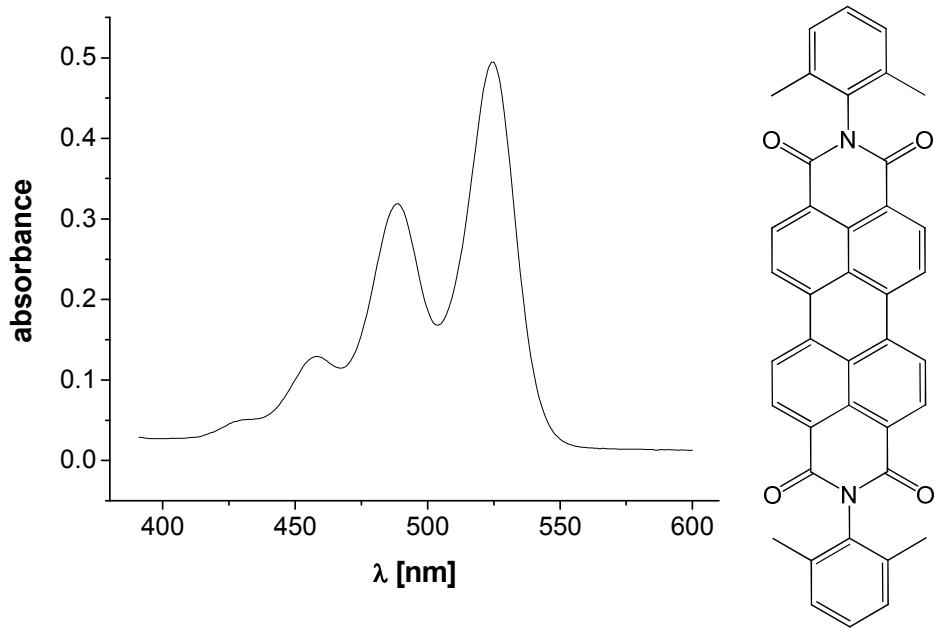

Figure 3.6. Structure and absorption spectrum of PTC.

This photosensitizer was chosen to label the polymer nanoparticles because of a high molar absorption coefficient at available CLSM Ar+-laser wavelengths (488 nm, 514 nm): ε(488 nm) = 4.55 •10^4 $cm^{-1}M^{-1}$, ε(514 nm) = 3.05 •10^4 $cm^{-1}M^{-1}$ [123], which is critical for fluorescence microscopy recording of small polymer nanoparticles (diameter < 200nm).

Confocal laser scanning microscopy experiments were performed with a Carl Zeiss Axiovert 200M microscope (Carl Zeiss AG, Oberkochen, Germany), equipped with a LSM 510 laser scanner. PVB and EC nanoparticles (stained with PTC) were detected through the 530-600 nm band-pass filter, after excitation with the 488 nm laser (4.8 % laser transmission). The nuclei stained with DRAQ5™ and the plasma membranes stained with CellMask™ Deep Red were detected with the 650 nm long-pass filter after excitation with the 633 nm laser (3.1 % laser transmission), as schematically depicted on Figure 3.7. Therefore, PTC fluorescence in particles was separated from the membrane stain fluorescence by both the excitation wavelength and emission filters and separated from the nuclear fluorescence (DRAQ5™) with emission filters. The objective used was a Plan-Apochromat 63R/1.4 with Immersol™ 518 F immersion oil for fluorescence microscopy (Carl Zeiss AG, Oberkochen, Germany).

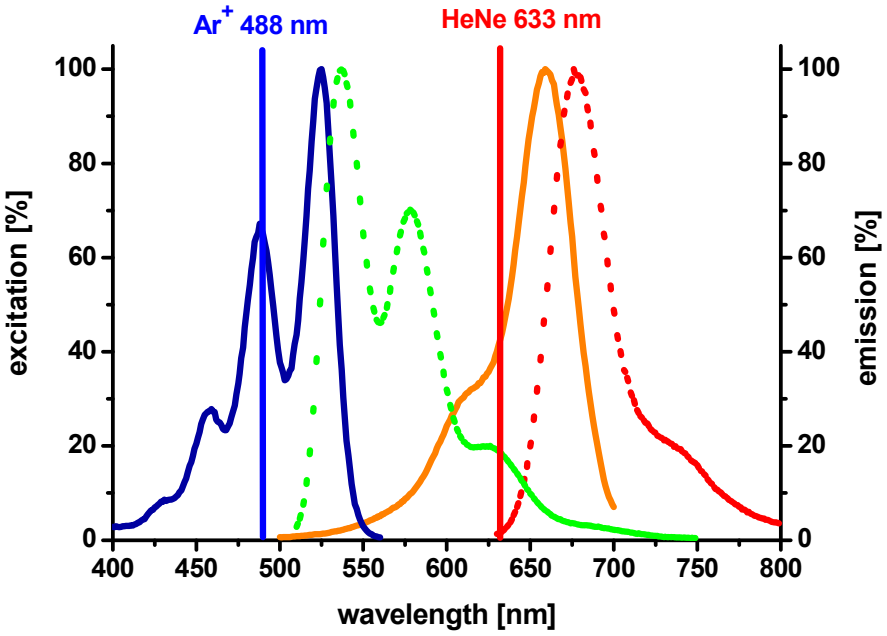

Figure 3.7. Normalized fluorescence excitation and emission spectra of PTC and CellMask™ Deep Red [124] dyes used in CLSM experiments. Solid lines are excitation spectra (blue: PTC, orange: CellMask™ Deep Red) and dotted lines emission spectra (green: PTC, red: CellMask™ Deep Red). Vertical lines are 488 nm and 633 nm laser excitation wavelengths, respectively.

3.6.2. Chemosensitivity Assay

The crystal violet chemosensitivity assays were performed with MDA-MB-231 human breast cancer cells [110] according to the procedure by Bernhardt et al. [111] In brief: tumor cell suspensions (100 µl/well) were seeded into 96-well flat bottomed microtitration plates (Greiner, Frickenhausen, Germany) at a density of 10-15 cells/microscopic field (magnification 32x). After 1-2 days the McCoy´s 5A or RPMI 1640 culture medium (containing 5 % FCS) was removed by suction and replaced with fresh medium (200 µl/well) containing varying drug concentrations or different carrier (liposomes or polymer, EC or PVB nanoparticles) formulations, respectively.

On every plate 16 wells served as controls and 16 wells were used per drug concentration. After various times of incubation the cells were fixed with glutardialdehyde and stored in a refrigerator. At the end of the experiment all plates were stained with crystal violet simultaneously. Absorbance, which corresponds to the living cells mass at each time-

point, was measured at 578 nm using a Biotek 309 Autoreader (Tecnomara, Fernwald, Germany). The absorbance values were transformed into corrected T/C values, expressing the net growth of the treated cells, relative to the growth of the untreated control cells [111]. Corrected T/C values were calculated according to equation

$$(T/C)_{corr}[\%] = \frac{A_T - A_{c,0}}{A_c - A_{c,0}} \cdot 100 \qquad (11)$$

where A_T is the mean absorbance of the treated cells, A_C the mean absorbance of the controls and Ac,o the mean absorbance at the time (t = 0) when drug was added [111].

In this context drug fomulations used were endoperoxides of various naphthalene derivatives (**N1, N2, N4, N5, N7**) embedded in various carrier materials (coated with Polysorbate-80™ or non-coated), which were suspended in double distilled water. In order to differentiate the effect of endoperoxides from the possible effect of their "parent molecules" (naphthalene derivatives) and/or carrier materials on the proliferation of MDA-MB-231 cells, for each aromatic endoperoxides drug formulation, two sets of control formulations were used:

1. non-irradiated undoped carrier material suspension of the same concentration (in ddH_2O) as in the drug formulation to determine the carrier effect on the cell proliferation and
2. non-irradiated naphthalene "parent molecule" of the same concentration as the endoperoxide and the same photosensitizer concentration (as in the drug formulation) embedded in the same carrier material suspension, also of the same concentration as in the drug formulation to determine the photosensitizer and "parent molecule" effect on the cell proliferation.

Prior to the cell incubation, each of these formulations was sterilised for 15 min by irradiation with a UV-A lamp.

As a positive control of the proliferation drug effect on the MDA-MB-231 cells, the clinically established cytostatics cisplatin (Sigma-Aldrich, Deisenhofen, Germany) or vinblastine (Sigma-Aldrich, Deisenhofen, Germany) were used.

4. RESULTS

4.1. NAPHTHALENE DERIVATIVES AS ENDOPEROXIDE PRECURSORS

As already stated in Chapter 1.2, naphthalene derivatives are adequate to intramolecularly "store" $^1O_2$ in form of endoperoxides. 1,4-dimethylnaphthalene (**N1**) and 1,4,5-trimethylnaphthalene (**N2**) were chosen, because they are both commercially available and because decay times of their endoperoxides were already experimentally measured in different solvents [22, 31] and found to be in range suitable for our purposes: in 1,4-dioxane at body temperature (37 ºC) calculated decay times of 1,4-dimethylnaphthalene-1,4-endoperoxide (**N1E**) amount to 1.5 h and of 1,4,5-trimethylnaphthalene-1,4-endoperoxide (**N2E**) 16.1 h, respectively. Moreover, energy changes for decay process of **N1E** and **N2E** were also calculated [31].

Also, it can be presumed that both **N1** and **N2** are non-toxic, according to MSDS data by Sigma-Aldrich N1 "present at levels greater than or equal to 0.1 % **N1** is not identified as probable, possible or confirmed human carcinogen by IARC [125]. Moreover, For **N2** there is unfortunately no toxicological information available.

4.1.1. Synthesis of Novel Naphthalene Derivatives

In order to extend the range of decay-time (and thus $^1O_2$ release-time) and also to adjust the solubility of the endoperoxide in media of different polarity, to enable incorporation into various biocompatible carrier materials such as liposomes or nanoparticles, and to introduce the possibility of synergistic interactions between multiple dioxygen activation sites in one molecule, a synthesis of several novel naphthalene derivatives was performed (see Scheme 1).

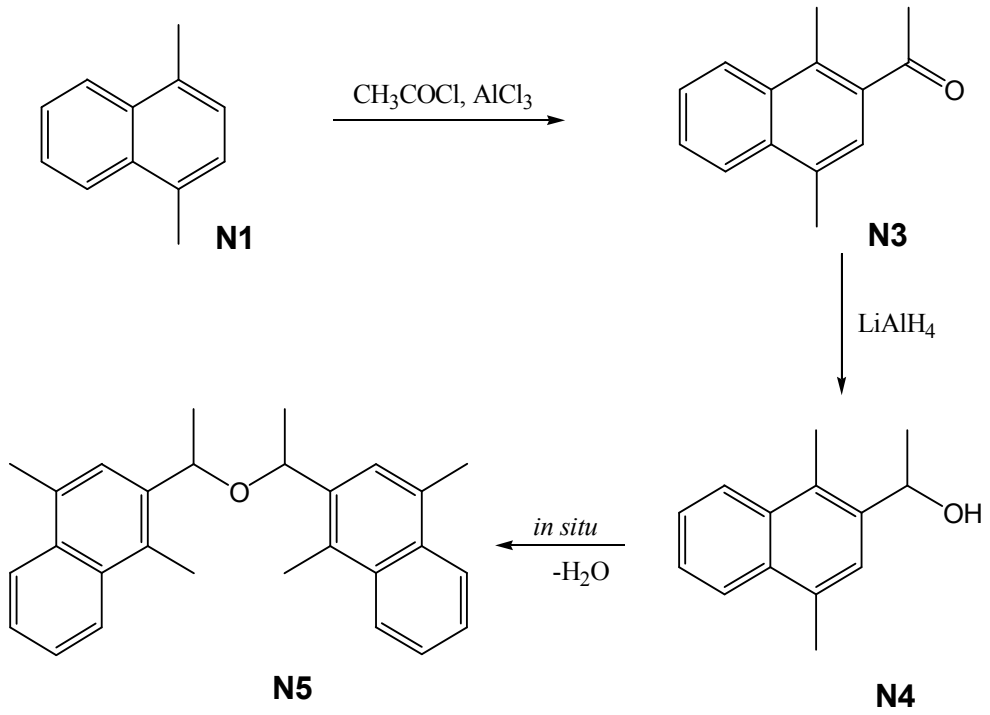

Scheme 1. Synthesis of various endoperoxide-forming naphthalene derivatives from starting **N1** derivative.

Figure 4.1 shows the structure of the 1-(1,4-Dimethyl-naphthalen-2-yl)-ethanol **(N4**) derivative, with selected bond distances and angles given in the Table 4.1. Compound **N4** crystallizes in the monoclinic space group P21/n, with four molecules present in the asymmetric unit. Each **N4** molecule forms H-bonds over O(1)-H(1o) side-group with 2 other neighbouring **N4** molecules, which is important for the discussion of 1-(1,4-dimethyl-naphthalen-2-yl)-ethanol-1,4-endoperoxide (**N4E**) decay-times in different matrices (see Chapter 6.1.)

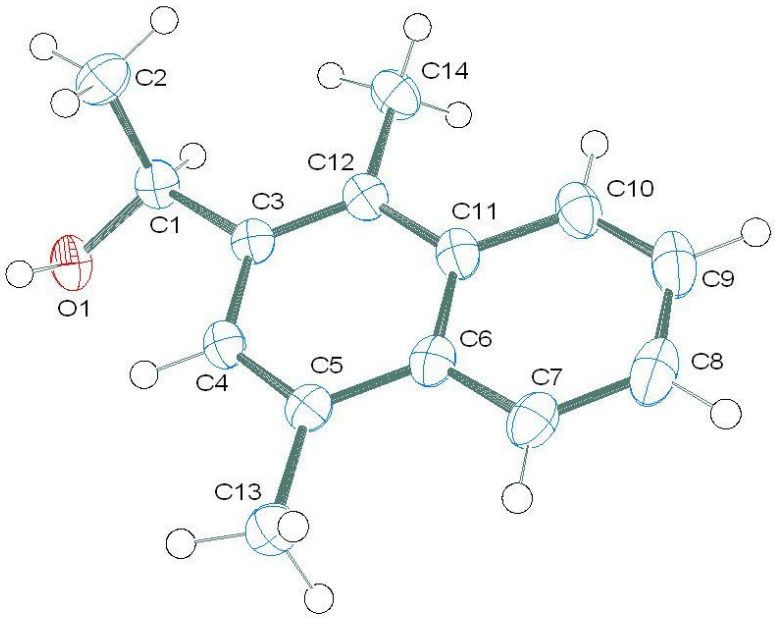

Figure 4.1. ORTEP diagram of **N4** X-ray crystal structure with an arbitrary atom numbering scheme. Displacement ellipsoids are at the 50 % probability level.

Table 4.1. Selected bond lengths (Å) and angles (deg) and torsion angles (deg) of **N4**.

Bond length (Å)	
C1-O1	1.4330(16)
O1-H1o	0.89(2)
C1-C3	1.5247(18)
C1-C2	1.5180(19)
Binding angles (deg)	
C1-O1-H1o	109.2(13)
O1-C1-C2	110.60(11)
O1-C1-C3	112.18(10)
C2-C1-C3	111.11(11)
Torsion angles (deg)	
O1-C1-C3-C4	-28.09(15)
O1-C1-C3-C12	154.20(11)

Figure 4.2. shows the structure of the di-1-(1,4-dimethylnaphthene-2-yl)-ethylether (**N5**) derivative, with selected bond distances and angles given in the Table 4.2. Compound **N5** crystallizes in the monoclinic space group P b c n, with four molecules present in the asymmetric unit.

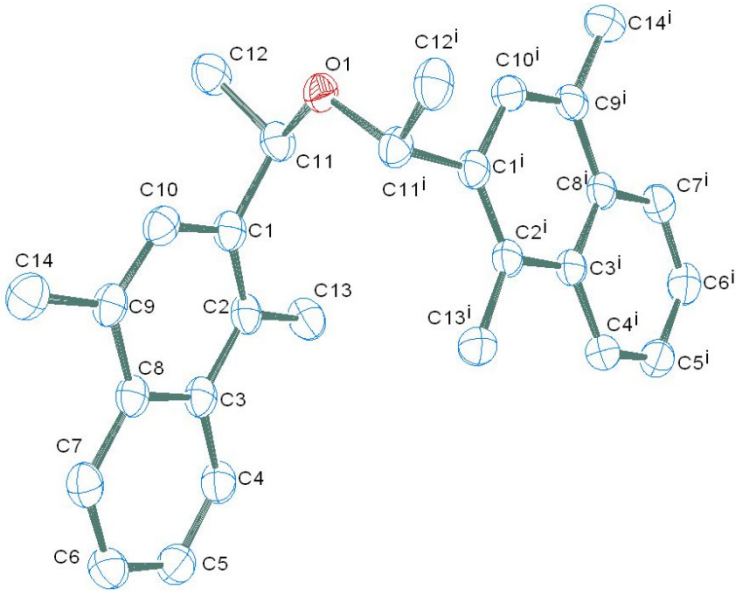

Figure 4.2. ORTEP diagram of **N5** X-ray crystal structure with an arbitrary atom numbering scheme. Hydrogen atoms are left out for a better overview. Displacement ellipsoids are at the 50 % probability level.

Table 4.2. Selected bond lengths (Å) and angles (deg) and torsion angles (deg) of **N5**.

Bond length (Å)	
C11-O1/C11^{i}-O1	1.4416(18)
C1-C11/C1^{i}-C11^{i}	1.523(2)
C11-C12/ C11^{i}-C12^{i}	1.518(2)
Binding angles (deg)	
C11-O1-C11^{i}	114.02(14)
O1-C11-C1/ O1- C11^{i} - C1^{i}	111.12(12)
O1-C11-C12/ O1- C11^{i} - C12^{i}	106.22(13)
C1-C11-C12/ C1^{i} - C11^{i} - C12^{i}	112.07(13)
Torsion angles (deg)	
C11^{i}-O1-C11-C1	61.47(14)
C11^{i}-O1-C11-C12	-176.39(11)

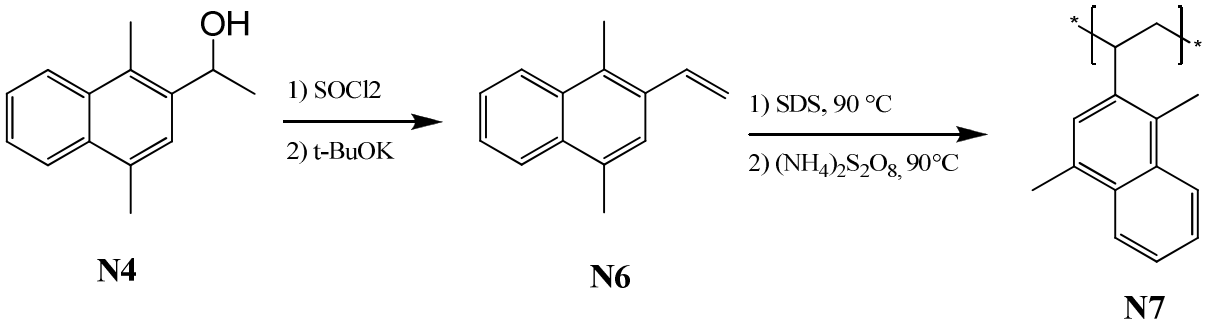

Scheme 2. Synthesis of poly(1,4-dimethyl-2-vinylnaphthalene), **N7,** from **N4** derivative.

4.1.2. Size Variation of **N7** Polymer Nanoparticles

Polymer poly(1,4-dimethyl-2-vinylnaphthalene), **N7,** in which each side group is an endoperoxide forming group, was synthesized in form of nanoparticles from **N4** derivative as shown in Scheme 2.

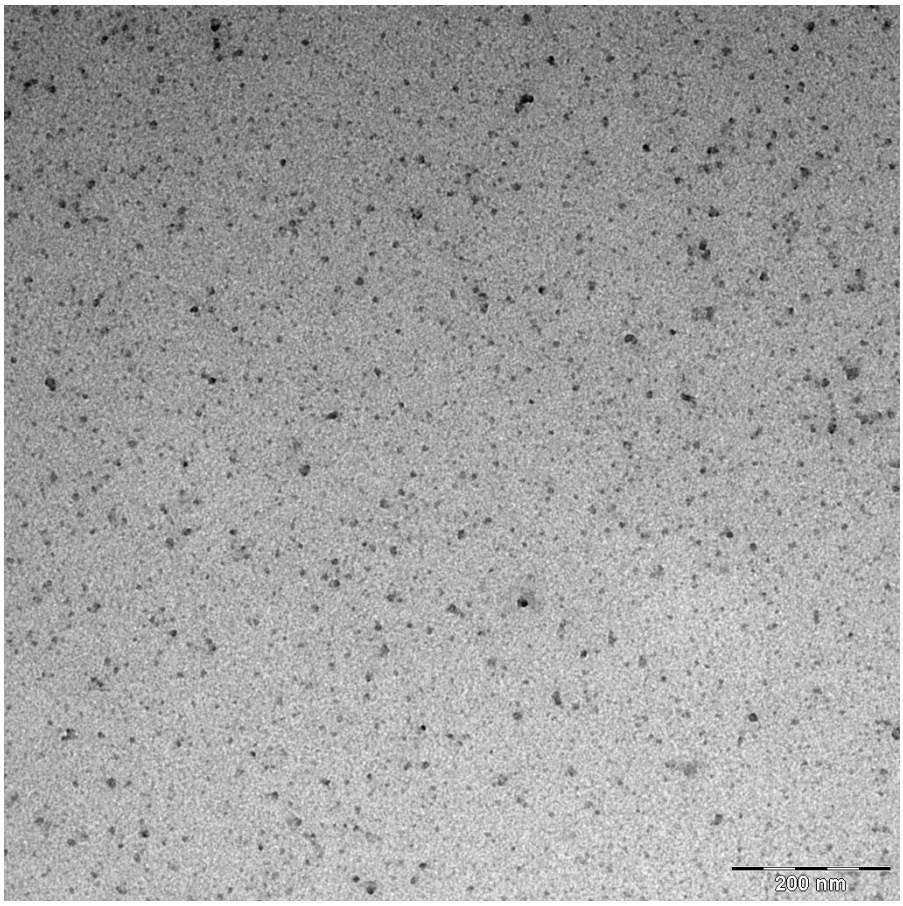

Figure 4.3. TEM image of smaller poly(1,4-dimethyl-2-vinylnaphthalene) nanoparticles (average diameter: 12 ± 3 nm).

Using DLS and TEM techniques, the **N7** nanoparticles average diameter was determined: 12 ± 3 nm, with the latter parameter being standard deviation (see Figure 4.3 when synthesized according to the procedure described in Chapter 3.3.5. For CLSM and chemosensitivity assay purposes (see Chapters 3.6.1. and 3.6.2. respectively) the **N7** synthesis procedure was varied in order to get nanoparticles of different average diameters. The most significant procedure parameters were the polymerization time and the relative amount of $(NH_4)_2S_2O_8$ added, compared to the amount of **N6** monomer in the reaction mixture. The average particles diameter increased with longer polymerization time and larger amounts of $(NH_4)_2S_2O_8$, whereas amount of SDS didn't have such a significant influence on the **N7** nanoparticles size. For example on a smaller scale, a mixture of 8 mg **N6**, 23 mg SDS, 6 mg $(NH_4)_2S_2O_8$ in 10 ml dd H_2O after 5h of polymerization produced **N7** nanoparticles of 95 ±24 nm, as measured with dynamic light scattering technique (see Figure 4.4.) whereas a mixture of 13 mg N6, 56 mg SDS, 16 mg $(NH_4)_2S_2O_8$ in 10 ml dd H_2O after 3h of polymerization produced **N7** nanoparticles of 58 ± 9 nm.

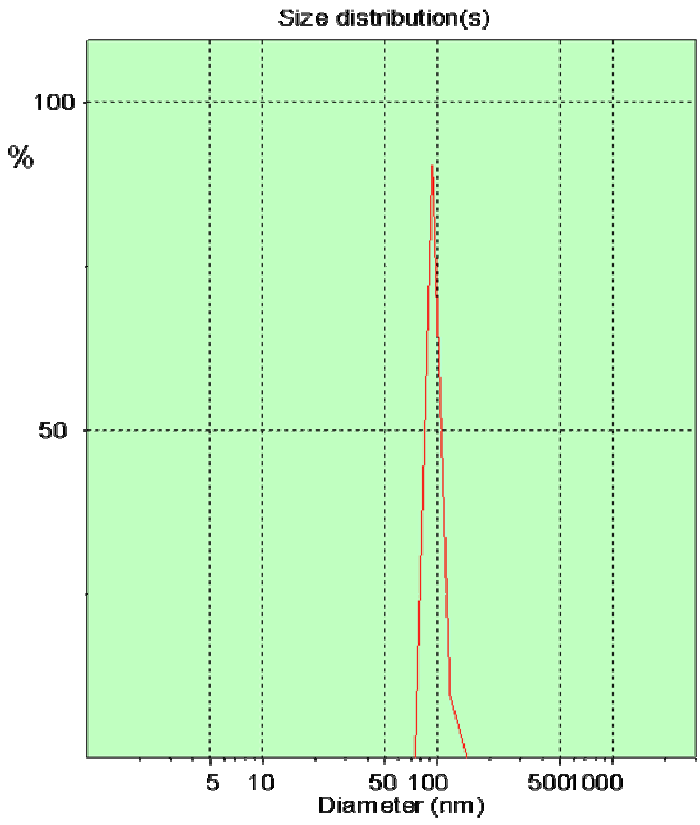

Figure 4.4. Size distribution of larger (average diameter: 95 ±24 nm) poly(1,4-dimethyl-2-vinylnaphthalene) particles measured with DLS method.

Note: It was not possible to freeze-dry the nanoparticles: the freeze-drying procedure caused particles aggregation. **N7** nanoparticles tend to slowly aggregate in H_2O suspension as well: the average diameter increases approximately 2-3 times after 1-2 months.

4.1.3. Optical Properties of Endoperoxide-Forming Naphthalene Derivatives

The electronic spectra of the endoperoxide-forming naphthalene derivatives were recorded in ethanol or chloroform solution. On Figure 4.5. the normalized absorption and emission spectra of **N5** in $CHCl_3$ are given as a typical example. The UV-spectra of other endoperoxide-forming naphthalene derivatives (**N1**-**N6**) are all very similar with strong absorption bands around 230 nm and weaker bands around 290 nm. This indicates that only a negligible perturbation of the electronic properties of the individual naphthalene chromophores occurs in the novel ether-bridged system (**N5**). Band maxima and calculated molar absorption coefficients for the naphthalene derivatives in methanol are given in Table 4.3.

Table 4.3 Band maxima of the electronic spectra of various endoperoxide forming naphthalene derivatives at room temperature in methanol solution.

compound	λ_{max} / nm (ε / $M^{-1}cm^{-1}$)	λ_{em} / nm
N1	287 (7 700)	329, 339, 355
N2	293 (10 100)	332, 343, 355
N4	289 (17 200)	332, 342, 355
N5	287 (14 600)	331, 341, 355

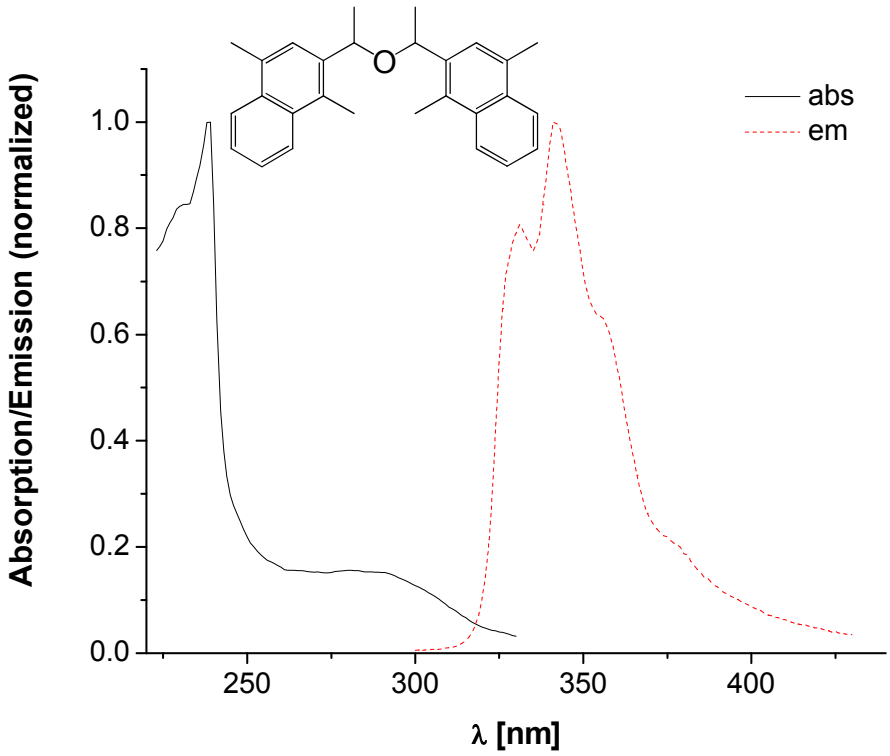

Figure 4.5. Absorption and emission spectra of **N5** derivative in $CHCl_3$.

The emission spectra of the compounds investigated in this study display a main peak at around 340 nm and two shoulders at about 330 nm and 355 nm, respectively (Figure 4.5.) These data are in agreement with the well-known features of regular fluorescence spectra of condensed aromatic hydrocarbons, which in the case of naphthalene derivatives usually consist of a principal series of three to four vibronic bands equally spaced at approximately 1000 cm^{-1} intervals [126]. In the concentration range applied for the present study, no conspicuous band splittings or other excited state interactions of the two equivalent fluorophore entities was detected in the bifunctional compound **N5**.

4.1.4. Endoperoxide Formation and Decay Kinetics in Solvents

N1E and **N2E** formation and decay, usually at 25 °C, in various solvents is described in the literature [22, 31, 12]. Average endoperoxide decay-times, $t_{1/2}$, of these two derivatives in various solvents at human body temperature of 37 °C, were calculated from the literature $t_{1/2}$ values at other temperatures and activation energy, E_a, values [22, 31] and are given in Table 4.4.

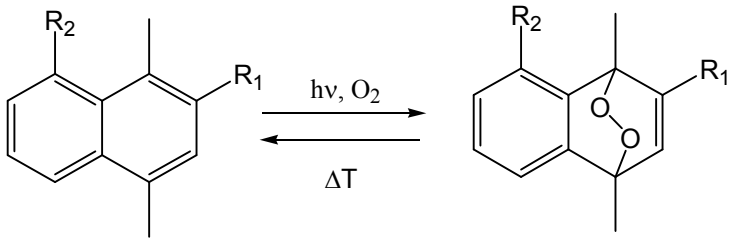

N,
fluorescent

NE,
non luminescent

N1: $R_1 = R_2 = H$

N2: $R_1 = H$, $R_2 = CH_3$

N3: $R_1 = COCH_3$, $R_2 = H$

N4: $R_1 = CHOHCH_3$, $R_2 = H$

N6: $R_1 = CH{=}CH_2$, $R_2 = H$

N7 = poly (**N6**)

Scheme 3. Endoperoxide formation and thermally induced decay on various naphthalene derivatives used in this work.

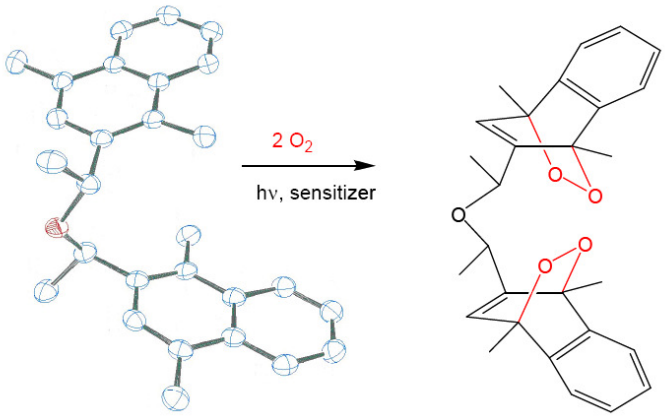

Scheme 4. Endoperoxide formation on the **N5** derivative, witch possesses double endoperoxide-forming (and $^1O_2$-releasing) function in comparison to derivatives in Scheme 3.

Endoperoxide formation and decay of novel naphthalene derivatives, **N4** and **N5** (see Schemes 3. and 4. respectively) were measured at 37 °C in ethanol with time-dependent fluorescence typical for each particular derivative. Fluorescence spectrum of 5 μM naphthalene derivative in ethanol was recorded prior to the light irradiation and photoreaction of endoperoxide formation. After the high power LED light irradiation (P = 120 mW/cm^2) of sensitizer (1 μM MB) for 2-3 hours at 20 °C, formed $^1O_2$ reacted with **N5** or **N4** to form endoperoxides causing the reduction of particular naphthalene derivative fluorescence intensity, from which the yield of this photoreaction was calculated. Such a simple endoperoxide formation procedure with a commercial light source at room temperature in an air atmosphere without O_2 saturation is unprecedented and enables endoperoxide formation in a relatively high yield (about 50 % after 2 h irradiation) without any high-tech equipment. Afterwards, the endoperoxide solution in ethanol was kept at a constant temperature (37 °C) causing a thermal decay of endoperoxides to form the "parent molecule" and therefore, the reappearance of its fluorescence signal. This process and the time-dependency of the fluorescence values of a particular naphthalene derivative (**N1, N2, N4, N5**) were used to calculate the relative quantity of endoperoxide molecules at each time-point in order to determine endoperoxide decay and $^1O_2$-release kinetics in ethanol.

Table 4.4. Endoperoxide-decay kinetic constants, k, and decay-times, $t_{1/2}$, of different endoperoxide-forming naphthalene derivatives in various organic solvents at 37 °C.

	N1[a]	**N2**[a]	**N4**[b]	**N5**[b]
k / **s**$^{-1}$	$1.618 \cdot 10^{-4}$	$1.19 \cdot 10^{-5}$	$(4.408 \pm 0.014) \cdot 10^{-5}$	$(8.532 \pm 0.031) \cdot 10^{-5}$
$t_{1/2}$ / **h**	1.19	16.2	4.37	2.26

[a] average value in 1,4-dioxane, dichloromethane

[b] in ethanol

4.2. ENDOPEROXIDE DECAY AND CYTOTOXICITY IN LIPOSOME CARRIER

First carrier choice was liposomes, as a widely-used, biocompatible material [127, 128 , 129, 130, 131]. Liposomes are often used as a drug-delivery system [132, 133]. Liposomes are artificially prepared vesicles made of lipid bilayer, which are stable in an aqueous environment. A liposome encapsulates a region of aqueous solution inside the liposome hydrophobic membrane where the dissolved hydrophilic solutes cannot pass through the lipid bilayer. Hydrophobic solutes can be dissolved into the membrane, and in this way liposome can carry both hydrophilic and hydrophobic substances, such as porphyrin-derived photosensitizers [46]. In several reports [134, 135] regarding classical photodynamic therapy, photosensitizers embedded in dimiristoyl-phosphatidylcholine vesicles exhibited greater efficiency of targeting cancer, compared with the same photosensitizers administered in a homogeneous aqueous solution. Namely, liposomes are long-circulating carriers in the blood stream and can rapidly enter tumour vessels (which lack the endothelial wall) from the blood, but are kept in the bloodstream by the endothelial wall in healthy tissue vasculature. This is known as the "enhanced permeability and retention (EPR)" effect [136]. Thus liposomes smaller than 400 nm typically accumulate much more in tumor tissue than in normal (healthy) tissues [133].

4.2.1. Liposomes Size and Loading Efficiency

On Figure 4.6. the size distribution of liposomes formed by extrusion, as described in Chapter 3.5.1.1., is shown.

Loading of endoperoxide-forming naphthalene derivatives in liposomes during liposome preparation was possible with various efficiencies. As the determination of naphthalene derivatives concentration in prepared liposome carrier (see Chapter 3.5.1.3.) showed, 60 - 90 % of **N1, N2** or **N4** molecules present in the solution in $CHCl_3$ with 1,2-dimyristoyl-L-α-phosphatidylcholine (DMPC) lipid were successfully embedded in liposomes. Hence, the dopant losses during the liposome preparation by extrusion were

10-40 %. The percentage of embedded molecules severely dropped in case of the **N5** derivative: only 10 - 20 % of **N5** molecules were embedded in prepared liposomes.

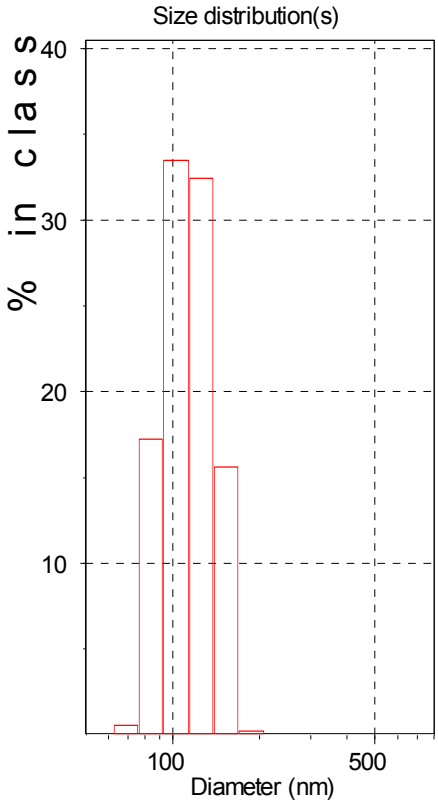

Figure 4.6. Size distribution of DMPC liposomes made with extrusion method, as measured with DLS. Average hydrodynamic diameter was 116 ± 32 nm.

4.2.2. Endoperoxide Formation and Decay Kinetics in Liposome Carrier

Formation of naphthalene-endoperoxides, **NE** (see Schemes 3. and 4.) in liposomes was very efficient: in general, after 15 min of light irradiation of the PS present in liposome matrix at 15 °C, about 90 % of a particular naphthalene derivative, **N**, reacted with $^1O_2$ to form endoperoxides, **NE**. All of the naphthalene endoperoxides studied here share the property of thermal instability regenerating singlet oxygen and the parent naphthalene molecule. Since the reversible formation of naphthalene-derived endoperoxides, their meta-stability and thermal singlet oxygen release is a known phenomenon with extensive literature [12, 13, 16, 22, 31, 137], formed endoperoxides of hereby examined naphthalene-derivatives

and subsequently released singlet oxygen were not detected, but rather taken as a given phenomena. Thus, the endoperoxide formation and thermal decay kinetics were verified only indirectly via the reversible changes of absorption/fluorescence intensity of the each naphthalene-derivative „parent molecule“ electronic spectra. Fluorescence intensity measurements data are shown in further text because of their better reproducibility and lower measurement error than of the absorbance measurements data of the same samples.

Endoperoxide formation and decay were recorded at different temperatures, mainly at the human body temperature of 37 °C, which is most important for possible medical applications, with time-dependence of fluorescence typical for the particular naphthalene derivative, as shown in Figure 4.7. on the example of **N1**. Fluorescence spectrum of **N1** embedded in liposomes was recorded prior to the light irradiation and photoreaction of **N1E** formation (pink curve on Figure 4.7.) After the light irradiation (LED, λ = 420nm, P = 35 mW, Φ = 140 mW/cm^2, T = 14 °C, for t = 0.5h) of embedded sensitizer (PPIX-DME, c= $2 \cdot 10^{-7}$M), generated $^1O_2$ reacted with **N1** in liposomes to form **N1E** causing the reduction of **N1** fluorescence intensity, from which the yield (87 %) of this photoreaction was calculated. Afterwards the liposome suspension with embedded endoperoxides was kept at a constant temperature (e. g. 37 °C) causing a thermal decay of **N1E** to form **N1** “parent molecule” and therefore the reappearance of **N1** fluorescence signal. This process and time-dependence of **N1** fluorescence values were used to calculate the relative quantity of **N1E** molecules at each time-point in a particular carrier in order to determine endoperoxide decay and $^1O_2$-release kinetics.

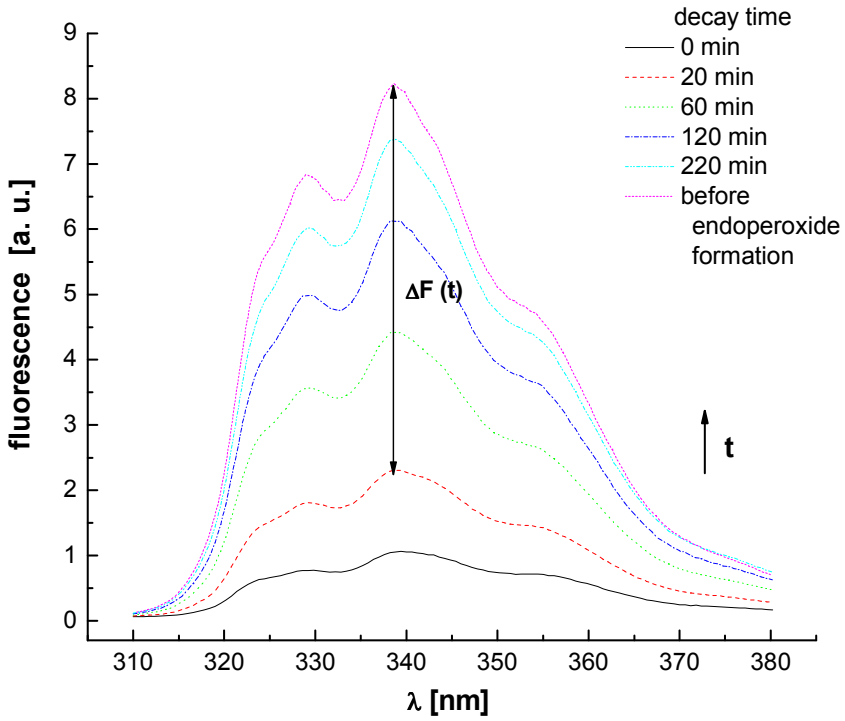

Figure 4.7. Recovery of **N1** fluorescence due to the decay of **N1E** with time. ΔF value and its time dependence is being calculated from the fluorenscence maxima, as demonstrated here on the example of **N1** embedded in liposomes.

The difference in fluorescence peak intensity measured before **N1E** formation, F, (pink curve in Figure 4.7.) and immediately after endoperoxide formation (black curve in Figure 4.7.) corresponds to the number of formed endoperoxide molecules in total, F_0. The other curves (with the reappearance of **N1** molecules) show the course of thermal **N1E** decay with time and hence provide information about the quantity of remaining endoperoxide molecules at each time-point, ΔF(t), which corresponds to the difference in peak intensity measured before endoperoxide formation and particular curve for a decay time-point.

Described experiments and ΔF(t) calculations were done for other (**N5, N4, N1, N2**) endoperoxide-forming naphthalene derivatives in liposome carrier material, as well as in other carriers (see later), at different thermolysis temperatures with emphasis on the human body temperature of 37 °C.

The calculated time-dependence of endoperoxide quantity in liposomes is exemplarily shown in Figure 4.8. for **N4E** at 37 °C. In this particular experiment PPIX-DME sensitizer, c = 0.9 μM, was irradiated with LED (λ = 420 nm, P = 35 mW, Φ = 140 mW/cm^2, T = 14 °C,

for t = 1.25 h) to generate $^1O_2$ which reacted with **N4** (c = 8 0 μM in suspension) to form **N4E** (yield 96 %). The slope on such a semi-logarithmic plot corresponds to the endoperoxide decay rate constant, *k*. The endoperoxide decay times, $t_{1/2}$, are then easily calculated [3, 12]:

$$t_{1/2} = \log 2 / k \qquad (12)$$

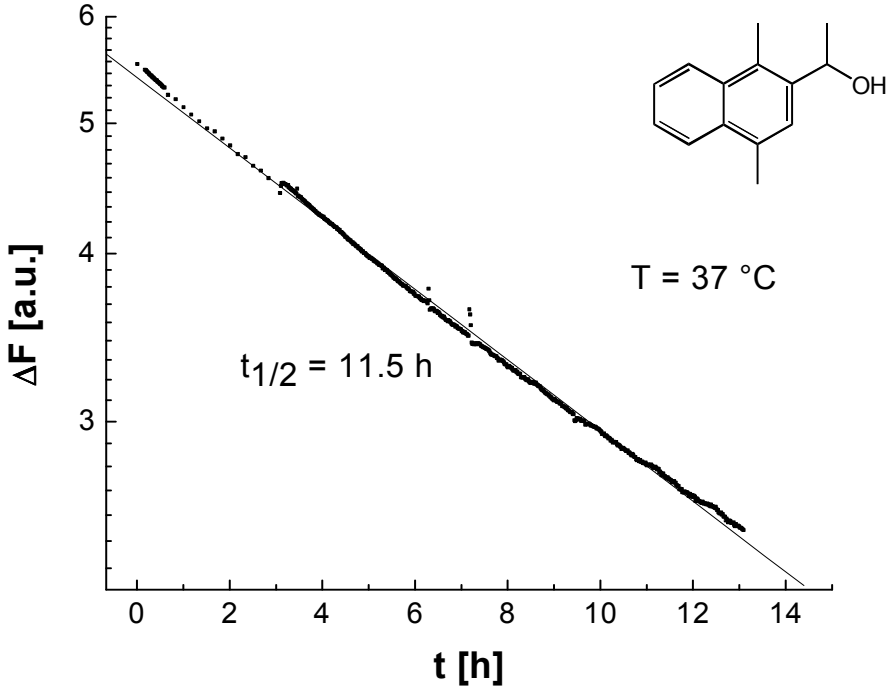

Figure 4.8. Semi-logarithmic plot showing the decay of **N4E** in liposome aqueous suspension (c = 0.9 mM, liposomes diameter 109 ± 12 nm) at 37 °C measured with **N4** fluorescence time-trace. On y-axis is the relative ΔF value, representing **N4** molecules which are in endoperoxide form.

In Table 4.5. endoperoxide decay times, $t_{1/2}$, of all naphthalene derivatives embedded in liposomes (average diameter 110 nm) at 37 °C are given. The sensitizer used was PPIX-DME in all cases, c = 0.9 M. Irradiation was done with LED (λ = 420nm, P = 35 mW, Φ = 140 mW/cm^2, at T =1 4 °C). In all cases monoexponential endoperoxide decay in liposomes was observed.

The stability factor, SF, which shows the increase of endoperoxide $t_{1/2}$ in liposome matrix (or other matrices, see later) in comparison to the average $t_{1/2}$ in various organic solvents (see values in Table 4.4.), was calculated according to the equation 13 and is also given in Table 4.5.

$$SF = t_{1/2}\ (\text{liposomes}) / t_{1/2}\ (\text{solvent}) \qquad (13)$$

Table 4.5. Monoexponential decay times of endoperoxides of different naphthalene derivatives embedded in liposomes (average diameter 110 nm) at 37 °C and calculated endoperoxide stability factors, SF, in comparison to the decay in organic solvents.

Molecule in liposomes	$t_{1/2}$ /h	SF
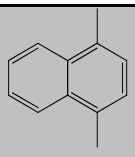 **N1**	1.1	0.95
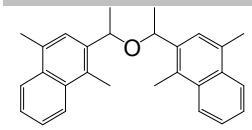 **N5**	1.5	0.66
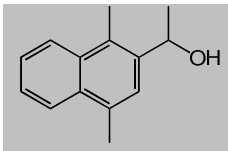 **N4**	11.5	2.63
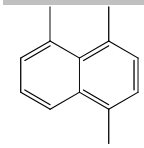 **N2**	17.1	1.06

Endoperoxide decay was also observed at 46 °C, the temperature used to model extreme hyperthermia in cancer treatment [138, 139]. On Figure 4.9. decay time of **N2E** in liposomes at 46 °C is given. PPIX-DME sensitizer, c = 0.18 μM, was irradiated with LED (λ = 420 nm, P = 35 mW, Φ = 140 mW/cm^2, T = 14 °C, for t = 0.4 h) to form $^1O_2$ which reacted with **N2** (c = 16 μM in aqueous liposome suspension) to form **N2E** (yield 94 %). On y-axis is the calculated percentage value of all **N2** molecules which are in endoperoxide form at each particular time-point. This endoperoxide % value was calculated by dividing the quantity of remaining endoperoxide molecules at each time-point, ΔF(t), with the quantity of total **N2** molecules before endoperoxide formation, F, (fluorescence peak intensity measured before **N2E** formation):

$$\%\ \text{endoperoxides} = \Delta F(t) / F \bullet 100 \qquad (14)$$

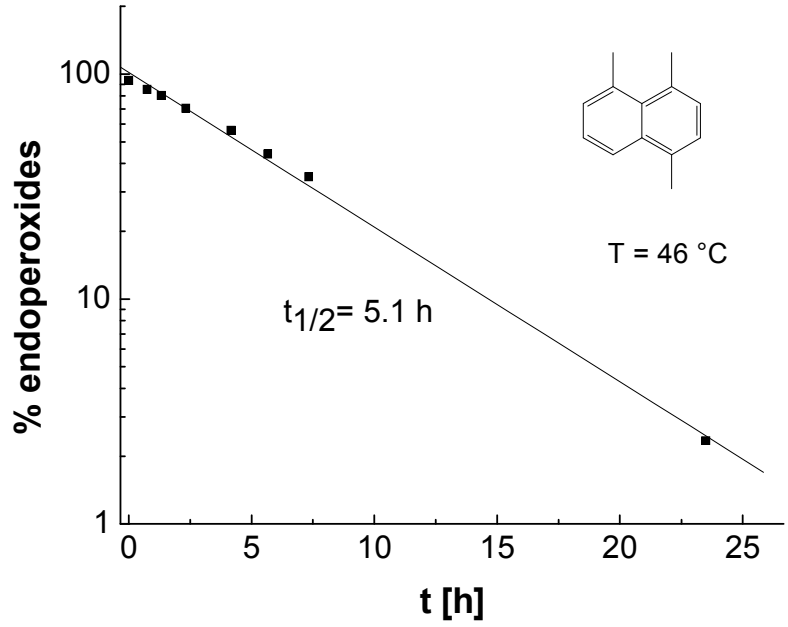

Figure 4.9. Semi-logarithmic plot showing decay of **N2E** in liposomes, c(lipid) = 0.9 mM, diameter 109±12nm, at 46°C measured with **N2** fluorescence time-trace. On y-axis is the percentage of all **N2** molecules which are in endoperoxide form at each particular time-point.

4.2.3. *In Vitro* Cytotoxicity of $^1O_2$-Releasing Endoperoxides in Liposome Carrier: Kinetic Chemosensitivity Assay Results

Based on the endoperoxide decay time and corresponding $^1O_2$-release time, **N2E** and **N4E** embedded in liposomes were most suitable for chemosensitivity assay on cancer cells [111]. As a positive control during the chemosensitivity assay, cisplatin, a standard cytostatic drug, was used. Thus, it was possible to compare the cancer cells chemosensitivity to endoperoxides and to such a standard drug. The chemosensitivity of MDA-MB-231 cells to cisplatin was determined at concentrations ranging from 300 nM to 10 μM cisplatin dissolved in DMF (see Figure 4.10.) The lowest cisplatin concentration (0.3 μM) yielded a very weak cytotoxic effect from which the cells recovered completely. 1.0 μM concentration had a strong cytotoxic effect with a slow cell population recovery after 125 h. 3.0 μM cisplatin had a cytostatic effect on MDA-MB-231 human breast cancer cells proliferation, whereas 10 μM cisplatin showed a cytocidal effect (see Figure 4.10.) The solvent DMF had no effect on the cell proliferation and was used as a negative growth control (☆).

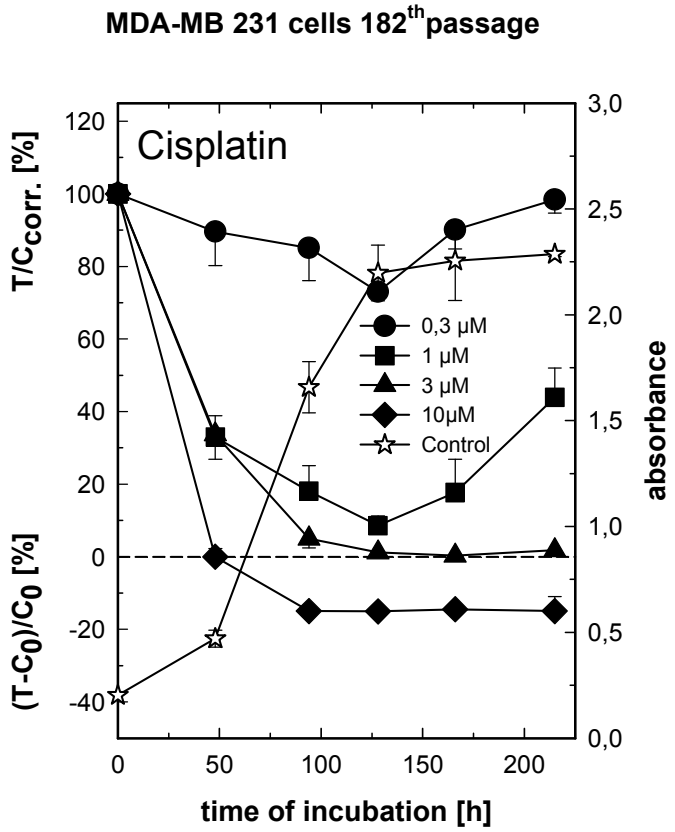

Figure 4.10. Chemosensitivity of MDA-MB-231 cells (182nd passage) against cisplatin, up to a 10 µM concentration in DMF solvent. DMF was used as a negative growth control (☆).

According to the procedure described in Chapter 3.5.1.1., the feed aqueous liposome suspensions for the chemosensitivity assays were prepared. The concentration of **N2** or **N4** in liposome stock suspension was determined photometrically according to Lambert-Beer's law as described in Chapter 3.5.1.3. To distinguish the effect of $^1O_2$-release from endoperoxides from the effect of **N2** (or **N4**) and from the effect of liposomes on the cell proliferation, 3 types of suspension were prepared:

1. Light-irradiated **N2** embedded in liposomes forming $^1O_2$-releasing **N2E** embedded in liposomes
2. Non-irradiated **N2** of the same **N2** concentration as in suspension 1
3. Non-irradiated liposome suspension of the same lipid concentration as in suspension 1 and 2.

The same 3 types of suspensions were prepared with **N4** embedded in liposomes.

4.2.3.1. Cytotoxicity of **N2E** Embedded in Liposomes

The chemosensitivity of MDA-MB-231 human breast cancer cells to $^1O_2$-releasing **N2E** was determined at a highest achieved **N2** concentration in the liposome suspension, which after dilution in the RPMI cell medium was 6.5 μM (Figure 4.11.) Photosensitizer concentration was c (PPIX-DME in cell medium) = 0.09 μM. PPIX-DME sensitizer was irradiated with LED (λ =4 20 nm, P = 35 mW, Φ = 140 mW/cm^2, T = 14°C, for t = 0.5 h) to form $^1O_2$ which reacted with **N2** to form **N2E** (yield 97 %). The cell incubation with a mixture of 6.3 μM $^1O_2$-releasing **N2E** and 0.2 μM **N2** embedded in liposomes yielded a cytotoxic effect of about 30 % (● on Figure 4.11.) compared to the growth of untreated cells. But the cells recovered until the end of the incubation period (ca. 200 hours). Non-irradiated 6.5 μM **N2** embedded in the same liposome suspension (○ on Figure 4.11.) produced approximately only 10 % inhibition of cell growth with a full cell recovery after ca. 150 hours. The proliferation of MDA-MB-231 cells was not inhibited by non-irradiated liposomes not carrying **N2** (◇ on Figure 4.11.) As a comparison a cytostatic effect of cisplatin, is visible on Figure 4.11. (★ symbols): growth of cells is about 70 % inhibited and cell population doesn't recover after treatment with 10 μM Cisplatin. This particular stock solution of cisplatin was prepared in DMSO and a slow exchange of ammine groups of cisplatin with sulphoxide groups of solvent occurred, which resulted in partial inactivation of the drug. Hence, a cytostatic, insead of a cytocidal effect of 10 μM cisplatin is visible on Figure 4.11. This phenomenon also appeared in other chemosensitivity assay experiments when cisplatin was dissolved in DMSO, see later Figs.

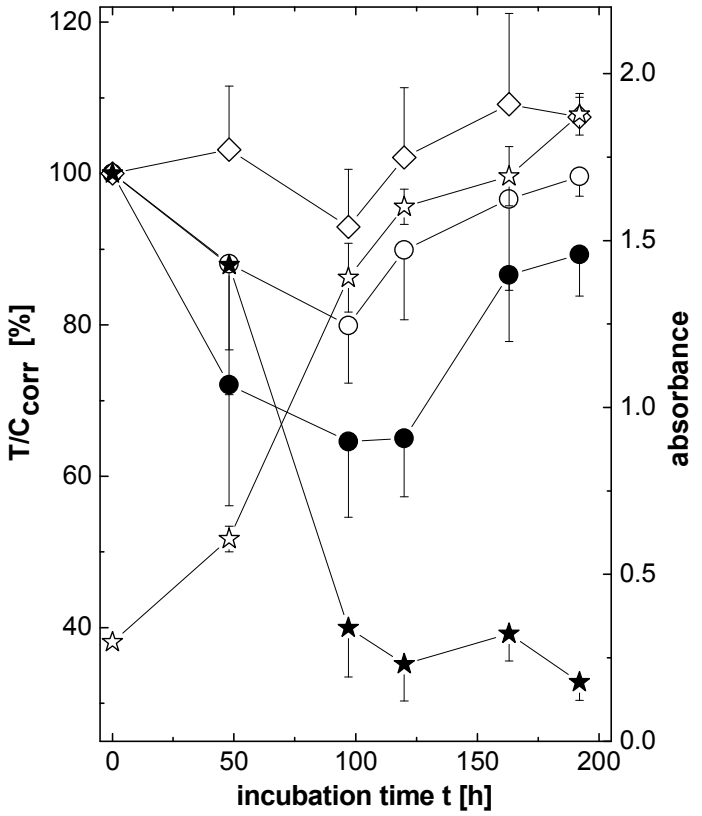

Figure 4.11. Demonstration of a cytotoxic drug effect of **N2E** embedded in liposomes (diameter 109 ± 12 nm) on human MDA-MB-231 breast cancer cells, passage 64, as a function of incubation time determined by the crystal violet assay. ○ **N2**, 6.5 μM, in liposomes, c(lipid)= 24 μM, ● **N2E**, 6.3 μM + **N2,** 0.2 μM in liposomes, c(lipid)= 24 μM, ◇ liposomes, c(lipid)= 24 μM, ★ positive control: Cisplatin, 10 μM, ☆ negative control: H_2O.

Probably with a higher concentration of **N2E** in the liposome suspension, a stronger cytotoxic or a cytostatic effect on the proliferation of MDA-MB-231 cells would have been achieved. But, it was not possible to produce a liposome suspension with a higher ratio of embedded **N2** molecules to DMPC lipid molecules forming liposome membrane than the suspension used in Figure 4.11. in which this ratio was **N2** / DMPC = 1 : 5 in $CHCl_3$ prior to preparation of liposome suspensions (described in Chapter 3.5.1.)

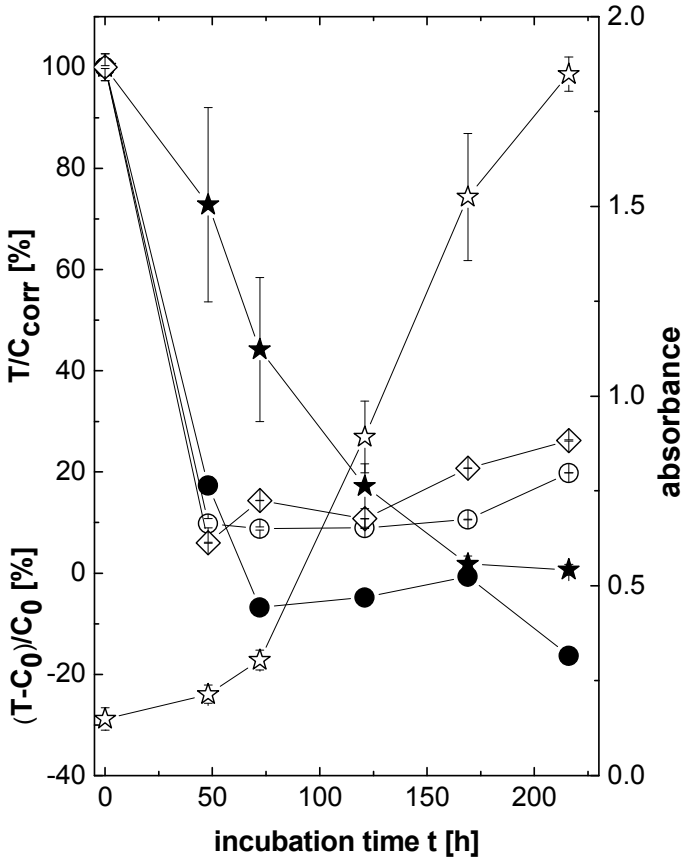

Figure 4.12. Cytocidal drug effect of **N2E** when embedded in a higher, cytotoxic liposomes concentration (c(lipid) = $4 \cdot 10^{-5}$ M, diameter 109 ± 12 nm) on human MDA-MB-231 breast cancer cells, passage 49, as a function of incubation time determined by the crystal violet assay. ○ **N2**, 2.4 μM, in liposomes, c(lipid)= 40 μM, ● **N2E**, 2.3 μM + **N2,** 0.1 μM in liposomes, c(lipid)= 40 μM, ◇ liposomes, c(lipid)= 40 μM, ★ positive control: cisplatin, 5 μM, ☆ negative control: H_2O.

However, when the liposome concentration in an aqueous suspension is increased (c(lipid) = 40 μM in cell medium, diameter 109 ± 12nm), a mixture of 2.3 μM $^1O_2$-releasing **N2E** and 0.1 μM **N2** embedded in liposomes of such a high concentration do have a cytocidal effect on the proliferation of MDA-MB-231 cells, (● onFigure 4.12.) Even though the **N2** concentration, c(**N2**) = 2.4 μM in cell medium (and therefore **N2E** concentration, as well) is lower than in the previous assay (Figure 4.11.), the inhibitory effect on the cells is much stronger because the empty liposomes alone inhibit the cells growth (◇ on Figure 4.12.) and on top of that $^1O_2$ from decaying **N2E** impacts the cell population growth. MDA-MB-231 cell population does slowly recover 120 h after non-loaded liposomes or **N2** in liposomes incubation (◇ and ○ symbols, respectively) but does not recover after incubation of **N2E** in liposomes (●). Cytocidal effect of **N2E** in liposomes is even stronger than the cytostatic

effect of 5 μM cisplatin (★ symbols). Photosensitizer concentration was c(PPIX-DME in cell medium) = 0.05 μM. PPIX-DME sensitizer was irradiated with LED (λ = 420 nm, P = 35 mW, Φ = 140 mW/cm^2, T = 14 °C, for t = 0.5h) to form $^1O_2$ which reacted with **N2** to form **N2E** (yield 95 %).

4.2.3.2. Cytotoxicity of **N4E** Embedded in Liposomes

The chemosensitivity of MDA-MB-231 human breast cancer cells to $^1O_2$-releasing **N4E** was tested, as well. The highest achieved **N4** concentration in liposome suspension (c(lipid) = 3±1•10^{-5}M in cell medium) diluted in RPMI cell medium was 10 μM. The chemosensitivity assay results of **N4E** formed from this highest concentrated **N4**-liposome suspension (see Figure 4.13.) were very similar to the cytotoxycity of 6.3 μM N2E in liposome suspension, shown in Fig. 4.11. The cells incubated with a mixture of 9.2 μM $^1O_2$-releasing **N4E** and 0.8 μM **N4** embedded in liposomes yielded a cytotoxic effect of about 30 % of growth inhibition compared to the normal growth of untreated cells, but the cells recovered until the end of the incubation period (ca. 200 hours). The photosensitizer concentration was c(PPIX-DME in cell medium) = 0.5 μM. PPIX-DME sensitizer was irradiated with LED (λ= 420 nm, P = 35 mW, Φ = 140 mW/cm^2, T = 14°C, for t = 0.6 h) to form $^1O_2$ which reacted with **N4** to form **N4E** (yield 92 %). Non-irradiated 10 μM **N4** embedded in the same liposome suspension (○ symbols on Figure 4.13.) and non-irradiated empty liposomes (◇ symbols on Figure 4.13.) produced only a slight insignificant inhibition of cell growth which was within the experimental errors of the treated cells. Therefore, even with a concentration increase of $^1O_2$-releasing endoperoxides for about 50% (**N4** in comparison to **N2** in liposomes), chemosensitivity assay results did not change, probably due to the shorter decay time of **N4E** than of **N2E**, see Table 4.5. Moreover, there can be a loss of the **N4E** because of the solubility equilibrium shift: **N4E** is more water soluble than **N4** because of polar hydroxyl group and polar endoperoxide bridge, and thus some of **N4E** can be dissolved in water (outside of liposomes) before the liposome cell uptake.

As a positive control again the cytostatic drug effect of 10 μM Cisplatin dissolved in DMSO is shown on (★ symbols on Figure 4.13.)

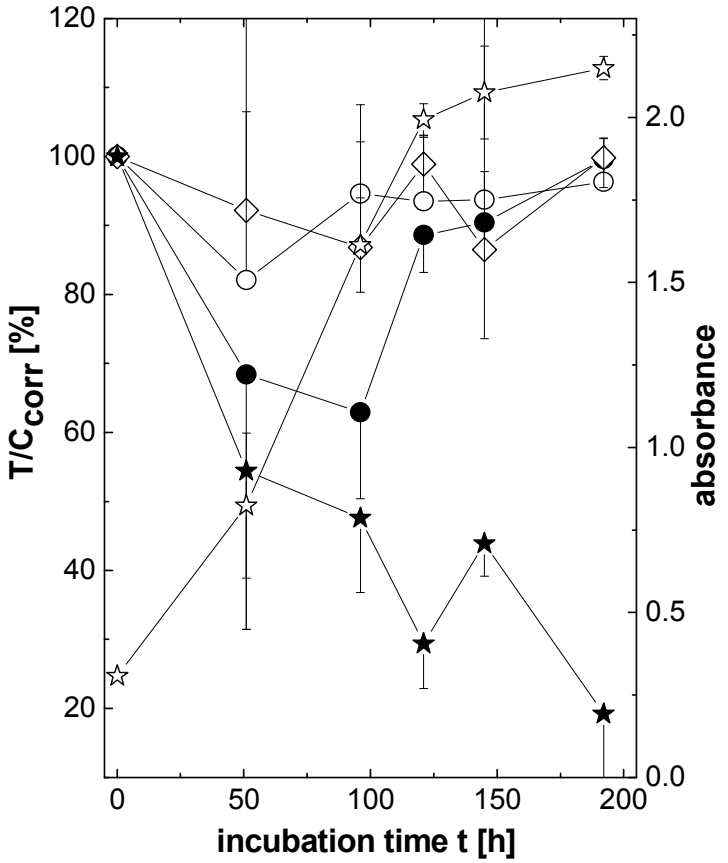

Figure 4.13. A weak cytotoxic drug effect of **N4E** (c = 9.2 μM) embedded in liposomes (diameter 109 ± 12 nm) on human MDA-MB-231 breast cancer cells, passage 77. ○ **N4**, 10 μM, in liposomes, c(lipid) = 30 ± 10 μM, ● **N4E**, 9.2 μM + **N4,** 0.8 μM in liposomes, c(lipid)= 30 ± 10 μM, ◇ liposomes, c(lipid)= 30 ± 10 μM,★ positive control: cisplatin, 10 μM in DMSO, ☆ negative control: H_2O.

Remarkably, liposomes could not be loaded with **N5** derivative in a high enough concentration for chemosensitivity assay (in μM range) using the extrusion method for liposome preparation. Namely, the highest reached N5 concentration was 22 μM in aqueous liposome suspension, what would amount to about 0.8 μM in cell medium.

Finally, in order to decrease the $^1O_2$ losses due to relaxation within the liposomes, a 50 nm diameter liposome production was tried using a 50 nm pore membrane in Liposofast™. Although some liposomes of such size were formed, the concentration of both liposomes and endoperoxide-forming derivatives was unusable for the chemosensitivity assay.

4.3. ENDOPEROXIDE FORMATION AND DECAY KINETICS IN THE PVB FILM

Polyvinyl butyral (PVB) is among the synthetic polymers that are produced annually on a very large scale. The composition of PVB (for details see Chapter 3.5.2.) proved to be useful in various applications [119]. Among other uses, film forming abilities and transparency of PVB in the visual range are being widely used in areas such as safety glass with PVB interlayers, e.g. for cars or buildings. PVB is an excellent substrate for dye incorporation, and many PVB-based paints, inks and lacquers are available. PVB is completely non-toxic and due to its composition of only carbon, hydrogen and oxygen it combusts with almost no residue, which resulted in its widespread use in food packaging.

PVB was used as a model polymer because of its completely amorphous structure and excellent optical properties (no light scattering) [140]. On top of that, PVB could possibly be considered as a carrier material in implants [141].

All the endoperoxide-forming naphthalene derivatives (**N1**, **N2**, **N5** or **N4**) were embedded in PVB film in a very high concentration, up to c = 5 mM in PVB film. TPFPP-Pd(II) sensitizer was also embedded in PVB films. Ratios of embedded TPFPP-Pd(II) : naphthalene derivative varied from 1:10 to 1:100.

4.3.1. Endoperoxide Formation in the PVB Film Carrier

Endoperoxide formation and decay were measured at different temperatures with time-dependence of fluorescence typical for the particular naphthalene derivative, as described in Chapter 4.2.2. As naphthalene fluorescence decreases, relative amount of naphthalene molecules in endoperoxide form increases. Efficiency of endoperoxide formation depends on the ethanol content in PVB film during light irradiation. Because the PVB film samples were kept in an ethanol atmosphere prior to the light-irradiation, endoperoxide formation process was remarkably fast, with 60-90 % of endoperoxides formed after 40-50 minutes of irradiation at room temperature, depending on the sample thickness, uniformity and ethanol content. An example of **N5**E formation in PVB film at room temperature

depending on the light irradiation-time is given in Figure 4.14. In general, endoperoxide-formation process in PVB film was approximately logarithmic, reaching saturation after ca. 1h of LED irradiation for each naphthalene derivative.

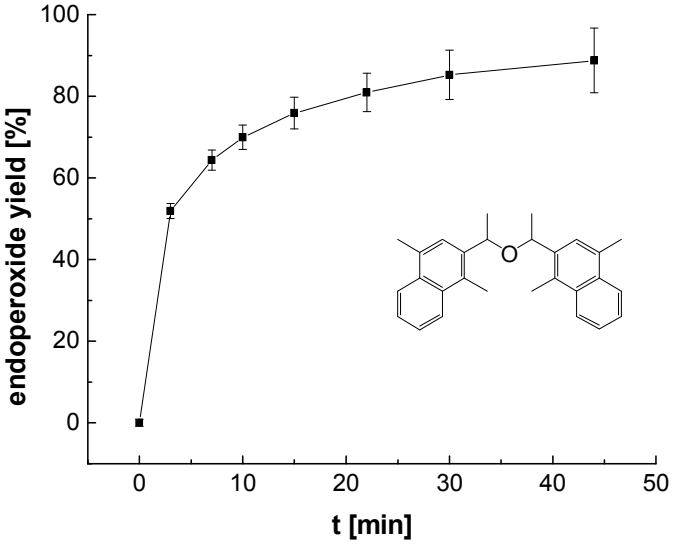

Figure 4.14. **N5E** formation yield in PVB polymer film at room temperature (25 °C) depending on LED irradiation-time measured with **N5** fluorescence time-trace. TPFPP-Pd(II) sensitizer, c = 15 μM in PVB film, was irradiated with LED (λ = 420nm, P = 35 mW, Φ = 140 mW/cm^2, T = 24 °C) to form $^1O_2$ which reacted with **N5**, c = 0.3 mM in PVB film, to form **N5E**.

4.3.2. Endoperoxide Decay Kinetics in the PVB Film Carrier

In order to determine endoperoxide decay and $^1O_2$-release kinetics thermally-induced process of endoperoxide decay was measured at different temperatures with time-dependence of fluorescence typical for the particular naphthalene derivative, as described in detail in Chapter 4.2.2. The percentage of still existing endoperoxide molecules at each time-point was calculated according to equation 14. In Figure 4.15. an example of **N4E** decay in PVB film at 37 °C is shown. TPFPP-Pd(II) sensitizer, c = 15 μM in PVB film, was irradiated with LED (λ = 420nm, P = 35 mW, Φ = 140 mW/cm^2, T = 28 °C, for t = 0.75 h) to form $^1O_2$ which reacted with **N4**, c = 3 mM in PVB film, to form **N4E** (yield 86 %). Remarkably, the endoperoxide decay of examined naphthalene derivatives (except **N5**) in PVB film was

biexponential and not monoexponential like in solvents (see Chapter 4.1.4.) or in liposomes (see Chapter 4.2.2.)

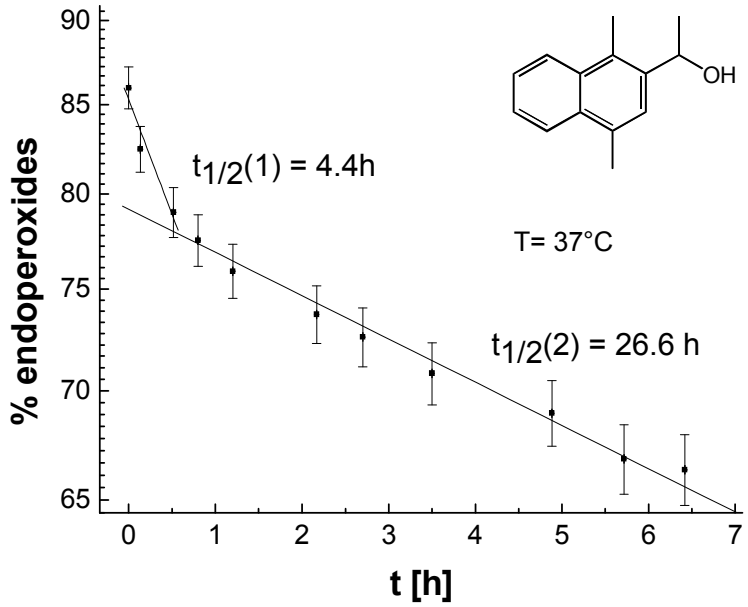

Figure 4.15. Semi-logarithmic plot showing decay of **N4E** in PVB polymer film at 37 °C measured with **N4** fluorescence time-trace. On y-axis is the percentage of all **N4** molecules which are in endoperoxide form at each particular time-point.

During the biexponential decay in PVB film there is a certain percentage of fast-decaying endoperoxides (FDE), with a decay-time shorter (**N2E, N4E**) or similar to the decay-time in liposome aqueous suspension. After the decay of FDE there is a sharp change in semi-logarithmic plots showing endoperoxide decay (e.g. see Figure 4.15.) of each examined naphthalene derivatives (**N1, N2, N4, N5**), marking the transition to another population of endoperoxide molecules, slowly-decaying endoperoxides, SDE. SDE are more stable than endoperoxides of the same "parent molecule" in liposome matrix. In Table 4.6. endoperoxide decay times of all examined naphthalene derivatives in PVB film matrix at 37 °C, as well as the correspondineg percentages of FDE and SDE are given.

Table 4.6. Decay times of endoperoxides of different naphthalene derivatives in PVB film matrix at 37 °C. In parenthesis are the percentages of formed endoperoxides decaying with corresponding $t_{1/2.}$ For both FDE and SDE calculated endoperoxide stability factors, SF, in comparison to the average decay in various organic solvents are given.

Molecule in PVB film	$t_{1/2}$ (% endoperoxides)
N1	1.7 h (30%) SF = 1.42; 7.3 h (12%) SF = 6.08
N4	4.4 h (8%) SF = 1.00; 26.6h (16%) SF = 6.09
N2	6.4 h (8%) SF = 0.39; 19.4h (18%) SF = 1.20
N5	6.0 h (50%) SF = 2.65

The sensitizer used were TPFPP-Pd(II), c = $1.5 \cdot 10^{-5}$ M in PVB film, and in case of **N1** derivative PPIX-DME, c = $6.0 \cdot 10^{-4}$ M in PVB film. Light-irradiation was done with LED (λ = 420 nm, P = 35 mW, Φ = 140 mW/cm^2, at room temperature), and in case of **N1** with Ar^+ laser (λ = 514 nm, P = 150 mW, Φ = 600 mW/cm^2, at room temperature). **N5E** had no significant FDE part and showed a monoexponential decay.

4.3.3. Systematical Adjustment of the Endoperoxide Decay Kinetics in the PVB Film

Influence of different parameters during the endoperoxide formation procedure on the endoperoxide decay-time and relative percentages of FDE and SDE was tried out. First of all, changing the ethanol content in the PVB sample before or shortly after light irradiation was tried by putting the PVB film sample under vacuum before or after light irradiation, as well as leaving it on a temperature (ranging 37 °C - 56 °C) higher than the room temperature for up to 1 day before light irradiation. By varying these parameters no significant or systematic increase of endoperoxide stability could be achieved. However, by varying the temperature on sample during the light irradiation this goal was achieved. The optimal temperature on sample during the light irradiation was 32 °C, see Figure 4.16. and Figure 4.17. When the sample was held during irradiation at even higher temperatures, such as 37 °C, the yield of endoperoxide formation was poor. For example, after 50 minutes of LED irradiation with 33

°C on **N1** in PVB sample, **N1E** yield was 84 %, and when temperature on the sample was 37 °C (with all the other parameters unchanged), the yield was only 40 %.

In Fig. 4.16. an example of endoperoxide decay-time prolongation is shown. **N2E** in PVB film were formed by light-irradiation with 32 °C on PVB sample during this process. The endoperoxide decay at 46 °C was examined. TPFPP-Pd(II) sensitizer, c= 15 μM in PVB film, was irradiated with Ar^+ laser (λ=514nm, P = 180 mW, Φ = 720 mW/cm^2, T = 32 °C, for t = 0.67 h) to form $^1O_2$ which reacted with **N2**, c = 3 mM in PVB film, to form **N2E** (yield 93 %).

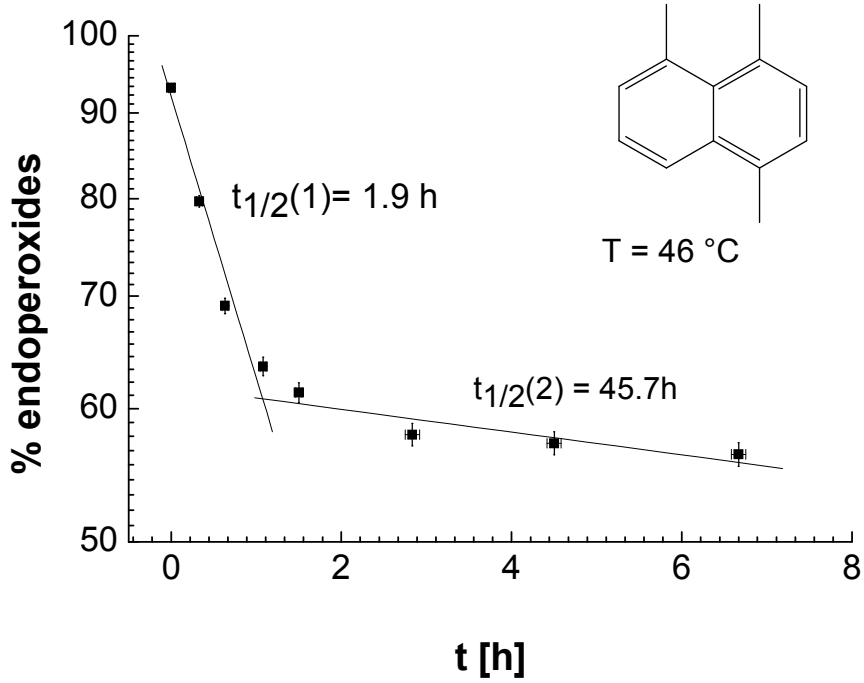

Figure 4.16. Semi-logarithmic plot showing decay of **N2E** in PVB polymer film matrix at 46 °C (hyperthermia model temperature) measured with **N2** fluorescence time-trace. On y-axis is the percentage of all **N2** molecules which are in endoperoxide form at each particular time-point.

A significant part is FDE, 32 % of formed **N2E** decay with $t_{1/2}$ = 1.9h, faster than in liposomes $t_{1/2}$ = 5.1 h, probably because this part of endoperoxide molecules have enough of free volume present in PVB matrix and are able to decay without any hindrance from PVB matrix wall. But, SDE part of formed **N2E** is stabilized presumably due to the physical processes of continuous forming and decay (thermal back-reaction) during irradiation at increased temperature. For more details, see Chapter 6.1. Decay-time of such stabilized SDE, $t_{1/2}$ = 45.7 h, is even at 46 °C longer than $t_{1/2}$ = 19.4 h at 37 °C (Table 4.6.) of SDE **N2E** formed at room temperature.

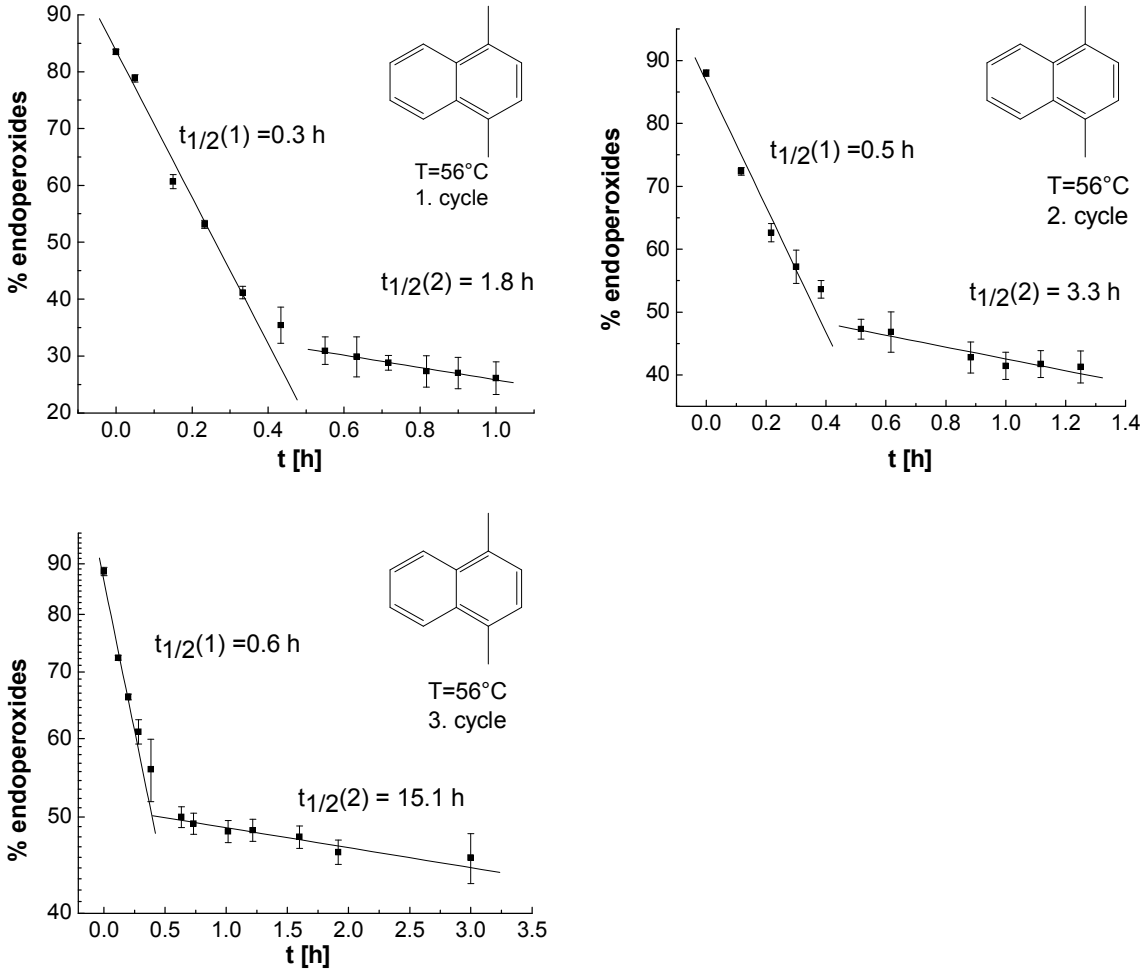

Figure 4.17. Demonstration of adjusting the decay-time of both FDE and SDE **N1E**, as well as their relative amount in PVB film at 56°C. The adjustment is done by the process of successive thermocycles of endoperoxide formation and decay. Semi-logarithmic plots showing decay of **N1E** in PVB polymer film after 3 sucessive thermocycles, measured with **N1** fluorescence time-trace.

Moreover, a possibility to adjust the decay-times (and therefore $^1O_2$ release-time) and relative amount of both fast-decaying and slowly-decaying endoperoxides with a more complex method consisting of successive repetition of light-induced endoperoxide formation and subsequent thermal decay was found. As demonstrated in Figure 4.17. on the example of **N1E** formation at 32 °C and decay at 56 °C, by cyclic use of aforementioned physical processes, the percentage of FDE decreases with each formation-decay cycle, whereas the percentage of SDE increases accordingly. On top of that, the decay-time of SDE is significantly prolonged, up to the factor of 8 from 1st to 3rd formation-decay cycle. TPFPP-Pd(II) sensitizer, c = 15 μM in PVB film, was irradiated with LED (λ = 420nm, P = 35 mW, Φ = 140 mW/cm^2, T = 32 °C, for t = 0.5 h) to form $^1O_2$ which reacted with **N1**, c = 0.6 mM in

PVB film, to form **N1E**. Only FDE and a small portion of SDE **N1E** was allowed to decay at 56°C before LED irradiation at 32°C was repeated and endoperoxides were formed again.

The same adjustment effect appeared for **N1E** decaying at 37 °C and is shown in Table 4.7. In parenthesis are the relative amounts of faster- and slowly-decaying **N1E** in PVB film at 37 °C, respectively. The LED irradiation of TPFPP Pd(II), c = 15 μM in PVB film and endoperoxide formation was performed at 32 °C, which turned out to be the optimal temperature for tuning the endoperoxide decay-time in PVB film.

Table 4.7. Decay-times and relative amounts of FDE and SDE **N1E** molecules with corresponding decay-time at 37 °C in PVB film after 1 and 2 cycles of **N1E** formation at 32 °C and decay at 37 °C. In parenthesis are the percentages of formed endoperoxides decaying with corresponding $t_{1/2}$. For both FDE and SDE calculated endoperoxide stability factors, SF, in comparison to the average decay in various organic solvents are given as well.

Cycle No.	**$t_{1/2}$ (% endoperoxides)**
1st	1.5h (36%) SF = 1.25; 7.6h (24%) SF = 6.33
2nd	1.7h (35%) SF = 1.42; 38.2h (55%) SF = 31.83

A model explaining all of these findings will be given in the Chapter 6.1. where the interaction between the embedded endoperoxide molecules and the matrix and influence modes on this interaction will be discussed in detail.

4.4. ENDOPEROXIDE DECAY AND CYTOTOXICITY IN PVB NANOPARTICLES CARRIER

PVB nanoparticles were prepared as described in Chapter 3.5.3. The aim was to produce such PVB nanoparticles which could be used as an intracellular drug delivery material, i. e. which would be small enough to permeate into cancer cells and deliver $^1O_2$-releasing endoperoxides in a short enough time after light-irradiation of particle-loaded naphthalene derivatives.

4.4.1. Systematical Adjustment of PVB Nanoparticles Size

The size of the resulting particles is a function of various parameters. In general, in order to obtain small particles, it is preferable to use a polymer with small molecular weight and therefore size. Initial tests (results not shown) were carried out with Mowital B60T (average molecular weight 60 kDa). This polymer formed rather large particles in the micrometer regime. All following experiments were carried out with PVB Mowital LPB 16H (average molecular weight 16 kDa), which proved to be better suited for synthesis of nanometer-sized beads.

Firstly, the results for variation of the solvent with constant PVB concentration of 1 g/L, and 0.8 mL/min flow rate of ddH_2O non-solvent drops addition at room temperature are summarized in Table 4.8.

Table 4.8. Mean PVB nanoparticle diameters depending on solvent during synthesis.

solvent	particle diameter (nm)
methanol	1058
TEMED	902
acetone	536
ethanol	442
1-propanol	448
2-propanol	430
DMF	362
DMSO	262

It was found that the particle size depends strongly on the solvent used with no clear trend visible with respect to polarity or groups present in the solvent. The smallest particle sizes were obtained for DMSO, DMF and 2-propanol solvents. Another parameter of investigation was the speed of addition of the non-solvent. For precise control of addition speed a peristaltic pump was employed. Table 4.9. shows the obtained nanobead size with constant PVB concentration of 1 g/L, and ddH_2O non-solvent drops addition at room temperature.

Table 4.9. Mean PVB nanoparticle diameters depending on addition speed of non-solvent.

solvent	flow rate (mL/min)	particle diameter (nm)
DMSO	0.095	518
DMSO	0.51	272
DMSO	1.96	246
DMSO	3.45	216
DMSO	5.71	176
DMSO	6.9	164
2-propanol	0.05	585
2-propanol	0.25	458
2-propanol	5.0	242
2-propanol	9.0	195

Clearly, the size of PVB nanoparticles decreases with increasing flow rate indicating a rapid mixing of solvent and non-solvent to be advantageous with respect to small particle formation. Even higher mixing rates did not result in smaller beads. Simply pouring one liquid onto another resulted in large particles in micrometer range and wide particle size distributions.

The dependence of particle diameter on reaction temperature was also examined. It would be expected that because of slower diffusion at lower temperatures (Einstein-Stokes equation) smaller particles are synthesized at lower T, whereas raising the temperature leads to larger particles. Table 4.10. summarizes syntheses with constant PVB concentration of 1 g/L in 2-propanol solvent, and 2.0 mL/min flow rate of ddH_2O non-solvent drops addition at different temperatures.

Table 4.10. Mean PVB nanoparticle diameters depending on temperature.

temperature (° C)	particle diameter (nm)
65	516
45	442
25	342
5	282

The results confirm that at lower temperatures smaller spheres are formed, therefore, low temperatures are preferred for synthesis. A roughly linear relationship is obtained between temperature T and average particle size suggesting diffusive contributions to be dominant for particle formation although the number of experimental points is too low in these experiments to obtain quantitative conclusions. Since the nanoaggregation of polymer chains depends on the availability of polymer in the solution it appears reasonable that the concentration of polymer is also a major factor in determining particle size. Results of particle syntheses performed at different polymer concentrations in 2-propanol solvent with constant 2.0 mL/min flow rate of ddH_2O non-solvent drops addition at 25 °C are displayed in Table 4. 11.

Table 4.11. Mean PVB nanoparticle diameters depending on polymer concentration.

concentration (g/L)	particle diameter (nm)
3	550
1	360
0.4	286
0.1	262

The dependence of particle size on PVB concentration is evident. Relating polymer concentration to particle diameter a roughly linear relationship is also obtained. Clearly, low polymer concentrations are favourable. However, in practice this parameter is not as useful as other parameters, since it is desirable to obtain the as-synthesized particles in as high of a concentration as possible. To sum up, systematic increase of ddH_2O non-solvent dropping

rate, temperature decrease and polymer concentration decrease all cause the mean PVB nanoparticle diameter decrease.

The effect of replacing the non-solvent ddH_2O with aqueous buffers of various ionic conc. and pH was also investigated. However none of those led to the formation of smaller particles than the respective synthesis in ddH_2O with other parameters unchanged. The addition of surfactants (SDS, tween 20, triton X-100, CTAB) to ddH_2O neither led to smaller particles.

Finally, an addition of a small volume, 2.5 % (v/v), of a second solvent to the 0.4 g/L PVB solution in 2-propanol prior to the addition of 9 ml/min ddH_2O non-solvent at 4 °C was tested, as shown in Table 4.12.

Table 4.12. Mean PVB nanoparticle diameters depending on the second solvent addition during synthesis.

solvent	**solvent 2**	**particle diameter (nm)**
2-propanol	chloroform	≥350: aggregates
2-propanol	1-octanol	≥350: aggregates
2-propanol	cyclopentanone	210
2-propanol	toluene	209
2-propanol	acetonitrile	155 (67%) 232 (33%)
2-propanol	acetyl acetone	172
2-propanol	dodecane	162
2-propanol	diethylether	158
2-propanol	ethyl acetate	154
2-propanol	1,4-dioxane	147
2-propanol	dichloromethane	135
2-propanol	DMSO	135
2-propanol	DMF	128
2-propanol	pentane	98

Again, no clear trend with respect to polarity or groups present in the second solvent on PVB particle size was established. Addition of some solvents caused strong particle aggregation to micrometer size, whereas some caused a formation of particles with 2 various average diameters, possibly due to various solvent miscibilities with H_2O. For the purposes of high incorporation of PTC and endoperoxide-forming dopants (see later) a combination of 2-propanol and dichloromethane solvents proved to be the best one.

The optimal parameters regarding the nanoparticle size included pumping dd H_2O dropwise through a syringe at a rate of 9 ml/min at 4 °C to produce nanoparticles of average 141 nm diameter. However, it was not possible to reduce the average diameter of the particles to less than 100 nm using the obtained PVB polymer. On the contrary, when drops of 1 mM NaOH were slowly (4-5 drops/s) dropped to the PVB solution in 2-propanol at the room temperature larger particles of 420 nm average diameter were synthesized (see Figure 4.19).

PVB nanoparticles show a very slow sedimentation over the course of several weeks to months in aqueous solution which may easily be reversed by stirring or shaking the suspension thoroughly. Apart from that the beads showed no significant aging effect in H_2O suspension as well as in cell culture RPMI medium at RT. No aggregates were detectable via DLS even after several months. It was possible to concentrate the suspension of PVB nanoparticles up to 300 ppm = 0.30 g/L using Amicon® Ultra-4 centrifugal filter membranes (10 000 NMWL) and a 3000 g centrifuge before aggregates detectable with DLS formed.

In order to determine the size uniformity, as well as the shape of the nanoparticles, transmission electron microscopy technique was used. Very good size uniformity and the particle's spherical shape were all confirmed with TEM of dried PVB particles (Figure 4.18.) Size distribution from DLS of this representative sample was calculated as (141 ± 40) nm with the latter parameter being one standard deviation.

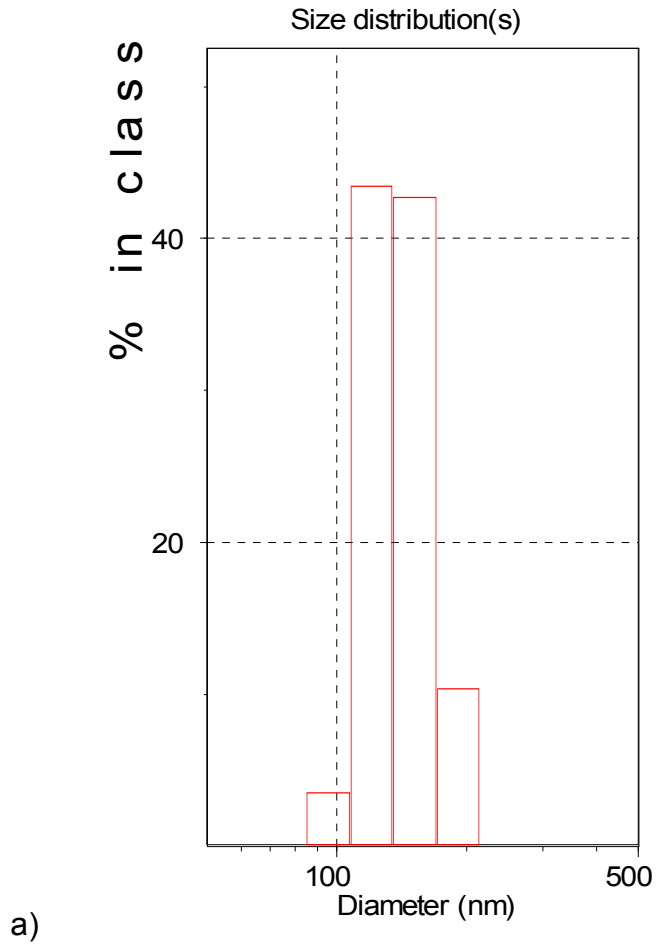

a)

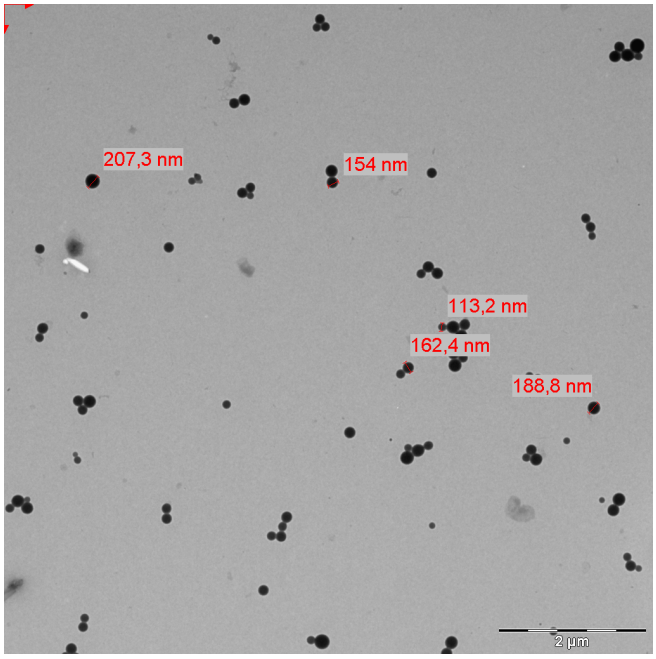

b)

Figure 4.18. PVB nanoparticles average diameter measured with DLS (a) and TEM (b).

4.4.2. PVB Nanobeads Doping with PTC

N,*N'*-bis(2,6 -dimethylphenyl)- perylene-3,4,9,10-tetracarboxylic diimide (PTC) was used as a PVB nanobeads dopant for CLSM purposes. PTC is soluble in alcohols and other solvents of intermediate polarity, but it is almost insoluble in water and nonpolar compounds. Therefore, PTC has similar solubility properties as PVB. 1 % (w/w) dopant concentration with respect to the PVB weight was chosen in order to obtain bright nanoparticles, but also to avoid excessive self-quenching of dye molecules.

The influence of PTC addition to PVB with respect to particle preparation and particle size was investigated using the solvents DMSO and 2-propanol (Table 4.13.) while 6 mL/min ddH_2O non-solvent was added at 5 °C.

Table 4.13. Parameters of PVB nanoparticle preparation using dopant molecules.

concentration (g/L)	solvent	particle diameter (nm)
0.2	2-propanol	190
0.2 (1 % PTC)	2-propanol	202
0.2	DMSO	176
0.2 (1 % PTC)	DMSO	250

It was found that using 2-propanol as solvent, bright fluorescent nanospheres are formed, where PTC is almost quantitatively incorporated. The influence of PTC addition on particle diameter was found to be negligible (within the standard deviation of particle diameter). On the other hand, PTC addition using DMSO as solvent system did not yield satisfactory results. Particles showed only weak fluorescence, as apparently most of the PTC precipitated before PVB particles formed, and particle diameter was also increased by about 40 %. Possibly, PTC is too poorly soluble in DMSO yielding rapid precipitation upon addition of non-solvent.

4.4.3. PVB Nanobeads Cell Uptake, Determined with CLSM

To determine if the PVB nanoparticles are taken up by the MDA-MB-231 breast cancer cells confocal microscopy was used. Firstly, larger particles (420 nm in average diameter) were tested. As it is visible on Figure 4.19. a) and b), these particles doped with PTC dye (green colour) are not taken up by the breast cancer cells (stained with nuclear dye 5 μM DRAQ5™, red colour), but stay adsorbed to the cell membrane, even 22 hours after incubation of the cells with the nanoparticles.

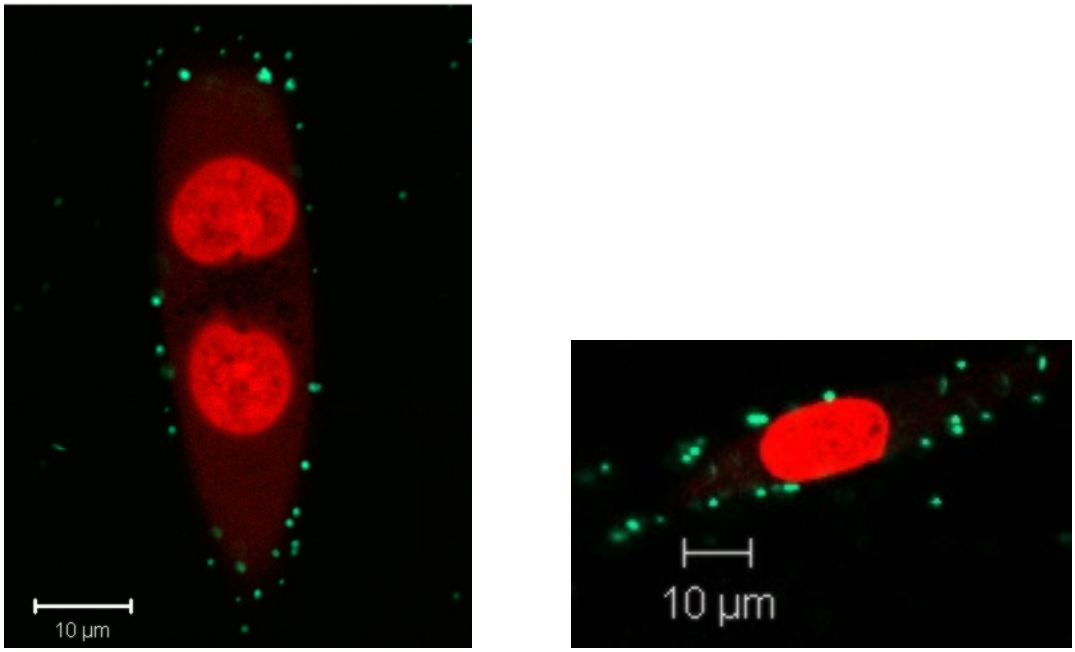

a) b)

Figure 4.19. False color multifluorescence CLSM images of living MDA-MB-231 cells, passage 323 (stained with nuclear counterstain DRAQ5™, (5 μM), red colour), incubated with uncoated PVB polymer nanoparticles (diameter: 420 ± 55 nm, doped with PTC, green colour). PVB nanoparticles remain at the cytoplasmic membrane a) 4 h and b) 22 h after incubation. Only a small part of the particles, even after 22 hours, is inside the cell. Plan-Apochromat 63x/1.4 oil, Ar 488, HFT 488, BP530-600; HeNe 633, HFT 488/543/633, LP650.

This result is contrary to the work of J. Rejman et al [142], where the beads with 500 nm diameter were taken up by the eukaryotic non-phagocytic B16 cells but remained on the cell periphery and were not to be found in the perinuclear region or lysosomes. In the same paper, it was stated that particles with diameter < 200 nm were internalized by the cells faster (than those with 500 nm diameter) and are accumulated in the perinuclear region and

subsequently ended in lysosomes. Due to this observations, the PVB nanoparticles with the average diameter smaller than 200 nm were prepared and the CLSM experiment repeated yielding a positive result, see Figure 4.20.

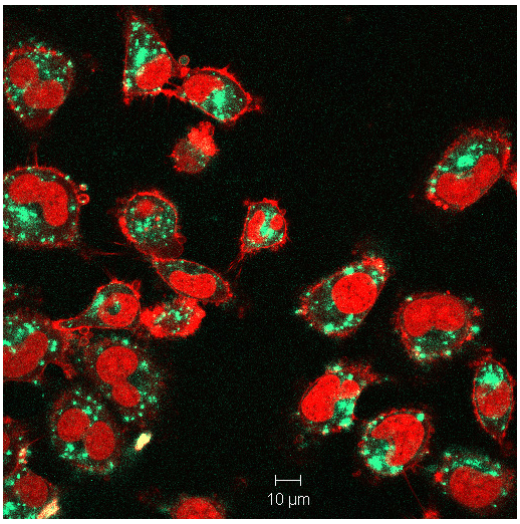

a)

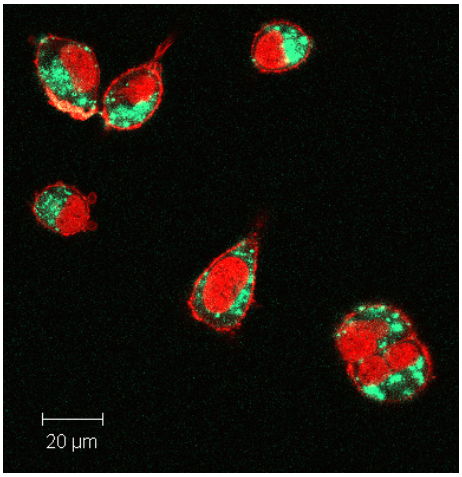

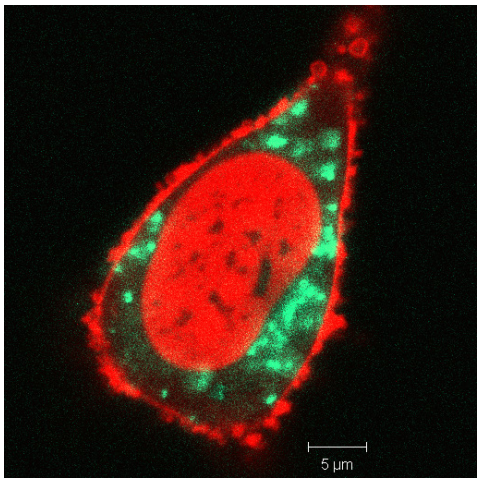

b) c)

Figure 4.20. CLSM images showing the time-scale of uncoated PVB nanoparticles (diameter :141 ± 40 nm, doped with PTC, green colour) uptake by the living MDA-MB-231 cells, passage 180 (stained with 5µM nuclear counterstain DRAQ5™ and 5µg/mL CellMask Deep Red™ plasma membrane stain, red colour). The PVB particles appear in all of cells, some are close to the cell membrane, and some are dispersed in the cell cytoplasm after **2 h** incubation (a). After **3.5 h** (b) and c)) the particles appear in all of the cells dispersed in the cell cytoplasm. Plan-Apochromat 63x/1.4 oil, Ar 488, HFT 488, BP530-600, Pinhole 122; HeNe 633, HFT 488/543/633, LP650, Pinhole 1000.

On Figure 4.20. CLSM images of living MBA-MB-231 human breast adenocarcinoma cells incubated with 141 ±4 0 nm average diameter PVB nanoparticles

loaded with PTC dye (green colour) can be seen. Cells were stained with nuclear counterstain DRAQ5™ (5 μM) and 5μg/mL CellMask Deep Red™ plasma membrane stain (red colour on Figure 4.20.) 2 h after the incubation PVB nanoparticles are already inside the living MBA-MB-231 cells: some nanoparticles remain at the cell membranel, and some are dispersed in the cytoplasm (Figure 4.20. a). After 3.5 h (Figure 4.20. b) and c) the particles appear in all of the cells dispersed in the cell cytoplasm. Therefore, it can be summed up that the average cell uptake time, t_u, of uncoated PVB nanoparticles (size 141 nm) is in the region of 2-3 hours.

Note: the CLSM microscope pinhole was opened to 122 μm (single layer scanned) in nuclei and plasma membrane channel (filter LP650), and to 1000 μm (all layers scanned, as with a fluorescence microscope) in PVB particles channel (filter BP 530-600). Therefore, the fluorescence of the particles is very strong and they appear to be much larger and the resolution is low. Prior to the recording of each figure, the cells were washed 3 times with Leibowitz's L-15 medium in order to make sure that all the fluorescence of PVB particles comes from intracellular particles.

Furthermore, PVB nanoparticles with the average diameter of 238 nm were synthesized as well. Using CLSM technique it was also found that these particles are taken up by the cells and dispersed in the cytoplasm, but after a longer time period than the particles with the average diameter of 141 nm.

Therefore, the cell uptake of these PVB nanoparticles is strongly size-selective with a threshold value for particles diameter at around 300 nm.

4.4.4. Cytotoxicity of Undoped PVB Nanobeads Determined with Kinetic Chemosensitivty Assay

After finding out that PVB nanoparticles are indeed cell-penetrable, the cytotoxicity of 141 nm average diameter PVB particles was tested using the kinetic crystal violet chemosensitivity assay [111] and compared with the cytotoxicity of conventional, unmodified liposomes (Chapter 4.2.3.) Cells were treated (T values) with PVB nanoparticles and liposomes and compared to control growth curve of untreated cells (C values) to yield a T/C profile (Figure 4.21.) which compares the growth speed of treated cells to the growth speed of untreated cells.

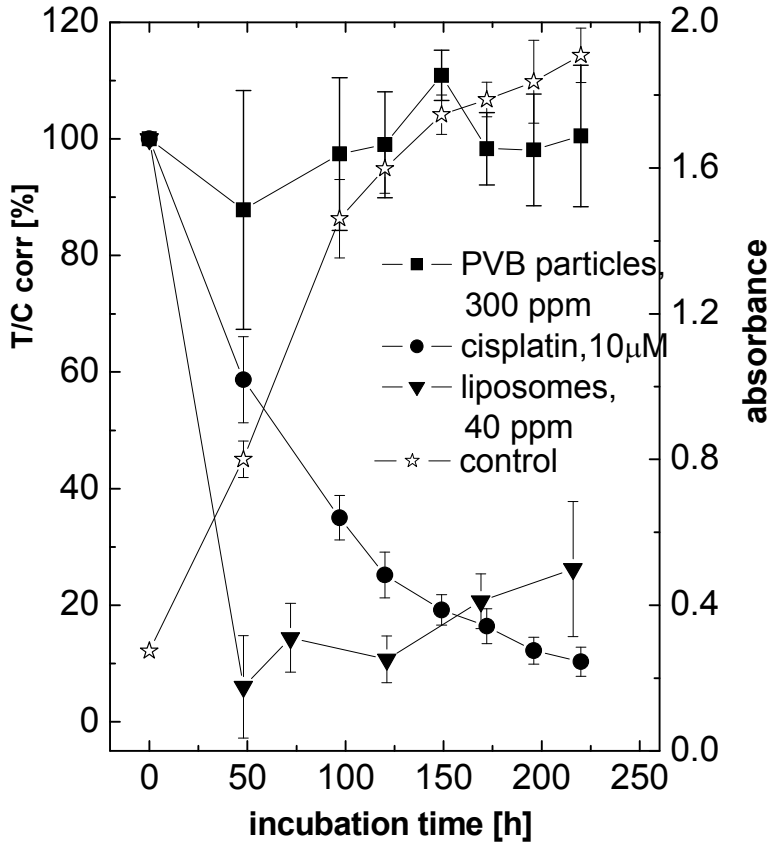

Figure 4.21. Comparison of non-toxic effect of 300 ppm (w/w) aqueous suspension of PVB nanoparticles (141 nm average diameter) with a strong cytotoxic effect of 40 ppm (w/w) DMPC liposomes aqueous suspension on proliferation of MDA-MB-231 cancer cells determined using a crystal violet chemosensitivity assay. For the positive control, a cytostatic effect of 10 μM cisplatin is shown.

As can be seen on Figure 4.21. a concentrated aqueous suspension (300 ppm w/w) of PVB nanoparticles (diameter 141 ± 40 nm) which contained no aggregates of nanoparticles, as measured with dynamic light scattering) showed no inhibitory effect on proliferation of human breast cancer cells MDA-MB-231 as a function of incubation time. On the contrary; an order of magnitude less concentrated aqueous suspension of conventional, unmodified liposomes, (40 ppm w/w, diameter 109 ± 8 nm) shows an initial inhibitory effect on the growth of MDA-MB-231 cells, after which the cell population slowly recovers after 125 h. PVB nanoparticles have no short-term cytotoxic effect whatsoever and regarding the achievable intracellular concentration are a favourable carrier comparatively to conventional liposomes. On Figure 4.21. a comparison with a cytostatic effect of cisplatin, is also shown.

Whereas the cells treated with 40 ppm (w/w) liposomes starts to multiply after 125 h, the growth of cells treated with cisplatin is fully inhibited and cell population doesn't recover.

300 ppm (w/w) PVB nanoparticles concentration in aqueous suspension was the highest achievable concentration with the preparation method described in Chapter 3.5.3. including the centrifuge procedure. At higher suspension concentrations PVB particles aggregated strongly forming aggregates of several micrometers.

4.4.5. Adjustment of Endoperoxide Decay Kinetics in PVB Nanobeads Carrier

It was found that naphthalene derivatives were not quantitavely incorporated into PVB nanobeads: it was reproducibally possible to incorporate about 10 % of added naphthalene derivatives into PVB nanobeads.

When the possibility of PVB nanoparticle use as a carrier for intracellular drug delivery purposes in high concentrations was established, endoperoxide decay times in PVB nanoparticles were explored. In Table 4.14. endoperoxide decay times, $t_{1/2}$, of all naphthalene derivatives embedded in PVB nanoparticles at 37 °C are given. The sensitizer used was MB in all cases, c = 10 μM. Irradiation to form endoperoxides was done with laser (λ = 658 nm, P = 70 mW, for t = 0.5 h at T = 14°C). In parenthesis the percentages of endoperoxides corresponding to the particular decay time are given. The stability factor, SF, showing the increase of $t_{1/2}$ in PVB nanoparticles matrix in comparison to $t_{1/2}$ in organic solvents (calculated according to equation 13), is also given in Table 4.14.

Table 4.14. Decay times of endoperoxides of different naphthalene derivatives embedded in PVB nanoparticles at 37 °C and calculated endoperoxide stability factors, SF, for comparison to the decay in various organic solvents. In parenthesis are the percentages of formed endoperoxides decaying with corresponding $t_{1/2,.}$.

Molecule in PVB nanoparticles	$t_{1/2}$ (% endoperoxides)
N1	0.8 h (75%), SF = 0.66; 1.6h (13%), SF = 1.33; 5.8h (5%), SF = 4.83
N2	18.7 h (20%), SF = 1.15
N4	7.5 h (28%), SF = 1.72; 17.5 h (19%), SF=4.01
N5	2.0 h (45 %), SF = 0.88; 2.65 h (20%), SF = 1.17

Equally as in PVB film carrier, influence of different parameters during the endoperoxide formation procedure in PVB nanoparticles on the endoperoxide decay-time was researched. In general, the yield of endoperoxide formation was lower than in liposomes or PVB film. For example, after 0.5 hours of laser (λ = 658 nm, P = 70 mW) irradiation at room temperature the yield of **N4E** in PVB nanoparticles was only 59 %, compared to 85 % in PVB film and 98 % in liposomes under similar conditions. Even after longer irradiation (up to 2 h) and/or irradiation at lower temperature (e. g. 4 °C), the highest endoperoxide yield in PVB nanoparticles was 77 %. This was probably due to the necessary transport of $^1O_2$ from dissolved MB sensitizer molecules ($^1O_2$ generation location) to the naphthalene molecules in PVB nanoparticles ($^1O_2$ local storage location in endoperoxide form).

Moreover, a method of successive repetition of light-induced endoperoxide formation and subsequent thermal decay (which was very valuable in adjustment of $^1O_2$ release time in PVB film, e. g. Figure 4.17.) was tested on endoperoxide-loaded PVB nanoparticles, as well. An example for decay of **N4E** in PVB nanoparticles (size: diameter 155 ± 41 nm) at 37 °C is given in Figure 4.22. By cyclic use of aforementioned physical processes it was possible to extend the decay time of FDE **N4E** in PVB nanoparticles for almost 50 % from 6.0 hours (in first formation-decay cycle decay of FDE only) to 8.8 hours in the second cycle. The FDE and SDE decay-times in the second cycle have rather similar values, but the approximation of biexponential decay is still acceptable, see Figure 4.22. b). MB sensitizer (c = 10 μM) was irradiated with laser (λ = 658 nm, P=70 mW, T = 32° C, for t = 0.5 h) to form $^1O_2$ which reacted with **N4** (c = 1.7 μM in aqueous suspension) to form **N4E** (yield 61 %), which subsequently decayed at 37 °C.

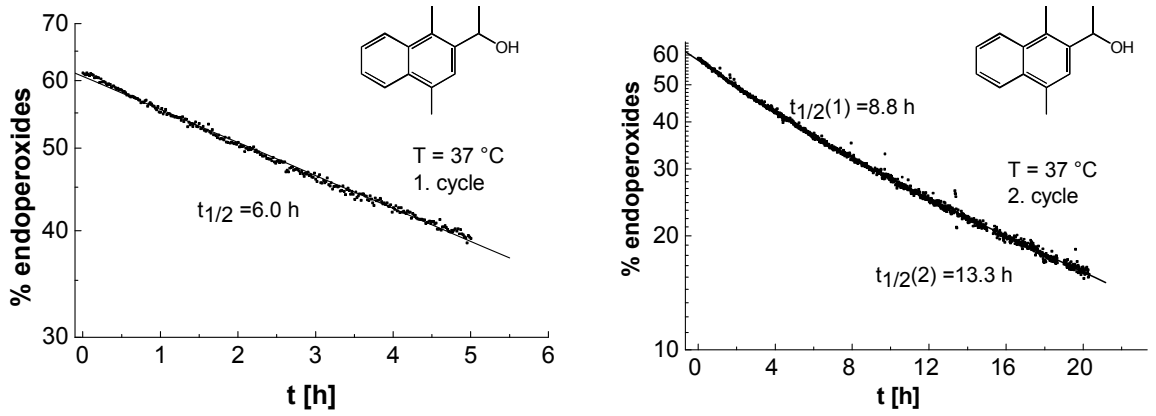

a) b)

Figure 4.22. Semi-logarithmic plot showing the adjustment of **N4E** decay times due to the processes of successive thermocycles of endoperoxide formation in PVB nanoparticles (size: diameter 155 ± 41nm) at 37 °C measured with **N4** fluorescence time-trace. Decay after 1 thermocycle (a) and after 2 successive thermocycles (b). On y-axis is the percentage of all **N4** molecules which are in endoperoxide form at each particular time-point.

Finally, the set of parameters which enabled the most appropriate adjustment of decay times and FDE and SDE relative amounts in PVB film was applied on endoperoxides in PVB nanoparticles. This included endoperoxide formation at 32 °C combined with repetitions of formation-decay cycle. The results of such experiments are shortly presented in the Table 4.15. on the example of **N1E** decay in PVB nanoparticles at 37 °C. The sensitizer used was methylene blue in all cases, c = 10 μM. Irradiation was done with laser (λ = 658 nm, P = 70 mW, for t = 0.5 h).

From the data in the Table 4.15. it is visible that FDE **N1E** are stabilized when formed at 32 °C, in comparison to endoperoxides formed at 14 °C, presumably due to the physical processes of continuous formation and decay (thermal back-reaction) during irradiation at the increased temperature. Decay-time of such stabilized FDE, $t_{1/2}$ = 5.3 h, is comparable to $t_{1/2}$ = 5.8 h of SDE **N1E** formed at 14 °C. On top of that, by cyclic use of endoperoxide formation-decay physical processes, the percentage of FDE decreased with each formation-decay cycle, whereas the percentage of SDE increased accordingly. Moreover, the decay-times of FDE and SDE are both extended in the second cycle up to the factor of 4 compared to $t_{1/2}$ values of FDE and SDE formed at 14 °C. Thus, $t_{1/2}$ of both FDE and SDE was adjusted to be longer than the cell-uptake time, t_u, of PVB nanoparticles (diameter 141±40 nm) by the MDA-MB-231 human breast adenocarcinoma cells.

Table 4.15. Decay times of **N1E** embedded in PVB nanoparticles at 37 °C depending on the endoperoxide-formation parameters: temperature during irradiation and number of successive cyclic repetitions of photoinduced endoperoxide formation and thermally activated decay. In parenthesis are the percentages of formed endoperoxides decaying with corresponding $t_{1/2.}$ Endoperoxide stability factors, SF, in comparison to the decay in organic solvents were calculated.

Endoperoxide-formation parameters	**$t_{1/2}$ (% endoperoxides)**
T = 14°C, 1 cycle	0.8 h (75%) SF = 0.66; 1.6h (13%) SF = 1.33; 5.8h (5%) SF = 4.83
T= 32°C, 1 cycle	5.3 h (45%) SF = 4.42
T= 32°C, 2 cycles	7.5 h (35%) SF = 6.25; 21.4 h (12%) SF = 17.83

4.4.6. *In Vitro* Cytotoxicity of $^1O_2$-Releasing Endoperoxides in PVB Nanobeads: Kinetic Chemosensitivity Assay Results

Cytotoxicity of **N4E, N5E and N2E** embedded in non-coated PVB nanoparticles in aqueous suspension on MDA-MB-231 cancer cells using crystal violet chemosensitivity assay was tested. The highest reached concentrations for each endoperoxide-forming derivative in cell medium were: 0.3 μM **N4** in 155±41 nm PVB (270 ppm w/w), 0.5 μM **N2** in 144 ± 43 nm PVB (290 ppm w/w) and 1.6 μM **N5** in 177±39 nm PVB (320 ppm w/w). On Figure 4.23. an example of non-inhibitory influence of both 0.3 μM **N4** in 155±41 nm PVB nanoparticles aqueous suspension (270 ppm w/w in cell medium) and a mixture of 0.25 μM **N4E** and 0.05 μM **N4** in the same PVB nanoparticle suspension, on the proliferation of MDA-MB-231 cells is shown. MB sensitizer (c = 0.11 μM) was irradiated with laser (λ = 658nm, P = 70 mW, T = 14 °C, for t = 1 h) to form $^1O_2$ and subsequently **N4E** (yield 83 %). A cytotoxic effect of 10 μM cisplatin dissolved in DMSO on the growth of MDA-MB-231 cells (★ symbols on Figure 4.23.) is given for a comparison.

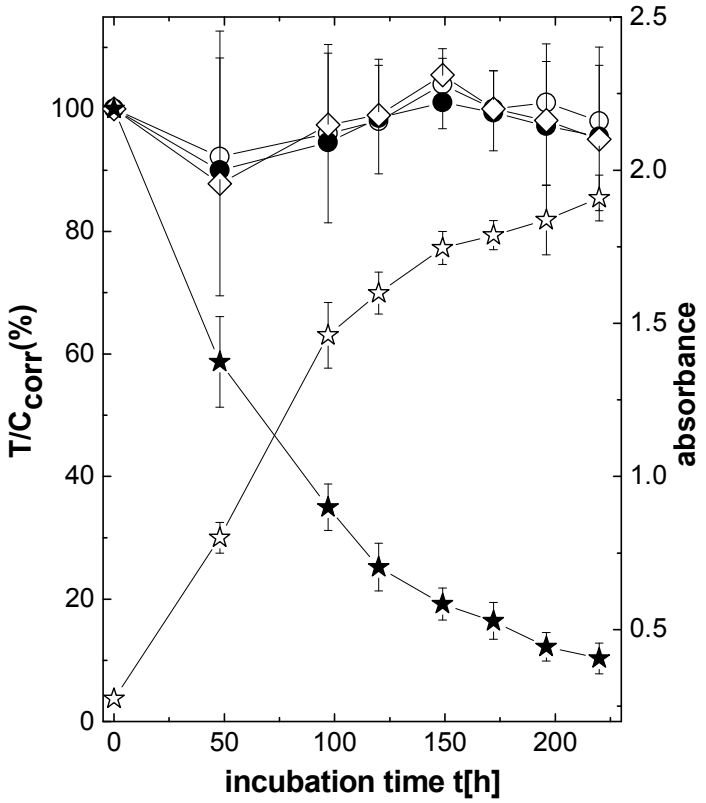

Figure 4.23. No cytotoxic effect of **N4E** in non-coated PVB nanoparticles (diameter 155 ± 41nm) on human breast adenocarcinoma cells MDA-MB-231, passage 331, as a function of incubation time determined by the crystal violet assay. Neither the non-coated PVB nanoparticles nor **N4** embedded in non-coated PVB nanoparticles exhibit any toxicity on the MDA-MB-231 cells. ○ **N4**, 0.30 μM, in PVB nanobeads, 270 ppm (w/w), ● **N4E**, 0.25 μM + **N4,** 0.05 μM in PVB nanobeads, 270 ppm (w/w), ◇ PVB nanobeads, 300 ppm (w/w), ★ positive control: cisplatin, 10 μM in DMSO, ☆ negative control: H_2O.

Necessary final endoperoxide concentrations in cell medium of 6 μM or higher (see Figure 4.11. and Figure 4.12.) were not reachable because of rather poor loading efficiency of PVB nanoparticles with naphthalene derivatives. The highest reached concentrations were insufficient for any of endoperoxide-forming derivatives in PVB nanoparticles to have any inhibitory effect on the growth of MDA-MB-231 cells.

4.5. ENDOPEROXIDE DECAY AND CYTOTOXICITY IN EC NANOPARTICLES CARRIER

4.5.1. EC Nanoparticles Reproducibility and Size Dependence on Preparation Parameters

Ethylcellulose nanoparticles were prepared as described in Chapter 3.5.4. Whereas the size of the EC nanoparticles was regularly < 150 nm in diameter as measured with DLS, using the TEM technique a considerable tendency of EC nanoparticles towards cluster formation was found out (see Figure 4.24.), which caused some problems with the reproducibility of naphthalene derivative doping concentration, as well as some precipitation of the EC nanoparticles from aqueous suspension after 1 - 2 weeks at RT conditions. The amount of EC clusters present in the aqueous suspension is difficult to quantify. It was not possible to destroy the EC clusters in an ultrasonic bath or by coating the EC with polysorbate 80™. This problem triggers reproducibility problems with chemosensitivity assays: EC concentration reproducibility, and doped endoperoxide-forming derivative concentration reproducibility in aqueous suspension.

The EC particles size dependence on similar preparation procedure parameters variation as in case of PVB nanobeads was tested, as well. The temperature had no significant influence on the EC particle diameter. Controlled, slower ddH_2O non-solvent addition using the peristaltic pump caused systematic increase in EC particles diameter in 200-400 nm range: the slower the ddH_2O flow rate, the larger were EC particles. Finally, the EC polymer concentrations of 0.4 % (and above) EC in THF/acetone caused more pronounced cluster formation in aqueous suspension.

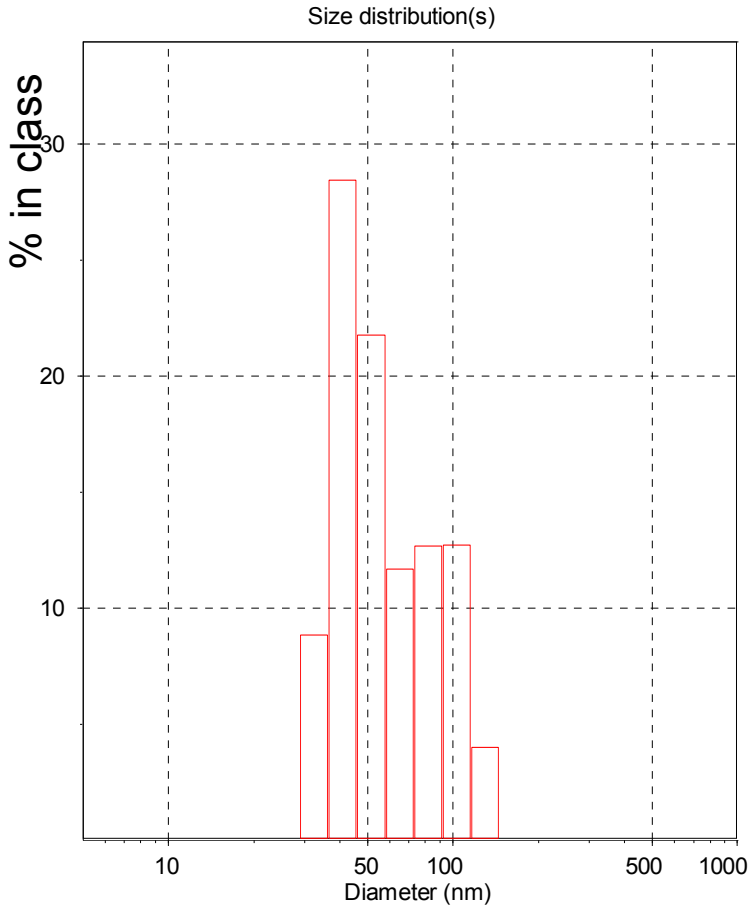

a)

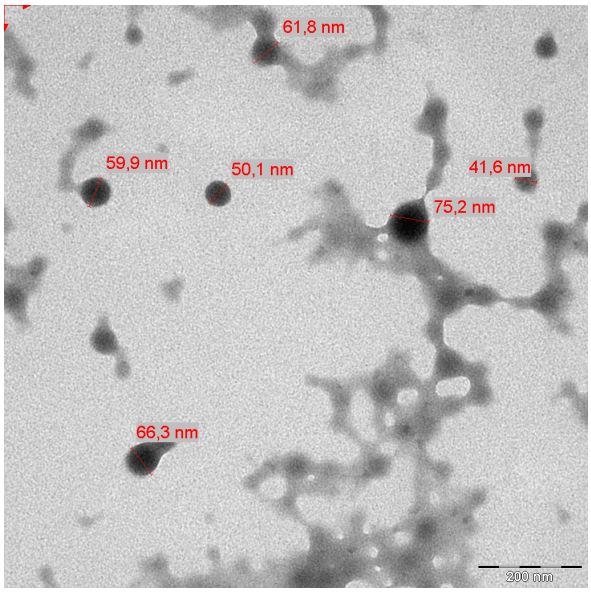

b)

Figure 4.24. Average diameter of EC nanoparticles loaded with **N4**, measured with DLS (a) and TEM (b).

The size of formed EC nanoparticles varied somewhat depending on the nature of the derivative loaded, as stated above. Later, it was possible with the same procedure as described above to produce **N4** loaded EC particles of 46±11 nm average diameter as measured with DLS. However, the main problem with EC particles production was cluster forming in aqueous suspension as seen on TEM picture on Figure 4.24. Moreover, EC nanoparticles underwent an aging effect in aqueous suspension: after 2 months approximately half of the EC nanoparticles with diameter under 150 nm formed clusters larger than 300 nm.

4.5.2. EC Nanoparticles Cell Uptake, Determined with CLSM

For confocal microscopy experiments the EC nanoparticles were doped PTC (1 % w/w to EC polymer), and particles production procedure (as described in Chapter 3.5.4.1.) gave particles of 90 ± 23 nm average diameter, as measured with DLS.

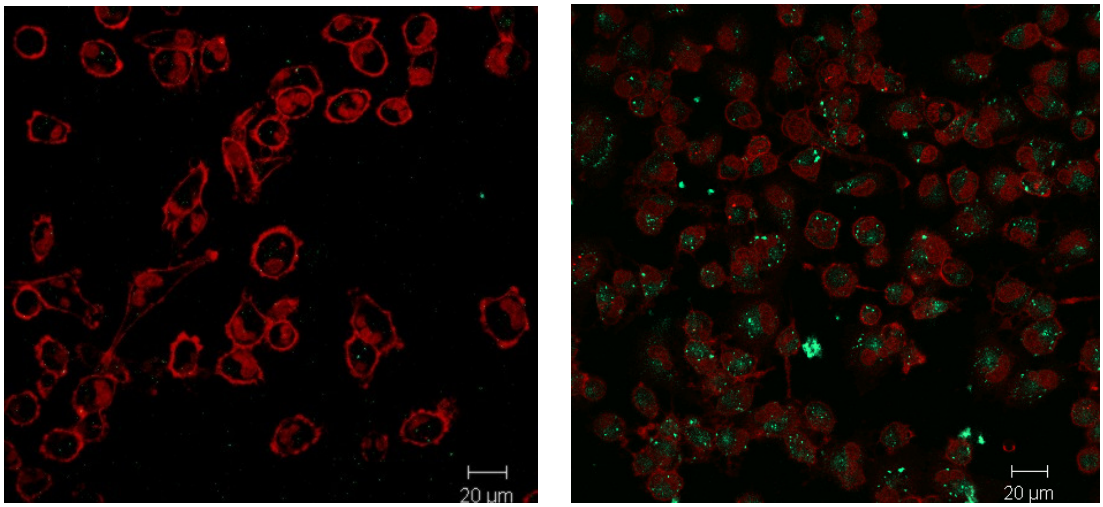

a) after 4h, uncoated b) after 9h, polysorbate 80™-coated

Figure 4.25. False color multifluorescence CLSM images of living MDA-MB-231 cells, passage 75 (stained with 5 µM nuclear counterstain DRAQ5™ and 5µg/mL CellMask Deep Red™ plasma membrane stain, red colour) incubated with EC nanoparticles (45 ppm w/w, diameter: 90 ± 23nm, doped with PTC, green colour). a) uncoated EC nanoparticles 4 h after incubation appear only in a few of living MDA-MB-231 cells and b) polysorbate 80™-coated (100 ppm w/w) EC nanoparticles 9 h after incubation appear in all of the cells, homogenously dispersed in the cell cytoplasm. Plan-Apochromat 63x/1.4 oil, Ar 488, HFT 488, BP530-600; HeNe 633, HFT 488/543/633, LP650.

To determine the potential of the EC nanoparticles as a drug-delivery carrier, cell uptake of EC nanoparticles by the MDA-MB-231 breast cancer cells the CLSM technique was used. Firstly, uncoated EC nanoparticles (average diameter 90 ± 23 nm) doped with PTC dye were tested, Figure 4.25. a). Only a few of uncoated EC nanoparticles (green colour on Figure 4.25.) appear after 4 hours of incubation in MDA-MB-231 cells (red colour on Figure 4.25.), which suggests a very slow cell penetration by the uncoated EC nanoparticles.

However, when the EC nanoparticles were coated with polysorbate 80™ surfactant, the cell uptake was much stronger, as can be seen on Figure 4.25. b): all of the polysorbate 80™-coated EC nanoparticles are inside of MDA-MB-231 cells 9 h after incubation. polysorbate 80™-coated ethylcellulose particles appear in all of the cells, homogenously dispersed in the cell cytoplasm. Cell nucleus and plasma membrane were stained with 5 μM DRAQ5™ and 5 μg/mL CellMask™ Deep Red, respectively. Prior to the CLSM recording of pictures, the cells were washed 3 times with Leibowitz's L-15™ medium in order to make sure that all the fluorescence of EC nanoparticles comes from intracellular particles.

When it was established that only the polysorbate 80™-coated EC nanoparticles enter the MDA-MB-231 cells, time-scale of the EC particles uptake (see Figure 4.26.) was determined using the same CLSM procedure. The EC particles appear in most of cells and are close to the cell membrane after 1 h incubation (Figure 4.26. a and b). After 2 h (Figure 4.26. c) the particles appear in all of the cells, some still close to the cell membrane, some dispersed in the cell cytoplasm. After 3 h (Figure 4.26. d) the particles appear in all of the cells, fluorescing strongly, dispersed in the cell cytoplasm. This suggests that polysorbate 80™-coated EC nanoparticles cell-uptake time, t_u, is in the 1 - 2 h range.

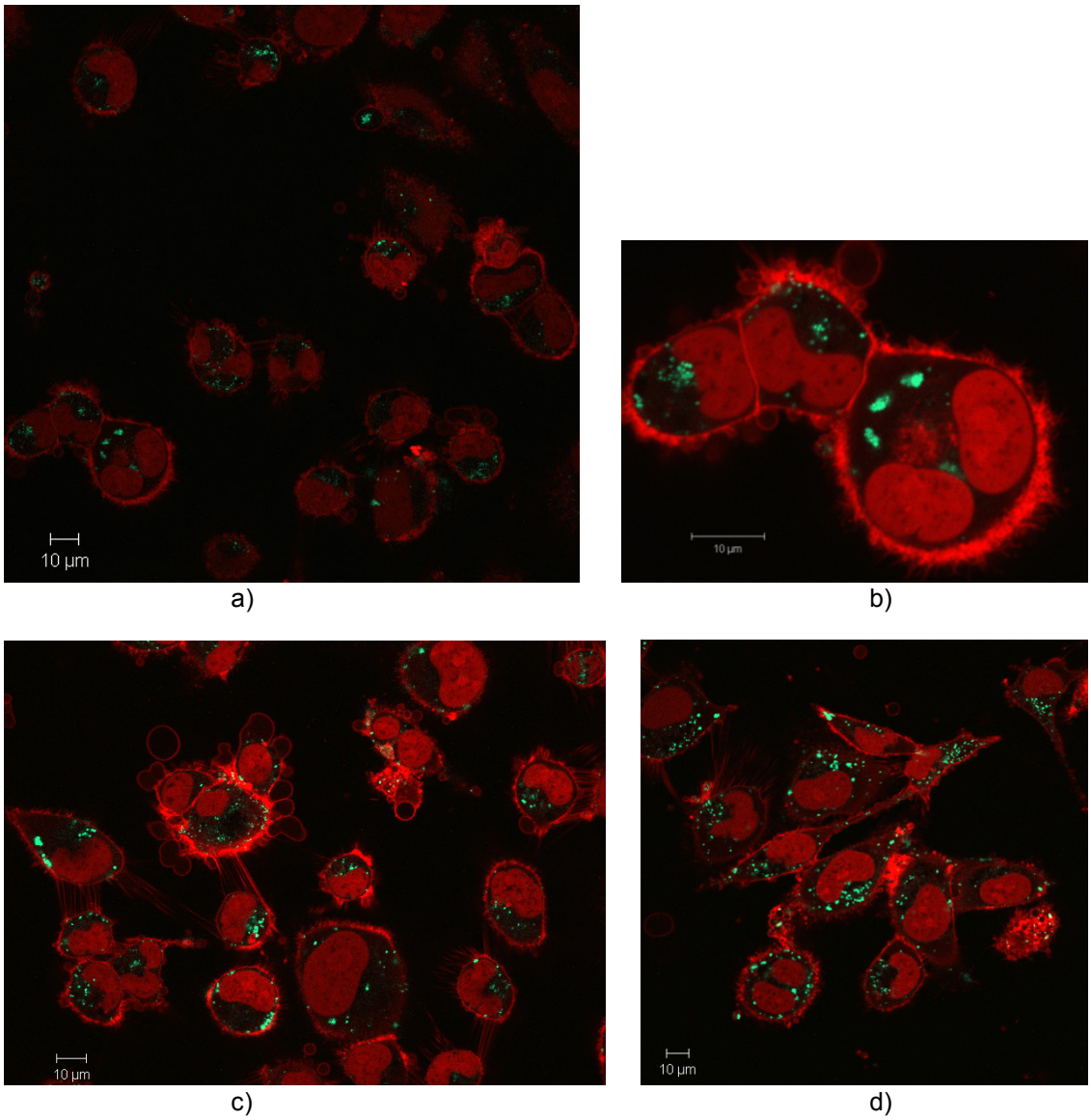

Figure 4.26. CLSM images showing the time-scale of polysorbate 80™-coated EC nanoparticles (diameter :94 ± 19nm, doped with PTC, green colour) uptake by the living MDA-MB-231 cells, passage 180th (stained with 5µM nuclear counterstain DRAQ5™ and 5µg/mL CellMask Deep Red™ plasma membrane stain, red colour). The EC particles appear in most of cells and are close to the cell membrane after 1 h incubation, Fig. a) and b). After 2h (Fig. c) the particles appear in all of the cells, some still close to the cell membrane, some dispersed in the cell cytoplasm. After 3h (Fig. d) the particles appear in all of the cells, fluorescing strongly, dispersed in the cell cytoplasm. Plan-Apochromat 63x/1.4 oil, Ar 488, HFT 488, BP530-600; HeNe 633, HFT 488/543/633, LP650.

Thus, it was found that the polysorbate 80™-coated EC nanoparticles are suitable to be used as a carrier for intracellular drug delivery purposes. After that endoperoxide decay times in EC nanoparticles were explored.

4.5.3. Adjustment of Endoperoxide Decay Kinetics in EC Nanoparticles Carrier

EC nanoparticles loaded with **N4** and **N5** were prepared. It was not possible to prepare EC nanoparticles loaded with **N2** or **N1**. Having **N1** or **N2** in the EC "cocktail" (see Chapter 3.5.4.1.) caused severe aggregation of EC polymer when dd H_2O was poured into the „cocktail" solution. The concentration of **N4** and **N5** in the aqueous EC suspension was determined with a standard addition method measuring UV-absorption, according to Lambert-Beer's law. In both cases a high concentration of loaded naphthalene derivative in EC particle suspension was reached. In case of **N4** EC particles with diameter of 98 ± 25 nm (measured with DLS) and **N4** concentration of 0.82 mM in aqueous particle suspension were produced. In case of **N5** EC particles with average diameter of 136 ± 38 nm (measured with DLS) and **N5** concentration of 0.42 mM in aqueous particle suspension were produced.

Endoperoxide decay of both **N4** and **N5** in EC particle aqueous suspension at 37 °C was examined. In general, the yield of endoperoxide formation was lower than in other carriers, liposomes or PVB film or even than in PVB nanoparticles. After 1.5 hours of MB sensitzer irradiation at T = 15 °C with laser (λ = 658 nm, P = 70 mW) the yield of **N4E** in EC nanoparticles was only 34 % (Figure 4.27.), and after 16 hours of irradiation the yield was 73 % (Figure 4.28.). Therefore the endoperoxide building was slower than in PVB nanoparticles, when after 0.5 hours of irradiation, the **N4E** yield was 59%.

The sensitizer (MB) and irradiation conditions were the same for EC and PVB nanoparticles, the lower yield is probably due to much higher concentration of loaded naphthalene derivatives in the core of EC particles. Probably most of the embedded **N5** or **N4** molecules are in the core of EC particles and not on the surface of particles, which hinders the transport of $^1O_2$ from iraddiated MB sensitizer dissolved in water ($^1O_2$ generation location) to the naphthalene derivatives in the core of the EC particles ($^1O_2$ storage location in endoperoxide form).

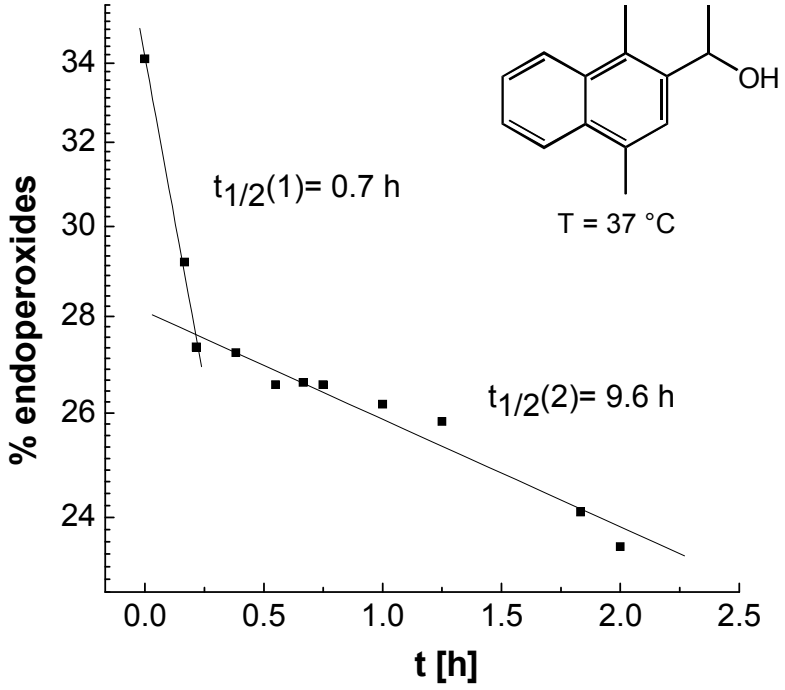

Figure 4.27. Semi-logarithmic plot showing **N4E** decay after short irradiation time of 1.5 h in EC nanoparticles (diameter 98±25nm, concentration 130 ppm w/w) at 37 °C measured with **N4** fluorescence time-trace. On y-axis is the percentage of all **N4** molecules which are in endoperoxide form at each particular time-point.

Endoperoxides of both **N4** and **N5** in EC particles showed biexponential decay, with FDE and SDE part. Due to a low yield of endoperoxide formation, it was relatively difficult to influence on the relative amounts of formed FDE and SDE by varying the procedure parameters during the endoperoxide formation. However, by extending the irradiation time from 1.5 hours to 16 hours, it was possible to adjust the $t_{1/2}$ of both FDE and SDE **N4E** in EC particles: $t_{1/2}$ of FDE was extended from 0.7 h to 8.5 h and $t_{1/2}$ of SDE from 9.6 h to 24.6 h (Figure 4.27. and Figure 4.28. respectively). Both FDE and SDE are stabilized in the carrier matrix during the longer irradiation time, due to the process of continuous forming and decay of endoperoxides. This will be further discussed in the Chapter 6.1.

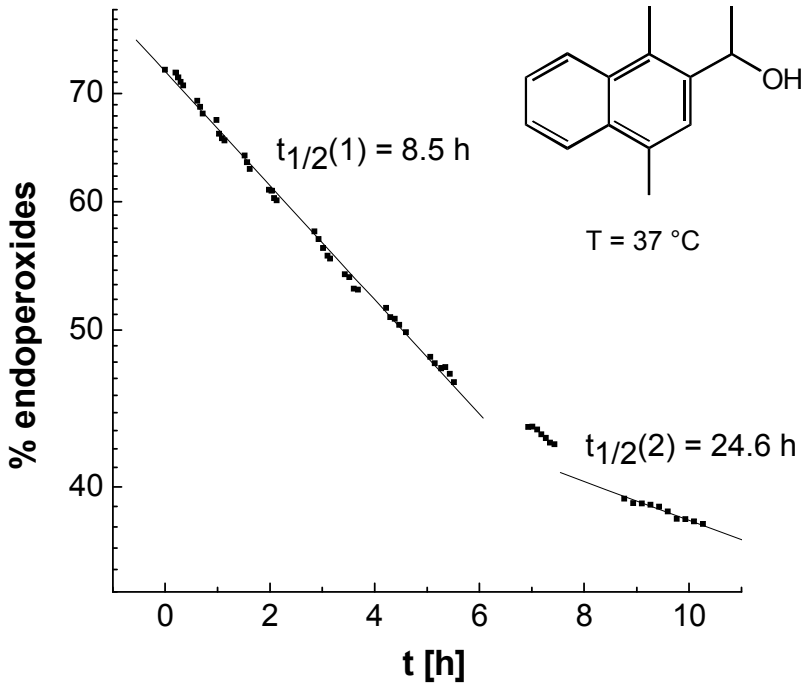

Figure 4.28. **N4E** decay after long irradiation time of 16 h in EC nanoparticles (diameter 98 ± 25nm, concentration 130 ppm w/w) at 37 °C measured with **N4** fluorescence time-trace. On y-axis is the percentage of all **N4** molecules which are in endoperoxide form at each particular time-point.

In order to be suitable for a chemosensitivity assay on MDA-MB-231 cancer cells, the endoperoxide decay time has to be longer than the cell-uptake time of polysorbate 80-coated EC nanoparticles, $t_{1/2} > t_u$. After short irradiation (1.5 hours) time only SDE part of formed endoperoxides have long enough of decay time (Figure 4.27.) to be suitable for cancer cell chemosensitivity assay, whereas after long irradiation time (16 hours) both FDE and SDE are stable long enough (Figure 4.28.) to satisfy the condition $t_{1/2} > t_u$.

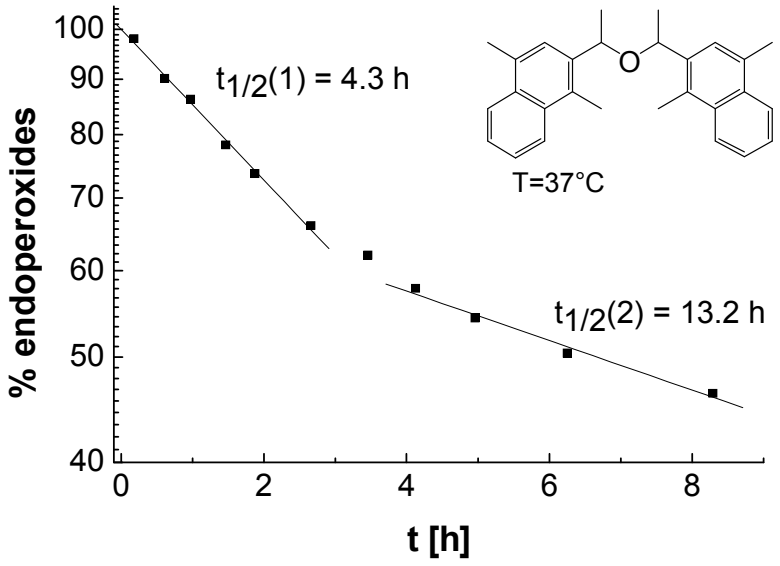

Figure 4.29. Decay of **N5E** after long irradiation time of 16 h in EC nanoparticles (size: diameter 136 ± 38 nm, concentration 130 ppm w/w) at 37 °C measured with **N5** fluorescence time-trace. On y-axis is the percentage of all **N5** molecules which are in endoperoxide form at each particular time point.

On Figure 4.29. decay of **N5E** in EC nanoparticles (average diameter 136 ± 38nm) at 37 °C is shown. Due to the long irradiation time of 16 hours, the **N5E** formation yield is a high 92 %. On top of that, $t_{1/2}$ of both FDE and SDE, though shorter than those of **N4E**, are suitable for a chemosensitivity assay on MDA-MB-231 cancer cells, $t_{1/2} > t_u$. Methylene blue sensitizer (c = 3 μM) was irradiated with laser (λ = 658nm, P = 70 mW, T =1 5 °C, for t = 16 h) to form $^1O_2$ which reacted with **N5** (c = 40 μM) to form **N5E** (yield 92 %).

4.5.4. *In Vitro* Cytotoxicity of $^1O_2$-Relasing Endoperoxides in EC Nanoparticles Carrier: Kinetic Chemosensitivity Assay Results

Cytotoxicity of **N4E** (Figure 4.32.) and **N5E** (Figure 4.33.) embedded in polysorbate 80™-coated EC nanoparticles in aqueous suspension on MDA-MB-231 cancer cells using crystal violet chemosensitivity assay [111] was tested. But firstly the cytotoxicity of polysorbate 80™ surfactant (Figure 4.30.) and of undoped EC nanoparticles (Figure 4.31.) on MDA-MB-231 breast cancer cells was tested. From the chemosensitivity assay results for polysorbate 80™ on Figure 4.30. it can be concluded that up to 0.005 % (v/v) Polysorbate 80™ does not affect MDA-MB-231 cancer cell proliferation, whereas in the 0.010-0.020 %

(v/v) range polysorbate 80™ is cytotoxic with full cell population recovery after 150 h, and 0.040 % (v/v) Polysorbate 80™ is cytocidal for MDA-MB-231 cells.

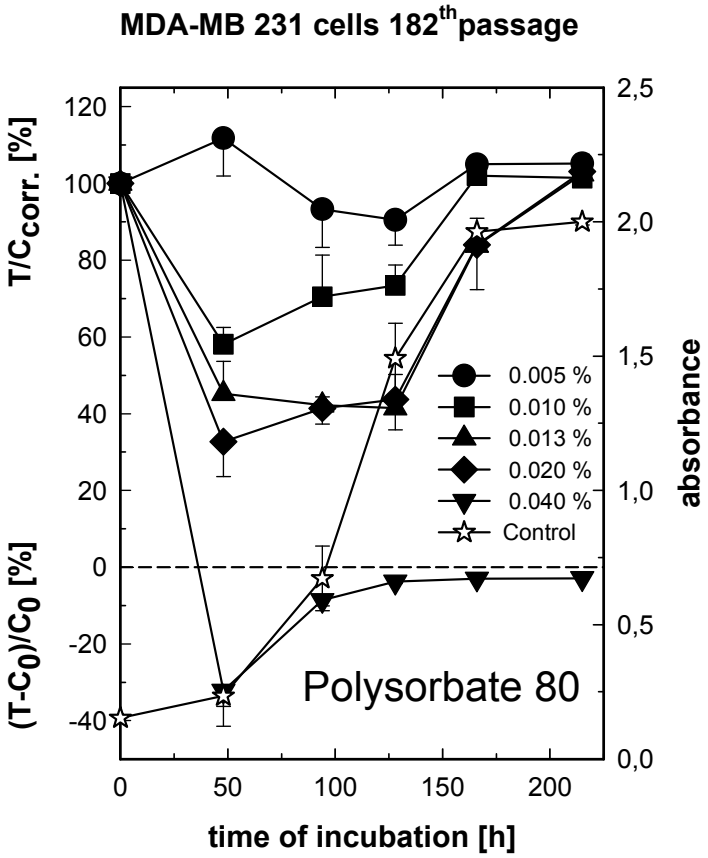

Figure 4.30. Chemosensitivity of MDA-MB-231 cells (182nd passage) against surfactant polysorbate 80™, up to 0.040 % (v/v) in cell medium. H_2O was used as a negative growth control (☆).

Chemosensitivity of MDA-MB-231 breast cancer cells on unloaded EC nanoparticles (diameter 62 ± 15 nm), both non-coated and polysorbate 80™-coated is shown on Figure 4.31. At a low concentration of 20 ppm (w/w) polysorbate 80™-coated (0.0021 % v/v), unloaded EC nanoparticles are not cytotoxic (◆ symbols on Figure 4.31.) However, with the EC nanoparticles concentration increase, a cytotoxic effect of the non-coated unloaded EC particles appears: 90 ppm (w/w) non-coated unloaded EC nanoparticles inhibit the cell proliferation process up to 50 %, with a full cell population recovery occurring after 180 h (○ symbols on Figure 4.31.) 140 ppm (w/w) non-coated unloaded EC nanoparticles exhibit an even stronger cytotoxic effect (□ symbols on Figure 4.31.), after which the cell population does not fully recover within the assay time-frame (190 h). Hence, the EC nanoparticles should not be used for drug-delivery at this or an even higher concentration. Furthermore, when the cytotoxic 90 ppm (w/w) EC particles were coated with a polysorbate 80™ cytotoxic

concentration of (0.0098 % v/v), a cytostatic effect on the MDA-MB-231 cell proliferation occurred (● symbols on Figure 4.31.) Therefore, in order to get a cytotoxic effect by $^1O_2$-releasing endoperoxides, and not by EC nanoparticles, the loading efficiency of such a complex carrier system is extremely important.

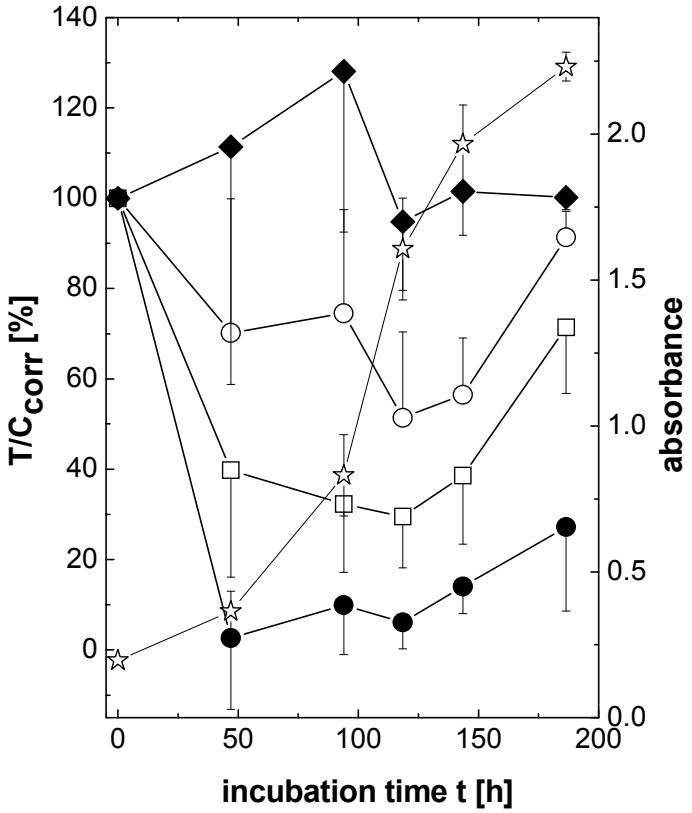

Figure 4.31. Chemosensitivity of MDA-MB-231 cells (181st passage) against non-coated and polysorbate 80™-coated unloaded EC nanoparticles (diameter 62±15nm). ◆ EC particles, 20 ppm (w/w), polysorbate 80™-coated (0.0021 % v/v); ○ EC particles, 90 ppm (w/w), non-coated; □ EC particles, 140 ppm (w/w), non-coated; ● EC particles, 90 ppm (w/w), polysorbate 80™-coated (0.0098 % v/v); H_2O was used as a negative growth control (☆).

The cell incubation with a highly-concentrated mixture of 21.5 µM $^1O_2$-releasing **N4E** and 5.5 µM **N4** embedded in polysorbate 80™-coated EC nanoparticles (diameter 98 ± 25 nm, concentration 120 ppm w/w) yielded a strong cytocidal effect on proliferation of MDA-MB-231 cells (● symbols, Figure 4.32.) Methylene blue sensitizer (c = 0.33 µM) was irradiated with laser (λ = 658nm, P = 70 mW, T = 4°C, for long irradiation time t = 15 h) to form $^1O_2$, which reacted with **N4** to form **N4E** (yield 79%). After the irradiation EC particles were coated with polysorbate80™, 0.033 % (v/v end-concentration). Non-irradiated 27 µM **N4** embedded in the same 120 ppm (w/w) EC nanoparticles produced approximately 40 %

inhibition of cell growth with a cell recovery starting after ca. 125 hours (○ symbols, Figure 4.32.) This effect was probably caused by polysorbate80™ surfactant cytotoxicity (compare Figure 4.30.) As a comparison a weak cytostatic effect of 10 µM cisplatin dissolved in DMSO is shown: growth of cells is about 70% inhibited and cell population doesn't recover after treatment with 10 µM cisplatin.

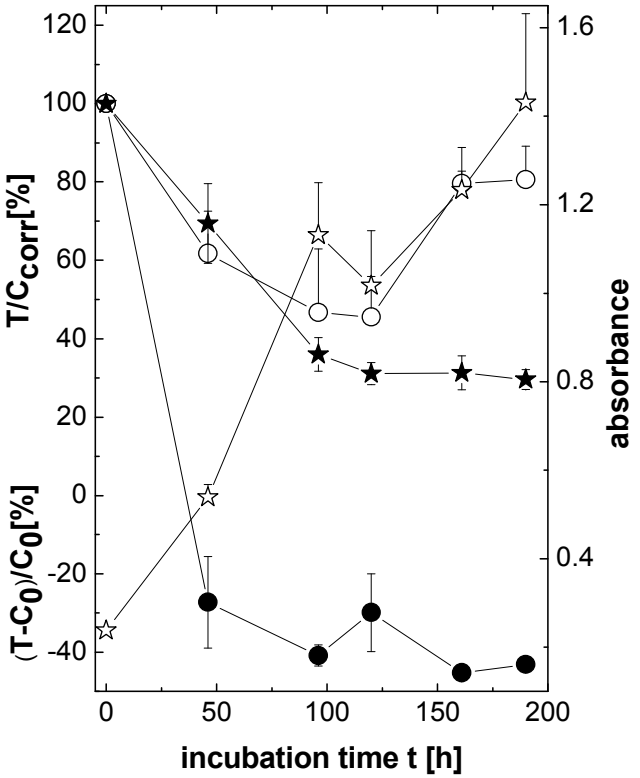

Figure 4.32. Cytocidal drug effect of highly concentrated **N4E** (c = 21.5 µM) in Polysorbate 80™-coated EC nanoparticles on human breast adenocarcinoma cells MDA-MB-231, passage 78, as a function of incubation time. On the contrary, non-irradiated **N4**, c = 27 µM, in the same polysorbate80™-coated EC nanoparticles suspension has only an initial inhibitory effect on the cell proliferation, after which the cell population recovers (after 125h). As a comparison, a cytostatic effect of cisplatin is shown. ○ **N4**, 27 µM, in EC nanoparticles, 120 ppm (w/w), coated with polysorbate80™, 0.033 % (v/v) ● **N4E**, 21.5 µM + **N4,** 5.5 µM in EC nanoparticles, 120 ppm (w/w), coated with polysorbate80™, 0.033 % (v/v), ★ positive control: Cisplatin, 10 µM in DMSO, ☆ negative control: H_2O.

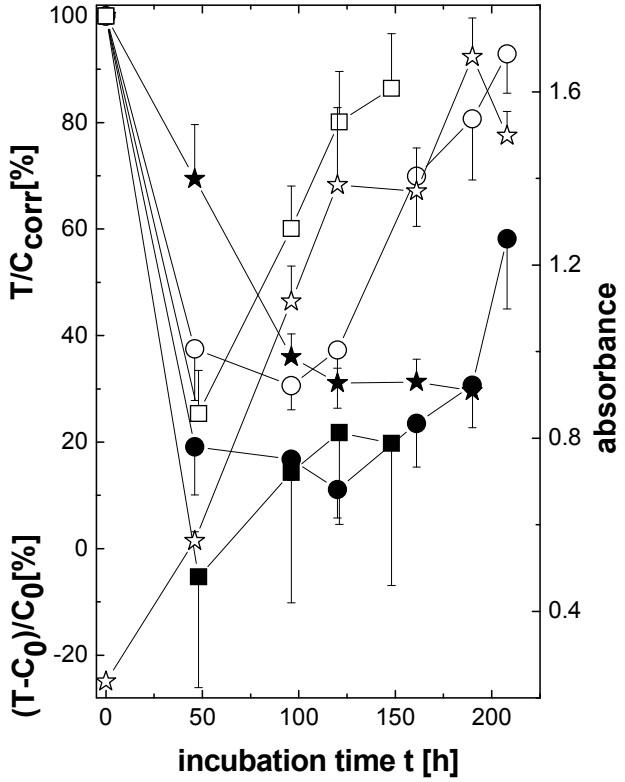

Figure 4.33. Cytostatic drug effect of **N5E** in polysorbate 80™-coated EC nanoparticles on human breast cancer cells MDA-MB-231, passage 78, as a function of incubation time, comparable to the effect of 10 µM cisplatin dissolved in DMSO. Non-irradiated **N5** in the same polysorbate 80™-coated EC nanoparticles has only an initial inhibitory effect on the cell proliferation, after which the cell population recovers (after ca. 150 h). □ **N5**, 3.5 µM, in EC nanoparticles, 70 ppm (w/w), coated with polysorbate80™, 0.020 % (v/v); ■ **N5E**, 3.0 µM + **N5,** 0.5 µM in EC nanoparticles, 70 ppm (w/w), coated with polysorbate80™, 0.020 % (v/v); ○ **N5**, 8.4 µM, in EC nanoparticles, 50 ppm (w/w), coated with polysorbate80™, 0.020 % (v/v); ● **N5E**, 7.2 µM + **N5,** 1.2 µM in EC nanoparticles, 50 ppm (w/w), coated with polysorbate80™, 0.020 % (v/v); ★ positive control: cisplatin, 10 µM in DMSO; ☆ negative control: H_2O.

The MDA-MB-231 cell incubation with $^1O_2$-releasing **N5E** embedded in polysorbate 80™-coated EC nanoparticles (two various batches: batch 1: diameter 136±28 nm, concentration 50 ppm w/w; batch 2: diameter 122±26 nm, concentration 70 ppm w/w) yielded a strong cytostatic effect of about 80 % of growth inhibition compared to the normal growth of untreated MDA-MB-231 cells (7.2 µM **N5E** in batch 1 (50 ppm w/w) EC nanoparticles, ● symbols, Figure 4.33. and 3.0 µM **N5E** in batch 2 (70 ppm w/w) EC nanoparticles, ■ symbols, Figure 4.33.) MB sensitizer (c = 0.2 µM) was irradiated with laser (λ = 658nm, P= 70 mW, T = 4°C, for long irradiation time t = 15 h) to form $^1O_2$ and subsequently **N5E** (yield 86 %). After the irradiation EC particles were coated with

polysorbate80™, 0.020 % (v/v in cell medium). Cytostatic effect of **N5E** in polysorbate 80™-coated EC nanoparticles is comparable to the effect of 10 μM cisplatin dissolved in DMSO on the growth of MDA-MB-231 cancer cells. On the contrary, non-irradiated 8.4 μM **N5** embedded in the batch 1 (50 ppm w/w) EC nanoparticles produced approximately 60 % inhibition of cell growth with a cell recovery after ca. 150 hours (○ symbols, Figure 4.33.). Similar effect had non-irradiated 3.5 μM **N5** embedded in the batch 2 (70 ppm w/w) EC nanoparticles: inhibiting the cell growth for approximately 75 % with a cell recovery after ca. 150 hours (□ symbols, Figure 4.33.). This cytotoxic effect of non-irradiated **N5** is rather caused by the cytotoxicity of 0.020 % (v/v) polysorbate80™ surfactant (compare results on Figure 4.30.) and for batch 2 by the cytotoxicity of 70 ppm (w/w) EC nanoparticles (compare results on Figure 4.30.)

4.6. ENDOPEROXIDE DECAY AND CYTOTOXICITY OF POLY(1,4-DIMETHYL-2-VINYLNAPHTHALENE) NANOPARTICLES

Poly(1,4-dimethyl-2-vinylnaphthalene) nanoparticles were prepared as described in Chapter 3.3.5. To determine the cell uptake of **N7** nanoparticles by the MDA-MB-231 breast cancer cells the CLSM technique was used. In order to enable their detection with CLSM, coating of **N7** nanoparticles (average diameter 12 ± 3 nm) with PTC fluorescencing dye was tried, but was rather unsuccessful. Thus, it was not possible to determine if **N7** nanoparticles do permeate the MDA-MB-231 cells and what is their cell-uptake time.

4.6.1. Endoperoxide Formation in Poly(1,4-Dimethyl-2-Vinylnaphthalene) Nanoparticles

N7E formation and decay were traced with **N6** absorption (294 nm) intensity change. In general, the yield of endoperoxide formation was relatively low, see Figure 4.34. After 7 hours of MB sensitizer (c = 3 μM) irradiation with laser (λ=658nm, P=70 mW, T=4°C) a saturation value of endoperoxide yield of 45 % was reached. Such a low yield complies with the explanation of endoperoxide formation yields in PVB and EC nanoparticles. Namely, due to a high concentration of **N6** in aqueous suspension and the necessary transport of $^1O_2$ from iraddiated MB sensitizer dissolved in water ($^1O_2$ generation location) to the **N7** in the core of its nanoparticles ($^1O_2$ storage location in endoperoxide form), the endoperoxide yield is low.

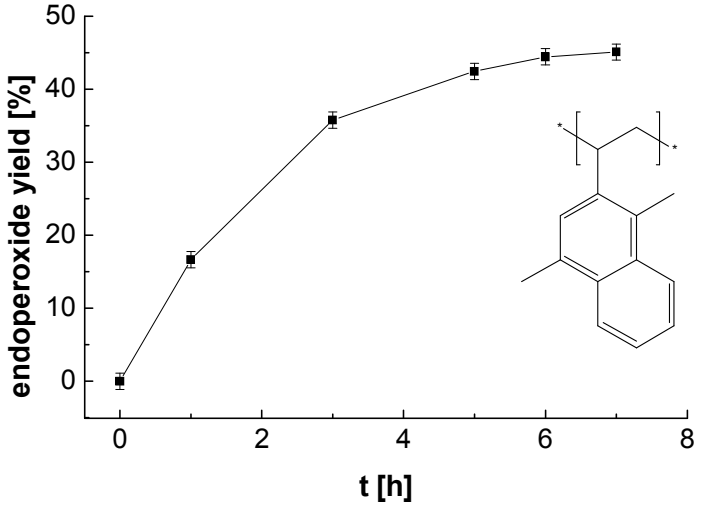

Figure 4.34. **N7E** formation yield in **N7** nanoparticles at 4°C depending on laser irradiation-time measured with **N6** absorbance change.

4.6.2. Endoperoxide Decay Kinetics in Poly(1,4-Dimethyl-2-Vinylnaphthalene) Nanoparticles

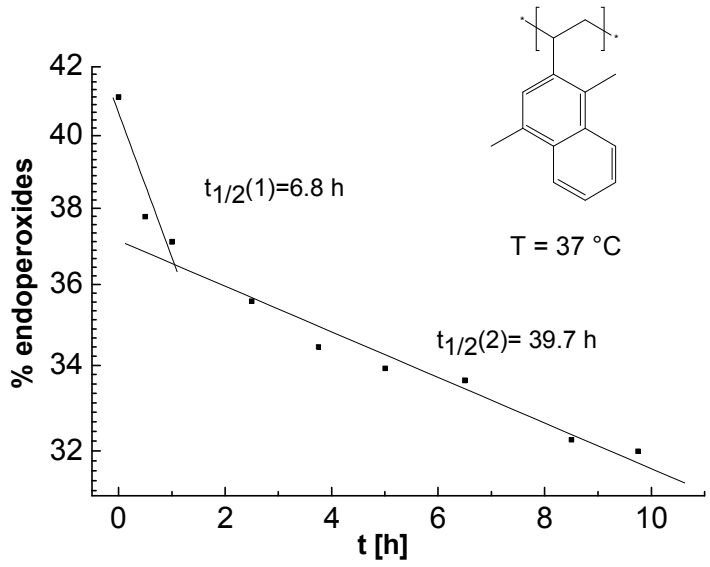

Figure 4.35. Decay of **N7E** in form of nanoparticles (size: diameter 12 ± 3 nm,) at 37 °C measured with **N6** absorbance change, after long (t = 9 h) laser irradiation of MB sensitizer (c= 3 μM). On y-axis is the percentage of all **N6** molecules which are in endoperoxide form at each particular time-point.

On Figure 4.35. the biexponential decay of **N7E** (in form of 12 ± 3 nm nanoparticles) is shown. Methylene blue sensitizer (c= 3 μM) was irradiated with laser (λ = 658 nm, P = 70 mW, T = 4°C, for t = 9 h) to form $^1O_2$ which reacted with **N7** polymer (**N6** concentration in aqueous suspension = 0.2 mM) to form **N7E** (yield 42 %). Both FDE with decay-time of 6.8 hours and SDE with decay-time of 39.7 hours at the human body temperature of 37 °C are suitable for cancer cell chemosensitivity assay.

4.6.3. *In Vitro* Cytotoxicity of $^1O_2$-Releasing Endoperoxides in **N7** Nanoparticles Carrier: Kinetic Chemosensitivity Assay Results

Cytotoxicity of various sizes and concentrations (measured with absorption: corresponding to **N6** monomer) of non-irradiated **N7** nanoparticles in aqueous suspension on MDA-MB-231 cancer cells using crystal violet chemosensitivity assay was tested (see Figure 4.36.) With the increase of non-coated **N7** (diameter 12 ± 3 nm) particles concentration in aqueous suspension, their cytotoxicity increases: at low concentration of c(**N6**) = 0.4 μM, there is no influence on the growth of MDA-MB-231 cancer cells by the **N7** particles (○

symbols on Figure 4.36.); whereas 1.9 µM **N7** nanoparticles are cytotoxic and inhibit the MDA-MB-231 cell growth for about 50 % after 235 hours (□ symbols on Figure 4.36.); and 6.3 µM **N7** nanoparticles (△ symbols on Figure 4.36.) show a cytostatic effect comparable to the effect of 100 nM vinblastine (★ symbols on Figure 4.36.), a known potent cytostatic drug used as a positive chemosensitivity control.

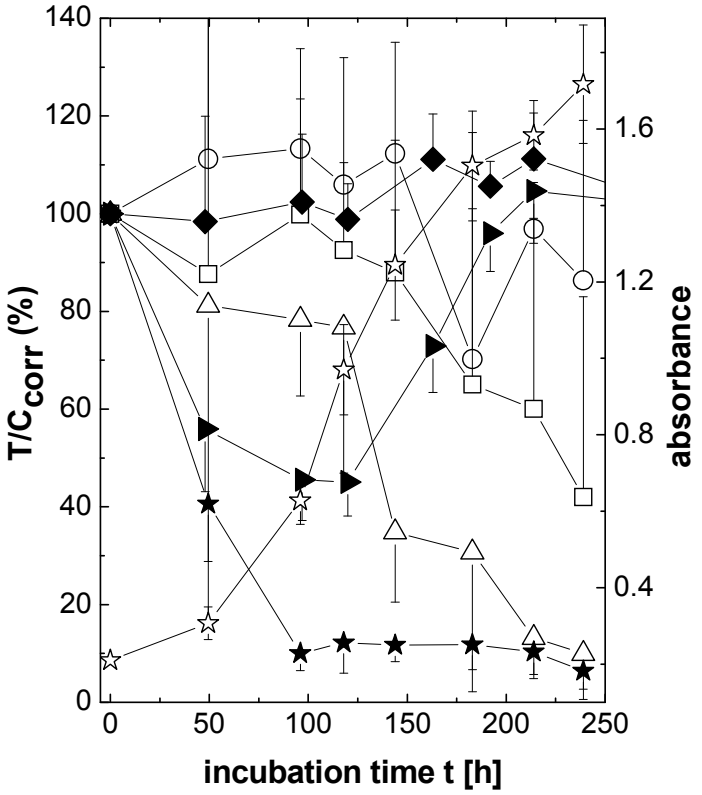

Figure 4.36. The chemosensitivity of MDA-MB-231 cancer cells, passage 64, on various sizes and concentrations of **N7** in form of nanoparticles. ○ **N7**, 0.4 µM, non-coated nanoparticles, diameter 12 ± 3 nm; □ **N7**, 1.9 µM, non-coated nanoparticles, diameter 12 ± 3 nm; △ **N7**, 6.3 µM, non-coated nanoparticles, diameter 12 ± 3 nm; ◆ **N7**, 12.5 µM, polysorbate80™-coated (0.005% v/v) nanoparticles, diameter 58 ± 9 nm; ◆ **N7**, 50.0 µM, polysorbate80™-coated (0.020% v/v) nanoparticles, diameter 58 ± 9 nm ★ positive control: vinblastine, 100 nM, ☆ negative control: H_2O.

On the other hand, larger N7 particles of 58 ± 9 nm average diameter were much less cytotoxic: 12.5 µM non-irradiated **N7** polysorbate80™-coated (0.005 % v/v) nanoparticles showed no inhibitory effect on MDA-MB-231 cell growh (◆ symbols on Figure 4.36.) even though they were in a much higher concentration in comparison to non-coated **N7** particles of 12 ± 3 nm diameter. Only at very high **N7** concentration of 50.0 µM, do polysorbate 80™-coated (0.02 % v/v) non-irradiated **N7** (58 ± 9 nm) nanoparticles inhibit the cell proliferation (▶ symbols on Figure 4.36.), for about 50% after 100 hours with subsequent cell culture

recovery (full recovery reached after 220 h). Probably the majority of this cytotoxic effect is caused by 0.02 % v/v polysorbate 80™ toxicity: compare with Figure 4.30.

The cytotoxicity of **N7E** in nanoparticle form on MDA-MB-231 human cancer cells was tested in the same concentration range and compared with the cytotoxicity of non-irradiated **N7** nanoparticles, see Figure 4.37. and Figure 4.38. Unfortunately, a mixture of **N7E** and **N7** (● symbols on Figure 4.37.) showed no cytotoxicity increase in comparison to non-irradiated **N7** nanoparticles (diameter 12 ± 3 nm, ○ symbols on Figure 4.37.), as seen on the example of 1.9 μM **N7** nanoparticles and the mixture of 0.7 μM **N7E**, and 1.2 μM **N7**. Remarkably, the cytotoxicity of **N7** nanoparticles (diameter 12 ± 3 nm) regularly decreased when endoperoxides were formed in the whole **N7** concentration range shown on Figure 4.36. **N7E** formation: 25 nM MB sensitizer was irradiated with laser (λ = 658nm, P = 70 mW, T = 20 °C, for long time t = 15 h) to form $^1O_2$ which reacted with **N7** to form **N7E** (yield 36 %).

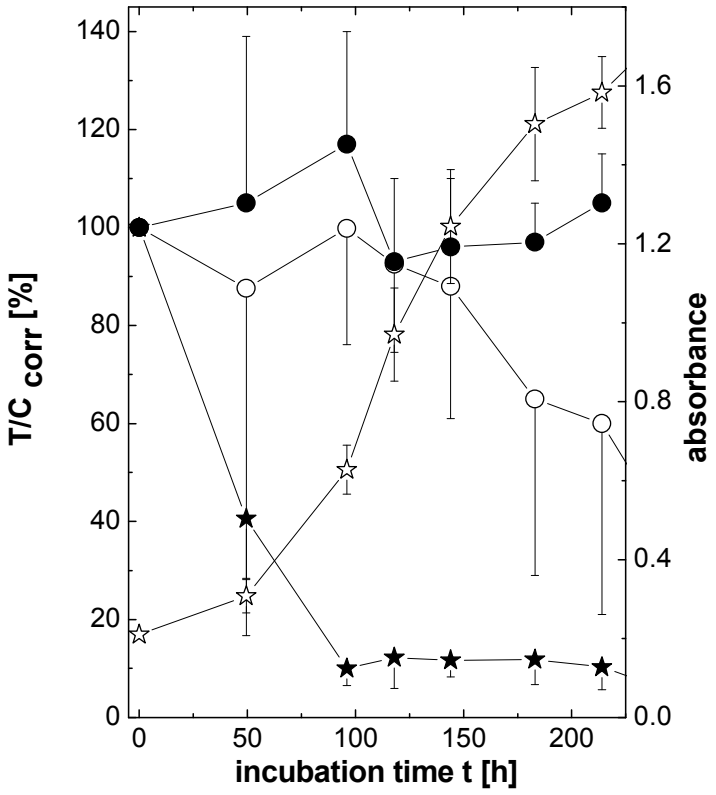

Figure 4.37. Chemosensitivity of MDA-MB-231 cells, passage 64, to N7E and N7 in form of non-coated nanoparticles (diameter 12 ± 3nm). ○ **N7**, 1.9 μM, non-coated nanoparticles; ● **N7E**, 0.7 μM, + **N7**, 1.2 μM in non-coated nanoparticles; ★ positive control: vinblastine, 100 nM, ☆ negative control: H_2O.

The cell damage mechanism by **N7** nanoparticles is unknown. Perhaps the very small **N7** nanoparticles interact with cell DNA. Therefore, further chemosensitivity assay experiments with larger **N7** nanoparticles (58 ± 9 nm average diameter) were performed. 12.5 μM non-irradiated **N7** polysorbate80™-coated (0.005% v/v) nanoparticles of this size showed no inhibitory effect on MDA-MB-231 cell growh (○ symbols, Figure 4.38.) However, when 41 % of **N7** reacted upon irradiation to form **N7E** in polysorbate80™-coated (0.005% v/v) nanoparticles, a weak inhibitory effect of about 30 % on cell proliferation (● symbols, Figure 4.38.) ocurred, with cell recovery after 150 h.

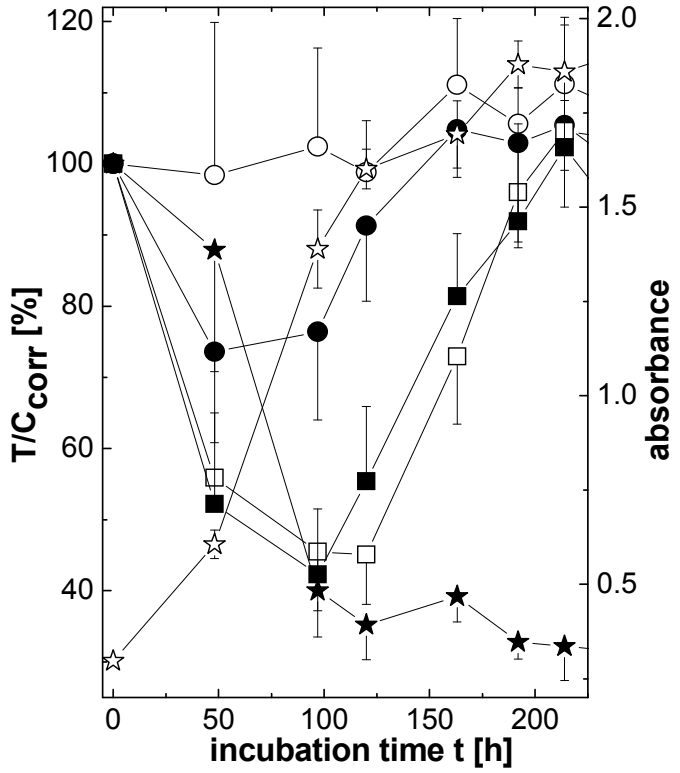

Figure 4.38. The cytotoxic effect of $^1O_2$-releasing **N7E** in polysorbate80™-coated nanoparticles (diameter 58 ± 9nm) on MDA-MB-231 cell growth, passage 79, determined by the crystal violet assay. ○ **N7**, 12.5 μM, polysorbate 80 ™-coated (0.005% v/v) nanoparticles; ● **N7E**, 5.1 μM, + **N7**, 7.4 μM polysorbate 80 ™-coated (0.005% v/v) nanoparticles; □ **N7**, 50.0 μM, polysorbate 80™-coated (0.020% v/v) nanoparticles; ■ **N7E**, 20.5 μM, + **N7**, 29.5 μM polysorbate 80™-coated (0.020% v/v) nanoparticles; ★ positive control: cisplatin, 5 μM in DMSO, ☆ negative control: H_2O.

When the **N7** concentration was increased to 50.0 μM, both non-irradiated **N7** polysorbate80™-coated (0.020% v/v) nanoparticles (□ symbols on Figure 4.38.), and a mixture of 41% formed **N7E** and 59 % **N7** in polysorbate80™-coated (0.020% v/v)

nanoparticles (■ symbols on Figure 4.38.) made a cytotoxic effect on the MDA-MB-231 cell proliferation. The inhibitory effect (rather by **N7** nanoparticles than $^1O_2$-releasing **N7E**) on the cell growth was 60 % after 100 hours with subsequent cell recovery: full recovery after 220 h. **N7E** formation: 40 nM methylene blue sensitizer was irradiated with laser (λ = 658nm, P = 70 mW, T = 20 °C, for t = 13 h) generating $^1O_2$ which reacted with **N7** to form **N7E** (yield 41 %). After irradiation nanoparticles were coated with polysorbate80™.

N7 nanoparticles with 95 ±10 nm average diameter were prepared, as well, for details see Chapter 4.1.2. However, the concentration (corresponding to the monomer **N6)** of such particles in aqueous suspension was rather low. The highest reached concentration in cell medium was 1.4 μM (size 95 ± 10 nm). Due to such a low concentration neither polysorbate80™-coated (0.01% v/v) **N7** nanoparticles, nor its polysorbate80™-coated (0.01% v/v) endoperoxides showed any inhibitory effect on the growth of MDA-MB-231 cells.

5. NAPHTHYL-SUBSTITUTED PORPHYRIN MULTICHROMOPHORE MOLECULES FOR THE SELF-PHOTOSENSITIZED FORMATION OF ENDOPEROXIDES

5.1. INTRODUCTION

In another project of this work it was desired to synthesize and characterize multichromophore molecules consisting of up to four endoperoxide-forming aromatic units (derivatives of **N1**) covalently linked to a red-light absorbing photosensitizer core (porphyrin derivatives). Such a system would combine the useful properties of tetrapyrrole derivatives as a sensitizer for photodynamic therapy with the ability of aromatic endoperoxides to release $^1O_2$ and thus would have an internal reactivity to generate and "store" $^1O_2$.

5.2. EXPERIMENTAL

5.2.1. Materials and Methods

The starting compounds and 1,3-diphenylisobenzofurane (DPBF) were obtained commercially from Sigma–Aldrich and were used without further purification. All reactions were carried out under nitrogen atmosphere in degassed solvents, which were dried using conventional methods.

NMR spectra were recorded with a Bruker Avance Spectrometer (^{1}H: 200 MHz; T = 308 K). Additionally, higher-resolved ^{1}H and ^{13}C HMBC spectra were recorded using a Bruker NMR spectrometer operating at 500 MHz for ^{1}H and 125.725 MHz for ^{13}C. The chemical shifts are reported in ppm releative to external standards (solvent residual peak) and coupling constants are given in Hertz.

EI-MS spectra were obtained with a Varian CH-5 spectrometer.

Electronic absorption spectra were recorded with a Varian Cary 300 Bio UV/Vis spectrophotometer and fluorescence spectra were obtained using a Horiba Jobin Yvon Fluorolog-3 spectrofluorometer equipped with two double-grating monochromators, a R928P

photomultiplier, and an FL-1040 phosphorimeter using Uvasol quality solvents and teflon stoppered 1-cm quartz cells under aerobic conditions.

5.2.2. Synthesis of 5,10,15,20-Tetrakis-(4-Methyl-Naphthyl)Porphyrin (**P1**)

To a refluxing mixture of 100 ml propionic acid, 850mg (5 mmol) 4-methylnaphthaldehyde, and 0.34 ml (4.9 mmol) of freshly distilled pyrrole were added. This mixture was refluxed for 10 days. Then the mixture was poured on 750ml of water and the precipitate formed was filtered off and dried. The raw material was purified by extensive column chromatoghaphy (SiO_2, pentane/toluene), and the first orange-red fraction was collected to obtain the pure free ligand **P1**. The compound was analysed with mass spectrometry and NMR.

ESI-MS (dichloromethane/methanol 1:1, positive ion mode): m/z 871.5 ([**P1**+H]$^+$);
ESI-MS (dichloromethane/methanol 1:1, negative ion mode): m/z 743.8 ([**P1**-$C_{10}H_6$]$^-$);

^{1}H NMR (200 MHz, CD_2Cl_2): δ -2.21 (s, 2H, pyrrole-NH), 3.07 (s, 12H, 4 CH_3), 5.9 & 6.6 (CH=CH of endoperoxide form), 7.24 (m, 8H), 7. 57 (t, *J* =7.15 Hz, 4H), 7.78 (d, *J* =7.6 Hz, 4H), 8.23 (m, 4H), 8.36 (d, *J* =8.7Hz, 4H), 8.52 (s, ß-pyrolle 8H)

5.2.3. Metalation of **P1**

200 mg of the ligand **P1** (0,23mmol) were dissolved in $CHCl_3$:CH_3OH (1:1, v/v) and 2g (ca. 9 mmol) of zinc-acetate tetrahydrate dissolved in 1ml of glacial acetic acid was added. The reaction mixture was refluxed on a water bath for 2 hours. Within this time the metallation was completed as could be seen by UV-Vis spectroscopy. The mixture was washed free of unreacted salts and the zinc complex **P2** was purified by column chromatography (SiO_2, chloroform). The first deeply coloured band was collected, yielding a purple-red product after slow evaporation of the solvent, which was analysed with mass spectrometry and NMR.

EI-MS (dichloromethane/methanol 1:1 + 10 mM NH_4OAc, positive ion mode): m/z 548.3 ($[M1+NH_4]^+$); 932.2 (M^+); 933.2 ($[M+H]^+$); 966.9 ($[M + H+ O_2]^+$); 994.6 ($[M +H+ 2\ O_2]^+$); 1030.7 $[M +H + 3\ O_2]^+$); 1058.9 ($[M + H + 4\ O_2]^+$); 1079.0 ($[M + H+4\ O_2 + OH]^+$); 1111.3 ($[M + H+4\ O_2 + 3\ OH]^+$)

EI-MS (dichloromethane/methanol 1:1 + 10 mM NH_4OAc, negative ion mode):
m/z 529.4 ($[M1 - H]^-$); 565.4 ($[M1 + Cl]^-$); 967.3 ($[M + Cl]^-$); 991.4 ($[M + CH_3COO]^-$);
M= **P2** = 932 Da, M1 = M+ 4 O_2 = 1060/2=530 Da

^1H NMR, (200 MHz, CD_2Cl_2)

δ 3.01 (s, 12H, 4 –CH_3), 6.7 (s, CH=CH of endoperoxide form), 7.20 (m, 8H), 7. 56 (t, *J* =7.5 Hz, 4H), 7.76 (d, *J* =7.8 Hz, 4H), 8.20 (dd, *J* =3.2 Hz, 4H), 8.34 (d, *J* =8.7Hz, 4H), 8.62 (s, ß-pyrolle 8H)

^1H NMR, ^{13}C NMR (500 MHz, $CDCl_3$)

δ_C/δ_H 133.05/8.56 (ß-pyrolle 8H), the assignment of methylnaphthyl substituent is given in the Table 5.1.

Table 5.1. ^1H-NMR, ^{13}C-NMR, HMBC data for **P2** compound.

Atom number	δ_C	δ_H
C1		
C1’	133.0	/
C2’	126.2	7.67
C3’	125.0	8.25
C4’	135.9	/
C4’a	126.7	/
C5’	130.7	7.25
C6’	126.7	7.09
C7’	126.3	7.50
C8’	130.7	7.25
C8’a	139.4	/
C9’	21.0	3.01

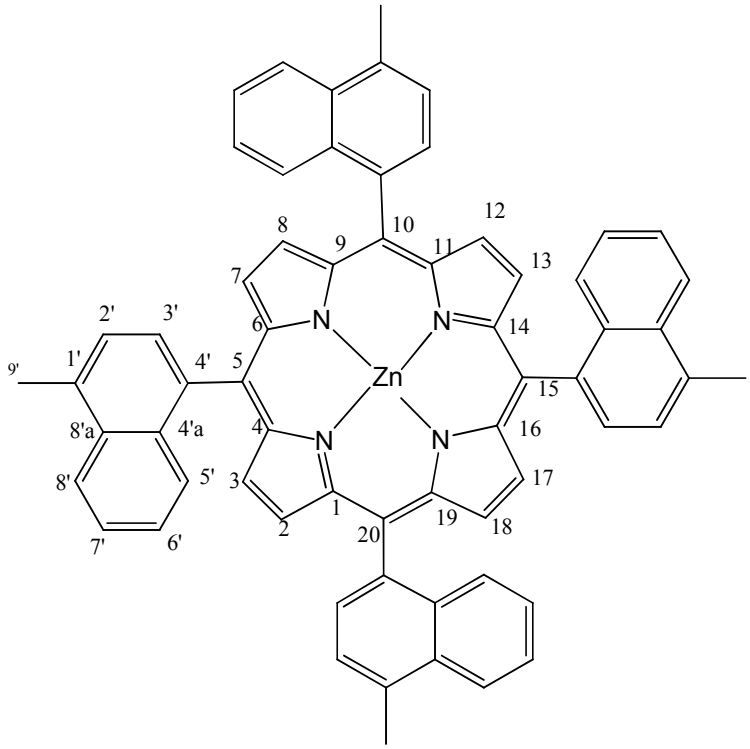

5.2.4. Self-Sensitized Peroxidation of **P2** Complex

P2 was dissolved in dichloromethane and irradiated with the full light of a high-pressure xenon lamp passing through a Schott GG 475 nm cut-off filter and a water-cooled infra-red filter. During the irradiation procedure solution of **P2** was constantly saturated with O_2. Light power in Q band region of **P2** was 11.3 mW cm^{-2}. The progress of peroxidation reaction was monitored by observing the appearance of endoperoxide peaks using ^1H NMR spectroscopy.

5.2.5. Singlet Oxygen Assay

Photosensitized singlet oxygen generation by novel 5,10,15,20-tetrakis-(4-methyl-naphthyl)porphyrinato-zinc(II) (**P2**) and zinc(II)-meso-tetraphenylporphyrin (ZnTPP) as a reference was monitored in aerobic toluene solution at room temperature by following the time-dependence of DPBF absorption at 412 nm depending on sample irradiation time. DPBF was acting as a $^1O_2$ scavenger [143]. The absorbencies of Q-band maxima of both **P2** and ZnTPP were set to approximately identical values of ca. 0.05. DPBF in toluene was added to a final concentration of 3×10^{-5} M and 2.0 ml samples were irradiated with the 533-548 nm polychromatic light of Hanovia Xe/Hg 977 B-1 lamp at ambient air conditions. Sample area of 2.02 cm^2 was irradiated with light power density of 1.8 mW cm^{-2}, which was measured with a Luzchem Research spectroradiometer SPR-4001. After each irradiation cycle DPBF absorbance at 412 nm was measured and sample absorbance value at 412 nm was deducted from it. As a control, only 2% bleaching of DPBF occurred during irradiation at the same conditions in absence of a $^1O_2$ producing porphyrin-derivative sample.

The $^1O_2$ quantum yields were determined using the following equation

$$\phi = -\frac{(C_t - C_0)VN_A}{I_{abs}St} \qquad (15)$$

where C_0 and C_t are the DPBF concentration prior to and after irradiation, respectively, V the reaction volume, S the irradiated area of the cell, t the irradiation time per cycle, N_A the Avogadro's number and I_{abs} the overlap integral of the irradiation light source intensity and the absorption of the particular sensitizer in the Q band region and is defined as

$$I_{abs} = \int (1 - 10^{A_\lambda}) I_\lambda \, d\lambda \qquad (16)$$

where I_λ is the intensity of light and A_λ the absorbance of the sensitizer at wavelength λ. Values of C_0 and C_t after irradiation were calculated using the extinction coefficient of DPBF in toluene, $\varepsilon_{toluene} = 21\ 000\ l\ mol^{-1}\ cm^{-1}$ [144].

5.3. RESULTS AND DISCUSSION

5.3.1. Characterization of Novel Multichromophore Molecules

5,10,15,20-tetrakis-(4-methyl-naphthyl)porphyrin (**P1)** was synthesized using the Adler method [145] and used as a precursor for synthesis of 5,10,15,20-tetrakis-(4-methyl-naphthyl)porphyrinato-zinc(II) (**P2)**, according to the reaction sequence shown in Scheme 5. Both substances were obtained as dark red powder materials and characterized with mass spectroscopy, NMR, and electronic absorption and emission.

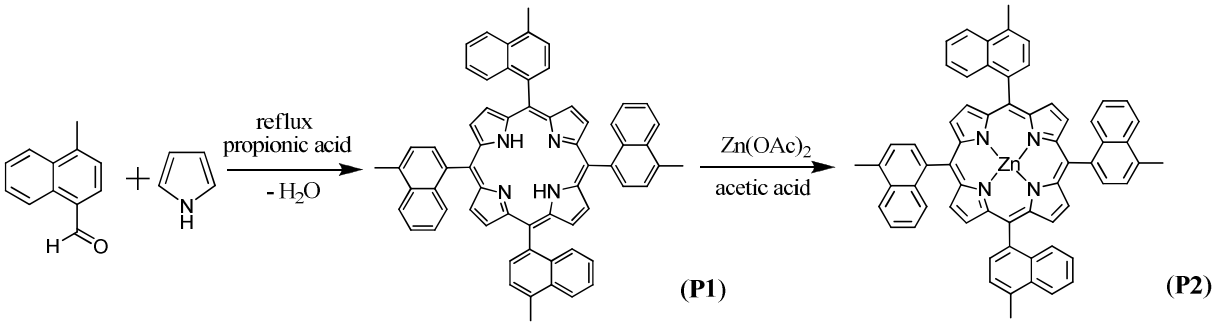

Scheme 5. Synthesis pathway of **P1** and **P2** with Adler method.

The electronic spectra of the functionalized porphyrin derivatives **P1** and **P2** were recorded in ethanol or chloroform solution. Fig. 5.1.a shows typical electronic absorption spectra of the free-base ligand **P1** and the zinc complex **P2** in chloroform and in Fig. 5.1.b extinction molar coefficient values of complex **P2** in ethanol are given. The absorption maximum at 425 nm corresponds to the Soret, or B band of **P1**. The free-base porphyrin complex shows the typical pattern of four Q bands in the visible spectral region with a phyllo-type intensity distribution. A further, weak absorption feature in the 280-300 nm

region is present and attributed to the π-electron system of the methylnaphthyl substituent. Metalation of **P1** causes a small Soret maximum redshift in **P2** spectrum (Fig. 5.1.a), and a change of Q band with only one maximum at 551 nm.

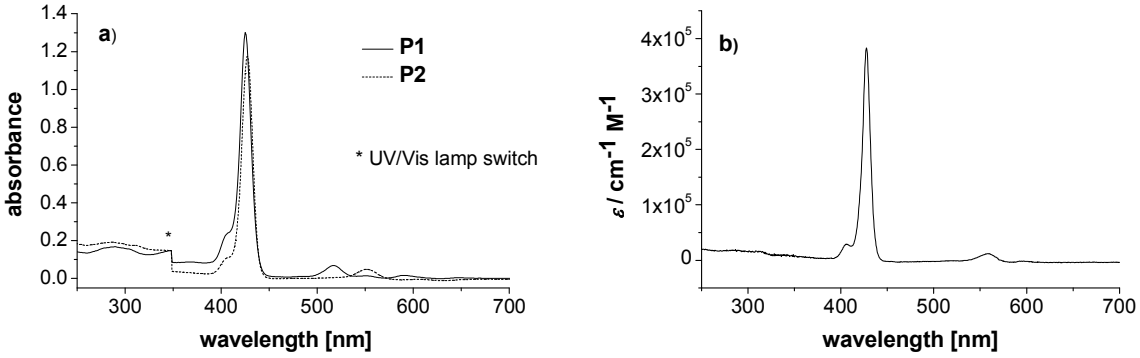

Figure 5.1. a) Absorption spectrum of **P1** and **P2** compounds in chloroform. b) Molar extinction coefficient of **P2** in ethanol.

A relatively strong electronic coupling of the porphyrin core with methylnaphthyl substituents occurs and causes an antenna effect by excitation of methylnaphthyl subsituents to porphyrin luminescence in multichromophore complexes **P1** and **P2**, see Figs. 5.2. a) and 5.3. a), respectively. When complex **P1** is excited at 290 nm absorption of methylnaphthyl substituent, a weak emission around 380 nm, coming from methylnaphthyl side-groups and a strong energy transfer (the antenna effect) to the porphyrin emitting part of the **P1** compound appears, with peaks at 650 nm and 716 nm, respectively (Fig. 5. 2. a). Excitation spectrum for 650 nm emission (shown in Fig. 5.2. c) confirms the antenna effect. For comparison the porphyrin emission with Soret band excitation is given in Fig. 5.2. b).

On Fig. 5. 2. a) there are several artifacts: solvent Raman spectrum peaks at 317 nm and re-absorption by the porphyrin Soret-band at 425 nm.

The excitation spectra for 650 nm emission (Fig. 5.2. c) and for 716 nm porphyrin emission bands of **P1** multichromophore compound do match. Excitations of both the naphthyl substituent (UV region) and Soret- and Q-bands of the porphyrin core cause the red light emission by **P1**.

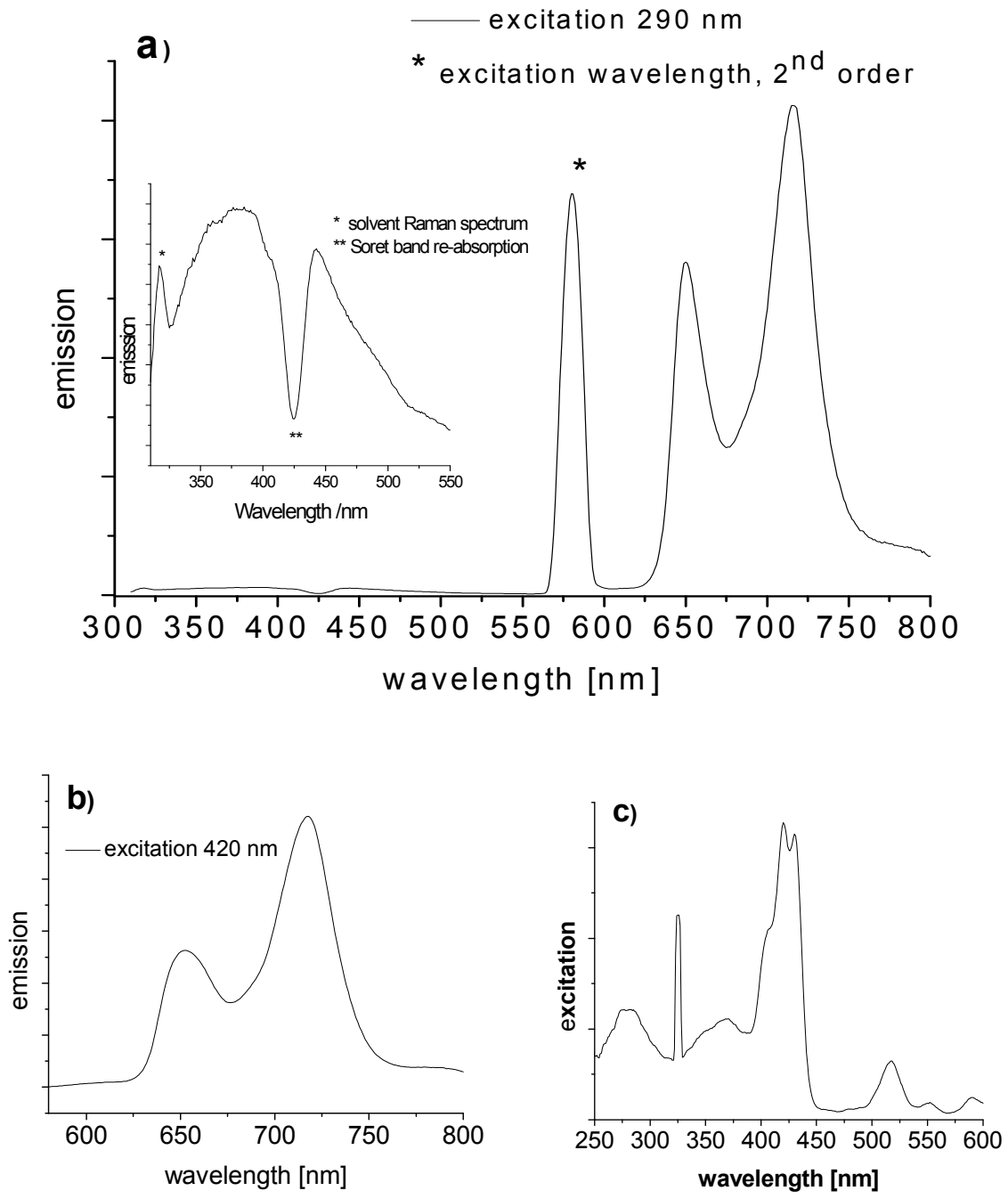

Figure 5.2. **P1** luminescence (a and b) and excitation (c) spectra in $CHCl_3$. Excitation of methylnaphthyl side-group with 290 nm (a) and in the Soret band of the porphyrin core with 420 nm light (b), respectively.

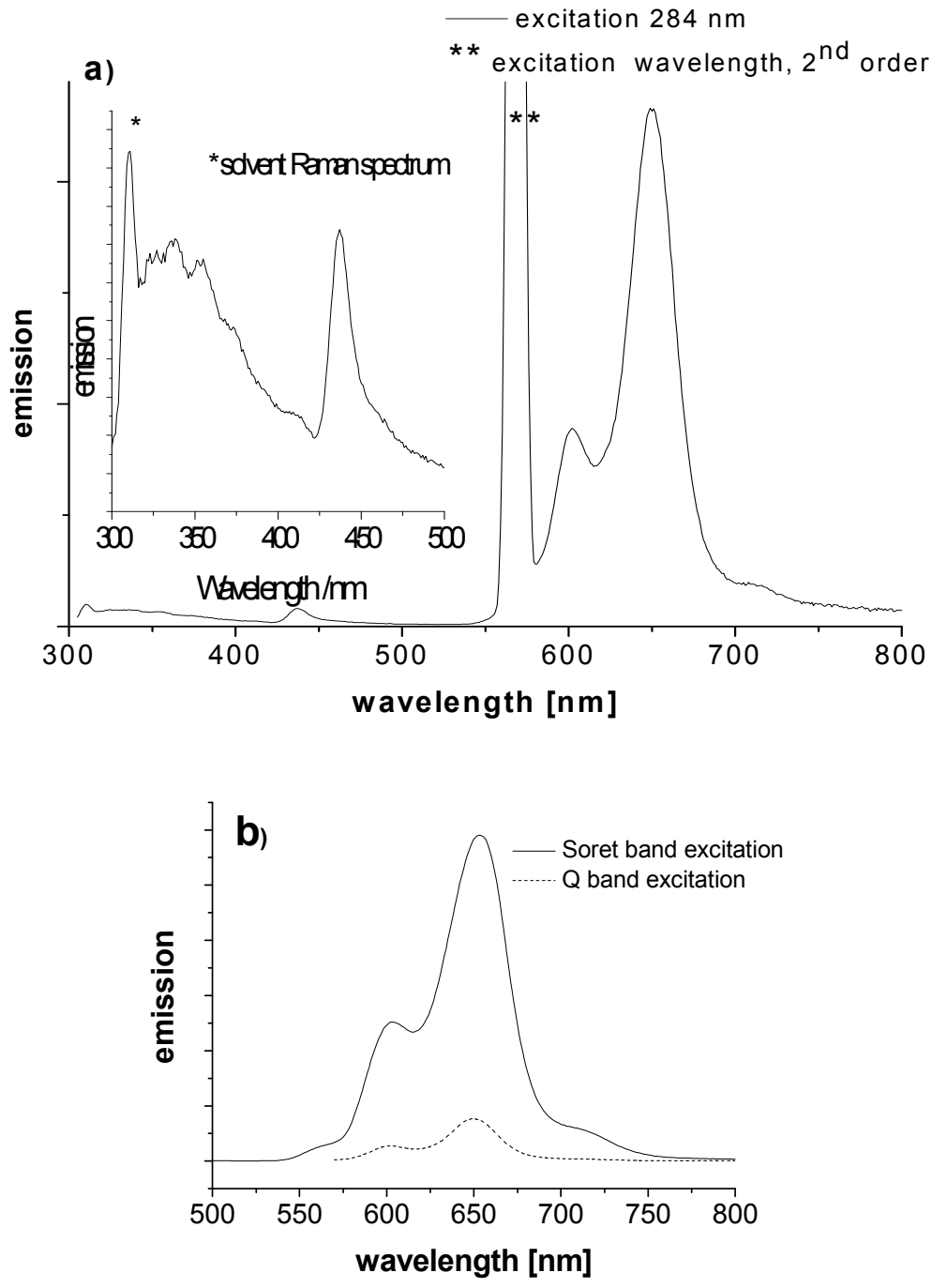

Figure 5.3. Luminescence spectra of **P2** in $CHCl_3$. a) Excitation of methylnaphthyl side-group of **P2** with 290 nm. b) Soret band (427 nm) and Q band (551nm) excitation of the porphyrin core of **P2** complex.

When complex **P2** is excited at 284 nm absorption of methylnaphthyl substituent, a very weak methylnaphthyl substituents' emission around 330 nm and a strong energy transfer

(antenna effect) to the S1 state of porphyrin emitting part of the **P2** complex with peaks at 605 nm and 652 nm appear, see Fig. 5.3. a). Moreover, a weaker emission from porphyrin S2 state occurs with maximum at 440 nm. S2 porphyrin emission of compound **P1** does not appear, compare Fig. 5.2. a). For comparison the porphyrin S1 state emission after Soret band excitation is given in Fig. 5.3. b). On Fig. 5.3. a) there is an artifact of solvent Raman spectrum at 310 nm.

On Fig. 5.4. the excitation spectra, which confirm that emission around 440 nm is by the S2 state of the porphyrin core and the emission around 650 nm is by the porphyrin S1 state, are shown. On top of that, the excitation spectrum of S1 state on Fig. 5.4. b) confirms the antenna effect from methylnaphthyl substituents to the S1 state of the porphyrin core.

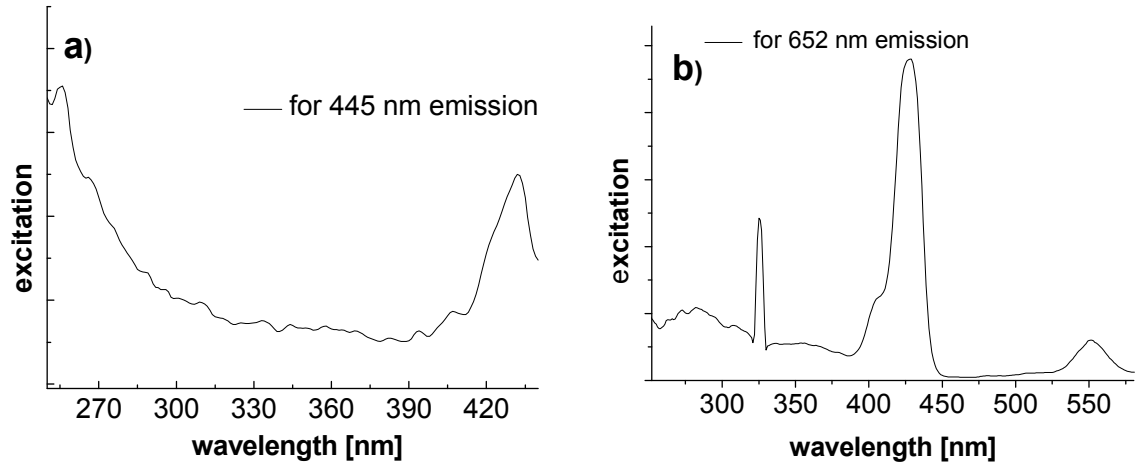

Figure 5.4. a) Excitation spectrum for the 445 nm S2 emission band; and b) for the 652 nm S1 emission band of the **P2** compound's porphyrin core.

5.3.2. Photogeneration of Singlet Oxygen by **P2** Complex

A standard assay with 1,3-diphenylisobenzofurane (DPBF) as singlet oxygen ($^1O_2$) scavenger was used to track the well-known $^1O_2$ generation by the commercial reference sensitizer zinc(II)-meso-tetraphenylporphyrin (ZnTPP) and by complex **P2**. As shown in Fig. 5.5. the formation rate of $^1O_2$ by multichromophore complex **P2**, when its oxygen saturated solution is irradiated in the Q band region, is very similar to the $^1O_2$ formation rate

by ZnTPP reference under the same conditions. The curve profiles on Fig. 5.5. suggest a rapid consumption of the dissolved dioxygen in the teflon-stoppered cuvettes used in the assay.

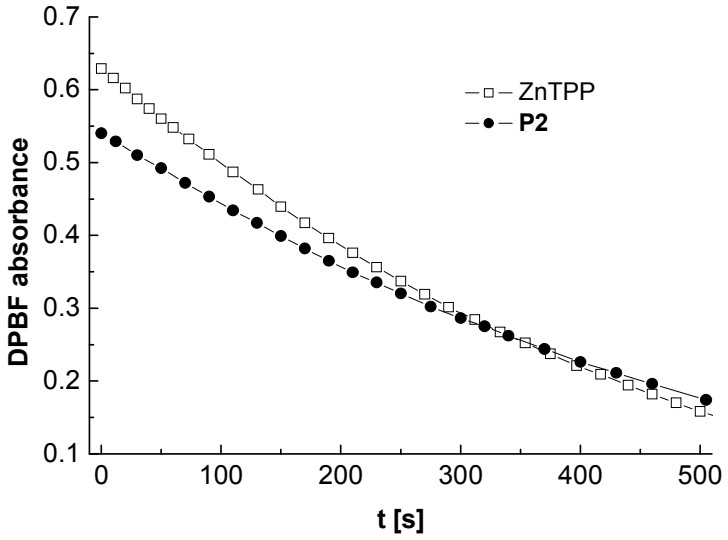

Figure 5.5. Photosensitized singlet oxygen generation by 4 μM **P2** and 3 μM ZnTPP reference detected with 412 nm DPBF absorption assay in oxygen saturated toluene solution at room temperature.

Both the ZnTPP reference and novel multichromophore **P2** complex were irradiated in the Q band region because irradiation in the Soret band caused immediate photobleaching of the DPBF $^1O_2$ trap. Moreover, using other light sources with stronger light intensity in the sensitizer Q band region caused even faster consumption of the dissolved dioxygen. Therefore, the 533-548 nm polychromatic light source with light intensity of about 10^{14} photons s^{-1} cm^{-2}, although not at the Q band maximum, showed to be best suitable for this assay.

Singlet oxygen yields, Φ_Δ, integrated over the overlap of the irradiation light source intensity and the absorption of each sensitizer were obtained from equations [146] and Stern-Volmer plots described in detail in literature [147] and are given in Table 5.2. The deviation of values obtained by our measurement from published values [147] is presumably caused by our inability to precisely measure and tune the light intensity used for sample irradiation. Therefore, both values were corrected with the same factor to reach the published yield value

of 0.94 for ZnTPP reference in toluene [147]. Nevertheless, Φ_Δ of complex **P2** is very similar to the Φ_Δ of ZnTPP reference sensitizer, as values in Table 5.2. show.

Table 5.2. Singlet oxygen quantum yields, Φ_Δ, of ZnTPP and ZnTMNP obtained with chemical quenching of DPBF in comparison to published values.

compound	λ[a](nm)	solvent	Φ_Δ, measured	Φ_Δ, corrected
ZnTPP	546	toluene	0.45	0.94
P2	546	toluene	0.41	0.86

[a] sample irradiation wavelength

5.3.3. Endoperoxide Formation on Methylnaphthyl Substituents of **P2** Complex

When it was established that **P2** reacts with dioxygen to generate $^1O_2$ upon short irradiation times, reaction of singlet oxygen with methylnaphthyl substituents of complex **P2** to form endoperoxides [12, 31] after longer irradiation (reaction) times and possible subsequent release of reactive oxygen species [13, 148] was investigated. Using ^{1}H-NMR and mass spectroscopy it was found that a very small, non-quantifiable portion of both **P1** and **P2** in solid state reacted spontaneously with ambient oxygen under room light to form endoperoxides (^{1}H-NMR weak peaks at 5.9 and 6.6 ppm, respectively), although the whole synthesis and purification procedure of both **P1** and **P2** complexes were performed under sunlight protection.

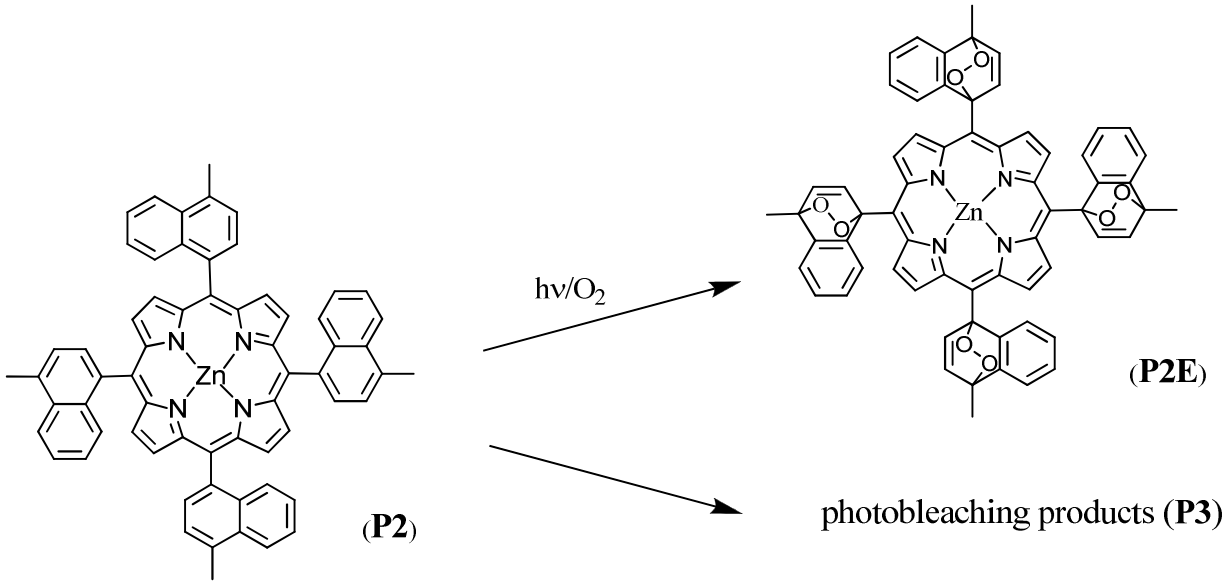

Scheme 6. **P2** photooxidation to a mixture of endoperoxides on methylnaphthyl substituents (**P2E**) and photobleaching products (**P3**).

Moreover, a constantly oxygen-saturated solution of multichromophore complex **P2** in dichloromethane was irradiated up to several hours, firstly in the Soret band region and later in the Q-band region. It was found that the Soret band irradiation causes a rather fast (in less than 1 hour) photobleaching process of compound **P2**. However, when the oxygen saturated solution of **P2** was irradiated in the Q band region with less light intensity, a mixture of endoperoxides on naphthyl substituents (**P2E**) and undefined photobleaching products (**P3**) was formed, according to Scheme 6. The endoperoxide formation reaction was confirmed with ^{1}H-NMR, electronic absorption and mass spectroscopy.

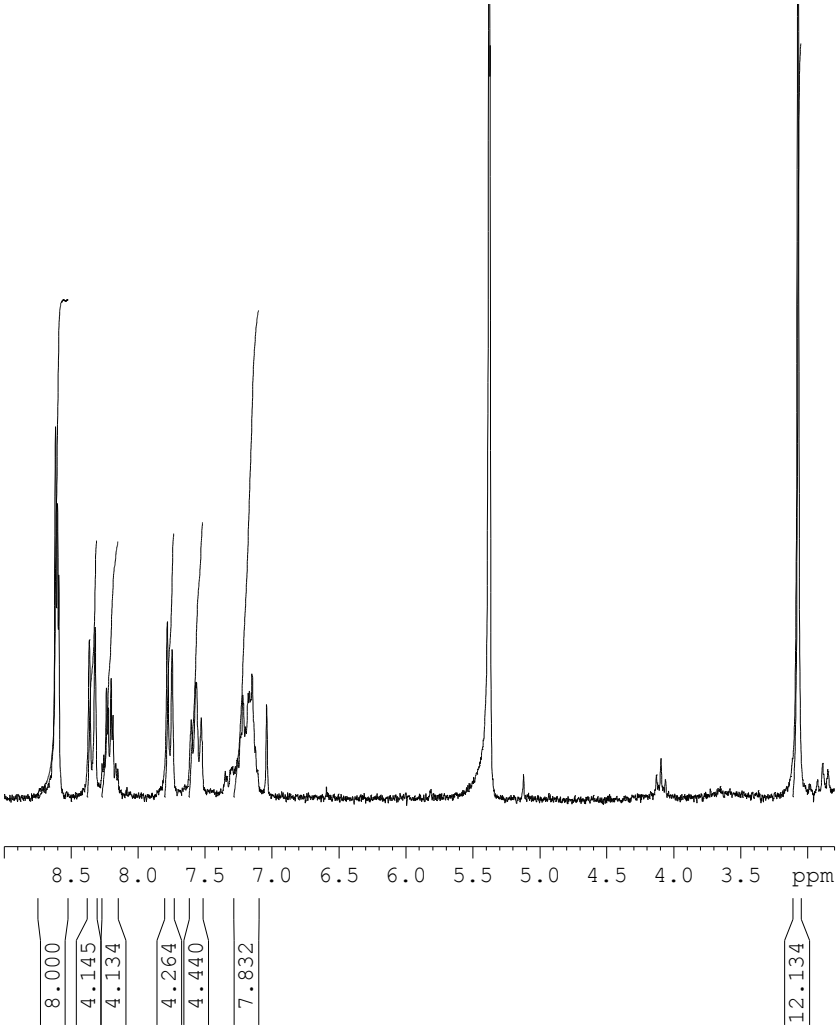

Figure 5.6. ^{1}H NMR spectrum of the **P2** complex in CD_2Cl_2 at 298 K. Below are numbers of protons corresponding to each peak.

On Fig. 5.6. a ^{1}H NMR spectrum of non-irradiated ZnTMNP (**P2**) in CD_2Cl_2 is shown. Below the spectrum numbers of protons corresponding to each peak are given. As can be seen on Fig. 5.7., upon longer irradiation of **P2** in the Q band region under aerobic conditions, a significant change in both the aromatic region and the methyl region of ^{1}H NMR occurs. Peaks assigned to complex **2** decrease and multiple new peaks appear: the multiplet around 2.7 ppm (Fig. 5.7. a) probably corresponds to methyl group protons [31, 34] of formed various number of methylnaphthyl-1,4-endoperoxide substituents and the multiplet in the aromatic region at about 6.55 ppm (Fig. 5.7. b) corresponds to 2 protons on HC=CH double-bond [31, 34] of methylnaphthyl-1,4-endoperoxide substituents. Due to formation of a mixture with various numbers (1-4) of endoperoxide substituents, **P2E**, a multiplet and not a singlet peak appears. Due to the undefined ptohobleaching products, several unassigned new

peaks appear in the aromatic region, which compromises the sensitizing potential of compound **P2** after several hours of irradiation.

a)

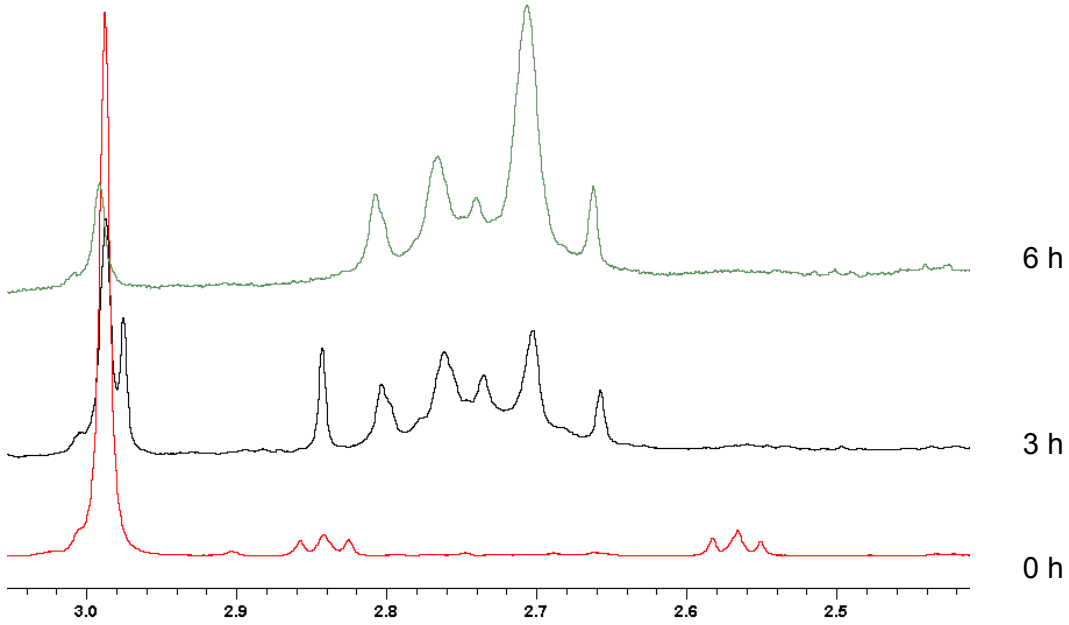

b)

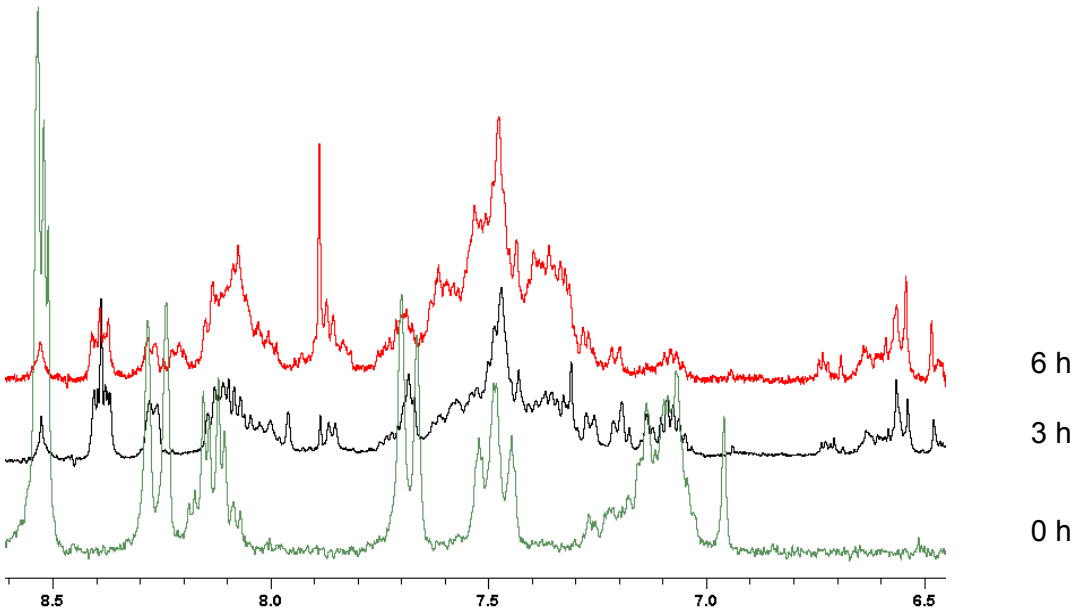

Figure 5.7. a) ^{1}H NMR spectra in MeOD at 308 K of the $-CH_3$ region showing the photooxidation reaction of **P2** to a mixture of **P2E** and **P3** after various irradiation times of **P2** in the Q band region under aerobic conditions in CH_2Cl_2. b) ^{1}H NMR spectra of the aromatic region showing the photooxidation reaction of **P2** to a mixture of **P2E** and **P3** taken under same conditions as in Fig. a).

The photoproducts **P2E** and **P3** were not isolated because a preparative amount of material after irradiation was not available.

The reaction mixture of **P2**, **P2E** and **P3** after various irradiation times was analysed using mass spectroscopy and 932.20 m/z peak of complex **P2** was detected, as well as 965.20 peak assigned to cation of **P2E** with one endoperoxide containing substituent.

On Fig. 5.8. the change of electronic absorption spectra depending on the irradiation time in the Q band region of **P2** under aerobic conditions is shown. The longer the irradiation time, the less is absorbance in both Soret and Q band, with a slight blueshift of both bands. After 13 h of irradiation the photobleaching of **P2** is almost complete: the porphyrin core opens up and the absorption in the UV region rises probably due to the absorption of single pyrrole rings which were previously forming the porphyrin core.

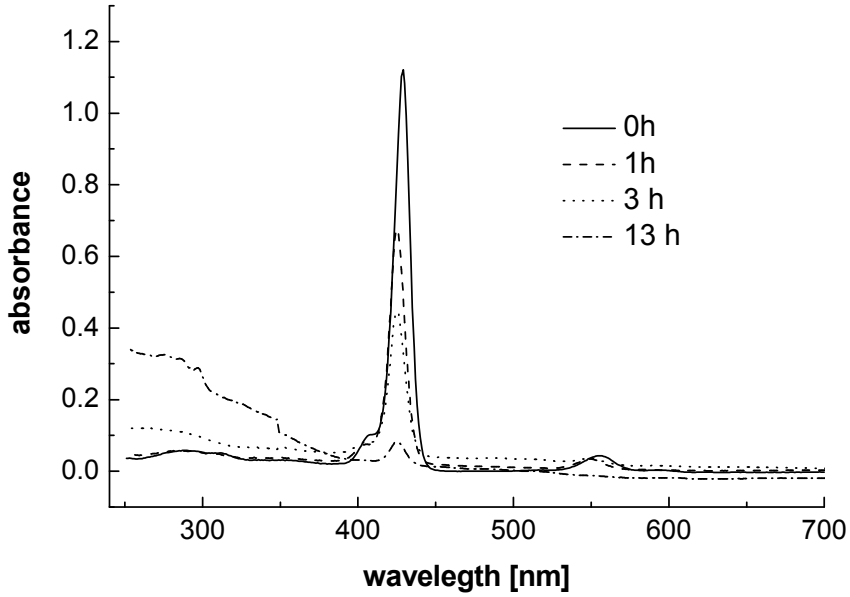

Figure 5.8. Electronic absorption spectra of **P2** and photoproducts showing the photooxidation reaction and the degradation of **P2** upon irradiation in the Q band region under aerobic conditions in CH_2Cl_2.

5.3.4. *In Vitro* Cytotoxicity of Non-Irradiated **P2** Complex

In vitro cytotoxicity of non-irradiated (5,10,15,20-tetrakis-(4-methyl-naphthyl)porphyrinato-zinc(II) (**P2**) sensitizer on MDA-MB-231 human breast cancer cells was also tested with the kinetic crystal violet chemosensitivity assay [111], see Fig. 5.9. The results were compared with cisplatin, a known cytostatic drug, which served as a positive control.

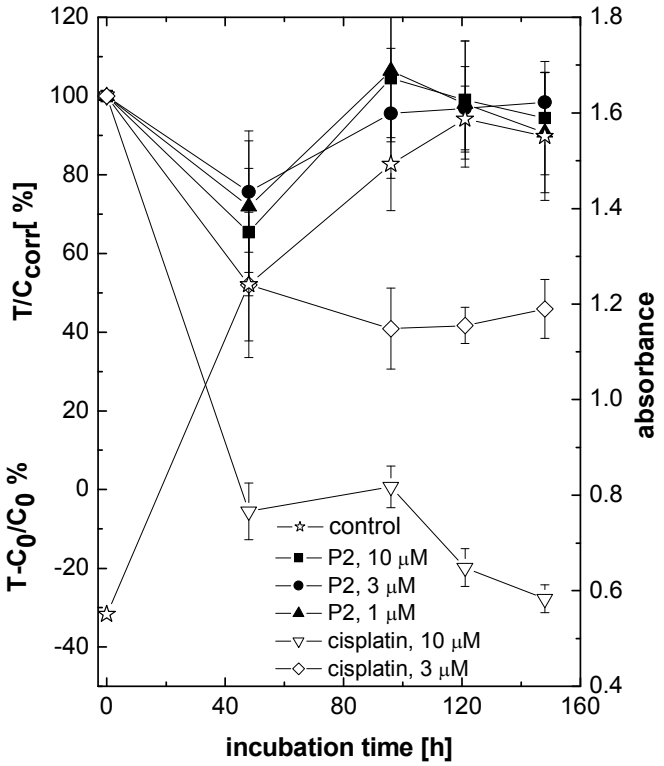

Figure 5.9. Non-inhibitory effect of non-irradiated 1-10 μM **P2** multichromophore on the proliferation of human MDA-MB-231 breast cancer cells, passage 179th, as a function of incubation time.

It was determined that non-irradiated complex **P2** in a 1-10 μM concentration range has only a minor initial inhibitory effect of about 30 % on the MDA-MB-231 cells proliferation, after which the cell population quickly recovers. Comparable cisplatin concentrations show a strong cytocidal effect (10 μM) and a cytostatic effect (3 μM) without cell recovery. Therefore, non-irradiated ZnTMNP diplays no cytotoxicity even at high concentrations up to 10 μM and could potentially be used in therapeutical applications such as PDT. Possible cytotoxicity of **P2** photooxidation products should be tested.

5.4. OUTLOOK: **P1** AND **P2** COMPLEXES' POSSIBLE MEDICAL APPLICATIONS

To sum up, the novel **P2** complex acts as a sensitizer, similar to the standard sensitizer ZnTPP, yielding $^1O_2$ after short irradiation times and after longer irradiation with long-wavelength light (in the Q-band region) it reacts with singlet oxygen to form endoperoxides which could potentially act as an internal source of $^1O_2$ in photodynamic therapy. Possible $^1O_2$-release from formed endoperoxide substituents in complex **P2E** should be further researched. Such a multichromophore system would then have a much broader time interval of singlet oxygen production than typical sensitizers, which generate $^1O_2$ only during the light irradiation itself. Hence it could possibly be used in a broad application range, such as chemotherapeutical applications with delayed triggering of singlet oxygen release inducing cellular damage in malignant tissue [12], or potential utilization of biomimetic endoperoxide-bond cleavage processes for the controlled deactivation of bacteria, viruses [149] and parasites such as *Plasmodium falciparum*, which is known to be responsible for the majority of fatal malaria infections [150].

5.5. CONCLUSION

Synthesis and characterization of two novel functionalized multichromophore molecules such as 5,10,15,20-tetrakis-(4-methylnaphthyl)porphyrin) (**P1**) and (5,10,15,20-tetrakis-(4-methyl-naphthyl)porphyrinato-zinc(II) (**P2**), is reported. These complexes were designed to act as sensitizers and moreover to enable singlet oxygen "storage" in endoperoxide bridges on their peripheral naphthyl substituents after self-sensitized peroxidation. Their photophysics and photochemical behaviour in the presence of dioxygen was investigated. Singlet oxygen yield of **P2** as a sensitizer was determined. Photooxidation reaction products of **P2** after irradiation in dioxygen presence were investigated. It could be shown by several spectroscopic methods (NMR, MS) that upon exposure to long-wavelength visible light, these multichromophore systems are forming $^1O_2$-derived adducts with up to four endoperoxide subunits attached to their peripheric aromatic substituents.

6. DISCUSSION AND OUTLOOK

In this chapter the adjustability of the endoperoxide (of various 1,4-dimethylnaphthalene derivatives) decay kinetics in various matrices, for the concept of controlled $^1O_2$ release as stated in Chapter 2 is discussed. It will be shown that such an adjustment of decay kinetics is a general principle. On the example of anti-cancer treatment possible applications of this concept are demonstrated.

One of the main goals of this work was to search for an endoperoxide-carrier matrix combination and a preparation procedure providing a much longer $^1O_2$-release time, $t_{1/2}$, than the time period required for the cellular uptake (t_u) of the carrier. Another goal was to analyse the decay kinetics on the basis of the knowledge of the endoperoxide decay process, in particular concerning structural changes of the endoperoxide molecule during the decay process.

6.1. COMBINED DISCUSSION OF THE ENDOPEROXIDE DECAY KINETICS IN VARIOUS CARRIER MATRICES

6.1.1. Mechanistic Properties of Aromatic Endoperoxides Decay

A three dimensional schematic drawing for the illustration of the molecule geometry change occuring during the decay process is here introduced and used as the basis for the microscopic model (see Chapter 6.1.2.) explaining the decay kinetics.

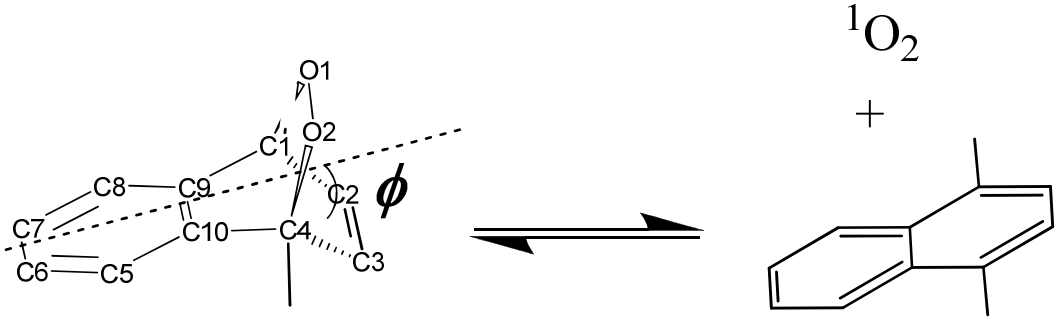

Figure 6.1. Mechanism of the endoperoxide decay: 1,4-cyclohexadiene moiety in endoperoxide molecule is bent for the angle ϕ and has to revert to the planar benzene ring releasing singlet oxygen during the decay process.

Unlike the planar aromatic "parent molecule", the 1,4-cyclohexadiene moiety of the tricyclic endoperoxides (used in this work) is bent for an angle ϕ between plane ($C_9C_1C_4C_{10}$) and plane ($C_1C_2C_3C_4$), as shown on Fig. 6.1. During the decay process, the endoperoxide molecule has to release O_2 from the endoperoxide bridge and the bent 1,4-cyclohexadiene moiety has to revert (restructure) back to the planar aromatic "parent molecule", see Fig. 6.1.

Interaction of substituents in various positions on naphthalene ring are described in literature [31˙, 137]. Moreover, during the decay process orbital rehybridization (sp^3 orbitals of the endoperoxide to sp^2 orbitals of the "parent molecule") at C1 and C4 atoms occurs, which is important for consideration of side-group interaction on *peri* substituted naphthalenes. In the naphthalene molecule the 1- and 8-positions are typically named to be *peri* to each other [137]. In view of the naphthalene geometry, substituents located at *peri* positions are in much closer proximity with stronger repulsion, than similar substituents located *ortho* to each other. The distance between peri-carbon atoms (C1 and C8, or C4 and C5 on Fig. 6.1.) is only about 2.4-2.5 Å [137]. In aromatic molecules, the normal nonbonded H…H distance is 2.4-2.5 Å, and the nonbonded C...C distance is 2.8-3.0 Å [137]. Thus substituents other than two hydrogens at the peri positions in naphthalene cause considerable steric interaction (strain), in the naphthalene ring (or *peri* stress, as classified by Schiemenz and co-workers [151]) due to repulsion, which is responsible for several unique properties of *peri* substituted naphthalenes, including ring distortion, with the larger 1- and 8- substituents bending away from each other both in the plane of the ring and perpendicular to it [152]. A major effect of *peri* "proximity effects" is a strong preference for sp^3- at the expense of sp^2-hybridised centres [153], because the strain (caused by interaction of *peri* substituents) is the driving force for reactions of *peri* substituted naphthalenes [152]. This *peri* interaction aspect is important for stabilization of **N2E** endoperoxide used in this work, which **N2** "parent molecule" is *peri* substituted.

In this work the endoperoxide decay kinetics was adjusted with various parameters influencing the mentioned restructuring process, e. g. by the variation of the matrix, which will be further discussed in some detail.

6.1.2. Functional Structure Consisiting of Endoperoxide Molecule and its Immediate Neighbourhood of the Surrounding Matrix: a Microscopic Model

The interaction between the embedded endoperoxide molecule and the surrounding carrier matrix has to be observed in more detail while having sp^3 to sp^2 rehybridization and endoperoxide reverting for the angle ϕ in mind. A scheme of a microscopic model of an endoperoxide molecule embedded in a polymer carrier matrix is given in Fig. 6.2. The endoperoxide molecule and the immediate neighbourhood of the surrounding carrier matrix form a functional structure.

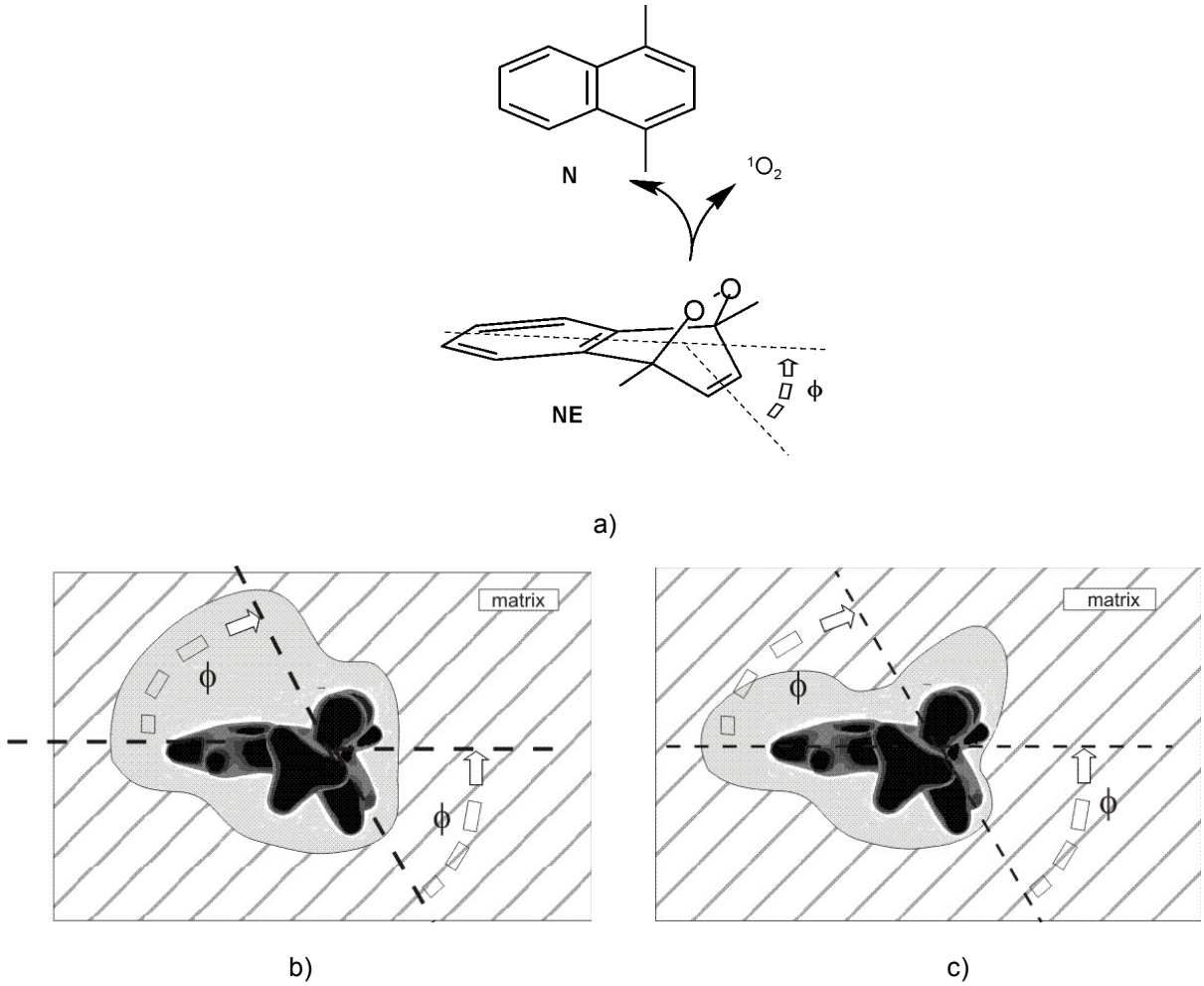

Figure 6.2. A microscopic model of an endoperoxide molecule embedded in a polymer carrier matrix forming functional structures. a) The 1,4-cyclohexadiene moiety of the endoperoxide molecule is bent for an angle ϕ. In order to revert the bent endoperoxide molecule, **NE,** to a planar, aromatic parent molecule, **N**, local free volume in the carrier matrix is needed. b) large local free volume and high endoperoxide (three dimensionally represented with its electron density distribution) mobility in the matrix, yielding FDE; c) small local free volume and reduced endoperoxide mobility in the matrix, yielding SDE.

The bent endoperoxide has two "wings": a shorter one, which is bent and a longer one with one intact aromatic ring. Obviously, if there is any steric hindrance in the functional structure, which restricts the reverting of the endoperoxide molecule for the angle ϕ to the planar aromatic "parent molecule" during the decay process (see Fig. 6.2. a), it will decay much slower. Thereby, the carrier matrix could cause the hindrance by disabling the decisive movement of either endoperoxide molecule "wing" (reverting for angle ϕ, as shown on Figure 6.2. b) and c), which is necessary for the decay process.

On Figures 6.2. b) and c), a **N1E** molecule (represented with an electron density distribution) embedded in a polymer matrix (e.g. PVB polymer matrix) and the matrix hindrance of the **N1E** decay are shown. The gray area around the **N1E** molecule on the Figures 6.2. b) and c) represents the local free volume present in the carrier matrix. This presence of free volume originates from the common features in the production of both polymer materials matrices: in the case of PVB film matrix the ethanol solvent molecules at first form a solvation shell [154] around 1,4-dimethylnaphthalene derivatives and the rigid polymer matrix cage is not in the immediate vicinity of the dissolved **N1** derivative. Thus, **N1** is still mobile in the liquid solvent cage [155]. Later, as the polymer film slowly dries on the glass substrate in the ethanol-saturated atmosphere, the solvent molecules slowly diffuse out of the polymer matrix leaving some free volume cavities around 1,4-dimethylnaphthalene derivatives in the soft matter polymer matrix. However, such cavities caused by the solvation shell do not remain infinitely, but disappear slowly through diffusion processes after some period of time [156], leaving the more rigid polymer matrix cage around **N1** derivative molecule. The same reasoning applies to polymer nanoparticle matrix: there is a solvation shell around **N1** derivative molecules prior to nanoparticles precipitation by non-solvent addition. During the particles precipitation, **N1** derivative molecule with its solvation shell is embedded in the polymer matrix. Subsequently, solvent molecules can slowly diffuse (e. g. during dialysis, see PVB nanoparticle preparation) through the polymer matrix, leaving local free volume cavities, because the polymer chains are already fixated.

In order to enable the endoperoxide decay and $^1O_2$ release, there has to be enough of local free volume not only in a region necessary to remove generated $^1O_2$ and at the same time for reverting of the bent form of the **N1E** to the planar aromatic **N1** molecule. When there is enough local free volume around the endoperoxide molecule present in the carrier matrix and/or endoperoxide is mobile to come to a position in which a fast endoperoxide

decay process occurs, i.e. FDE part of formed endoperoxides (Figure 6.2. b). This is valid for all other combinations of various endoperoxide-forming derivatives and polymer matrices. For FDE part of **N2E** and **N4E** in PVB film matrix $t_{1/2}$ values (see Table 4.6.) are even shorter than in liposome matrix, or even in organic solvents, probably due to the large localized free volume in PVB film. When the local free volume in the carrier matrix is small, the mobility of endoperoxides in the matrix is low (Figure 6.2. c), and the endoperoxide molecule has to diffuse to the area with larger local free volume in the polymer matrix to enable the endoperoxide decay, i.e. only SDE part of endoperoxide decay occurs. In polymer matrices there are 2 types of functional structures corresponding to FDE and SDE decay occurrence. Principally it is a statistical distribution of functional structures which can be characterized with the free volume presence.

6.1.3. Influence of Various Substituents of the **N1** Derivative on the Endoperoxide Decay Kinetics: Chemical Change of the Functional Structure

By introducing various substituents on the main N1 derivative, interaction of the endoperoxides with the matrix was influenced (the functional structures were modified chemically) and the decay times changed accordingly.

The half-life of examined 1,4-dimethylnaphthalene derivatives in organic solvents, for the particular endoperoxide decay, see Table 4.4. will be now compared. An explanation for a strong difference of **N1E** and **N2E** $t_{1/2}$ values is given by Wasserman et al. [31, 137]. A large steric strain caused by the nonbonded *peri* interaction (see Chapter 6.1.1.) between adjacent methyl groups at the 4- and 5- positions (i.e. methyl-methyl repulsion) is present in the **N2** derivative and not present in **N1** derivative.

Orbital rehybridization (sp^2 to sp^3) of C1 and C4 atoms (Fig. 6.1.) resulting from the endoperoxide formation significantly reduces the steric interaction between adjacent *peri* methyl groups (at C4- and C5-positions on Fig. 6.1.) in the bent **N2E** compared to the planar parent **N2** molecule [31, 137]. The aforementioned steric methyl-methyl interaction does not exist in the **N1** molecule, where the C5- substituent is a hydrogen atom, and therefore causes no stabilization of the **N1E** (compare Scheme 3). For a better overview of used naphthalene derivatives structure, Schemes 3 and 4 are here repeated.

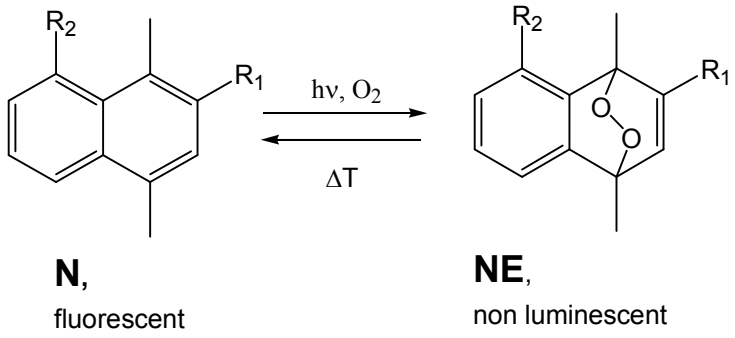

N,
fluorescent

NE,
non luminescent

N1: $R_1 = R_2 = H$

N2: $R_1 = H$, $R_2 = CH_3$

N3: $R_1 = COCH_3$, $R_2 = H$

N4: $R_1 = CHOHCH_3$, $R_2 = H$

N6: $R_1 = CH{=}CH_2$, $R_2 = H$

N7 = poly (**N6**)

Scheme 3. Endoperoxide formation and thermally induced decay on various naphthalene derivatives used in this work.

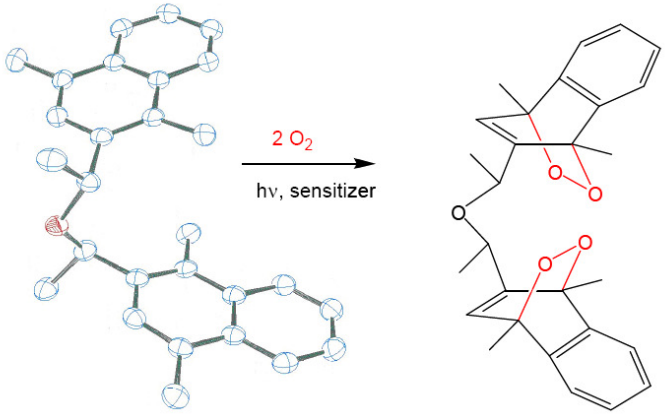

Scheme 4. Endoperoxide formation on the **N5** derivative, witch possesses double endoperoxide-forming (and $^1O_2$-releasing) function in comparison to derivatives in Scheme 3.

Furthermore, **N5E** with a $t_{1/2}$ value of 2.26 h at 37 ºC is closer to the **N1E** value $t_{1/2}$ of 1.19 h than to the **N2E** value $t_{1/2}$ of 16.2 h, which is also in agreement with the literature: energy levels calculation of the endoperoxide stability performed by Wasserman et al. using the Density Functional Theory (DFT) with the B3LYP functional and employing the 6-311G* basis set [31]. Repulsive steric interaction of *ortho* substituents in C1- and C2-position (Fig. 6.1.) of the **N5** derivative is much smaller than *peri* interaction in **N2** derivative (for details see Chapter 6.1.1.) Therefore, comparatively **N5E** formation (*ortho* interaction)

causes much smaller intramolecular strain reduction than **N2E** formation (*peri* interaction). Hence, the endoperoxide stabilization of the **N5E** is smaller than of **N2E** derivative. In this regard, when **N5E** with 2 endoperoxide bridges is formed (see Scheme 4.), apparently the effective side-group in C2-position on naphthyl ring for each of these 2 endoperoxides is only a 1-methoxy-ethyl group without naphthyl rest (for detail perspective see structure on Fig. 4.2., page 61). Thus, there is no significant additional strain by the other naphthyl group in **N5** which would stabilise the endoperoxide molecule and prolong its decay. There is an additional weak dipole-dipole interaction between ethanol solvent molecules and polar 1-methoxy-ethyl substituent of **N5** (C12-C11-O1 group on Fig. 4.2.) and/or endoperoxide bridge, which reduces the **N5E** mobility.

With that in mind, the difference in decay kinetics of **N4E** and **N5E** and their half-life times in ethanol (Table 4.4.) is probably caused by a dipole-dipole interaction of **N4E** and surrounding solvent molecules as well as by a weak H-bonding between ethanol molecules and **N4E** over polar hydroxylethyl substituent of **N4** (C2-C1-O1-H1o group on Fig. 4.1., page 60), which reduces the mobility of **N4E** molecules and thus slows down its decay kinetics.

6.1.4. Influence of Physical Changes of Functional Structure on the Endoperoxide Decay Kinetics

Decay times of **N1E** and **N2E** in liposomes (Table 4.5) are comparable to their decay time values in organic solvents, with SF values close to 1. **N5E** (1.5 h at 37 °C) has again a $t_{1/2}$ value similar to **N1E** (1.1 h at 37 °C) in liposome carrier, but a shorter $t_{1/2}$ than in ethanol, SF = 0.66. Probably this is caused by an increased mobility of endoperoxides in the liposome matrix due to the large hydrophobic aromatic part of the **N5** molecule embedded between the hydrophobic alkyl chains, what would prevent endoperoxide stabilisation by the dipole-dipole interaction with the polar lipid „heads“.Since the decay was measured at 37 °C, above the temperature of liposome phase transition from gel to liquid-crystalline phase, T_c, (24 °C for DMPC lipid used in this work) [157], liposome membranes were in the liquid-crystalline phase with higher membrane permeability and high translational lipid mobility in the lipid bilayer [127], and thus the mobility of embedded endoperoxides was increased.

However, $t_{1/2}$ of **N4E** in liposomes is longer (11.5 h at 37 °C, SF = 2.63) probably because of a much stronger dipole-dipole interaction between the hydroxylethyl substituent of the **N4** molecule (over O1-H1o atoms in Fig. 4.1. page 60) and the polar "heads" of liposomal membrane. The dipole-dipole interaction over the hydroxylethyl side – group attracts **N4** molecules close to the stacked lipid "heads" and is hindering the reverting of the bent endoperoxide molecule to the planar aromatic ring of the parent **N4** molecule, which is necessary for the decay process (Figure 6.1.)

Polymer matrices were explored in order to try to increase the $t_{1/2}$ and SF values in comparison to the values in liposome matrix. Two main polymer matrices used were polyvinyl butyral and ethyl cellulose. Whereas the endoperoxide decay of all 1,4-dimethylnaphthalene derivatives in liposome matrix and organic solvents was monoexponential and with similar $t_{1/2}$ values to literature [22, 31] (the only exception was **N4E** in liposome matrix), the decay in PVB and EC matrices was in a good approximation biexponential. There is a fast-decaying endoperoxide part and a slow-decaying endoperoxide part due to embedding in different functional structures, see Figure 6.2.

A summary of all 1,4-dimethylnaphthalene derivatives endoperoxide $t_{1/2}$ values, endoperoxide half-life times and corresponding endoperoxide percentages are given in Table 6.1. In these data the endoperoxide decay kinetics without any further stabilization due to the physical changes by endoperoxide formation and decay repetition (for detailed explanation see e.g. Chapter 4.3.3.), is presented. **N7** nanoparticles are here treated as a **N1** variation: a polymer with each side-group on the polymer back-bone being a **N1** group. The largest endoperoxide stabilization was in **N7** matrix, with $t_{1/2}$ (1) = 6.8 h, SF (1) = 5.7 and $t_{1/2}$ (2) = 39.7 h, SF (2) = 33.1 values. SF factors were in this case calculated in regard to the **N1E** half-life time in organic solvent. However, the endoperoxide formation yield in **N7** nanoparticles was the lowest: about 45 % after 7h laser irradiation was the highest achieved yield, see Figure 4.34.

Table 6.1. Endoperoxide $t_{1/2}$ values for different 1,4-dimethylnaphthalene derivatives depending on the carrier matrix. Further stabilisation due to the physical changes of the functional structure is not presented. The percentage of formed endoperoxides decaying as FDE and SDE, when applicable, is given in parenthesis.

	N1	**N5**	**N4**	**N2**
organic solvents	1.2 h	2.3 h	4.4 h	16.2 h
lipsomes	1.1 h	1.5 h	11.5 h	17.1 h
PVB film	1.7 h (30%); 7.3 h (12%)	6.0 h	4.4 h (8%); 26.6h (16%)	6.4 h (8%); 19.4h (18%)
PVB nanobeads	0.8 h (75%); 1.6h (13%); 5.8h (5%)	2.0 h (45 %); 2.65 h (20%)	7.5 h (30%); 13 h (25%)	18.7 h (20%)
EC nanoparticles	/	/	0.7 h (20%); 9.6 h (14%)	/
N7 nanoparticles	6.8h (10%); 39.7 h (12%)			

A possible explanation of shorter endoperoxide half-life times in certain matrices (e.g. **N2** in PVB film, **N4** in EC particles) than in organic solvents would be the reduction of strain caused by *peri* interaction in functional structures with large local free volume regions.

In case of **N4E** in PVB and EC nanoparticles the interaction between the endoperoxide molecule and its immediate surrounding of the matrix is significantly changed chemically: a polar hydroxylethyl side-group on **N4** molecule causes weak H-bonding to the polar groups of the PVB and EC matrices, as discussed above. Thus, **N4E** mobility is reduced and $t_{1/2}$ of the FDE in PVB nanoparticles is significantly longer than $t_{1/2}$ of **N1E** in the same matrix. The same weak H-bonding interaction with EC matrix causes longer $t_{1/2}$ of **N4E** than of **N5E** in EC nanoparticles under the same nanoparticle and endoperoxide formation conditions (compare Figure 4.28. and Figure 4.29.)

FDE and SDE half-life times of all examined naphthalene derivatives in PVB film are given in the Table 4.6. Existence of functional structures with small free volume in the PVB film caused SDE decay and thus endoperoxide stabilization with SF values of about 6 for **N1E** and **N4E** derivatives. **N2E** decay in PVB film at 37 °C was actually too slow to reach SDE region during the experiment period: in total only 26 % of formed **N2E** actually decayed during the measurement. Probably SDE population of **N2E** in the PVB film decays with even longer $t_{1/2}$ values. However, such phenomena were only investigated at higher decay temperatures of 46 °C (see Figure 4.16.) and 56 °C. On the other hand, **N5E** derivative in PVB film matrix decays monoexponentially, with only the SDE component. FDE component is not present due to the low mobility of the larger **N5** molecule in PVB matrix.

Unfortunately, the loading efficiency of PVB nanobeads with 1,4-dimethylnaphthalene derivatives was rather low. Probably most of the loaded endoperoxide-forming molecules remained on, or close to the nanobead surface. The high FDE percentage of all **N1** derivatives with SF values around 1 (see Table 4.14.) can be explained by large regions of local free volume in the matrix. However, it was possible to repeatedly use the PVB nanobead formulations in endoperoxide decay examinations: with the method of successive repetition of light-induced endoperoxide formation and subsequent thermal decay a regular prolongation of both FDE and SDE $t_{1/2}$ values and an increase of SDE relative amount in the PVB matrix, both in PVB film and in PVB nanobeads (see Figs. 4.17. and 4.22. and Tables 4.7. and 4.15., respectively), was achieved. This can be explained by the physical changes of the functional structures consisting of endoperoxide molecules and immediate neighborhood of the polymer matrix forming the cage wall. During the decay process complete rearrangement of the electronic and geometrical structures of the involved endoperoxide molecule occurs (see Fig. 6.1.) Geometrical rearrangement concerns e.g. the endoperoxide reverting to the planar parent molecule. The mentioned electronic and geometrical rearrangements create localized vibrational excitations. The relaxation of these excitations corresponds to an ultra short local heating, which can provide a physical change of the functional structure. Such changes include modification of the cage wall, and therefore, changes of the regions of localized free volume in the matrix. According to the common features of the polymer preparation procedures of the polymer film and the polymer nanoparticles in both cases there is a large local free volume in the functional structures (see above) corresponding to a localized non-equilibrium state. The changes of the polymer matrix cage wall result in a reduction of localized free volume, and, thus in a decay time

prolongation of both FDE and SDE population. Moreover, a variation in the statistical distribution of the functional structures (see above) occurs, i. e. the whole decay kinetics is influenced, adjusted. The large local free volume was reduced by letting a decay process occur as a part of the sample preparation procedure. The physical changes of the functional structures were accomplished either

1. by stepwise separate processes of endoperoxide formation and subsequent (thermally induced) decay during the preparation (as described above), or

2. by a continuous process of the formation and superimposed decay during a very long time (e.g. in experiments with 16h irradiation time in the EC matrix, Figure 4.28.)

Furthermore, a decay time increase of **N1E** by more than a factor of 30, compared to the $t_{1/2}$ value in organic solvents could be achieved by physical changes of the functional structure in polymers.

EC nanoparticles loaded with **N1** or **N2** could not be produced. **N5E** and **N4E** decay in EC nanoparticles was also biexponential. The FDE relative amount was significantly smaller and SDE amount significantly larger in comparison to the PVB carrier matrix. When **N4E** was formed in EC nanoparticles with a short (t = 1.5 h) light irradiation of MB sensitizer (see Figure 4.27.), the small FDE part had $t_{1/2}$ = 0.7 h, probably due to large free volume effect, and larger SDE part had $t_{1/2}$ = 9.6 h. A long irradiation time enabled significant stabilisation of both FDE ($t_{1/2}$ value increase from 0.7 h to 8.5 h) and SDE ($t_{1/2}$ value increase from 9.6 h to 24.6 h) of **N4E** derivative in the EC matrix (compare Fig. 4.27. with irradiation time of 1.5 h and Fig. 4.28. with irradiation time of 16 h). The same principle was applied on **N5** in EC matrix: after 16 h laser irradiation endoperoxide yield was very high (92 %) with stabilized both FDE and SDE (Fig. 4.29.) Thus, the goal of $t_{1/2}$ endoperoxide values adjustment to > 15 h for the *in vitro* application against cancer cells was reached.

Such longer $t_{1/2}$ of **N4E** in PVB and EC nanoparticles can be even more prolonged with additional (physical) changes of the functional structure in PVB matrix (Fig. 4.22.) and EC matrix (Figs. 4.28. and 4.29.)

6.1.5. Summary of Endoperoxide Decay Kinetics Adjustment

To sum up, varying of the endoperoxide decay-time and thus $^1O_2$-release time at 37 °C in a broad range was achieved chemically, by synthesis of **N4** and **N5** endoperoxide-forming molecules, as well as with polymer **N7** synthesis, in which each monomer on the polymer back-bone has an endoperoxide-forming group. In case of **N7** the highest $t_{1/2}$ value was reached. Moreover, by choosing matrices with various interactions with endoperoxides (e. g. steric hindrance, hydrogen bonding with **N4** compound), variations of $t_{1/2}$ values of synthesized and comercially available endoperoxide-forming molecules were achieved. The decisive adjustment of $t_{1/2}$ values and relative amounts of FDE and SDE population in these matrices was made with physical changes by endoperoxide formation and decay cycles or by the continuous procedure as described above for EC matrix. The highlight of such $^1O_2$-release time adjustment in a broad range is the example of **N1E** derivative in PVB film matrix: with $t_{1/2}$ values from 1.5 h to 38.2 h and SF = 31.8 in 2nd cycle (see Table 4.7.) Even an additional enhancement of the endoperoxide stabilization is reachable by performing further cycles of sample irradiation and thermolysis, as shown for **N1E** decay in PVB film matrix at 56 °C (Figure 4.17.) The SDE **N1E** $t_{1/2}$ values at 37 °C after 3rd cycle can then be roughly estimated to be in 50-60 hours range. Thus, by such a prolongation of $^1O_2$-release, the potential pharmaceutical applications of the **N1** biocompatible parent molecule, as described in Chapter 2 [107, 108] are more numerous.

6.2. DISCUSSION OF THE CYTOTOXICITY ASSAY RESULTS OF ENDOPEROXIDE-LOADED NANOPARTICLES ON HUMAN BREAST CANCER CELLS

In this work the concept of a novel $^1O_2$-release procedure for potential pharmaceutical applications, based on the photodynamic therapy is presented. The main difference is the introduction of an intermediate step of $^1O_2$-„storage“ in the endoperoxide form and then delayed adjustable release. Hence, the patient would not be directly irradiated with light, as in the classical photodynamic therapy, but the irradiation of the sensitizer and endoperoxide formation would be performed externally, and thus, would not be dependent on the oxygen concentration at the target (in tissue, cells). Such an endoperoxide would then be delivered in a biocompatible carrier to the body region of interest and then the effective $^1O_2$ would be released. Thus, the application range of such a therapy would be much broader than of classical PDT, which is restricted to diseases within the light penetration depth, see Chapter 1.3.5. Furthermore, within this concept it would be possible to extract the sensitizer (e.g. methylene blue) after the light irradiation and prior to the drug delivery to the patient. This would also remove the problem of patient sunlight sensitivity after the PDT procedure when the sensitizer is not quickly cleared from the body.

Obviously, the adjustment of $^1O_2$-release periods to the particular therapeutic demands is here of a crucial interest. Appropriate biocompatible carries for drug-delivery and selective delivery restricted to diseased tissue are two additional aspects which must be adressed. The latter two challenges are also a hot topic in the PDT field, trying to increase the PDT therapeutic options range through development of delivery systems for hydrophobic sensitizers [82].

In order to exploit the cytotoxicity of $^1O_2$-release by the aromatic endoperoxides, several factors (requirements) have to be taken into account: $^1O_2$-lifetime and diffusion radius in water/cell medium, $^1O_2$-release time which equals the endoperoxide decay time, endoperoxide‘s $^1O_2$ yield, endoperoxide‘s carrier material drug-delivery potential, including cell-uptake time, carrier loading with a high-concentration of endoperoxide-forming “parent molecule”, endoperoxide-formation yield in the carrier matrix.

$^1O_2$-lifetime data in water, blood plasma and leukemia cells are known [3], see Table 1.1. Skovsen et al. calculated a $^1O_2$-diffusion radius of 268 nm with a $\tau(^1O_2)$ = 3 μs [6] in a single D_2O-incubated nerve cell, which is a rather controversial topic, as stated in Chapter 1.1.2., see references [6, 7] On the other hand, other reports point to 0.3 μm diffusion length of singlet oxygen in cellular membranes [158], with a possibility of $\tau(^1O_2)$, and thus, diffusion radius, increase up to 7 times in case of high *Staphylococcus aureus* bacteria concentration [159]. Therefore, at the time-point of $^1O_2$-release, the carrier loaded with endoperoxides should be either in cells, or in cell membrane, with the carrier diameter at least ≤ 200 nm in order to $^1O_2$ be able to diffuse out of carrier and be effective.

$^1O_2$ yield of **N1E** and **N2E** is in the 69-76 % range [22], and the rest is than lost as pharmaceutically inactive $^3O_2$. Presumably, endoperoxides of **N4** and **N5** derivatives have similar $^1O_2$ yield values, which should be experimentally confirmed in the future work.

Obviously, it is crucial that the endoperoxide half-life $t_{1/2,}$ in a particular carrier, is much longer than the carrier cell-uptake time, $t_{u,}$ so that as few as possible endoperoxide molecules release $^1O_2$ prior to the cell-uptake. How long should $t_{1/2}$ precisely be depends on the particular pharmaceutical application: cancer therapy, antimicrobial treatment etc. On the other hand, the $^1O_2$-release time should not be too long: there have to be a high enough local concentrations of $^1O_2$ in an interval of a few hours in order to induce a strong enough cell-damage which would cause cell death by apoptosis or necrosis. $^1O_2$-release in mitochondria or nucleus is likely to induce apoptosis and release in the plasma membrane is likely to cause necrosis [46]. A too low $^1O_2$ concentration would cause only moderate cell damage and trigger cellular repair mechanisms. Additionally, after some time (estimated 1-2 days) the carrier materials land in lysosomes, as shown for liposome carrier with CLSM images [160] where $^1O_2$ can no longer be effective. The threshold value of necessary intracellular $^1O_2$ concentration for a photodynamic therapy modification, as done in this work, is rather difficult to estimate, because of all the factors mentioned above. Thus, the appropriate $^1O_2$-releasing endoperoxide/carrier concentration combination is rather empirical and can not be precisely stated as in the classical drug pharmacology.

What can be measured is the endoperoxide-forming molecule concentration, its carrier concentration and, if applied, coating material concentration. The concentration of formed endoperoxide is than determined (spectroscopically: with absorption or fluorescence intensity

change of "parent molecule") immediately after the light irradiation of the sensitizer. If the endoperoxide yield is low, the following options should be considered: longer irradiation and/or stronger light intensity and/or higher photosensitizer concentration.

With this in mind, the kinetic chemosensitivity assay results are shortly reviewed:

6.2.1. Limitations of Carrier Loading and Cytotoxicity

When liposomes or PVB nanobeads or poly(1,4-dimethyl-2-vinyl-1,4-dimethylnaphthalene) (N7) nanoparticles were used as endoperoxide carriers, several problems regarding carrier loading ability and/or carrier *in vitro* cytotoxicity occurred.

6.2.1.1. Cytotoxicity of Endoperoxide-Loaded Liposomes

N1E $t_{1/2}$ value was too short, but **N4E** and **N2E** both had a $t_{1/2}$ value longer than t_u (estimated at 0.5-1.0 h) of the liposome carrier. Conventional non-coated liposomes, a familiar biocompatible carrier used for cancer targeting, because of the enhanced permeability and retention (EPR) effect [136], and for intracellular drug delivery [132, 161] were the first-choice carrier. The highest reached **N2E** doping concentration of 6.3 μM in unmodified liposomes, c (lipid) = 20 μM made a cytotoxic effect on MDA-MB-231 human breast cancer cells growth. For a desired cytostatic effect, an endoperoxide concentration of 10 μM or higher is probably necessary. This was not reachable without increasing the liposome concentration in such a manner that even the unloaded liposomes inhibited the cell growth. With such a tightly packed naphthalene derivatives in liposomes, possibly naphthalene dimers are formed which would have an unknown effect on the endoperoxide-formation and $^1O_2$-release dynamic. **N4E** in liposome concentration increase in comparison to the loaded **N2E** concentration was probably negated by a shorter $t_{1/2}$ value and therefore faster endoperoxide decay and $^1O_2$ loss prior to the liposomes' cellular uptake.

6.2.1.2. PVB Nanobeads Low Endoperoxide Loading Ability

Spherical nanoparticles of PVB polymer were formed. PVB nanobeads were developed as a potential biocompatible carrier: non-coated PVB nanobeads with diameter smaller than 300 nm were capable of cell penetration and reached the perinuclear region within a few hours, as determined with CLSM. As shown on Figure 4.21. PVB nanobeads may be employed at concentrations at least one order of magnitude higher than liposomes' cytotoxic concentration for intracellular drug-delivery purposes. It is also conceivable, that PVB nanobeads could enable passive cancer targeting through the EPR effect, which is applicable for any biocompatible macromolecular compounds above 40 kDa [162], but this needs to be tested. Dopants, such as PTC may also be included into PVB nanospheres at concentrations of at least one percent with respect to the polymer, which enables PVB nanobeads use as an excellent imaging agent, and not only as a biocompatible carrier.

Decay times of both **N2E** and **N4E** in PVB nanobeads were significantly longer (see Table 4.14.) than the PVB nanoparticles t_u range. Thus, **N2E** and **N4E** in PVB nanobeads were conceivably usable for the cancer cell therapy, as imagined in this project. However, PVB nanospheres could not be loaded, at least not with the precipitation method and subsequent post-concentration by centrifugation as employed in this work, with a high enough 1,4-dimethylnaphthalene derivative concentration in order to cause a significant cytotoxic effect due to $^1O_2$-release during the endoperoxide decay. Possibly loading with a high enough concentration could be reached with some high-pressure preparation procedure [163].

6.2.1.3. Cytotoxicity of **N7** Particles

Synthesized **N7** nanoparticles had the highest endoperoxide-forming groups concentration of all derivatives used in this work. However, above a certain treshohld concentration (depending on the particle size, see Figure 4.36.) **N7** particles without any endoperoxide formation had an antiproliferative effect on MDA-MB-231 cells growth. This rendered a use of **N7E** in too low of a concentration (also due to the low endoperoxide formation yield, ≤ 40 %) in cytotoxicity assays to have any inhibitory effect on the breast

cancer cells growth. Thus, our results are to the contrary of Käsermann and Kempf work in which they used endoperoxides of poly(1,4-dimethyl-6-vinyl-1,4-dimethylnaphthalene) for inactivation of two viruses, Semliki Forest virus and vesicular stomatitis virus [149]. Furthermore, their endoperoxide formation yield was ≥ 90 % using the methylene blue sensitizer and the endoperoxide half-life time was short, in the 40 min range at 37 °C [149].

The mechanism of the **N7** particles interaction with cancer cells causing cell growth inhibition remains unknown. Further investigations should be performed, to determine whether **N7** nanoparticles, with or without polysorbate 80™-coating, indeed penetrate into cells or not. A stable fluorescent labeling of the **N7** nanoparticles would provide a major advantage for monitoring a potential cellular uptake *in vitro*, and consequently elucidate the mechanism of possible nanoparticle drug delivery.

6.2.2. Problem Solution: Cytotostatic Effect of Endoperoxide-Loaded EC Nanoparticles and General Demands of the Endoperoxide Concentration

In contrast to the PVB nanobeads, non-coated EC nanoparticles were excluded from MDA-MB-231 cancer cells. Only polysorbate80-coated EC nanoparticles were a suitable potential drug delivery carrier, with t_u < 2 h, as determined with CLSM. However, the loading capacity of the EC nanoparticles was for about 2 orders of magnitude higher than of PVB nanobeads. Moreover, by means of a long irradiation it was possible to stabilize the endoperoxides of **N4** and **N5** (see Figs. 4.28. and 4.29., respectively) and reduce the FDE percentage, in order to keep the percentage of extracellularly released $^1O_2$ (due to the endoperoxide decay prior to the intracellular delivery of EC nanoparticles) low. It can be roughly estimated that only 10-15 % of **N4E** and 20-30 % of **N5E** in EC particles are not delivered, but decay extracellularly. On top of that, from cytostatic concentrations of **N4E** and **N5E** (Figs. 4.32. and 4.33.), it can be fairly estimated that on **N5** derivative a 2 times higher number of singlet oxygen binding sites is present. These sites may not release $^1O_2$ simultaneously, but rather depending on the free volume in carrier matrix present in the immediate vicinity of 2 endoperoxide bridges. Nevertheless, a concentration of intramolecular $^1O_2$-releasing sites is in case of **N5** twice larger than for other 1,4-

dimethylnaphthalene derivatives, which lowers the necessary **N5E** concentration for a positive therapeutic effect.

Thus, it can be stated that generally, a ca. 15 μM concentration of endoperoxide groups in the system will generate a cytostatic drug effect on the growth of MDA-MB-231 cells with conditions used in this work (average carrier diameter 50-100 nm, t_u = 2-3 h, $t_{1/2}$ > 10 h).

However, tests regarding the reproducibility of loading the EC particles with **N4** and **N5** showed inconsistencies regarding the doping efficiency. Hence, it seems to be difficult to keep the ratio dopant/EC particle constant. Practically, this causes a need to vary the EC w/w concentration to keep the **N4** or **N5** concentration constant for cytotoxicity assays. During the EC nanoparticles formation crystalline (up to 48 %) and amorphous regions of ethyl cellulose on the nanometer scale are formed [164, 165]. 1,4-dimethylnaphthalene derivatives are loaded only in amorphous regions of EC nanoparticles. Additionally, the nanocrystalline regions cause EC aggregation, nanocluster formation (in 200-400 nm range as determined with DLS and TEM) and after a week a strong aging effect of EC nanoparticles with an inclination towards precipitation, crystallization out of the aqueous suspension is present. Therefore, it is difficult to estimate the optimal polysorbate 80™ coating concentration for adsorption on EC particles carrier. It was found that free, not adsorbed on the EC surface, polysorbate80™ and non-coated EC nanoparticles both cause inhibitory effects on MDA-MB-231 cells proliferation. Therefore, extensive and careful preparation optimization regarding the EC particles loading and coating parameters is necessary. The goals would be to reach as high a dopant/EC particle ratio as possible, as low EC cluster building and optimal coating (monolayer, if possible) on the EC carrier surface.

6.3. OUTLOOK

The procedure as designed here could be used for tumour therapy, as done in this work *in vitro*, and furthermore $^1O_2$-release from thin polymer films (e.g. PVB) could be tried out as an anti-infectional protection layer after medical implants surgeries, where until now, amongst others, polymer films with antibiotics are used [166], e. g. for knee, hip and dental implants. Beside antibiotics, in literature also the PDT use for the bacteria inactivation is mentioned [167], including the multiresistant bacteria, such as *Staphylococcus aureus*, as reported for classical PDT procedure [168]. A possible anti-bacterial use of the $^1O_2$-releasing polymer film would be two-fold: FDE population could be applied against bacteria during the implantation procedure and SDE population could be used against bacteria colonies settling on the implants after surgery.

A possible solution for problems regarding carrier cytotoxicity and loading ability for the tumour therapy application (as stated in Chapter 6.2.1.) would be to covalently bind a 1,4-dimethylnaphthalene derivative to PVB polymer (see Scheme 7. in Appendix) and then form nanoparticles of such a polymer. This covalent binding would resolve the problem of loading the PVB nanoparticles with a high enough 1,4-dimethylnaphthalene derivative concentration because each alcohol group in PVB structure would have a covalently bound endoperoxide-forming 1,4-dimethylnaphthalene side-group. Hence, the concentration of $^1O_2$-releasing group would be large enough for a possible cytostatic effect (necessary concentration estimated > 15 µM, see previous page) and such nanoparticles would conceivably employ all the advantageous properties of PVB nanobeads: amorphous structure, non-cytotoxicity, cellular permeability without coating, formation reproducibility, neglegible aging effect.

In addition, PVB polymer films could be perceivably used for surface coating of magnetic nanoparticles, which are also used in local hyperthermia (up to 45 °C) treatment [138] and are now also considered as promising agents for drug delivery into regional lymph nodes and for diagnostic imaging purposes [132]. It would be possible to load a 100 nm thin PVB film with a very high concentration (up to mM range) of 1,4-dimethylnaphthalene derivatives, with an endoperoxide-formation yield in 80-90 % range after 45 min LED irradiation and to adjust the $^1O_2$-release time in a broad range by means of endoperoxide

formation and decay cycle repetition, see Figure 4.17. Thus, $t_{1/2}$ could be adjusted in such a manner that a large portion of endoperoxides would be stable enough at the human body temperature of 37 °C (during magnetic nanoparticles transfer to tumour region) and then would preferentially release $^1O_2$ in the tumour region when magnetic nanoparticles reach higher temperatures in the alternating magnetic field.

Another advantageous possibility for the cancer therapy application would be to grow **N1**- or **N2**-doped polymer onto the mesoporous silica particles by hyperbranching surface polymerization procedure [169]. Such a hybrid poly(ethylene imine)-silica nanoparticles are taken up to HeLa cervical cancer cells by the receptor-mediated endocytosis followed by accumulation in endosomes and cargo-release into the cytoplasm [169]. In general, the surface adsorption of **N1** derivatives on inorganic nanoparticles used in pharmaceutical applications, such as γ-Al_2O_3, could be tried out.

Conceivably, other carrier materials (already under development for PDT drug delivery purposes) could be tested for loading with, and drug delivery of endoperoxides used in this work. For example, PEGylated gelatin nanoparticles [170] with long blood circulation and preferential tumour distribution properties could be tested. Another possibilities worth exploring would be biodegradable nanoparticle carriers such as FDA approved [171], biocompatible, amorphous stereoisomer of poly(D,L-lactide) (PLA) [172] or biodegradable poly(D,L-lactide-co-glycolide) nanoparticles [173, 174, 175] with various copolymer ratios, which are both used for *in vitro* delivery of various sensitizers. For the purpose of drug encapsulation, the use of amorphous PLA is preferred over the semi-crystalline PLLA and PDLA isomers [176] as it enables more homogeneous dispersion of the drug in the polymer matrix.

The use of other established drug-delivery polymer nanoparticles such as poly(butylcyanoacrylate) (PBCA) nanoparticles could be also tried out. Moreover, non-biodegradable ceramic-based nanoparticles with great stability, easily functionalized surface and size, shape, and porosity control [177] are worth exploring for non-covalent doping, as well.

7. SUMMARY

The decay kinetics of aromatic endoperoxide molecules embedded in carrier matrices (liposomes, polymer films and nanoparticles) was studied to provide a method for the adjustment of the thermally induced release time of singlet oxygen ($^1O_2$) to the requirements of possible pharmaceutical applications.

Excitation of a sensitizer with a laser or LED generated $^1O_2$, which reacted with aromatic molecules (1,4-dimethylnaphthalene and its derivatives) forming endoperoxides. The decay of these photoproducts enabled the delayed release of $^1O_2$. Some of the endoperoxide-forming molecules, such as 1-(1,4-dimethyl-naphthalen-2-yl)-ethanol (**N4**), di-1-(1,4-dimethylnaphthene-2-yl)-ethylether (**N5**), and poly(1,4-dimethyl-2-vinylnaphthalene (**N7),** were synthesized and characterized, while others were commercially available: 1,4-dimethylnaphthalene (**N1**) and 1,4,5-trimethylnaphthalene (**N2**). In addition, multichromophore molecules such as 5,10,15,20-tetrakis-(4-methylnaphthyl)porphyrin) (**P1**) and (5,10,15,20-tetrakis-(4-methyl-naphthyl)porphyrinato-zinc(II) (**P2**), acting as sensitizers and forming endoperoxides in their peripheral naphthyl subunits (**N1** derivatives) by autoperoxidation, were synthesized and characterized. $^1O_2$ generation and endoperoxide decay by the compounds **P1** and **P2** were also studied.

The **N1** derivatives were embedded in several different carrier systems: biocompatible liposomes or polymer materials such as nanoparticles of ethyl cellulose (EC) and polyvinyl butyrale (PVB) and PVB films. The sensitizer (porphyrin derivatives) was embedded in the carrier, as well. Only one sensitizer (methylene blue) was separately dissolved in aqueous carrier suspension, thus composing in both cases multichromophore systems. The average diameter of nanoparticles, as determined by dynamic light scattering and/or transmission electron microscopy, was in the 50-150 nm range.

Endoperoxide formation in the selected matrix could be determined by the time-dependent decrease of fluorescence intensity in the course of the irradiation, because the endoperoxides are non-absorbing at the excitation wavelength of the original aromatic molecule. Moreover, the reappearance of the fluorescence signal (of the “parent molecule”) enabled the measurement of the decay of the endoperoxides. The decay kinetics of the endoperoxides (**N1E, N2E, N4E, N5E, N7E**) was examined at different temperatures (with emphasis on the human body temperature of 37°C) in the various carrier materials.

For the experiments with cancer therapy application the decay time had to be adjusted to be significantly longer than the average time period of cellular uptake t_u, (determined with confocal microscopy) for the particular carrier. The basis for the adjustment of the decay kinetics is the structural change by reverting of the bent 1,4-cyclohexadiene moiety of the endoperoxide to the planar, "parent molecule". The decay kinetics is generally determined by the distribution of the (supramolecular) functional structures consisting of the endoperoxide molecule and the immediate neighbourhood of the surrounding carrier matrix. The endoperoxide decay time, $t_{1/2}$, was adjusted by chemical and/or physical modifications of the functional structure. Chemical changes were the introduction of various substituents (e.g. 1-hydroxyethyl), whereby the endoperoxide mobility was reduced (e.g. by H-bonding to the matrix). Physical changes, in particular a reduction of the large local free volume regions in the functional structures, were obtained for both types of sample preparation (i. e. polymer films and nanoparticles). These large local free volume regions occur in both types due to a common feature in the sample preparation procedures. This reduction was obtained by letting an endoperoxide decay process occur as a part of the sample preparation procedure. The reduction of the local free volume was performed either

- by stepwise separate processes of endoperoxide formation and subsequent (thermally induced) decay during the preparation, or

- by a continuous process of the formation and superimposed decay during a very long irradiation time.

A prolongation of the decay time up to a factor of 30 (in comparison to $t_{1/2}$ in organic solvents) could be achieved in both cases.

The kinetic crystal violet assay was used to determine the *in vitro* cytotoxicity of the endoperoxides in above mentioned carriers against human breast cancer cells (MDA-MB-231) at 37 °C. On the basis of the results obtained with **N4E** and **N5E** it can be concluded that a ca. 15 µM concentration of endoperoxide groups results in a cytostatic effect on MDA-MB-231 cells growth.

The role of the decay adjustment for various possible applications such as cancer therapy or anti-microbial treatment is discussed.

A. APPENDIX: COVALENT BINDING OF **N4** DERIVATIVE TO THE PVB POLYMER BACKBONE

A.1. Motivation

Due to the problems regarding carrier cytotoxicity (liposomes, EC nanoparticles, **N7** nanoparticles) and loading ability (not high enough concentration of 1,4-dimethylnaphthalene derivatives in liposomes, PVB nanobeads), a possibility to covalently bind a 1,4-dimethylnaphthalene derivative to a nanoparticle-forming polymer was searched for. This would also enable to reach a very high concentration of endoperoxide-forming groups in the polymer carrier. Practically it would be possible to use a high polymer (and endoperoxide group) concentration up to the cytotoxic threshold value of the particular polymer carrier. Furthermore, the endoperoxide decay and $^1O_2$-release time would thus be prolonged according to the demands of *in vitro* application on the cancer cells.

The PVB polymer was aimed at because of high PVB nanobeads formation reproducibility, low aging effect, non-cytotoxicity, and cellular uptake of non-coated PVB nanobeads in a relatively short time-frame (about 2-3 h, see Fig. 4.20.) Thus, binding of 1-(1,4-dimethyl-naphthalen-2-yl)-ethanol (**N4**) to hydroxyl groups of the PVB polymer using the dicyclohexylcarbodiimide (DCC)-method [178, 179] was performed.

A.2. Experimental

Materials:

LP B 16H polyvinyl butyral (PVB) powder was from Kuraray Specialities Europe GmbH, Frankfurt, Germany. Solvents ethyl acetate, hexane, dichloromethane were purchased from Sigma-Aldrich, Munich, Germany. Succinic anhydride (SAH), dicyclohexylcarbodiimide (DCC), and N,N-dimethylaminopyridine (DMAP) were also from Sigma-Aldrich, Munich, Germany.

UV-Vis absorption spectra were recorded with a Varian Cary 300 Bio UV/Vis Spectrometer with a 1-cm quartz cell (Hellma GmbH & Co. KG, Müllheim, Germany) and Uvasol® quality solvents from Sigma-Aldrich (Munich, Germany).

^{1}H-NMR measurements were carried out by the Centre for Chemical Analysis of the Faculty of Chemistry and Pharmacy of the University of Regensburg.

FTIR spectra were recorded with a Jasco (Tokyo, Japan) FTIR-610 using a ZnSe-ATR device of Pike Technologies (Madison, USA).

Synthesis:

Step 1: 1.5 g of LP B 16H PVB powder (6.14 mmol of PVB OH-groups) was dissolved in 120 ml of ethyl acetate at b.p. (with reflux) and stirred for 1 hour. 6.14 mmol (0.614 g) of succinic anhydride was dissolved in 70 ml of ethyl acetate using an ultrasonic bath for 5 minutes, and added to the PVB solution. This mixture was stirred over night at ethyl acetate b.p. of 77 °C (with reflux) and later cooled slowly to room temperature (RT). Hexane was added to the mixture until a white suspension appeared. The suspension was filtrated leaving a white product (PVB-SAH). Product characterization was done with ^{1}H NMR, FTIR and UV absorption.

Step 2: 187 mg of PVB-SAH was dissolved in 5 ml of dichloromethane, to which DCC (158 mg, 0.767 mmol), DMAP (6.25 mg, 0.0511 mmol), and finally, **N4** derivative (104.5 mg, 0.767 mmol) were added. The mixture was vigorously stirred at RT for 72 h. Hexane was added until white DCC-urea precipitated. The solution was filtrated and hexane evaporated until a white oily product (PVB-N4) remained. Product characterization was done with ^{1}H NMR, FTIR and UV absorption.

A.3. Results

The binding of **N4** derivative to the hydroxyl group of the PVB polymer was done according to Scheme 7 by transforming the hydroxyl group of PVB to a carboxylic acid

(PVB-SAH) using succinic anhydride and then acid esterification with **N4** alcohol with the DCC-activation method [178, 179].

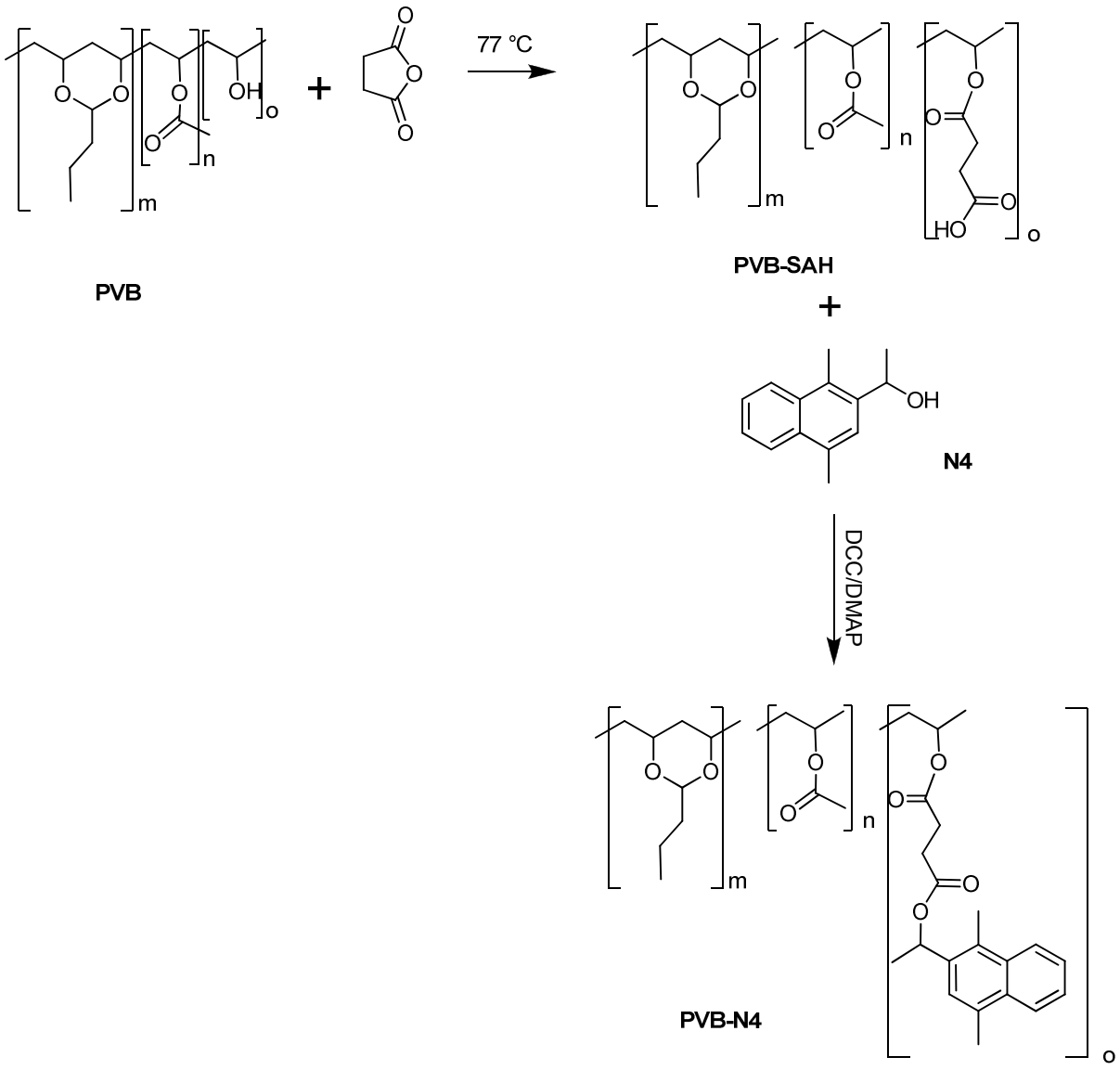

Scheme 7. Binding **N4** to the PVB backbone using the DCC-method.

On following Figs. the comparative characterization of PVB-N4 product, PVB-SAH intermediate product and PVB polymer educt with ^{1}H-NMR (Fig. A.1), UV-Vis (Fig. A.2), and FTIR (Fig. A.3) is shown.

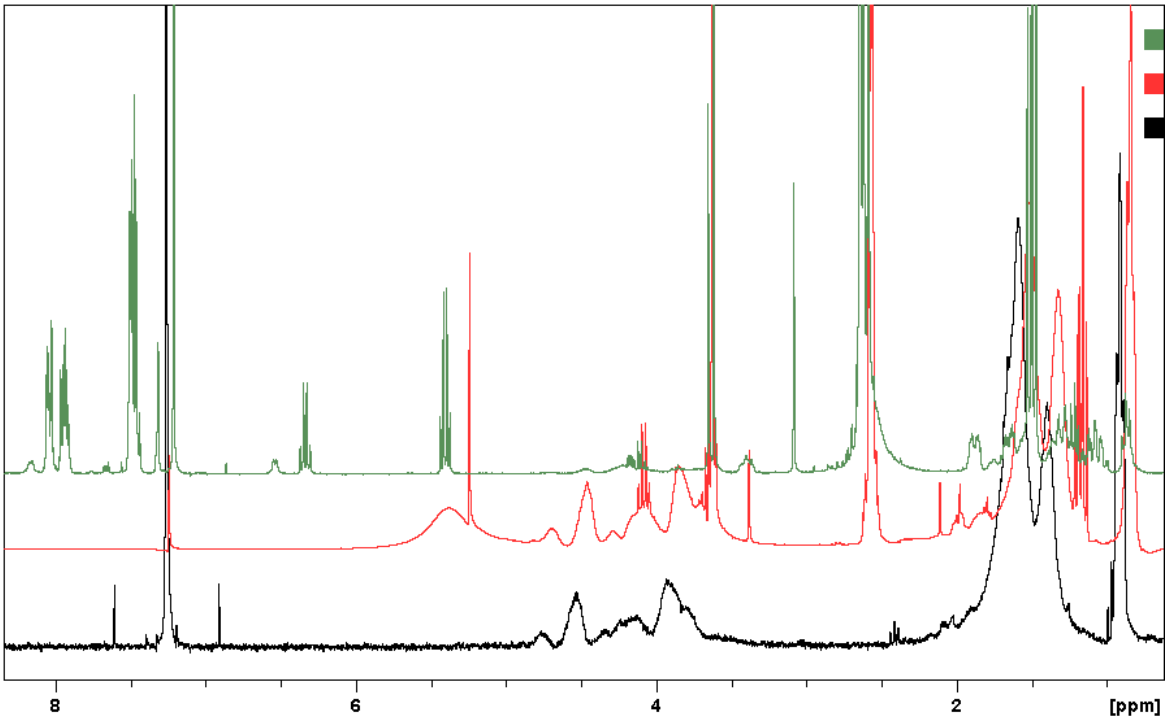

Figure A.1. ^{1}H NMR spectra in $CDCl_3$ demonstrating the PVB (black line) reaction with succinic anhydride to give PVB-SAH (red line) intermediate and esterification with **N4** to give PVB-N4 product (green line).

After the step 1 reaction from the PVB polymer (Fig. A.1. black line) PVB-SAH intermediate product was formed with a strong peak at 2.6 ppm corresponding to CH_2 protons between the ester and carboxylic acid group (Fig. A.1. red line). Upon step 2 reaction PVB-N4 product with characteristic aromatic ^{1}H NMR peaks in 7.2-8.1 ppm region (Fig. A.1. green line) in $CDCl_3$ appeared.

The UV-absorption spectra of the same polymers: PVB (dashed line), PVB-SAH (dotted line) and PVB-N4 (solid line) are shown on Fig. A.2. Clearly, in case of PVB-N4 absorption peaks typical for 1,4-dimethylnaphthalene derivatives (compare Fig. 4.5.) appear, hinting at successful binding of **N4** to the PVB backbone.

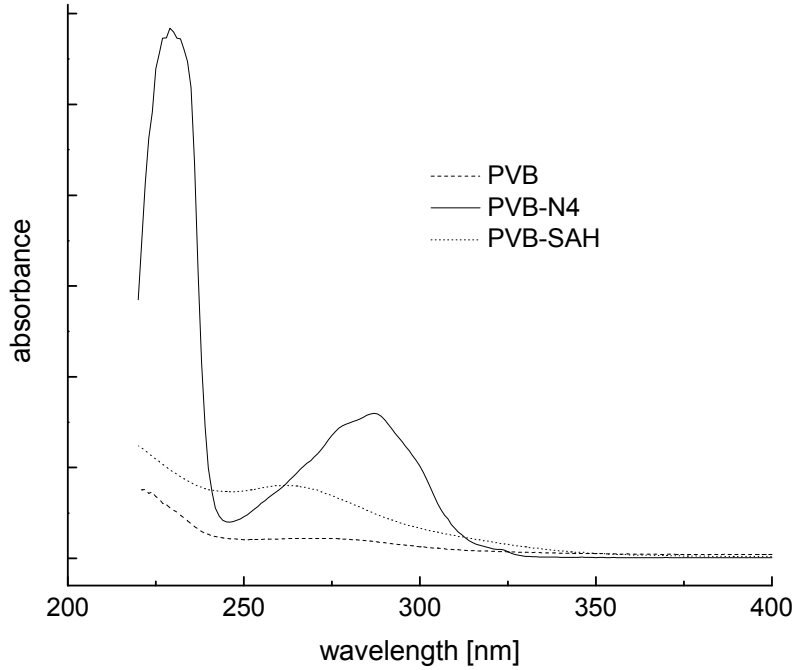

Figure A.2. UV-absorption spectra of PVB educt, PVB-SAH intermediate and PVB-N4 product in methanol, with appearance of typical naphthalene derivative's peaks at about 230, 290nm.

Furthermore, the FTIR spectra of PVB (dashed line, Fig. A.3.) PVB-SAH (dotted line, Fig. A.3.) and PVB-N4 (solid line, Fig. A.3.) similarly demonstrate the reaction on Scheme 7.

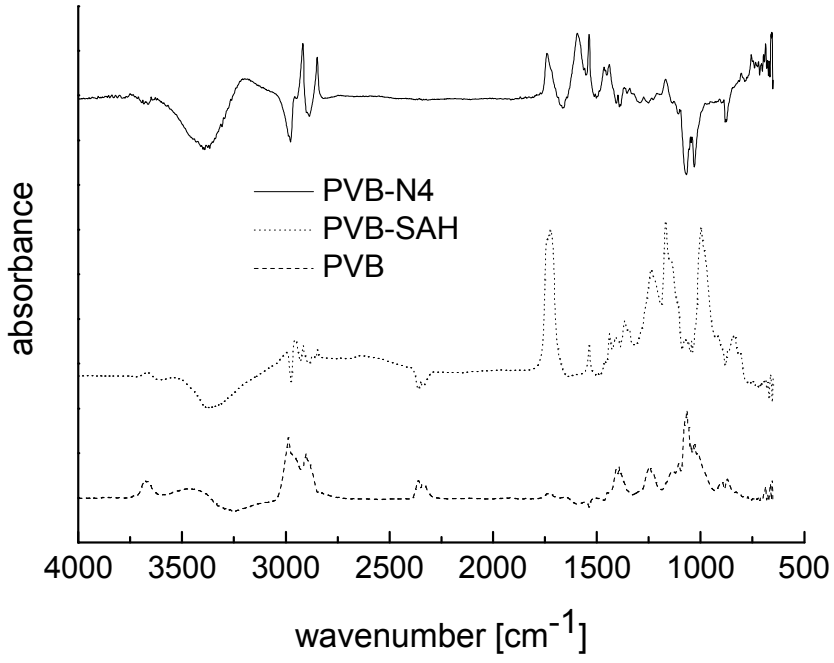

Figure A.3. FTIR absorption spectra of PVB educt, PVB-SAH intermediate and PVB-N4 product in ethanol. Ethanol solvent spectrum was used as a reference.

The characteristic carbonyl stretching band at 1778 cm^{-1} [180] appears in the PVB-SAH and PVB-N4 FTIR spectra and is not present in the PVB spectrum on Fig. A.3. The negative peaks appearing in the PVB-SAH and PVB-N4 FTIR spectra on Fig. A.3. most probably appear due to lower ethanol solvent concentration: the peak at 3388 cm^{-1} corresponds to –O-H stretching of the ethanol solvent, the peak at 2975 cm^{-1} corresponds to $–CH_2-$ stretching of the ethanol solvent, and 1072 cm^{-1} and 1028 cm^{-1} peaks correspond to –C-O- stretching of the ethanol.

A.4. Outlook

The synthesized polymer PVB-N4 with endoperoxide-forming 1,4-dimethylnaphthalene each covalently bound to alcohol groups in PVB structure could potentially be used for *in vitro* chemosensitivity assay on human cancer cells, as done in this work. In any case, the concentration of endoperoxide group in PVB-N4 is high enough for a possible cytostatic effect (estimated necessary concentration > 15 μM).

The future steps would be: nanoparticles of this polymer should be made. Endoperoxides on the mentioned side-groups of such nanoparticles should be photochemically formed and their decay kinetics should be investigated. Appropriate coating, which would prevent the polymer hydrolysis reaction in aqueous media, for these nanoparticles should be searched for. Finally, the cytotoxycity of such high-endoperoxide concentration carrying nanoparticles should be tested.

8. REFERENCES

[1] D. Weldon, T. D. Poulsen, K. V: Mikkelsen, P. R. Ogilby, *Photochem. Photobiol.* **70(4)** (1999) 369-379

[2] N. Dam, T. Keszthelyi, L. K. Andersen, K. V: Mikkelsen, P. R. Ogilby, *J. Phys. Chem. A* **106** (2002) 5263-5270

[3] D. Wöhrle, M.W. Tausch, W.-D. Stohrer, *Photochemie,* Wiley-VCH, Weinheim, 1998. Ch. 4.4.1.

[4] C. Schweitzer and R. Schmidt, *Chem. Rev.*, **103 (**2003) 1685-1757.

[5] M. Tsushima, K. Tokuda, T. Ohsaka, *Anal. Chem.* **66 (**1994) 4551-4556

[6] E. Skovsen, J. W. Snyder, J. D. C. Lambert, P. R. Ogilby, *J. Phys. Chem. B*, **109** (2005) 8570

[7]M. K. Kuimova, G. Yahioglu, P. R. Ogilby, *J. Am. Chem. Soc.* **131** (2009) 332-340**.**

[8] F.S. De Rosa, M.V.L.B. Bentley, *Pharmaceut. Res.* **17** (2000) 1447-1455.

9 F. Wilkinson, W. P. Helman, A. B. Ross, *J. Phys. Chem. Ref. Data* **22** (1993) 113-262.

[10] S. E. Braslavsky, G. E. Heibel, *Chem. Rev.* **92** (1992) 1381.

[11] W. Spiller, H. Kliesch, D. Wöhrle, S. Hackbarth, B. Roeder, G. Schnurpfeil, *J. Porphyrins Phthalocyanines*, **2** (1998) 145-158.

[12] C. Pierlot, J.-M. Aubry, K. Briviba, H. Sies, P. Di Mascio *Methods Enzymol.* **319**, (2000) 3-20.

[13] J.-M. Aubry, C. Pierlot, J. Rigaudy, R. Schmidt, *Acc. Chem. Res*. **36** (2003) 668-675.

[14] A. J. Bloodworth, H. J. Eggelte, Endoperoxides in *Singlet* O_2; A. A. Frimer, (Ed.), CRC Press: Boca Raton, FL, 1985; Vol. II, Ch. 4.

[15] E. L. Clennan, C. S. Foote, in *Organic Peroxides*; W. Ando (Ed.), J. Wiley and Sons Ltd: New York, 1992. Ch. 6.

[16] J.-M. Aubry, B. Mandard-Cazin, M. Rougee, R. V. Bensasson, *J. Am. Chem. Soc.* **117** (1995), 9159-9164.

[17] M. Bobrowski, A. Liwo, S. Oldzieg, D. Jeziorek, T. Ossowski, *J.Am. Chem. Soc.* **122** (2000), 8112-8119.

[18] C. Schweitzer, R. Schmidt, *Chem. Rev.* **103** (2003), 1685-1757.

[19] V. Nardello, J.-M. Aubry, *Methods Enzymol.* **319** (2000), 50-58.

[20] C. Dufraisse, L. Velluz, *C. R. Acad. Sci.* **208** (1939) 1822.

[21] B. H. Wasserman, D. L. Larsen, *J. C. S. Chem. Comm.* **253** (1972)

[22] N. J. Turro, M.-F. Chow, J. Rigaudy, *J. Am. Chem. Soc.* **103** (1981) 7218-7224.

[23] T. Noh, H. Gan, S. Halfon, B. J. Hrnjez, N.-C. C. Yang, *J. Am. Chem. Soc.* **119** (1997) 7470-7482.

[24] M. Schäfer-Ridder, U. Brocker, E. Vogel, *Angew. Chem., Int. Ed. Engl.* **15** (1976), 228-229.

[25] J. Rigaudy, C. Breliere, P. Scribe, *Tetrahedron Lett.* **7 (**1978) 687-690.

[26] R. Schmidt, H.-D. Brauer, *J. Photochem.*, **34**, (1986) 1-12.

[27] I. Corral, L. Gonzalez, A. Lauer, W. Freyer, H. Fidder, K. Heyne, *Chem. Phys. Lett.* **452** (2008) 67-71.

[28] R. Schmidt, W. Drews, H.-D. Brauer, *J. Am. Chem. Soc.* **102** (1980), 2791-2797.

[29] R. Schmidt, H.-D. Brauer, J. Rigaudy, *J. Photochem.* **34** (1986) 197-208.

[30] K. B. Eisenthal, N. J. Turro, C. G. Dupuy, D. A. Hrovat, J. G. Langan, T. A. Jenny, E. V. Sitzmann, *J. Phys. Chem.* **90** (1986) 5168-5173.

[31] H. H. Wasserman, K. B. Wiberg, D. L. Larsen, J. Parr, *J. Org. Chem.* **70** (2005) 105-109.

[32] W. Freyer, H. Stiel, M. Hild, K. Teuchner, D. Leupold, *Photochem. Photobiol.* **66** (1997), 596-604.

[33] A. W. M. Nieuwint, J. M. Aubry, F. Arwert, H. Kortbeek, S. Herzberg, H. Joenje, *Free Radic. Res. Commun.* **1** (1985) 1

[34] I. Saito, T. Matsuura, K. Inoue, *J. Am. Chem. Soc.* **103** (1981), 188-190.

[35] C. Pierlot, J.-M. Aubry, *Chem. Commun.* **1997**, 2289-2290.

[36] K. Müller, K. Ziereis, *Arch. Pharm.* **325**, (1992), 219-223.

[37] I. Saito, R. Nagata, H. Moriyama, T. Matsuura, K. Inoue, *Free Radical Res. Commun.*, **2** (1987) 327-336.

[38] I. Saito, R. Nagata, T. Matsuura, *J. Am. Chem. Soc.* **107** (1985) 6329-6334.

[39] A. Twarowski, P. Dao *J. Phys. Chem.* **92** (1988) 5292-5297.

[40] M.J. Gannon, S.B. Brown, *Br. J. Obstet. Gynae.* **106** (1999) 1246-1254.

[41]Q. Peng, K. Berg, J. Moan, M. Kongshaug, J.M. Nesland, *Photochem. Photobiol.* **65** (1997) 235-251.

[42] F. S. De Rosa, M. V. L. B. Bentley, *Pharmaceut. Res.* **17** (2000) 1447-1455.

43 C. Fritsch, K. Lang, W. Neuse, T. Ruzicka, P. Lehmann, *Skin Pharmacol. App. Skin Physiol.* **11** (1998) 358-373.

44 N. J. Turro, *Modern Molecular Photochemistry*, University Science Books, Sausalito, USA, 1991.

45 Y.N. Konan, R. Gurny, E. Allemann, *J. Photochem. Photobiol. B Biol.* **66** (2002) 89-106.

46 T. J. Dougherty, C. J. Gomer, B. W. Henderson, G. Jori, D. Kessel, M. Korbelik, J. Moan, Q. Peng, *J. Nat. Cancer Inst.* **90** (1998) 889-905.

47 M. Oschner, *J. Photochem. Photobiol. B Biol.* **39** (1997) 1-18.

[48] K. Kalka, H. Merk, H. Mukhtar, *J. Amer. Acad. Dermatol.* **42** (2000) 389-413.

[49] J. Moan, G. Streckyte, S. Bagdonas, O. Bech, K. Berg, *Int. J. Cancer* **70** (1997) 90-97.

[50] A. S. Sobolev, D.A. Jans, A.A. Rosenkranz, *Prog. Biophys. Mol.Biol.* **73 (**2000), 51.

[51] T.J. Dougherty, *J. Clin. Laser. Med.* **14** (1996), 219–221.

[52] K. Szaciłowski, W. Macyk, A. Drzewiecka-Matuszek, M. Brindell, G. Stochel, *Chem. Rev.* **105 (**2005**),** 2647-2694.

[53] E.S. Nyman, P.H. Hynninen, *J. Photochem. Photobiol., B: Biol.* **73 (**2004) 1.

[54] H. Ali, J.E. van Lier, *Chem. Rev.* **99** (1999), 2379.

[55] F. Wilkinson, W. P. Helman, A. B. Ross, *J. Phys. Chem. Ref. Data* **22** (1993) 113-262.

[56] K. Lang, J. Mosinger, D. M. Wagnerova, *Coord. Chem. Rev.* **248** (2004) 321.

[57] J. L. Sessler, G. Hemmi, T. D. Mody, T. Murai, A. Burell, S. W. Young, *Acc. Chem. Res.* **27** (1994) 43-50.

[58] L. I. Grossweiner, M. D. Bilgin, P. Berdusis, T. D. Mody, *Photochem. Photobiol.* **70** (1999) 138-145.

[59] J. C. Kennedy, R. H. Pottier, D. C. Pross, *J. Photochem. Photobiol. B Biol.* **6 (**1990) 143-148.

[60] P.J.N. Meijnders, W.M. Star, R.S. De Bruijn, *et al*. *Lasers Med. Sci.* **11** (1996) 123-131.

[61] R. F. Donnelly, P. A. McCarron, D. Woolfson, *Recent Pat. Drug Del. Form.* **3** (2009) 1-7.

[62] H.B. Ris, H. J. Altermatt, B. Nachbur, J. C. Stewart, Q. Wang, C. K. Lim, et al. *Int. J. Cancer* **53** (1993) 141–146.

[63] L.O. Svaasand, *Med. Phys.* **12** (1985) 455–461.

[64] B. W. Henderson, S. M. Waldow, W.R. Potter, T.J. Dougherty, *Cancer Res.* **45** (1985) 6071–6077.

[65] M. Leunig, A. Leunig, P. Lankes, A.E. Goetz, *Int. J. Hyperthermia* **10** (1994) 297–306.

[66] J.P.A. Marijnissen, P. Baas, J.F. Beek, J.H. van Moll, N. van Zandwijk, W.M.Star, *Photochem. Photobiol.* **58** (1993) 92–99.

[67] P.M. Ripley, *Lasers Med. Sci.* **11** (1996) 71–78.

[68] J. X. Zhou, X. Hou, S. J. Tsai, K. X. Yang, R. G. Michel, *Anal. Chem.* **69 (**1997) 490–499.

[69] D. Dolphin, *Can. J. Chem.* **72** (1994) 1005-1013.

[70] D. J. Robinson, P. Collins, M. R. Stringer, *et al*. *Acta Dermatol. Venereol.* **79** (1999) 451-455.

[71] E. Schick, A. Ruck, W.-H. Boehncke, R. Kaufmann, *J. Dermatologic Treat.* **8** (1997) 17-19.

[72] M. Wainwright, *J. Antimicrob. Chemotherapy* **42** (1998) 13-28.

[73] R. F. Donnelly, P. A. McCarron, D.I.J. Morrow, S. A. Sibani, A. D.Woolfson, *Expert Opin. Drug Del.* **5** (2008) 757-766.

[74] M. Korbelik, *J. Clin. Laser Med. Surg.* **14** (1996) 329.

[75] M.L. Agarwal, M. E. Clay, E. J. Harvey, H. H. Evans, A. R. Antunez, N. L. Oleinick. *Cancer. Res.* **51** (1991) 5993–5996.

[76] X. Y. He, R. A. Sikes, S. Thomsen, L. W. Chung, S. L. Jacques, *Photochem. Photobiol.* (1994) **59** 468–473.

[77] S. I. Zaidi, N. L. Oleinick, M. T. Zaim, H. Mukhtar, *Photochem. Photobiol.* **58** (1993) 771–776.

[78] J. Webber, Y. Luo, R. Crilly, D. Fromm, D. Kessel, *J. Photochem. Photobiol. B* **35 (**1996) 209–211.

[79] D.L. Vaux, A. Strasser, *Proc. Natl. Acad. Sci. U S A* **93** (1996) 2239–2244.

[80] T.H. Foster, R.S. Murant, R.G. Bryant, R.S. Knox, S.L. Gibson, R. Hilf, *Radiat. Res.* **126** (1991) 296–303.

[81] B.W. Henderson, V.H. Fingar, *Photochem. Photobiol.* **49** (1989) 299–304.

[82] D. K. Chatterjee, L. S. Fong, Y. Zhang, *Adv. Drug Deliv. Rev.* **60** (2008) 1627-1637.

[83] R. Duncan, *Nature Rev. Drug Discov.* **2** (2003) 347-360.

[84] E. Allemann, N. Brasseur, O. Benrezzak, J. Rousseau, S.V. Kudrevich, R.W. Boyle, J.C. Leroux, R. Gurny, J.E. Van Lier, *J. Pharm. Pharmacol.* **47** (1995) 382–387.

[85] A.C. Samia, X. Chen, C. Burda, *J. Am. Chem. Soc.* **125** (2003) 15736–15737.

[86] R. Bakalova, H. Ohba, Z. Zhelev, M. Ishikawa, Y. Baba, *Nat. Biotechnol.* **22** (2004) 1360–1361.

[87] W. Chen, J. Zhang, *J. Nanosci. Nanotechnology* **6** (2006) 1159–1166.

[88] P. Zhang, W. Steelant, M. Kumar, M. Scholfield, *J. Am. Chem. Soc.* **129** (2007) 4526–4527.

[89] Y.N. Konan-Kouakou, R. Boch, R. Gurny, E. Allemann, *J. Control. Release* **103** (2005) 83–91.

[90] A. Khdair, B. Gerard, H. Handa, G. Mao, M.P.V. Shekhar, J. Panyam, *Mol. Pharmaceutics,* **5** (2008) 795-807.

[91] R.L. Juliano, *Adv. Drug Deliv. Rev.* **2** (1988) 31–54.

[92] P. H.M. Hoet, I. Brüske-Hohlfeld, O. V. Salata, *J. of Nanobiotechnology* **2** (2004) 12-26.

[93] N. Sanvicens, M. P. Marco, *Trends Biotechnol.* **26** (2008) 425-433.

[94] L. Araujo, R. Lobenberg, J. Kreuter, *J. Drug Target.* **6** (1999) 373-385.

[95] M. Tijerina, K.D. Fowers, P. Kopeckova`, J. Kopecek, *Biomaterials* **21** (2000) 2203–2210.

[96] N.S. Soukos, M.R. Hamblin, T. Hasan, *Photochem. Photobiol.* **65** (1997) 723–729.

[97] L. Morlet, V. Vonarx, M.T. Foultier, A. Gouyette, C. Steward, P. Lenz, T. Patrice, *J. Photochem. Photobiol. B. Biol.* **39** (1997) 249–257.

[98] P. Westermann, T. Glanzmann, S. Andrejevic, D.R. Braichotte, M Forrer, G.A. Wagnieres, Ph. Monnier, H. van den Berg, J.-P. Mach, S. Follio *Int. J. Cancer* **76** (1998) 842–850.

[99] R. Hornung, M.K. Fehr, J. Monti-Frayne, T.B. Krasieva, B.J. Tromberg, M.W. Berns, Y. Tadir, *Photochem. Photobiol.* **70** (1999) 624–629.

[100] N. Brasseur, R. Ouellet, C. La Madeleine, J.E. Van Lier, *Br. J. Cancer* **80** (1999) 1533–1541.

[101] P. Juzenas, W. Chen, Y.-P. Sung, M. A. N. Coelho, R. Generalov, N. Generalova, I. L. Christensen, *Adv. Drug Deliver. Rev.* **60** (2008) 1600-1614.

[102] D. Gal, P.C. MacDonald, J.C. Porter, E.R. Simpson, *Int. J. Cancer* **28** (1981) 315–319.

[103] Th.J.C. van Berkel, *J. Control. Release* **24** (1993) 145–155.

[104] W.G. Love, M.J. Cook, D.A. Russell: US20036630128B1 (**2003**).

[105] W.G. Love, D. Brundish, D. Rhys-Williams, X.D. Feng, B. Pugin: US20077244841 B2 (**2007**).

[106] P.W. Taylor, W.G. Love, B.C.H. van der Zanden: US5616602 (**1997**).

[107] M. A. Campbell, A. Gleischner, R. Alsbury, D. Horvath, J. Suttle, *Plant Mol. Biol.* **73** (2010) 181-189.

[108] *Federal Register*, **60** (1995) 7456-7457.

[109] S. Ben-Shabat, Y.Itagaki, S. Jockusch, J. R. Sparrow, N. J. Turro, K. Nakanishi, *Angew. Chem., Int. Ed. Engl.* **41**, (2002), 814-817.

[110] R .Cailleau, R. Young, M. Olive, W.J. Reeves, *J. Natl. Cancer Inst.* **53** (1974) 661-673

[111] G. Bernhardt, H. Reile, H. Birnböck, T. Spruss, H. Schönenberger, *J. Cancer Res. Clin. Oncol*. **118** (1992) 35-43.

[112] U. Bogner, G. Bernhardt, G.Knör, *Endoperoxidhaltige Nanosysteme mit Anpassung der Singulett Sauerstoff-Freisetzung für pharmazeutische Anwendungen,* Patentanmeldung (DE102009034279.6)

[113] *CrysAlis CCD,* Oxford Diffraction Ltd., Version 1.171.30.3 (release 12-05-2006 CrysAlis171.NET).

[114] P. H. Gore, J. A. Hoskins, *J. Chem. Soc. (C)* **1971** 3347-3350.

[115] S. Nagl, Dissertation, Universität Regensburg, 2008, http://epub.uni-regensburg.de/10753/1/Dissertation_Stefan_Nagl.pdf

[116] Oregon Medical Laser Center, http://omlc.ogi.edu/spectra/mb/index.html, accessed on 2010-02-22.

[117] R. R. C. New, *Liposomes, a practical approach*, Ed. R. R. C. New, Oxford University Press, New York, 1990, Ch. 3, p. 105-107.

[118] A. Mueller, C. Serain, *Acc. Chem. Res.* **33** (2000) 2-10.

[119] Kuraray Specialities Europe – Mowital – Polyvinyl butyral of superior quality 2003, www.kuraray-am.com/pvoh-pvb/downloads/Mowital_brochure.pdf, accessed on 2010-04-09.

[120] Kuraray Specialities Europe – Mowital –Technical datasheet, http://www.kuraray-am.com/pvoh-pvb/downloads/Technical_Data_Sheet_Mowital_EN.pdf, accessed on 2010-08-05.

[121] J. M. Kuerner, I. Klimant, C. Krause, H. Preu, W. Kunz, O. S. Wolfbeis, *Bioconjugate Chem.* **12** (2001) 883-889.

[122] S.M. Borisov, T. Mayr, G.Mistlberger, K. Waich, K. Koren, P. Chojnacki, I. Klimant, *Talanta* **79** (2009) 1322–1330.

[123] M. Sildrai, L. Hadel, R. R. Saws, S. Husain, K. Krogh-Jespemn, J. D. Westbrook, G. R. Bird, *J. Phys. Chem. B*, **96** (1992) 7988-7996.

[124] Molecular Probes, http://www.invitrogen.com/site/us/en/home/support/Product-Technical-Resources/Product-Spectra.10046.html, accessed on 2010-07-02.

[125] Sigma-Aldrich, 1,4-Dimethylnaphthalene Safety datasheet, http://www.sigmaaldrich.com/MSDS/MSDS/DisplayMSDSPage.do, accessed on 2010-02-05.

[126] J. B. Birks, *Photophysics of Aromatic Molecules*, Wiley, London, 1970, p.106.

[127] R. R. C. New, *Liposomes, a practical approach*, Ed. R. R. C. New, Oxford University Press, New York, 1990, Ch. 1, p.1-32

[128] R. D. Issels, S.W. Prenninger, A. Nagele, E. Boehm, H. Sauer, K.W. Jauch, H. Denecke, H. Berger, K. Peter, W. Wilmanns, *J. Clin. Oncol.,* **8** (1990)1818-1829.

[129] G. Gregoriadis, D.E. Neerunjun, *Eur. J. Biochem*. **47** (1974) 179-185.

[130] S.L. Fossheim, K. A. Il'yasov, J. Hennig, A. Bjørnerud, *Acad. Radiol.* **7** (2000) 1107-1115.

[131] D.D. Lasic, *Liposomes from Physics to Applications,* Elsevier, Amsterdam, 1993, p. 63-107.

[132] V. P. Torchilin, *Adv. Drug. Deliv. Rev.* **58**(14) (2006) 1532-1555.

[133] J. W. Park, *Breast Cancer Res.* **4** (2002) 95-99.

[134] G. Jori, E. Reddi, I. Cozzani, L. Tomio. *Br. J. Cancer* **53** (1986) 615–621.

[135] G. Jori, *J. Photochem. Photobiol. B* **36** (1996) 87–93.

[136] T. M. Allen, P. R. Cullis, *Science* **303** (2004) 1818-1822.

[137] V. Balasubramaniyan, *Chem. Rev.* **66** (1966) 567-641.

[138] M. H. Falk, R. D. Issels, *Int. J. Hypertherm.* **17(1)** (2001) 1-18.

[139] D. S. Kapp, G. M. Hahn, R. W. Carlson, Principles of Hyperthermia. In R. C. Bast, D. W. Kufe, R. E. Pollock et al., editors, *Cancer Medicine*, 5th ed. : B. C. Decker Inc., Hamilton, 2000.

[140] R. Bauer, W. J. Finkenzeller, U. Bogner, M. E. Thompson, H. Yersin, *Org. Electr.* **9(5)** (2008) 641. and references 21, 29 and 31 therein.

[141] Vogelhuber, P. Rotunno, E. Magni, A. Gazzaniga, T. Spruss, G. Bernhardt, A. Buschauer, A. Göpferich, *J. Control. Release* **73 (1)**, (2001) 75-88.

[142] J. Rejman, V. Oberle, I. S. Zuhorn, D. Hoekstra, *Biochem. J*. **337** (2004) 159-169.

[143] D. Wöhrle, M.W. Tausch, W.-D. Stohrer, *Photochemie,* Wiley-VCH, Weinheim, 1998. p. 448

[144] W. Spiller, H. Kliesch, D. Wöhrle, S. Hackbarth, B. Roder, G. Schnurpfeil, *J. Porphyrins Phthalocyanines*, **2** (1998) 145-158.

[145] *The Porphyrin Handbook*, Eds. K. M. Kadish, K. M. Smith, R. Guillard, Academic Press, San Diego, 1999, Vol. 1 Ch. 2.

[146] M. D. Maree, N. Kuznetsova, T. Nyokong, *J. Photoch. Photobio. A Chem***, 140** (2001) 117-125.

[147] W. Spiller, H. Kliesch, D. Wöhrle, S. Hackbarth, B. Roder, G. Schnurpfeil, *J. Porphyrins Phthalocyanines*, **2** (1998) 145-158.

[148] T. Wilson, A. U. Khan, M. M. Mehrothra, *Photochem. Photobiol.* **43 (**2008) 661-662.

[149] F. Käsermann, C. Kempf, *Antiviral Res.* **38** (1998) 55-62.

[150] S. R. Meshnick, T. E. Taylor, S. Kamchonwongpaisan, *Microbiol. Rev.* **60 (**1996) 301-315.

[151] G. Dyker, M. Hagel, G. Henkel, M. Köckerling, C. Nather, S. Petersen, G. P. Schiemenz, *Z. Naturforsch., Teil B*, **56** (2001) 1109–1116.

[152] J. Clayden, C. McCarthy, M. Helliwell, *Chem. Commun.* **1999** 2059-2060.

[153] A. J. Kirby, J. M. Percy, *Tetrahedron*, **44** (1998) 6903-6910.

[154] M. R. Kurban, *J. Chem. Phys.* **130** (2009) 104502.

[155] M. Kasha, A. Sytnik, B. Dellinger, *Pure & Appl. Chem.* **65** (1993) 1641-1646.

[156] S. L. Chang, T.-M. Wu, *Chem. Phys. Lett.* **324** (2000) 381-388.

[157] S. Mabrey-Gaud, *Differential scanning calorimetry of liposomes,* in: "Liposomes: from physical structure to therapeutic applications" Ed. C.G. Knight, Elsevier, Amsterdam, 1981, p. 105-138.

[158] J. Baier, M. Maier, R. Engl, M. Landthaler, W. Bäumler, *J. Phys. Chem. B*, **109** (2005) 3041.

[159] T. Maisch, J. Baier, B. Franz, M. Maier, M. Landthaler, R.-M. Szeimies, W. Bäumler *Proc. Natl. Acad. Sci.* **104** (2007) 7223-7228.

[160] F.-P. Kalz, Dissertation, Universität Regensburg, 2006, http://epub.uni-regensburg.de/12310/1/DissertationvonFranz_Peter_Kalz.pdf.

[161] G. Storm, D. J. A. Crommelin, *Pharm. Sci. Technol. Today* **1** (1998) 19-31.

[162] H. Maeda, G. Y. Bharate J. Daruwalla, *Eur. J. Pharm. Biopharm.* **71** (2009) 409-419.

[163] A. S. Ziegler, *Med. Monatsschrif. Pharm.* **31** (2008) 455-468.

[164] A. M. Agrawal, R. V. Manek, W. M. Kolling, S. H. Neau, *AAPS Pharm. Sci. Tech.* **4** (2005) 60.

[165] K. Mazeau, *Cellulose***, 12** (2005) 339-349.

[166] H. Gollwitzer, Dissertation, Technischen Universität München, 2002, http://tumb1.biblio.tu-muenchen.de/publ/diss/me/2002/gollwitzer.pdf.

[167] K. König, M. Teschke, B. Sigusch, E. Glockmann, S. Eick, W. Pfister, *Cell Mol. Biol.* **46** (2000) 1297-1303.

[168] M. Grinholc, B. Szramka, K. Olender, A. Graczyk, *Acta Biochim. Pol.* **54** (2007) 665-670.

[169] J. M. Rosenholm, E. Peuhu, J. E. Eriksson, C. Sahlgren, M. Linden, *Nano. Lett.* **9** (2009) 3308-3311.

[170] G. Kaul, M. Amiji, *J. Drug Target.* **12** (2004) 585-591.

[171] R. A. Jain, *Biomaterials*, **21** (2000) 2475–2490.

[172] M. Zeisser-Labouebe, N. Lange, R. Gurny, F. Delie, *Int. J. Pharm.* **326** (2006) 174–181.

[173] Y. N. Konan, M. Berton, R. Gurny, E. Allemann, *Eur. J. Pharm. Sci.* **18** (2003) 241–249.

[174] Y. N. Konan, R. Cerny, J. Favet, M. Berton, R. Gurny, E. Allemann, *Eur. J. Pharm. Biopharm.* **55** (2003) 115–124.

[175] E. Ricci-Junior, J. M. Marchetti, *J. Microensapsul.* **23** (2006) 523-538.

[176] F. Luderer, M. Lobler, H. W. Rohm, C. Gocke, K. Kunna, K. Kock, H. K. Kroemer, W. Weitschies, K.-P. Schmitz, K. Sternberg, *J. Biomater. Appl.* published online 17 March 2010, DOI: 10.1177/0885328209360696.

[177] I. Roy, T. Y. Ohulchanskyy, H. E. Pudavar, E. J. Bergey, A. R. Oseroff, J. Morgan, T. J. Dougherty, P. N. Prasad, *J. Am. Chem. Soc.* **125** (2003) 7860–7865.

[178] B. Neises, W. Steglich, *Angew. Chem.* **90** (1978) 556-557.

[179] P. Antoni, Y. Hed, A. Nordberg, D. Nyström, H. von Holst, A. Hult, M. Malkoch, *Angew. Chem. Int. Ed.* **48** (2009) 2126 –2130.

[180] C. Schramm, B. Rinderer, *J. Mater. Sci.* **43** (2008) 4215–4219.